Collective Phenomena in Strongly Correlated Electron Systems

By

Ian Peter McCulloch

November 6, 2001

Corrected Version: May 20, 2002

A thesis submitted for the degree of Doctor of Philosophy

of the Australian National University

Declaration

I certify that the work contained in this thesis is my own original research, produced in collaboration with my supervisor – Doctor M. Gulácsi. All material taken from other references is explicitly acknowledged as such. I also certify that the work contained in this thesis has not been submitted for any other degree.

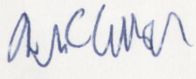

Ian McCulloch

Acknowledgments

First and foremost I would like to thank my supervisor Doctor Miklós Gulácsi, who initially inspired me to work in condensed matter physics almost five years ago and has had a defining influence ever since.

I will always remember fondly the summer I spent working at KTH Stockholm on the invitation of Professor Anders Rosengren. Thanks also to the graduate students at Theoretical Physics, KTH, especially Aušrius Jouzapavičius and Jirij Šmakov, for showing me around Stockholm. Progress on the Kondo lattice calculations may have been slow, but it was ultimately fruitful. Thanks also to Sergio Caprara for lots of useful conversations while I was learning the DMRG method.

I would also like to thank Alan R. Bishop for the invitation to visit Los Alamos National Laboratory to work on the striped phase of the $t-J$ model. Many thanks to the members of T-11 and CNLS, especially Gerardo Ortiz, Ivar Martin and Jim Gubernatis, from whom I learned a lot about how to approach numerical calculations.

I would like to thank my advisors Professor Vladimir V. Bazhanov and Professor Stjepan Marcelja. Although we did not have a huge amount of contact during my candidature, the occasional feedback was useful and it was reassuring to know that there was expert direction available as needed.

I am grateful to John Ballard for the huge amount of guidance provided during my PhD, especially during the production of this thesis. Conversations with John provided much of the basis of my views on the nature of science.

Thanks to the staff of the Australian National University Supercomputer Facility for advice and assistance in running the DMRG program on the APAC SC machine. This machine came at a critical time in my research and was used to obtain virtually all of the numerical results presented in this thesis. The amount and quality of the results obtained in the short time since its 'birth' makes the previous three years of calculations pale into insignificance.

Thanks to Paul Huddleston for making living in Canberra much more exciting

and proof-reading parts of this thesis.

Finally, no list of acknowledgements would be complete without expressing sincere thanks to my parents Professor Peter McCulloch and Rosemary McCulloch and my sisters Wendy and Fiona for endless support and encouragement. Special thanks to my Father. When all is said and done, you have been the biggest influence on my life and I am glad that I inherited your love of physics.

Abstract

In recent years the discovery of new types of of materials with novel electronic properties has given rise to a new field of theoretical condensed matter physics. These systems are characterized by strong interactions, collective excitations and low effective dimension. These properties mean that traditional theoretical techniques, such as perturbation expansions and mean-field approximations, often fail. On the other hand, the remarkable range of anomalous behavior in these systems produces such effects as organic conductors, high-temperature superconductivity, heavy-fermion metals, fractional charges *etc.* , making these among the most interesting and potentially useful materials in nature. Many quite simple models have been put forward as a basis for understanding these systems. Unfortunately, even though the models are simple, the solutions are not. In many cases, the only way to calculate the properties of these models is by numerical techniques. The most successful numerical techniques have been Monte-Carlo simulation and, more recently, the Density-Matrix Renormalization-Group (DMRG). The latter technique is the main focus of this thesis.

Historically it has been very difficult to deal with higher symmetries in either analytical or numerical calculations. For example, while the Clebsch-Gordan coefficients are extremely useful for few-body total spin states, they do not lend themselves easily to constructing *thermodynamic* eigenstates of total spin. Numerically, the situation is similar. Monte-Carlo and exact diagonalization calculations do not lend themselves easily to the utilization of total spin. Hence it is a refreshing surprise that these symmetries are relatively easy to incorporate into DMRG. This thesis describes the extensions to the DMRG algorithm required to utilize $SU(2)$ symmetries of spin and pseudospin and also non-Abelian geometric lattice symmetries. This is the main technological result of this thesis, which has enabled significant improvements in the accuracy and scope of the numerical calculations.

In this thesis, the properties of several models of strongly correlated behavior are examined using the symmeterized DMRG approach. The one dimensional Kondo

lattice model has been extensively studied for two decades, but this thesis shows that we are still far from understanding the complexities of the model. In particular it is shown here that even the ground state phase diagram is more complex than previously thought. The numerical calculations show the existence of an additional, previously unrecognized, ferromagnetic regime. The work also emphasizes the importance of spin polarons in understanding the model. Spin polarons are collective states which arise when a cloud of electrons screen the spin of the localized moments. Due to excess localized spins the polarons are locally ferromagnetic; the paramagnetic phase of the Kondo lattice arises when neighboring polarons align non-parallel. For a smaller value of the Kondo coupling, the conduction electrons have a larger kinetic energy which makes the polarons more mobile, forcing them to align parallel. This is the origin of the additional ferromagnetic phase.

There has been much recent excitement over the discovery of the striped phase in high T_c superconductors. This was heightened with the discovery, in a DMRG study by Steven White, of a striped phase in the two dimensional $t-J$ model. However it is still far from clear what the relationship is between stripes and superconductivity; more recent experimental work suggests that, instead of providing a mechanism for superconductivity, stripes in fact *inhibit* superconductivity. This thesis extends the accuracy of the DMRG calculations on the two dimensional $t-J$ model and goes some way to elucidating the properties of the striped phase. The use of symmetries of the $t-J$ model in the calculation leads naturally to a geometric view of stripe formation and the recent ideas that stripe formation is due to a hidden geometric ordering arising from sublattice parity. From this point of view, the same ordering that leads to spin-charge separation in one dimensional systems gives rise to stripe formation in two dimensions.

List of Publications

The bulk of the original research content of this thesis is contained in Chapters 2, 3 and 4 and appendix A. Various parts of this research are, or are soon to be, published as follows.

The DMRG results for the comparison with the matrix product method from chapter 1, section 1.4.3 will appear in the paper:

- Comment on "J. Dukelsky, M. A. Martín–Delgado, T. Nishino and G. Sierra: Equivalence of Variational Matrix Product Method and the Density Matrix Renormalization Group" *To be submitted to Europhys. Lett.*

The results on the extension of the DMRG algorithm to non-Abelian symmetries described in chapter 2 appear in the papers:

- I. P. McCulloch and M. Gulácsi: Density matrix renormalization group method and symmetries of the Hamiltonian, *Aust. J. Phys.* **53** 4, (2000).

- I. P. McCulloch and M. Gulácsi: Total Spin in the density matrix renormalization group algorithm, *Phil. Mag. Lett.* **81** 447, (2001).

- I. P. McCulloch and M. Gulácsi: The non-Abelian Density Matrix Renormalization Group Algorithm, *Euro. Phys. Lett.* **57** 852, (2002).

The results for the Kondo lattice model described in chapter 3 appear in the papers:

- I. P. McCulloch, M. Gulácsi, S. Caprara, A. Jouzapavičius and A. Rosengren: Phase diagram of the 1D Kondo lattice model, *J. Low Temp. Phys* **117** 323, (1999).

- I. P. McCulloch, A. Jouzapavičius, A. Rosengren and M. Gulácsi: Ferromagnetism in Kondo lattice models, *Phil. Mag. Lett.* **81** 869, (2001).

- A. Juozapavicius, I. P. McCulloch, M. Gulácsi and A. Rosengren: Ferromagnetic phases in the Kondo lattice model, *to appear in Phil. Mag. B.*

- A. Jouzapavičius, I. P. McCulloch, M. Gulácsi and A. Rosengren: On the dilute Kondo lattice model, *to appear in Phys. Rev. B.*

- I. P. McCulloch, A. Jouzapavičius, A. Rosengren and M. Gulácsi: Localized spin ordering in Kondo lattice models, *Phys. Rev. B* **65** 052410, (2002).

- I. P. McCulloch and M. Gulácsi: New phases in the 1D periodic Anderson model, *in preparation.*

The results for the two–dimensional $t-J$ model described in chapter 4 appear in the paper:

- I. P. McCulloch, A. R. Bishop and M. Gulácsi: Density matrix renormalization group algorithm and the two-dimensional $t-J$ model, *Phil. Mag. B* **81** 1603, (2001).

Contents

Introduction

The theoretical description of strongly correlated electrons poses a formidable problem. Exact solutions are usually impossible, except in certain one-dimensional models. Fortunately, exact solutions are rarely required when comparing theory with experiment. Most measurements only probe correlations on energy scales that are small compared with the Fermi energy E_F, so that only the *low-energy* sector of a given model is of importance.

Correlated fermions in three dimensions are a well-understood problem. The theoretical description, given by Fermi-liquid theory, becomes asymptotically exact at low energies and small wave vectors. The key observation behind Fermi liquid theory is that the macroscopic properties involve only excitations of the system on energy scales (temperatures) small compared with the Fermi energy. The state of the system can be specified in terms of the Fermi surface of the ground state and its low-lying elementary excitations, which are pictured as a rarefied gas of 'quasi-particles'. These quasi-particles evolve continuously out of the states of a free Fermi gas when the interactions are adiabatically switched on. Although the dynamical properties are renormalized by the interaction, the quasi-particles remain in one-to-one correspondence with the bare particles.

In interacting one-dimensional systems, the low-energy excitations are collective density fluctuations and involve large numbers of electrons acting coherently. This destroys the one-to-one correspondence between non-interacting and interacting quasi-particles. The non-interacting quasi-particles obviously remain particle-like in 1D, but the interacting quasi-particles have a bosonic character. The breakdown of Fermi-liquid theory is also seen in the typical divergence of second-order perturbation theory in one dimension. This signals the lack of adiabatic continuity between the non-interacting and the interacting quasi-particles. On a more formal level, the Green function of an electron is

$$G(\boldsymbol{k},\omega) = \frac{1}{\epsilon_0(\boldsymbol{k}) - \omega - \Sigma(\boldsymbol{k},\omega)}\,, \tag{0.1}$$

where $\epsilon_0(\boldsymbol{k})$ is the bare dispersion and $\Sigma(\boldsymbol{k},\omega)$ is the self-energy containing all the many-body effects. The poles of the Green function give the single-particle excitation energies and the imaginary part of the self-energy provides the damping of these excitations. $\Sigma(\boldsymbol{k},\omega)$ is continuous in $\boldsymbol{k}$ and for $\boldsymbol{k}$ fixed, a smooth function of ω. This guarantees solutions of the equation

$$\epsilon_0(\boldsymbol{k}) - \omega - \Sigma(\boldsymbol{k},\omega) = 0 \,, \tag{0.2}$$

which determines the single-particle excitation energies. In Fermi-liquid theory, there is a single solution to this equation; the quasi-particle pole with finite residue.

In one-dimension, expanding the self-energy to second order in perturbation theory yields *two* poles of the Green function. This violates the single-pole assumption built into Fermi-liquid theory and heralds the phenomena of *spin-charge* separation, ubiquitous in one-dimensional systems. The residue of the poles of the Green function vanish, therefore the momentum distribution is continuous and the system does not support the low-energy quasi-particle excitations characteristic of Fermi liquids, instead giving rise to collective bosonic charge and spin fluctuations. The theory of the one-dimensional electron sea was pioneered by Haldane [1] and has been developed since by many people. It is known as Luttinger-liquid theory, in an analogy with its higher dimensional cousin.

The validity of the Fermi-liquid description for interacting electrons is well accepted for three-dimensional systems, while the Luttinger-liquid description applies to one-dimensional systems. To date, the understanding of two-dimensional systems remains unsatisfactory. Prior to the discovery of the high-temperature superconductors, there were only a few studies of interacting two-dimensional systems, mostly in the low-density limit, which turns out to be a Fermi-liquid state [2].

The search for a non-Fermi-liquid ground state in two-dimensional systems arose from the theoretical problems posed by the high-temperature superconductors and is mainly credited to Anderson [3]. The low dimensionality of the cuprates and the absence of characteristic Fermi-liquid behavior in the optical conductivity and resistivity led Anderson to the suggestion that there is a qualitative difference between the normal-phase ground state and that of other superconducting materials.

The breakdown of Fermi-liquid theory in low dimensional systems of interacting electrons implies the need for powerful non-perturbative methods [4]. With the advent of high-performance computing, numerical simulation has become one such method.

The main numerical algorithms in use today for the solution of models of strongly correlated electrons are various forms of Monte Carlo, exact diagonalization and

the Density-Matrix Renormalization-Group (DMRG). Exact diagonalization calculations are necessarily limited by the exponentially large Hilbert space of lattice models, and so is useful only for very small systems. Monte Carlo calculations are usually performed at finite-temperature and are plagued by the so-called fermionic sign problem, where the anticommutation of fermions causes the weight function to oscillate in sign, with exponential loss of precision (for a review, see reference [5] and references cited therein).

The DMRG algorithm was invented by Steven White [6], and has been in existence for under a decade. In that time the formulation has been under constant development. The initial formulation described an algorithm for solving the ground state of the spin 1/2 Heisenberg chain [6]. Since then, the algorithm has been applied to many models, from one-dimensional fermionic systems [7, 8], ladder models [9] and some two-dimensional models both in real-space [10–12] and momentum-space [13, 14]. In addition, generalizations of the DMRG algorithm have been proposed, for the calculation of thermodynamic properties [15], 2D classical systems [16], phononic models [17], dynamical correlation functions [18], and even for diverse applications such as nuclear structure calculations [19] and asymptotic freedom in high-energy physics [20]. In recent years it has proven to be the most accurate tool for the numerical solution of one-dimensional models. For two-dimensional models, current DMRG calculations are of similar accuracy to Monte Carlo calculations. Monte Carlo calculations have the advantage of being essentially independent of the dimensionality of the lattice, while real-space DMRG calculations suffer greatly when long-range interactions are introduced, which, due to the nature of the algorithm, are inevitable when the algorithm is applied to higher-dimensional models. However, two-dimensional DMRG calculations are still possible, if enough basis states can be kept to achieve the required accuracy. Unfortunately, increasing the number of basis states kept in the DMRG calculation causes a substantial increase in the amount of computation time required.

It is clear then that one line of progress is to improve the DMRG algorithm itself, so that more accuracy can be achieved with fewer basis states. One way of doing this is to utilize more of the symmetries of the system. In the original DMRG algorithm [6], the only symmetries that are allowed by the construction are compact, Abelian Lie algebras (hence isomorphic to $U(1)$) or Abelian finite groups (such as reflection symmetries, isomorphic to Z_2). In chapter 2, the extension to non-Abelian Lie algebras is presented, which significantly increases the accuracy of all DMRG calculations for Hamiltonians that admit such a symmetry group. While this method has so far only been tried in real-space calculations, the procedure also

applies to non-Abelian finite groups, such as the dihedral D_L symmetry of a one-dimensional ring, which should substantially increase the accuracy of momentum-space calculations. The technique should also apply to other types of symmetries, such as supersymmetric models and quantum group symmetries, without additional complications.

The structure of this thesis is as follows. Chapter 1 reviews the current state of development of the DMRG algorithm as applied to the ground state of one- or two-dimensional finite lattices. The optimizations required to produce an efficient algorithm are discussed in detail, along with the convergence properties and the important work of Östlund and Rommer [21] on the form of the wavefunction obtained by DMRG. Chapter 2 describes the generalization of the DMRG algorithm to conserve non-Abelian global symmetries, which is the main technical result in this thesis and was essential for the success of the applications of the non-Abelian DMRG algorithm, presented in chapters 3 and 4. The usefulness of the algorithm is shown by some calculations on the one-dimensional Hubbard model, as the symmetry group is enlarged from $U(1) \times U(1)$ to $SO(4)$. Some of the efficiency issues with real-space DMRG in higher dimensions can be resolved by a momentum-space formulation. The potential for utilizing non-Abelian discrete lattice symmetries in a momentum space formulation is an exciting area of future research, therefore this chapter also contains a discussion of the relevant issues, although as yet no calculations have been performed utilizing non-Abelian lattice symmetries. Chapter 3 contains the bulk of the numerical calculations presented in this thesis, and describes the physics and numerical physics of the Kondo lattice model [22] in one dimension. The most interesting new result is the discovery of a previously unrecognized region of ferromagnetism for intermediate coupling strength, at conduction band filling $0.5 \lesssim n \lesssim 1$. This ferromagnetic region is also shown to exist in the periodic Anderson model. Chapter 4 describes an application of DMRG to a two-dimensional system, to determine the properties of the striped phase in the two-dimensional $t - J$ model. The $t - J$ model was proposed by Anderson [23] and Zhang and Rice [24] to be an effective model of the copper-oxide planes in the cuprate high-temperature superconductors, and it is therefore important to determine the ground state properties of this model.

Chapter 1

The Density-Matrix Renormalization-Group Algorithm

This chapter is a review of the history and current state of the art of the Density-Matrix Renormalization-Group method, concentrating on the particular algorithm (finite-size ground state DMRG) used in the numerical calculations presented in later chapters. The bulk of the material in this chapter is a summary of several variations on the DMRG algorithm, taken from pre-existing literature. In addition to the original articles cited explicitly in the text, many review articles [25–27] and useful descriptions of implementations of DMRG [28,29] have appeared. Most of the original work presented on the DMRG algorithm itself appears in chapter 2, with applications discussed in chapters 3 and 4. However portions of this chapter, sections 1.3.2 and 1.6 also contain original work. Also, additional numerical results have been obtained to compliment the reported results in several places, most notably in section section 1.4.3, where the obtained results were in disagreement with the previous publications.

1.1 Historical Background

The Density-Matrix Renormalization-Group formulation was invented by Steven White [6], who was working on the problem of why the Wilson Numerical Renormalization-Group (NRG) [30] procedure, which had been so successful in solving the single impurity Kondo problem, fails so badly when applied to other quantum lattice models. Wilson solved the single impurity Kondo problem by mapping the three-dimensional model onto a one-dimensional chain, by way of a real-space renormalization-group transformation. Thereafter, the numerical calculation is per-

formed on a one-dimensional effective Hamiltonian on a N-site lattice,

$$H_N = \Delta^{(N-1)/2} \left[\sum_{\alpha=\{\uparrow,\downarrow\},n=0}^{N-1} \Delta^{-n/2} (c^\dagger_{\alpha,n} c_{\alpha,n+1} + c_{\alpha,n+1} c^\dagger_{\alpha,n}) - J \sum_{\alpha,\beta} c^\dagger_{\alpha,0} c_{\beta,0} \boldsymbol{\sigma}_{\alpha\beta} \cdot \boldsymbol{S} \right], \tag{1.1}$$

where $c^\dagger_{\alpha,i}$ is the conduction electron creation operator of spin α at site i and $\boldsymbol{S}$ is the impurity spin. $\Delta^{\frac{N}{2}}$ is the width of the N'th 'shell' of the three dimensional model; the actual value of Δ is arbitrary (but ≥ 1) and can be tuned numerically. The purpose of the factor $\Delta^{(N-1)/2}$ is so that the smallest term in H_N is of order unity, this term being $c^\dagger_N c_{N-1} + c_{N-1} c^\dagger_N$. The addition of one lattice site to the one-dimensional effective model corresponds to increasing the size of the three-dimensional lattice by a factor $\Delta^{\frac{1}{2}}$, via a renormalization-group transformation,

$$H_{N+1} = T[H_N] = \Delta^{\frac{1}{2}} H_N + \sum_\alpha (c^\dagger_{\alpha,N+1} c_{\alpha,N} + c^\dagger_{\alpha,N} c_{\alpha,N+1}) - E_{G,N+1} , \tag{1.2}$$

where $E_{G,N+1}$ is chosen so that the ground state energy of H_{N+1} is zero. This is a true renormalization-group procedure, in the sense that the energy eigenvalues will flow toward the fixed points as the calculation proceeds. The main focus of the NRG is then to solve this one-dimensional lattice Hamiltonian. The essential feature of Wilson's solution is to consider a group of lattice sites to be a "block" and diagonalize the Hamiltonian for that block to find a set of eigenstates. This set of eigenstates is then truncated, keeping only the m states of lowest energy. Then the Hamiltonian for a larger block is constructed in this basis and the process repeats. The question becomes what to do with the boundary conditions (BCs) at the join of the two blocks. For the single impurity Kondo problem, excellent results were achieved by simply taking open boundary conditions, corresponding to an infinite potential at each end of the lattice. It turns out though, that this success depends critically on the nature of the specific renormalization-group transformation Eq. (1.2). The same approach was tried several times for other problems without success. For example, Lee [31] implemented this scheme for the problem of Anderson localization on a 2-dimensional lattice. The major result, that there is a critical parameter that separates scaling toward extended or localized states, was later shown by Lee and Fisher [32] to be incorrect.

The main focus since this time has been on solving one-dimensional models directly, without using a renormalization-group transformation. The analogous version of the NRG for a one-dimensional system is to double the block size at each iteration by joining two identical blocks of m states each and taking the m lowest energy eigenstates (out of m^2 states in total) as the 'renormalized' block for the

next iteration. This program has also not been successful. The work of White and Noack [33] was instrumental in pinning down the cause of this failure: the set of low-lying states kept in the standard NRG approach is, in the general case, too incomplete to obtain an accurate eigenstate for the next largest lattice size. To illustrate the problem, they used a simple example, of a lattice version of a single particle in a box, with Hamiltonian matrix,

$$H_{ij} = \begin{cases} 2, & \text{if } i = j, \\ -1, & \text{if } |i-j| = 1, \\ 0, & \text{otherwise.} \end{cases} \tag{1.3}$$

In the limit of large lattice size, this Hamiltonian converges to that of a free particle in a box, bounded by an infinite potential. The procedure for applying NRG to this system is to begin with a block which represents a single site, H^1, a 1×1 matrix and the matrix that represents the interaction between two blocks (in this case just the hopping term), $T^1 = -1$. The iterations are started by forming the Hamiltonian matrix composed of two blocks of the previous iteration,

$$\bar{H}^s = \begin{bmatrix} H^{s-1} & T^{s-1} \\ (T^{s-1})^\dagger & H^{s-1} \end{bmatrix}, \tag{1.4}$$

and

$$\bar{T}^s = \begin{bmatrix} 0 & 0 \\ T^{s-1} & 0 \end{bmatrix}, \tag{1.5}$$

$\bar{H}^s$ is diagonalized and the lowest m eigenstates are taken, discarding the rest. A change of basis is then performed to construct a diagonalized but truncated Hamiltonian matrix H^s and associated interaction operator T^s. The iterations then proceed starting again at equation (1.4), to construct $H^{\bar{s}+1}$ and $T^{\bar{s}+1}$. The necessary requirement is that the higher energy states at the current iteration are unimportant in making up the lower energy states at the later iterations. Unfortunately, this is not true. To see why, we merely need to look at the low-lying states at two successive iterations, illustrated by Figure 1 (after reference [33]). Any state made up of low-lying states from the previous iteration must have a "kink" located in the center of the system. In order to represent accurately states in the larger block, almost all of the states of the previous iteration are required.

In this case, the loss of accuracy can be fixed by a more sophisticated treatment of BCs. There is no particular reason why the Hamiltonian $\bar{H}^s$ must use open BCs. Of course, the Hamiltonian matrix used to construct the block at the next iteration must use open BCs, otherwise there would be extraneous hopping terms, but it is

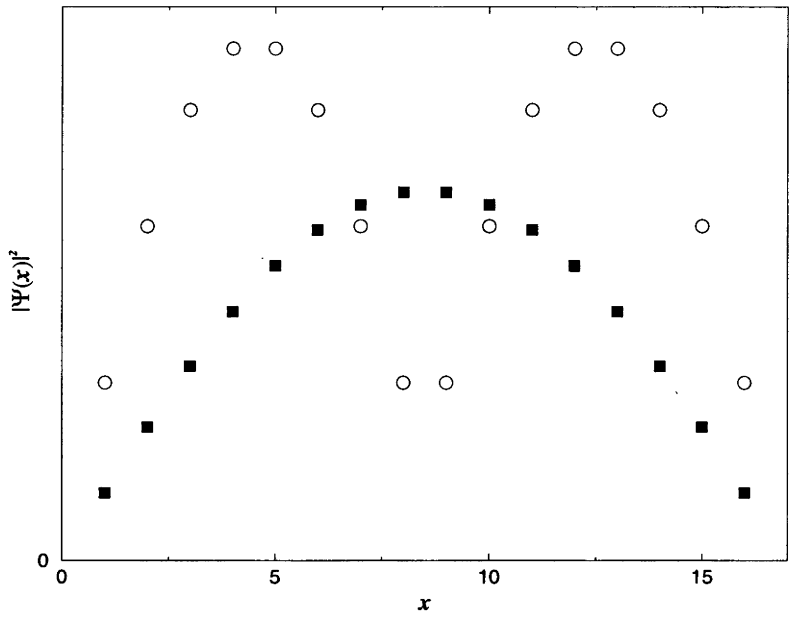

Figure 1.1: Lowest eigenstates of two 8-site blocks (open circles) and a 16-site block (solid squares) for the one-dimensional model with open BCs.

possible to use a different Hamiltonian matrix for constructing the low-lying eigenstates than the one used to construct the next block. However, White and Noack [33] found that using alternate BCs does not substantially improve the convergence of the algorithm. For example, periodic BCs allow exact representation of the ground state (which is a constant) but, since the boundaries of the wavefunction are forced to have the same value, any higher energy states are represented very poorly. Free BCs, where the derivative of the wavefunction is set to be zero at the block edges, does not fare any better. White and Noack did have success, however, with combining the results from several different choices of BC when choosing which eigenstates to keep. In particular, by taking all four possible ways of combining two blocks with either open or free BCs and taking the span of the lowest $m/4$ eigenstates of each of the resulting Hamiltonians as the truncated Hilbert space for the next iteration, they achieved considerable success for the single particle free electron system. They also achieved success in calculating arbitrary excited states, by choosing the $m/4$ states of closest energy to what is desired. This algorithm has since been entitled the "combination of boundary conditions" approach [26].

An alternative approach was also suggested by White and Noack [33], which they call the "superblock" procedure. Here one diagonalizes a larger system containing $p > 2$ blocks, with a single choice of BC. The idea is that the surrounding blocks provide the boundary conditions on the blocks of interest, which are placed

in the middle of the system. m states are extracted from the diagonalization of the superblock and then one projects the basis onto the portion of the lattice corresponding to the two blocks of interest. This was successful for the non-interacting single particle model, but high accuracy was achieved only for a fairly large number of blocks, of the order of 20. This algorithm was the immediate precursor to the DMRG algorithm.

It is important to note here that the notion of the "renormalization-group" has been lost. Neither the combination of boundary conditions algorithm, nor the superblock algorithm, contains any notion of renormalization-group flow, or any block scaling transformation. This is also true of DMRG itself. The name Density-Matrix Renormalization-Group is now mostly a historical misnomer which still causes occasional confusion in the literature.

1.2 DMRG Fundamentals

Rather than continue in an historical vein, it is instructive to introduce to DMRG from the point of view of a variational calculation in a truncated Hilbert space. In this sense, DMRG is much closer to exact diagonalization than it is to Wilson's numerical renormalization-group.

In exact diagonalization, one directly constructs the Hamiltonian matrix for the lattice system and diagonalizes it using some numerical diagonalization algorithm, usually the Lanczos algorithm [34–36] or similar. The problem with this approach is that the dimension of the Hilbert space increases exponentially with the lattice size. For example, the Hubbard model requires four basis states per site; hence the full Hilbert space of an L-site lattice contains 4^L states. Even with sophisticated numerical techniques, diagonalizing such a matrix for a reasonably large value of L (say, around 20 or so) rapidly becomes impractical. One way of making such calculations more efficient is to use symmetries to reduce the size of the Hilbert space. For example, if one labels the states by their total momentum, then if one knows that the total momentum of the ground state is zero, one can leave out all the states with non-zero momentum. In fact, diagonalizing an M-dimensional matrix takes $\sim M^3$ steps; thus even if the quantum numbers of the ground state are not known it will always be beneficial, in the large M limit, to subdivide the Hilbert space into symmetry sectors and diagonalize each matrix separately. However, these symmetries do not change the the nature of the exponential increase in matrix dimension as the lattice size is increased. Also, efficient numerical computation of the matrix diagonalization requires that the matrix elements are stored in sparse

form and readily addressable. This requirement makes utilizing higher symmetries, such as $SU(2)$ total spin symmetry, difficult although certainly not impossible.

The DMRG algorithm is based around an approximation whereby the lattice system is split into two halves, called the left block and the right block (denoted A and B here) and the basis in each block is then truncated. The wavefunction is written in the basis of the tensor product of the two-block basis (usually called the "superblock" basis),

$$|\Psi\rangle = \sum_{a=1}^{N_A} \sum_{b=1}^{N_B} \psi_{ab} \, |a\rangle \otimes |b\rangle, \tag{1.6}$$

where the dimension of the left block is N_A and the dimension of the right block is N_B. The choice of division of the system into the two blocks is arbitrary here and, as we shall see later, is different for the various types of DMRG algorithm. The essential approximation is to reduce the size of the blocks, such that the wavefunction is affected in the smallest possible way. To see how this works, we will construct the basis states in the left block that are the most important in the representation of the wavefunction. Let $|\phi\rangle$ be an arbitrary state in the left block basis,

$$|\phi\rangle = \sum_{a=1}^{N_a} \phi_a |a\rangle. \tag{1.7}$$

The weight of this state in the superblock wavefunction is simply the norm of $\langle\phi|\Psi\rangle = \sum_{ab} \phi_a \psi_{ab} |b\rangle$,

$$W(|\phi\rangle) = \sum_{a=1}^{N_a} \sum_{b=1}^{N_b} |\phi_a \psi_{ab}|^2 \ . \tag{1.8}$$

Now we calculate the expansion coefficients ϕ_a such that $W(|\phi\rangle)$ is a maximum, subject to the constraint that $\langle\phi|\phi\rangle = 1$. This can be done simply with Lagrange multipliers, giving the result that

$$\phi_{a'} = \lambda \sum_{a}^{N_a} \rho_{a'a} \phi_a \ , \tag{1.9}$$

where λ is a maximum and $\rho_{a'a}$ is the *reduced density-matrix*,

$$\rho_{a'a} = \sum_{b=1}^{N_b} \psi_{a'b} \psi^*_{ab} \ . \tag{1.10}$$

Hence the important states required in the system basis are the eigenstates of the reduced density-matrix that have largest eigenvalue.

An alternative construction of this result can be obtained through linear algebra. This is the method originally used by White [6]. The critical realization is that the

basis states in (1.9) can be constructed via a singular value decomposition. By regarding ψ as a $N_a \times N_b$ matrix the singular value decomposition can be effected,

$$\psi = UDV^T, \tag{1.11}$$

where U is a $N_A \times N_A$ orthogonal matrix, D is a $N_A \times N_A$ diagonal matrix and V^T is a $N_A \times N_B$ column-orthogonal matrix. We assume that $N_A \leq N_B$, but the singular value decomposition can be performed similarly in the case of $N_A > N_B$. The diagonal matrix D contains the singular values of ψ. The matrices U and V apply a basis transformation on the system and environment blocks respectively, that has the effect of diagonalizing ψ. It is important to note that the dimension of the environment block after the V transformation is N_A, which is, in general, *less* than the original dimension of this basis. However, ψ is still represented exactly. Substituting the definition of the reduced density-matrix, Eq. (1.10), we find that it can be written in terms of the singular value decomposition operators,

$$\rho = UD^2U^T. \tag{1.12}$$

Hence U diagonalizes ρ and the eigenvalues of ρ are simply the squares of the singular values.

We now summarize the important results. The eigenstates of the reduced density-matrix (for each block) with largest eigenvalue λ_i are the optimal states to keep, with the eigenvalue being the weight of the basis state in the superblock wavefunction. The truncation of basis states is effected by keeping only the largest m eigenstates of the density-matrix. The sum of all reduced density-matrix eigenvalues is unity and the deviation of the sum of kept eigenvalues $P_m = \sum_{i=1}^{m} \lambda_i$ from unity measures the accuracy of the truncation. A result, that follows directly from the singular value decomposition construction, is that the maximum number of non-zero eigenvalues of the density-matrix is $\min(N_A, N_B)$. Hence, for the truncation procedure to be meaningful we must have

$$m \leq \min(N_A, N_B)\ . \tag{1.13}$$

If this condition is not satisfied, some of the states kept will have zero weight in the superblock wavefunction. While these states do not harm the calculation, they provide little benefit while adding to the computation requirement. In the limit of large m, P_m becomes 1 and the 'truncation' is exact.

It is conventional to refer to the block that is being actively truncated as the 'system block' and the other block as the 'environment block'. This notation comes from an analogy with thermodynamics. An isolated system is in an eigenstate

of the Hamiltonian and the density-matrix eigenstates coincide with the those of the Hamiltonian. However, if the system is not isolated, but is instead connected to an 'environment' (for example, a heat bath), the system is in a mixed state and the density-matrix eigenstates no longer coincide with the eigenstates of the Hamiltonian. So in the DMRG algorithm, it is possible to consider one block to be the 'system', which is not isolated and connected to an 'environment' (the other block) that provides the boundary conditions. This is a nice analogy; however it does not work well when applied to actual DMRG algorithms. As discussed below, in the infinite-size algorithm, the left and right blocks each represent exactly half of the (often reflection symmetric) lattice, so there is no distinction as to which block is the 'system' and which is the 'environment'. This notation works better for the finite-size algorithm, where the overall lattice size (system + environment) is fixed while the boundary point of the two blocks shifts at each iteration. In this thesis, the only use of the 'system' and 'environment' notation is in this context. But even in this case the analogy does not carry over completely, as one is usually interested in the properties of the lattice as a whole, not just the system block.

It is useful to be able to make use of symmetries of the Hamiltonian in applying the truncation. In the simplest case, let the symmetry operators of the Hamiltonian be of the form of a set of R operators $Q_1, Q_2, \ldots, Q_R$ which commute with each other as well as with the Hamiltonian and suppose that each operator separately generates a one-dimensional compact Lie algebra (hence isomorphic to $U(1)$). Examples of such operators would be the number of particles operator, N and the $z-$component of total spin, S^z. In each block, the states can be labeled by the eigenvalues of the symmetry operators Q_1, ..., Q_R, so we write the left block basis as

$$|(a), q_1^A, \ldots, a_R^A\rangle;\ a = 1 \ldots N_{q_1^A,\ldots,q_R^A}\ , \tag{1.14}$$

which represents the a'th basis state of quantum numbers $q_1^A, \ldots, q_R^A$. Similarly, the right block basis can be written as

$$|(b), q_1^B, \ldots, q_R^B\rangle;\ b = 1 \ldots N_{q_1^B,\ldots,q_R^B}\ . \tag{1.15}$$

The Lie-algebra structure of the symmetry operators implies that the r'th superblock symmetry operator is of the form

$$Q_r = Q_r^A \otimes I^B + I^A \otimes Q_r^B\ , \tag{1.16}$$

where I^A and I^B are the identity operators acting on the left and right blocks respectively. The tensor product of any left block basis state with any right block basis state is itself an eigenstate of the superblock symmetry operators, with eigenvalues

$q_1^A + q_1^B, \ldots, q_R^A + q_R^B$. Thus it is easy to project the superblock basis onto some arbitrary symmetry sector given by the superblock quantum numbers $q_r^S = q_r^A + q_r^B \; \forall r$. This is called the *target state* in usual DMRG terminology. Inserting the quantum number labels into the definition of the reduced density matrix, Eq. (1.10), we obtain

$$\rho_{a'a}^{q_1^A,\ldots,q_R^A} = \sum_{q_1^B,\ldots,q_R^B} \sum_{b=1}^{N_{q_1^B,\ldots,q_R^B}} \psi_{(a),q_1^A,\ldots,q_R^A;(b),q_1^B,\ldots,q_R^B} \psi^*_{(a'),q_1^A,\ldots,q_R^A;(b),q_1^B,\ldots,q_R^B} \,. \tag{1.17}$$

This matrix is block diagonal with respect to the quantum numbers of the left block, $q_1^A, \ldots, a_R^A$, as required for the truncation to preserve the quantum numbers. Thus, there is no complication in implementing these symmetry operators into the truncation procedure. Later on we will see how to generalize this procedure to other symmetry operators which do not necessarily mutually commute, having the structure of *e.g.* a semi-simple Lie algebra or a finite group.

Since the density-matrix is block diagonal, the condition on m for the truncation to be meaningful, Eq. (1.13) can be applied separately to each quantum number sector. This means that, in practice, the overall equality can be difficult to satisfy and one usually requires that $m \ll \min(N_A, N_B)$. The exception arises when one or both blocks contain very few sites and all states should be kept even if they are not yet used in the superblock basis. It is also possible to craft robust DMRG algorithms where, due to the particular choice of states kept, the equality in Eq. (1.13) holds strictly, without any extraneous zero eigenvalues of the reduced density-matrix (*cf.* section 1.4).

1.2.1 The infinite-size algorithm

The simplest implementation of a numerical scheme based on the density-matrix truncation is the so-called infinite-size DMRG. In this scheme, a single lattice site is added to each of the left and right blocks at each iteration; thus the length L of the superblock grows by two sites at a time. Prior to the first iteration, the left and right blocks each consist of a single site. The iterations are started by adding a single site to each block and forming the superblock as the tensor product of the resulting two blocks. In the usual graphical notation, this is given by the first line of Fig. 1.2. Here, solid rectangles indicate truncated blocks with at most m basis states and open circles indicate bare sites. The ground state wavefunction of the superblock is found using a matrix diagonalization algorithm, for example the Lanczos or Davidson algorithms. At the first iteration, this is simply an exact diagonalization on a four-site system. From the resulting wavefunction. the reduced

density-matrix is constructed and the truncation to m basis states is performed as described previously. This is done for the left and right blocks separately. New sites are then added to each block and the process is repeated. If the system is reflection-symmetric, the right block can be the spatial reflection of the left block and only one reduced density-matrix needs to be constructed. This is called the infinite-size algorithm because it is commonly supposed that the limit of a large number of iterations corresponds to taking the thermodynamic limit to an infinite lattice size. It must be remembered however, that infinite-size DMRG only converges to the exact ground state in the limit $m \to \infty$ and this limit must be taken *before* the limit $L \to \infty$. Thus the infinite-size algorithm is very useful for calculating *densities*, for example the energy per unit length, but not so useful for calculating quantities such as an excitation energy. To see why this is so, firstly suppose that we take m to be as large as possible, so that no basis states are truncated at all. The infinite-size DMRG is then equivalent to a sequence of exact diagonalizations on successively larger lattices and it is clear that the limit $L \to \infty$ will give the thermodynamic limit. On the other hand, for m fixed, every iteration involves an approximation and it is not *a priori* clear that the error due to the approximation is bounded as L is increased. In other words, it is not necessarily true that $\lim_{L\to\infty} \Delta E(L)/L = 0$, where $\Delta E(L)$ is the difference between the true energy and the energy obtained by DMRG. A typical example of a quantity that is difficult to calculate with the infinite-size algorithm is the Haldane gap in integer spin chains [37]. For a small system (corresponding to the first few iterations of the infinite-size DMRG algorithm), the Haldane gap between the singlet ground state and the first excited triplet state is reproduced with reasonable accuracy and initially scales well toward the thermodynamic value of the gap. However, beyond some critical lattice size (that depends on the number of states kept m), the gap starts to diverge linearly with the lattice size. This is illustrated extremely well in figure 1 of reference [38]. It is simply not possible to calculate the gap from the converged limit of an infinite-size DMRG calculation, no matter how many states are kept.

In the infinite-size algorithm, the target quantum numbers need to be chosen for each lattice size $L = 4, 6, 8, \ldots$, which means that, in general, the values of the quantum numbers will fluctuate around the desired value. For example, Fig. 1.3 shows the energy per site at each step of the algorithm, for a portion of a DMRG calculation on the Kondo lattice model with density $n = 4/5$ electrons per site. The electron density fluctuates around the mean value and the density only matches the desired density once every 5th iteration. In addition, the periodic fluctuations in the density introduces an artificial peak in the correlation functions

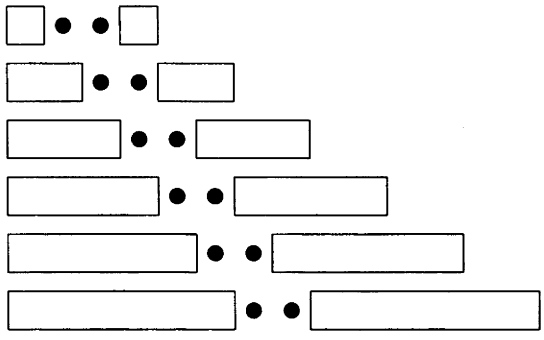

Figure 1.2: Schematic form of the infinite-size DMRG algorithm. Open rectangles represent truncated blocks, solid circles are bare lattice sites.

at the wave number of the density fluctuations. If the electron density per site is $n = \frac{p}{2q}$, where p and q are integers with no common factor, then the period of the fluctuations is q iterations. This introduces additional correlations with wave number $2\pi q/p = \pi n = 2k_F$, twice the Fermi momentum of a non-interacting band of electrons. In some cases, these artificial correlations can skew considerably the results of a calculation. For example, in the calculations on the Kondo lattice model, described in detail in chapter 3, an important feature of the ground state phase diagram is a crossover of the Fermi momentum from the weak interaction value of $\pi n/2$ to the so-called 'large' Fermi surface value of $\pi(n+1)/2$. This is accompanied by a change in the location of the peak in the spin structure factor from πn to $\pi(1-n)$. The location of this crossover is considerably distorted by the presence of additional correlations at πn caused by the density fluctuations inherent to the infinite-size algorithm. Thus, while the envelope of the energy fluctuations in figure 1.3 appears to be convergent from both above and below, it is not clear how closely the calculation converges to the true thermodynamic state.

Moukouri and Caron [39] demonstrated an approach that, while it cannot completely eliminate the density fluctuations, reduces their effect significantly. At each iteration, the wavefunction is obtained for two sets of quantum numbers that bracket the desired density. The density-matrix used to construct the truncation operator is then a linear combination of the density-matrices of the two ground-states.

The Hamiltonian matrices and truncation operators in the infinite-size algorithm eventually converge to a fixed point where the matrix elements at each iteration are identical, save for a scale factor and possibly sign inversions arising from the algebraic properties of the Hamiltonian for different chain lengths. In the case of

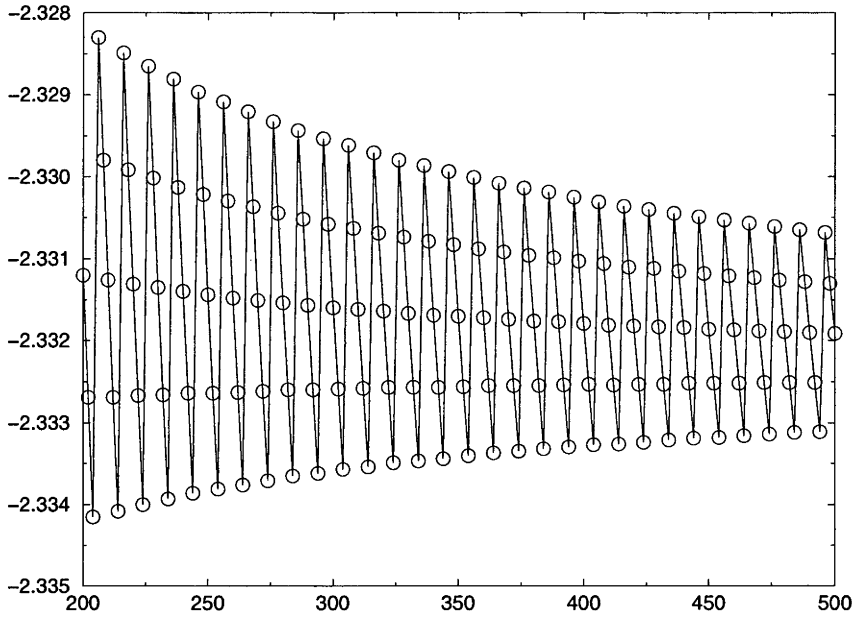

Figure 1.3: A section of a DMRG run showing the energy per site as a function of the iteration number.

fractional density this fixed point has period q. This is a renormalization, although not of the same quantities that are renormalized in the usual renormalization-group approach. This renormalization property can be used to accelerate the computation, first shown by Schollwöck [40], where Marshall's sign rule was used to predict the sign changes in the elements of the wavefunction vector. This gives an accurate estimation of the ground state wavefunction to use as an initial guess vector in the matrix diagonalization.

1.2.2 The finite-size algorithm

If one is interested in calculating accurately the properties of a system of some specific size, then it is possible to significantly improve upon the accuracy of the infinite-size algorithm. Constructing an L site system using the infinite-size algorithm requires the construction of blocks of all sizes $2, 3, \ldots L/2$. In the infinite-size algorithm these smaller blocks are not needed and can be discarded on the next iteration. However, the overall system size can be maintained at L if we take the next left block to be size $L/2 + 1$ and the right block to be the block from the previous iteration, of size $L/2 - 1$. This procedure can be carried further, so that the n'th iteration uses a left block of size $L/2 + n$ and a right block of size $L/2 - n$. Once the right block gets small enough that it can be represented exactly (ie. when the dimension of the Hilbert space becomes less or equal to m), the direction of iter-

ation is reversed. This is illustrated schematically in Fig. 1.4. Many 'sweeps' can be performed over the system, so that the target state is iteratively improved. It was recognized early [6] that an important improvement in efficiency can be achieved by gradually increasing the number of block states kept for each sweep. The number of states in the environment block, m', is then the number of states kept in the system block of the previous sweep. It is important not to make m/m' too large. There is no point making this ratio larger than the number of states in a single site, as then Eq. (1.13) will not be satisfied and some of the basis states kept will be random vectors and not useful in representing the target state.

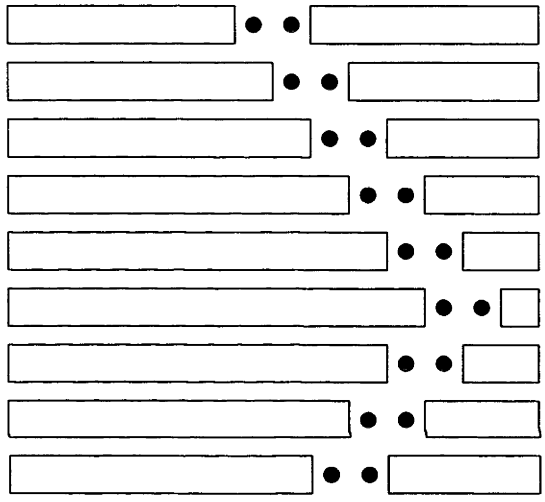

Figure 1.4: Schematic form of the finite-size DMRG algorithm.

If the system is reflection symmetric the sweeps need to go only to the half way point, where both blocks are the same size. At this point, the spatial reflection of the system block can be used as the environment block and the direction of the sweeping is reversed. This reduces the computation time and storage requirement by a factor of two, since only one block of each lattice size is required. If the system is not reflection symmetric then separate left and right blocks need to be stored for each lattice size and updating all the blocks requires one complete sweep over the lattice in each direction.

A hybrid finite/infinite-size algorithm is also possible, that eliminates the density fluctuations of the pure infinite-size algorithm. Given a density with a periodicity of q iterations, one can use smaller size blocks from previous iterations to maintain a lattice size that is an exact multiple of $2q$. After the system size is built up to be

at least $4q$ sites, the density is thereafter a constant. This procedure is illustrated in Fig. 1.5, for an example density with $q = 3$. The system size is built up to 12 sites using the infinite-size algorithm. Thereafter, the system size can be increased without limit while maintaining a system size that is always a multiple of 6 sites.

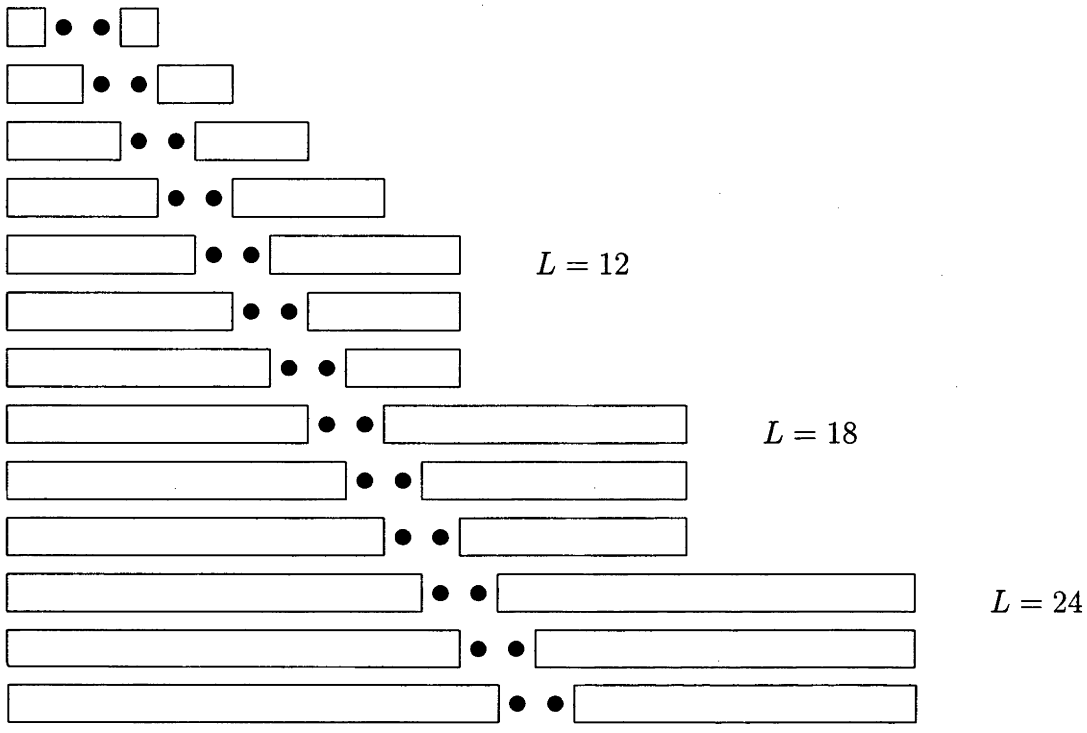

Figure 1.5: Schematic form of the hybrid finite/infinite-size DMRG algorithm. $q = 3$ in this example.

As illustrated, this algorithm requires reflection symmetry because, after the initial iterations to build the system size up to $4q$, sites are only ever added to the left block, while re-using smaller spatially-reflected left blocks as the current right block. For a system without reflection symmetry, it would be necessary to perform some left-moving iterations to construct the right blocks of the required sizes.

The software infrastructure required to implement the hybrid algorithm differs little from that required for the full finite-size algorithm. Hence there is little advantage to using this algorithm for a one-dimensional system; it is generally preferable to do a finite-size scaling based on more accurate calculations from the finite-size algorithm. As far as the author knows, the only published use of this algorithm is in the context of two-dimensional DMRG [41], which is discussed in detail in section 1.5.

1.2.3 Matrix operators

To actually construct the superblock Hamiltonian, a matrix representation of all the relevant operators is required. These matrix representations must preserve all the commutation relations of the algebraic form of the Hamiltonian. As an example, consider a one band electron model (*e.g.* the Hubbard model), with 4 basis states per site, $|0\rangle$, $|\uparrow\rangle$, $|\downarrow\rangle$, $|\uparrow\downarrow\rangle$. After the choice of basis vectors $(1,0,0,0)$, $(0,1,0,0)$, $(0,0,1,0)$, $(0,0,0,1)$ to represent these four states, the explicit form of the creation operators on a single site is given by,

$$C_{\uparrow}^{\dagger} = \begin{pmatrix} 0 & 0 & 0 & 0 \\ 1 & 0 & 0 & 0 \\ 0 & 0 & 0 & 0 \\ 0 & 0 & 1 & 0 \end{pmatrix} , \tag{1.18}$$

$$C_{\downarrow}^{\dagger} = \begin{pmatrix} 0 & 0 & 0 & 0 \\ 0 & 0 & 0 & 0 \\ 1 & 0 & 0 & 0 \\ 0 & -1 & 0 & 0 \end{pmatrix} . \tag{1.19}$$

The annihilation operators are the Hermitian conjugate of these. It is easy to show that these operators obey the required algebra,

$$\{C_{\sigma}^{\dagger}, C_{\tau}^{\dagger}\} = \{C_{\sigma}, C_{\tau}\} = 0 , \tag{1.20}$$

$$\{C_{\sigma}^{\dagger}, C_{\tau}\} = \delta_{\sigma\tau} . \tag{1.21}$$

To include the site index, an ordering relation on the sites is required because of the anticommutation of operators acting on different sites. Choosing the simplest ordering of sites, from 1 to L left to right, the creation operator acting on the j'th site is

$$C_{j,\sigma}^{\dagger} = (-1)^{\sum_{i=1}^{j-1} N_i} \underbrace{I \otimes I \otimes \ldots \otimes I}_{j-1 \text{ terms}} \otimes C_{\sigma}^{\dagger} \otimes \underbrace{I \otimes \ldots \otimes I}_{L-j \text{ terms}} , \tag{1.22}$$

where the sign is positive if there is an even number of electrons to the left of site j and negative if there is an odd number of electrons to the left of site j. This can be written in a more useful form as

$$C_{j,\sigma}^{\dagger} = \underbrace{P \otimes P \otimes \ldots \otimes P}_{j-1 \text{ terms}} \otimes C_{\sigma}^{\dagger} \otimes \underbrace{I \otimes \ldots \otimes I}_{L-j \text{ terms}} , \tag{1.23}$$

where $P = (-1)^N$ is the single site *parity operator*,

$$P = \begin{pmatrix} 1 & 0 & 0 & 0 \\ 0 & -1 & 0 & 0 \\ 0 & 0 & -1 & 0 \\ 0 & 0 & 0 & 1 \end{pmatrix} . \tag{1.24}$$

An electron of spin σ hopping between sites i and j, is written in algebraic form as

$$T(i,j,\sigma) = T^{\dagger}_{\sigma i} T_{\sigma j} + \text{h.c.}\,. \tag{1.25}$$

We assume without loss of generality that $i < j$. Since $P^2 = 1$, the matrix representation of this interaction simplifies to

$$T(i,j,\sigma) = \quad I \otimes \cdots \otimes I \otimes C^{\dagger}_{\sigma i} P \otimes P \otimes \ldots \otimes P \otimes C_{\sigma j} \otimes I \otimes \ldots \otimes I \; + \text{h.c.}\,. \tag{1.26}$$

A more convenient form for storing the operators required for this superblock term when site i is in the left block and site j is in the right block, is to use the operators

$$C^{L}_{i,\sigma} = I \otimes I \otimes \ldots \otimes I \otimes C_{\sigma} P \otimes P \otimes \ldots \,, \tag{1.27}$$

and

$$C^{R}_{j,\sigma} = P \otimes P \otimes \ldots \otimes P \otimes C_{\sigma} \otimes I \otimes \ldots \,, \tag{1.28}$$

where the L and R indices indicate operators acting on the left and right blocks respectively. In this form, $T(i,j,\sigma) = \sum_{\sigma} C^{L\dagger}_{i,\sigma} C^{R}_{j,\sigma} + \text{h.c.}$ Unfortunately this matrix is not reflection symmetric; interchanging all site indices with the spatial reflection, $n \to L+1-n$, does not produce the same matrix as a hopping between sites $L+1-i$ and $L+1-j$. This is because, in Eq. (1.26), the left-most non-trivial matrix is of the form $C^{\dagger}_{i,\sigma} P$, whereas the corresponding matrix of the spatially reflected operator is $C^{\dagger}_{i,\sigma}$. The origin of this difficulty is physical. In choosing our basis, we have specified the choice of ordering $|{\uparrow\downarrow}\rangle$ for the double-occupied state. Taking the spatial reflection requires that this ordering is reversed, so that instead the basis state $|{\downarrow\uparrow}\rangle = -|{\uparrow\downarrow}\rangle$ is used. Thus to effect a spatial reflection, simultaneously with changing the labeling of the sites a basis transformation R must be applied to every site, which gives

$$\begin{aligned} C_{i,\sigma} &\to R C_{i,\sigma} R^{-1} = C_{i,\sigma} P \\ C^{\dagger}_{i,\sigma} &\to R C^{\dagger}_{i,\sigma} R^{-1} = P C^{\dagger}_{i,\sigma} = -C^{\dagger}_{i,\sigma} P\,, \end{aligned} \tag{1.29}$$

where R is the single site spatial reflection operator,

$$R = \begin{pmatrix} 1 & 0 & 0 & 0 \\ 0 & 1 & 0 & 0 \\ 0 & 0 & 1 & 0 \\ 0 & 0 & 0 & -1 \end{pmatrix}. \tag{1.30}$$

This is inconvenient. When the left and right blocks are the same size, we would like the Hamiltonian matrix to be exactly reflection symmetric without the need to

apply a basis transformation. Then, the superblock wavefunction matrix is either totally symmetric or totally antisymmetric, depending on whether the wavefunction is even or odd with respect to spatial reflection. This symmetry reduces by a factor ~ 2 the number of degrees of freedom in the diagonalization.

One solution to this problem is to use a different basis for the right block, whereby the operators are stored in the spatially reflected basis. This requires reversing the order of the operators in the tensor product expansion in Eqn. (1.28) and applying the spatial reflection transformation to each site. Once this is done, $C^L_{\sigma i}$ and $C^R_{\sigma L-i+1}$ have exactly the same matrix elements; reflection symmetry is recovered and the right block operators are the same matrices as the left block operators. This representation is equivalent to that described by Sørensen [42], although in that work the system under consideration is the Heisenberg spin chain in which the single site reflection operator R is the identity operator.

In principle, expectation values are rather easy to calculate using DMRG. Arbitrary operators can be constructed in the same way as described above, making the calculation of expectation values on the ground state wavefunction relatively simple. In addition, expectation values of operators that act only on one block can be calculated readily from the reduced density-matrix due to the usual identity,

$$\langle A \rangle = \mathrm{tr}(\rho A) \; . \tag{1.31}$$

However there are some complications that occur [43]. Because of the usual open BCs, translational invariance of expectation values is not preserved, even relatively far away from the boundaries. The usual solution is to calculate the expectation values for several neighboring sites and form the average. This is especially necessary for correlation functions.

Because the blocks are truncated at each step, operators that act on sites far from the block edge lose accuracy and tend to converge to the mean value. If sites i and j of a two-point correlation (for example $\langle S^z_i S^z_j \rangle$) are in the same block, it is not a good idea to calculate the expectation value from the product of separate operators S^z_i and S^z_j after the Hilbert space has been truncated. In matrix form, this expectation value is

$$\langle S^z_i S^z_j \rangle = \sum_{\alpha\beta\gamma\delta} \psi^*_{\alpha\delta} S^z_{i,\alpha\beta} S^z_{j,\beta\gamma} \psi_{\gamma\delta} \; . \tag{1.32}$$

The internal summation over β in the term $S^z_{i,\alpha\beta} S^z_{j,\beta\gamma}$ is over the truncated basis, hence the matrix elements of $S^z_i S^z_j$ will be calculated only approximately. If, however, sites i and j are in different blocks, the calculation of the expectation value

changes to,

$$\left\langle S_i^z S_j^z \right\rangle = \sum_{\alpha\beta\gamma\delta} \psi^*_{\alpha\gamma} S^z_{i,\alpha\beta} S^z_{j,\gamma\delta} \psi_{\beta\delta} \ . \tag{1.33}$$

In this case, the operator $S_i^z S_j^z$ involves no internal summation over the truncated basis and the expectation value $\left\langle S_i^z S_j^z \right\rangle$ is determined exactly (remembering that the wavefunction itself is approximate; there is no further loss of accuracy when calculating expectation values).

Further properties of DMRG correlation functions are discussed in section 1.4, where it is shown [21] that all correlation functions calculated via DMRG decay exponentially; power-law behavior cannot occur even when the exact solution would be critical.

1.3 Numerical Optimizations

Since the original description of DMRG [6], several optimizations have been proposed, some purely implementation details and some with a more physical basis. This section describes the optimizations that are *de facto* essential to the finite-size algorithm, as well as other minor and theoretical optimizations. Optimizations relating directly to the superblock diagonalization are saved for the later section on convergence, section 1.6.

1.3.1 Block storage

The original implementation of DMRG [6] constructed the superblock Hamiltonian explicitly, as a large, sparse matrix. However, in most cases this is not optimal in either storage space or computation time. The superblock Hamiltonian, in the tensor product basis, has the form

$$H = H^A \otimes I^B + I^A \otimes H^B + \text{interactions}, \tag{1.34}$$

where the interaction terms are of the form $M^A \otimes M^B$, where M^A and M^B may be dense matrices, in the worst case with order $(N_A)^2$ (respectively $(N_B)^2$) non-zero matrix elements. This means that, for some forms of interaction, the number of non-zero matrix elements in the tensor product $M^A \otimes M^B$ can be very large, of the order $(N_A N_B)^2$, loosely $O(N^4)$. Hence the number of non-zero matrix elements in the Hamiltonian itself can be very large. The storage requirement is thus also correspondingly large, much larger than the combined storage size of the individual block operators. Hence, it is possible to achieve a reduction in memory requirement

by *not* explicitly constructing the Hamiltonian matrix and simply calculating the matrix elements on-the-fly, term by term as needed.

The important realization is that representing the Hamiltonian as a tensor product also leads to a performance improvement. As far as the author knows, this procedure was first described by P. Schmitteckert [29]. Using the matrix form of the wavefunction, ψ_{ab}, the matrix-vector product $H\psi$ can be written as

$$(H\psi)_{a'b'} = \sum_{ab} \left(H^A_{a'a}\psi_{ab'} + \psi_{a'b}H^B_{b'b} + \text{interaction terms} \right), \tag{1.35}$$

where the general form of an interaction term is

$$([M^A \otimes M^B]\psi)_{a'b'} = \sum_{ab} \left(M^A_{a'a} M^B_{b'b} \psi_{ab} \right) . \tag{1.36}$$

Calculating the matrix-vector product for the interaction terms in this form requires, in the worst case, two dense matrix-matrix multiplies, of $O(N^3)$ operations. This is an order of magnitude better than the worst case of $O(N^4)$ in the original formulation.

The performance can be improved further, by noticing that the operators acting on a bare site are usually very sparse (if they are not, then an arbitrary unitary transformation could be applied to make them so). Hence it is beneficial to further unroll the tensor product so that the bare sites added to the left and right blocks are treated separately. Also, the block operators are sparse in the quantum number indices, further simplifying the numerical complexity of the multiplication operation. The origin of this sparseness is physical and arises from the symmetry of the Hamiltonian. Each operator appearing in a Hamiltonian or expectation value transforms as an irreducible representation of the global symmetry group of the Hamiltonian. In the case of *e.g.* particle number symmetry, this implies that each operator has a well-defined effect on the number of particles in the system. The Hamiltonian conserves the particle number, hence the block Hamiltonian matrix is block diagonal with respect to this quantum number. Also, a creation operator always increases the particle number by exactly one and an annihilation operator always decreases the particle number by exactly one. Thus these operators also have a predictable structure. This theme is expanded upon in chapter 2, where the symmetry properties of the DMRG algorithm are discussed in detail.

The block-storage optimization was used in all the DMRG calculations presented in this thesis.

1.3.2 Wavefunction transformations

So far, the initial 'guess vector' for the superblock diagonalization procedure has not been specified. As mentioned earlier (section 1.2.1), for the infinite-size algorithm it is possible to obtain an estimate of the target state for use as an initial condition by using the renormalization properly of the Hamiltonian and truncation matrices. A similar procedure is possible for the finite-size algorithm, although in this case the system size is a constant, making the procedure a pure basis transformation rather than a renormalization. Steven White [44] was the first to describe the steps necessary to transform the target state wavefunction from the tensor product basis of a left block of size n and a right block of size $(L-n)$, to the basis of block sizes $(n+1)$ and $(L-n-1)$, for use as the initial guess vector in the superblock diagonalization at the next iteration.

We first introduce some notation. The notation used here is similar to that used by Östlund and Rommer [21] in their seminal work on the nature of the DMRG wavefunction (*cf.* section 1.4). At some point of the sweep, let there be n sites in the left block and $L-n$ sites in the right block. Let $|s_i\rangle$, $s_i = 1, 2, \ldots N_i$ be the single site basis at site i, of dimension N_i. We write the left block+site basis as

$$|\alpha_{n-1}\rangle \otimes |s_n\rangle = |\alpha_{n-1}\, s_n\rangle \ , \tag{1.37}$$

where $|\alpha_{n-1}\rangle$ is the truncated basis for the left-most $n-1$ sites, with $\alpha_{n-1} = 1, 2, \ldots, m$. Similarly, the right block basis is written

$$|s_{n+1}\rangle \otimes |\beta_{n+2}\rangle = |s_{n+1}\, \beta_{n+2}\rangle \ . \tag{1.38}$$

Here $|\beta_{n+2}\rangle$ represents the truncated basis for the right most $L-n-1$ sites (*i.e.* sites $n+2, n+3, \ldots, L$).

We write the truncation operators on the left and right blocks respectively as

$$|\alpha_i\rangle = \sum_{\alpha_{i-1}, s_i} {}^{L}T^{(i)}_{\alpha_i;\alpha_{i-1}s_i} |\alpha_{i-1}\, s_i\rangle \ , \tag{1.39}$$

$$|\beta_i\rangle = \sum_{s_i, \beta_{i+1}} {}^{R}T^{(i)}_{\beta_i;s_i\beta_{i+1}} |s_i\, \beta_{i+1}\rangle \ . \tag{1.40}$$

In the first case, this represents the transformation from the tensor product of the left most $i-1$ sites and the i^{th} bare site to the truncated basis for the left most i sites. In the second case, this represents the transformation from the tensor product of the i^{th} site and the right most $L-i-1$ sites, to the truncated basis for the right most $L-i$ sites. At the n^{th} step of the sweep, the superblock basis is written

$$|\alpha_{n-1}\, s_n\rangle \otimes |s_{n+1}\, \beta_{n+2}\rangle \ . \tag{1.41}$$

The wavefunction in the superblock basis is denoted,

$$\left|\Psi^{(n,n+1)}\right\rangle \sum_{\substack{\alpha_{n-1}\\ s_n\\ s_{n+1}\\ \beta_{n+2}}} \psi^{(n,n+1)}_{\alpha_{n-1}\, s_n\, s_{n+1}\, \beta_{n+2}} \left|\alpha_{n-1}\, s_n\right\rangle \otimes \left|s_{n+1}\, \beta_{n+2}\right\rangle \ , \tag{1.42}$$

where the coefficients $\psi^{(n,n+1)}_{\alpha_{n-1}\, s_n\, s_{n+1}\, \beta_{n+2}}$ are obtained by the diagonalization algorithm. We wish to apply basis transforms to this state so that it is written in the basis used by the next iteration, ie

$$\left|\Psi^{(g)\,(n+1,n+2)}\right\rangle \sum_{\substack{\alpha_n\\ s_{n+1}\\ s_{n+2}\\ \beta_{n+3}}} \psi^{(n+1,n+2)}_{\alpha_n\, s_{n+1}\, s_{n+2}\, \beta_{n+3}} \left|\alpha_n\, s_{n+1}\right\rangle \otimes \left|s_{n+2}\, \beta_{n+3}\right\rangle \ , \tag{1.43}$$

which can be used as a guess vector to accelerate computing the true $\left|\Psi^{(n+1,n+2)}\right\rangle$. It is easiest to split this transformation into parts. Firstly, the left block basis is truncated giving the truncated wavefunction,

$$\left|\Psi^{(T)\,(n,n+1)}\right\rangle = \sum_{\alpha_n, s_{n+1}, \beta_{n+2}} \psi^{(T)\,(n,n+1)}_{\alpha_n, s_{n+1}, \beta_{n+2}} \left|\alpha_n\right\rangle \otimes \left|s_{n+1}\, \beta_{n+2}\right\rangle \ , \tag{1.44}$$

with matrix elements obtained by

$$\psi^{(T)\,(n,n+1)}_{\alpha_n, s_{n+1}, \beta_{n+2}} = \sum_{\alpha_n, s_{n+1}, \beta_{n+2}} \sum_{\alpha_{n-1}, s_n} {}^{L}T^{(n)}_{\alpha_n; \alpha_{n-1}\, s_n} \psi^{(n,n+1)}_{\alpha_{n-1}\, s_n\, s_{n+1}\, \beta_{n+2}} \ . \tag{1.45}$$

This state is not properly normalized; the norm $\langle \Psi^{(T)\,(n,n+1)} | \Psi^{(T)\,(n,n+1)} \rangle$ is equal to the sum of the density-matrix eigenvalues of the kept states, P_m. Thus a small amount of information has been lost so that, even in the limiting case where the DMRG has converged completely, the transformed wavefunction is still not identical to the target eigenstate.

The transformation from the basis $\left|\alpha_n\right\rangle \otimes \left|s_{n+1}\, \beta_{n+2}\right\rangle$ to the basis $\left|\alpha_n\, s_{n+1}\right\rangle \otimes \left|\beta_{n+2}\right\rangle$ is, in the ordinary case completely trivial. However, when reflection symmetry is used, as discussed in section 1.2.3 above, the right block is stored in a different basis to the left block. Thus it is necessary to apply a basis transform to the site basis when shifting the site from the right block to the left block. This basis transformation is effected by the R operator,

$$\left|\alpha_n\, s'_{n+1}\right\rangle \otimes \left|\beta_{n+2}\right\rangle = \sum_{s_{n+1}} R_{s'_{n+1}; s_{n+1}} \left|\alpha_n\right\rangle \otimes \left|s_{n+1}\, \beta_{n+2}\right\rangle \ . \tag{1.46}$$

Usually, the obvious choice of single site basis means that the R operator is diagonal. This makes the transformation of $\psi^{T}_{\alpha_n, s_{n+1}, \beta_{n+2}}$ to the shifted basis very easy to

apply. When non-Abelian symmetries are used (described in detail in chapter 2), the transformation is non-trivial even in the non-reflection-symmetric case and requires the $6j$ coefficients of the algebra.

The final step is to 'undo' the truncation on the right basis,

$$\psi^{(g)}_{\alpha_n\, s_{n+1}\, s_{n+2}\, \beta_{n+3}} = \sum_{\beta_{n_2}} \psi^{T}_{\alpha_n\, s_{n+1}\, \beta_{n+2}}\, {}^{R}T^{(n+2)}_{\beta_{n+2};s_{n+2}\beta_{n+3}} \,. \tag{1.47}$$

Strictly speaking, the truncation operator is not invertible and this operation expands the dimension of the superblock basis from m^2N_{i+1} to $m^2N_{i+1}N_{i+2}$ states. Hence there are many entries of the guess wavefunction that are not yet specified. In particular, it is possible to add any quantity of the form $\phi_{\alpha_n\, s_{n+1}\, s_{n+2}\, \beta_{n+3}}$, such that

$$\sum_{s_{n+2},\beta_{n+3}} {}^{R}T^{(n+2)}_{\beta_{n+2};s_{n+2}\beta_{n+3}} \phi_{\alpha_n\, s_{n+1}\, s_{n+2}\, \beta_{n+3}} = 0 \,, \tag{1.48}$$

for each value of β_{n+2}, α_n and s_{n+1}. In the absence of any information as to what these entries should be, the easiest approach is to use Eq (1.47) directly, equivalent to setting the undetermined coefficients to zero. The reverse transformation, to shift the wavefunction from blocks of size $n, (L-n)$ to blocks $(n-1), (L-n+1)$, is the exact mirror of the transformation described above.

This transformation requires storing all the truncation operators used on the previous left moving sweep, ${}^{R}T$, for later use on the next right moving sweep and *vice versa*. These operators would otherwise not be required to be stored, so this optimization requires a small additional storage overhead. The operators that are not required for the current iteration can easily be stored on disk rather than main memory, so there is no additional RAM requirement, only additional disk space is required.

This optimization is extremely important, indeed it could be regarded as an essential component of the finite-size algorithm. As the DMRG sweeps converge, the overlap between the initial guess wavefunction and the final wavefunction tends to P_m, which in a typical calculation is of the order $1 - 10^{-5}$ or larger. Thus only a very small number of iterations of the matrix diagonalization algorithm need to be performed. Indeed, a possible approach suggested by White [44] † is to restrict the number of iterations of the matrix diagonalization algorithm to a small constant (two or three) and relying on repeated DMRG sweeps to obtain a converged state. The balance between convergence of the matrix diagonalization and convergence of the DMRG basis is a subtle and little-studied area. However some investigations are detailed in section 1.6 below. Even when the number of iterations of the matrix

†although it is not clear whether White actually used this scheme in the published calculations

diagonalization is not fixed but a conventional eigenvalue convergence criteria is used, the number of iterations is usually very small and essentially independent of the dimension of the superblock. Thus, for a superblock dimension of N, the wavefunction transformation effectively reduces the computation time for obtaining the wavefunction from $O(N^3)$ to $O(N^2)$ operations.

At the central point of a reflection symmetric model, an additional step is required to obtain the correct wavefunction. To see why, let $n = L/2 - 1$, so that the obtained initial guess wavefunction will be on the symmetric basis of left and right blocks of equal size. At this point one uses the spatial reflection of $|\alpha_n\rangle$ as the right block basis $|\beta_{n+3}\rangle$. The third step, of 'undo'ing the right block truncation, fails because the truncation operator ${}^{R}T^{(n+2)}_{\beta_{n+2};s_{n+2}\beta_{n+3}}$ is defined over the basis β_{n+3} of the *previous* sweep, but the required basis is the spatial reflection of $|\alpha_n\rangle$, obtained from the *current* sweep. This is clarified by a change in notation. Let the superblock basis at the central point of the *previous* sweep be denoted

$$|\Psi^{aa}\rangle = \sum_{a_L,a_R} \psi_{a_L a_R} |a_L\rangle \otimes |a_R\rangle , \tag{1.49}$$

which is defined over the tensor product of left block basis $|a_L\rangle$ with its spatial reflection $|a_R\rangle$. Let the superblock basis at the current iteration be denoted

$$|\Psi^{bb}\rangle = \sum_{b_L,b_R} \psi_{b_L b_R} |b_L\rangle \otimes |b_R\rangle \ . \tag{1.50}$$

In this notation, the wavefunction transformation above results in a superblock wavefunction in the mixed basis

$$|\Psi^{ba}\rangle = \sum_{b_L,a_R} \psi_{b_L a_R} |b_L\rangle \otimes |a_R\rangle \ . \tag{1.51}$$

To transform this to the required basis, a transformation operator is required,

$$\sum_{b_R,a_R} |b_R\rangle T_{b_R a_R} \langle a_R| \ , \tag{1.52}$$

that can be used to construct desired wavefunction $|\Psi^{bb}\rangle$ out of $|\Psi^{ba}\rangle$. Constructing this operator requires more than just the mixed wavefunction $|\Psi^{ba}\rangle$ and the wavefunction at the previous step, $|\Psi^{aa}\rangle$ is also required. The desired transformation, Eq. (1.52) is the one that maximizes the overlap $\langle\Psi^{ba}|\Psi^{aa}\rangle$. The matrix elements $T_{b_R a_R}$ can be obtained directly by solving the maximization problem with the constraint that T is row- or column-orthogonal. This is done in full in appendix A, the result being

$$T_{ba} = \sum_{\alpha} U_{b\alpha} V_{a\alpha} \tag{1.53}$$

where U and V are obtained from the singular value decomposition of the quantity $\rho_{a_L b_L} = \sum_{a_R} \psi_{a_L a_R} \psi_{b_L a_R}$. This quantity looks similar to a density-matrix, although that is only superficial, *e.g.* it is not in general a square matrix.

This transformation is rather complicated, requiring knowledge of the wavefunction at the symmetric point of the previous sweep and the calculation of a singular value decomposition, in addition to the three transformation steps required for the non-reflection symmetric case. However it is well worth the effort. In the experience of the author, without using this transformation the calculation of the ground state wavefunction at the symmetric point takes roughly as long to calculate as the total calculation time for the rest of the DMRG sweep put together, thus essentially negating the advantages of using the reflection symmetry at all. With the transformation, the initial guess vector is very good, although not quite so good as the non-reflection-symmetric case. In addition to the loss of accuracy from the truncation of the basis, there is an additional loss in accuracy because the previous sweep will typically be not as well converged. A measure of this convergence is how far the overlap $\langle \Psi^{ba} | \Psi^{aa} \rangle$ deviates from unity.

As far as is known, this thesis is the first derivation and use of the symmetric wavefunction transformation.

1.3.3 Basis state factorization

So far it has been assumed that the site basis used in the DMRG as exactly corresponds with a single site of the lattice model. There is no particular requirement for this however. The only condition that is required is that the full Hilbert space of the model can be written as a tensor product of subspaces,

$$|s_1\rangle \otimes |s_2\rangle \otimes \cdots \otimes |s_L\rangle \ . \tag{1.54}$$

The obvious way to achieve this is to map a DMRG site onto a lattice site. However, in some circumstances the lattice sites are factorizable. For example, the Hilbert space of a single band of electrons is composed of tensor products of the four dimensional site basis $|0\rangle$, $|\uparrow\rangle$, $|\downarrow\rangle$, $|\uparrow\downarrow\rangle$. This four dimensional basis is factorizable into the tensor product of two subspaces, $U \otimes D$, with

$$\begin{aligned} U &= |0\rangle \oplus |\uparrow\rangle \\ D &= |0\rangle \oplus |\downarrow\rangle \ . \end{aligned} \tag{1.55}$$

Thus it is possible, in this case, to map a single lattice site onto two DMRG sites. The DMRG basis is then the tensor product of $2L$ 'sites', of alternating U and D basis. The advantage of this procedure is that it halves the number of states

in the tensor product basis when adding sites to the blocks. Since two sites are added at each iteration, the effect is to reduce the dimension of the superblock basis by a factor of four. Thus a saving of $\sim 4^2$ in time required to diagonalize the superblock is achieved, at the expense of having to do twice as many iterations per sweep. Of course, for the same number of states kept this optimization would have the effect of *reducing* the accuracy, as fewer states are considered in the superblock diagonalization. But the performance increase allows more states to be kept for the same amount of computation time, which leads to an overall increase in accuracy per unit of computation.

This optimization has been used by the author, but not in the majority results presented in this thesis. In the spin case, this optimization is superseded by the $SU(2)$ invariant non-Abelian DMRG method described in chapter 2. However, this optimization still applies in the case of multi-band models, or where the single lattice site basis can be factorized without violating any symmetry operators. In particular, it would be possible to apply this to the Kondo lattice model (chapter 3), to factor the single site basis into the tensor product of a conduction band site and an f-spin site, even when using $SO(4)$ symmetry. However the non-Abelian DMRG algorithm is accurate enough that this was not necessary. Basis state factorization was used in the calculations of the phase diagram of the periodic Anderson model, described in section 3.8.

1.3.4 Minor optimizations

A small optimization that was used in the numerical calculations is to diagonalize the left block Hamiltonian in the truncated basis. This is simply an additional unitary transformation that can be combined with the truncation operator, so there is very little overhead. The advantage is that the contribution to the superblock Hamiltonian from the block Hamiltonians, $H^A \otimes I^B + I^A \otimes H^B$ is then completely diagonal. These matrix elements are of the order of the ground state energy, typically much larger in magnitude than the interaction terms. Thus this transformation makes superblock Hamiltonian matrix more diagonally dominant and hence easier to diagonalize. It is not a large effect though, the saving is around 10% - 30% of the number of matrix-vector multiplies. This is small compared with the acceleration due to other optimizations, but it still makes a noticeable improvement. As far as we know, this thesis is the first use of this optimization.

1.4 Variational Properties

This section is based around the work, starting with Östlund and Rommer [21], with additional details by Rommer and Östlund [45], on the exact form of the converged DMRG wavefunction. This is an important work, because from the form of the wavefunction it is possible to obtain many properties, such as the nature of the correlation functions. In addition, there are some systems, *i.e.* the so-called "AKLT" models [46], in which the obtained form is in fact exact even when only a single basis state is kept.

1.4.1 The matrix product ansatz

The easiest way to construct this form is to start with the infinite DMRG algorithm. Using the notation of section 1.3.2, we write the truncation of the basis at the n^{th} step as

$$|\alpha_n\rangle = \sum_{s,\alpha_{n-1}} T^{(n)}_{\alpha_n;s\,\alpha_{n-1}} |s\rangle \otimes |\alpha_{n-1}\rangle \,. \tag{1.56}$$

It is assumed that the single site basis $|s\rangle$ is independent of the lattice position n. Changing notation to use a form similar to that of [21], we set $T^{n}_{\alpha_n;\alpha_{n-1}}[s_n] \equiv T^{(n)}_{\alpha_n;\alpha_{n-1}s_n}$, where $T_n[s_n]$ is, for each fixed n and s_n, an $m \times m$ matrix. If the limit $n \to \infty$ exists in Eq. (1.56), we have $T_n[s] \to T[s]$, so the basis $|\alpha_n\rangle$ can be written, for large n, as

$$|\alpha_n\rangle = \sum_{\beta,s_1,s_2,\ldots,s_n} \left(T[s_n]T[s_{n-1}]\cdots T[s_1]\right)^{\alpha_n\,\alpha_0} |s_n\, s_{n-1}\cdots s_1\rangle \otimes |\alpha_0\rangle \,. \tag{1.57}$$

Here $|\alpha_0\rangle$ represents the initial state for the recurrence relation Eq. (1.56). This leads to a natural *ansatz* for the form of the bulk wavefunction, as a *matrix product* wavefunction [21,46]. For each $m \times m$ matrix Q, let

$$|Q\rangle_{MP} = \sum_{\{s_i\}} \mathrm{Tr}\left(Q\,T[s_n]T[s_{n-1}]\cdots T[s_1]\right) |s_n\, s_{n-1}\cdots s_1\rangle \,. \tag{1.58}$$

The notation $|Q\rangle_{MP}$ denotes the matrix product state specified by the choice of Q. Q specifies the boundary conditions on the state. In particular, the choice $Q = I$ corresponds to periodic boundary conditions. The cyclic invariance of the matrix trace implies that the resulting state $|I\rangle_{MP}$ is translationally invariant. This is the state that Östlund and Rommer used in their calculations [21].

The infinite-size DMRG algorithm provides a way of calculating the operator $T[s]$, however it is clear that this is not the only possibility. Indeed, the matrix elements could be determined variationally, by a direct calculation of $\langle\, I \,|\, H \,|\, I \,\rangle_{MP}$

as a function of $T[s]$. This is the approach taken by Östlund and Rommer [21]. For small values of m, there are enough conditions on the form of $T[s]$ that there are very few parameters to this calculation. For example, the projection given by T should preserve the orthonormality of the basis, $\langle\alpha'|\alpha\rangle = \delta_{\alpha'\alpha}$. Using Eq. (1.56), Östlund and Rommer demonstrated that the required condition on $T[s]$ is

$$\begin{aligned}\delta_{\alpha',\alpha} &= \sum_{\alpha'_{n-1},\alpha_{n-1},s',s} T^{*\alpha',\beta'}[s']T^{\alpha,\beta}[s]\,\langle s|s\rangle\,\langle\beta'|\beta\rangle \\ &= \sum_s \left(T[s]T^{\dagger}[s]\right)^{\alpha'\alpha} .\end{aligned} \tag{1.59}$$

This condition drastically reduces the number of independent degrees of freedom in $T[s]$. In addition, it follows from this relation, that $|I\rangle_{MP}$ is normalized, $\langle\, I \,|\, I\,\rangle_{MP} = 1$.

In the calculation of Östlund and Rommer [21], the Heisenberg chain with bilinear and biquadratic interactions was studied. This model has the Hamiltonian

$$H = \sum_n \boldsymbol{S_n}\cdot\boldsymbol{S_{n+1}} - \beta(\boldsymbol{S_n}\cdot\boldsymbol{S_{n+1}})^2 . \tag{1.60}$$

For $\beta = 1/3$, this is the "AKLT" model, where the ground state is exactly solvable as a matrix product wavefunction with $m = 1$ states kept. This Hamiltonian Eq. (1.60) conserves total spin symmetry, which Östlund and Rommer used to obtain further constraints on the matrix elements of $T[s]$. With all of the the constraints, keeping $m = 12$ states involves only 8 free parameters, which is enough to solve variationally without difficulty. The only use of the DMRG method was in deciding how many states should be kept for each quantum number. However, this too could easily be done variationally [21].

It is of interest to find out whether the matrix product state $|I\rangle_{MP}$ is an eigenstate of parity P. Östlund and Rommer showed that a sufficient condition is that there exists an invertible matrix Q_P such that

$$Q_P T[s] = p\,(T[s])^T\,Q_P\ , \tag{1.61}$$

where $p = \pm 1$. Then, by inserting $Q_P Q_P^{-1}$ into the trace in Eq. (1.58) and commuting Q_P through each term to ultimately cancel with Q_P^{-1} again, it can easily be shown that $P|I\rangle_{MP} = p^n|I\rangle_{MP}$. Östlund and Rommer also found the form of Q_P,

$$Q_P^{\alpha\beta} = p\sum_{s,\tau,\nu}\left(T^T[s]\otimes T[s]\right)^{(\alpha\beta),(\tau\nu)} Q_P^{\tau\nu}\ , \tag{1.62}$$

showing that Q_P, if it exists, is the eigenmatrix of the operator $\sum_s \left(T^T[s]\otimes T[s]\right)$ that has eigenvalue ± 1. Although Östlund and Rommer did not prove that Q_P always exists, they were able to construct the matrix in every case they examined.

1.4.2 Expectation values and correlation functions

From Eq. (1.58), The expectation value of some operator X has the form

$$\begin{aligned}\langle I \,|\, X \,|\, I \rangle_{MP} = \sum_{\{s_j\}\{s'_j\}} \; & \mathrm{Tr}(A^*[s'_n] \cdots A^*[s'_1]) \\ & \times \mathrm{Tr}(A[s_n] \cdots A[s_1]) \\ & \times \langle\, s'_n \cdots s'_1 \,|\, X \,|\, s_n \cdots s_1 \,\rangle \,.\end{aligned} \tag{1.63}$$

Using the trace and matrix product identities $\mathrm{Tr}(A)\,\mathrm{Tr}(B) = \mathrm{Tr}(A \otimes B)$ and $(AB) \otimes (CD) = (A \otimes B)(C \otimes D)$, this becomes

$$\begin{aligned}\langle I \,|\, X \,|\, I \rangle_{MP} = \; & \sum_{\{s_j\}\{s'_j\}} \mathrm{Tr}\left[(A^*[s'_n] \otimes A[s_n]) \cdots (A^*[s'_1] \otimes A[s_1])\right] \\ & \times \langle\, s'_n \cdots s'_1 \,|\, X \,|\, s_n \cdots s_1 \,\rangle \,.\end{aligned} \tag{1.64}$$

Östlund and Rommer [21] showed that this can be further simplified by making use of a "hat mapping", from a single site matrix operator M to a $m^2 \times m^2$ matrix $\hat{M}$, defined by

$$\hat{M} = \sum_{s',s} M_{s's} A^*[s'] \otimes A[s] \,. \tag{1.65}$$

The spin-spin correlation function $\langle I \,|\, \boldsymbol{S}_j \cdot \boldsymbol{S}_{j+l} \,|\, I \rangle_{MP}$ then takes on the form [21]

$$\begin{aligned}\langle I \,|\, \boldsymbol{S}_j \cdot \boldsymbol{S}_{j+1} \,|\, I \rangle_{MP} &= \mathrm{Tr}(\hat{I}^{n-2} \hat{\boldsymbol{S}} \cdot \hat{\boldsymbol{S}}) \\ \langle I \,|\, \boldsymbol{S}_j \cdot \boldsymbol{S}_{j+l} \,|\, I \rangle_{MP} &= \mathrm{Tr}(\hat{I}^{n-l-1} \hat{\boldsymbol{S}} \cdot \hat{I}^{l-1} \hat{\boldsymbol{S}})\end{aligned} \tag{1.66}$$

Thus the correlation length is determined by the eigenvalues of $\hat{I}$. In general, this applies to any two point correlation function $\langle M_x | M_y \rangle$. Due to the property Eq. (1.59), $\hat{I}$ is guaranteed to have one eigenvalue equal to unity. Östlund and Rommer [21] found numerically that all other eigenvalues have absolute value strictly less than unity. It is not true however that this eigenvalue itself determines the nature of the correlation function; if all of the rows of M_x and columns of M_y are orthogonal to the eigenvector of $\hat{1}$ with eigenvalue 1, then this eigenvalue gives zero contribution to the expectation value. In this case the relevant eigenvalue will have a value strictly *less* than unity. The eigenvalue that determines the behavior of the correlation function is the largest eigenvalue p (which depends on the number of states kept m) such that the corresponding eigenvector has non-zero overlap with at least one row of M_x and one column of M_y. Then, the long range properties of the correlation function are

$$\langle M_x | M_y \rangle = a\, p^{-|x-y|} \,. \tag{1.67}$$

This implies that the correlation functions decay exponentially, with correlation length

$$\xi = -\frac{1}{\ln p} \,. \tag{1.68}$$

It would appear to be impossible to obtain algebraic correlation functions from the matrix product ansatz (and therefore, by conjecture [21], in DMRG also). The only situations where long range order appears is when the relevant eigenvalue of the $\hat{1}$ operator is $p = 1$, which corresponds to $\langle M_x | M_y \rangle$ tending to a finite constant as $|x - y| \to \infty$. It is important to note that this result refers to the correlations inherent in the form of the wavefunction itself and has nothing to do with the way that the correlation function is actually evaluated. In particular, this result should also apply to *e.g.* Friedel oscillations and arbitrary n-point correlation functions.

This result is in apparent contradiction to some DMRG calculations, where good results have been achieved in determining exponents of algebraic correlations (see, for example reference [47]). In practice, at short-to-intermediate distances, the correlations in a DMRG wavefunction for a gapless system do decay as approximately algebraic functions. In principle, if enough states are kept that the exponential correlation length due to the matrix product ansatz is very long, then it is conceivably possible to observe algebraic decay of the correlations for small distances. However, the situation is in fact rather better than this; the exponential decay of the correlation functions only starts for distances $|x-y| > k$, where k is a threshold distance that depends on the number of states kept m. This is shown in Fig. 1.6, which illustrates the exponential decay of the spin-spin correlation functions for the half-filled Hubbard model. We define

$$g_m(r) = |\langle \boldsymbol{S}_0 \boldsymbol{S}_r \rangle| \,, \tag{1.69}$$

to be the envelope of the correlation function at a distance of r sites, for the ground state with m states kept. Fig. 1.6 shows the quantity

$$\ln \left[\frac{g_m}{g_\infty} \right] \,, \tag{1.70}$$

which should behave as $-r/\xi_m$, where ξ_m is the m-dependent correlation length. However, Fig. 1.6 indicates that the correlation decays closer to

$$\ln \left[\frac{g_m}{g_\infty} \right] \sim \begin{cases} 0, & \text{if } r < k_m \\ (k_m - r)/\xi_m, & \text{if } r \geq k_m \end{cases} \,, \tag{1.71}$$

where k_m is a threshold such that the correlation function decays exponentially only for $r \geq k_m$.

This curious behavior has been noted before [21,48], but the explanation remains elusive. Very recently a possible line of progress in this issue was made by Osborne and Neilsen [49], who have studied the correlations of the DMRG wavefunction from a quantum information point of view. In DMRG, the choice of states kept

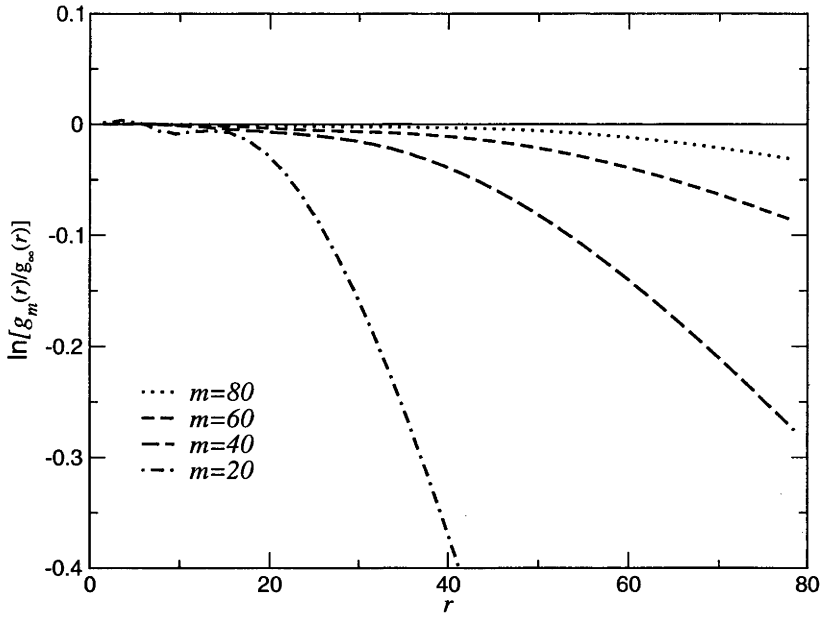

Figure 1.6: Logarithm of the decay of the spin-spin correlation function for the half-filled Hubbard model with m = 80,60,40 and 20 states kept, using the $SO(4)$-invariant algorithm described in chapter 2. The correlation function starts to decay exponentially only at distances r larger than an m-dependent threshold.

via the density-matrix eigenvalues maximizes the overlap between the ground state before and after the truncation, but it does not maximize the *entanglement* between the left and right blocks. By instead taking a truncation operator that maximizes the entanglement between the two blocks, Osborne and Neilsen *et al.* conjecture that it is indeed possible to obtain algebraic correlations [49]. In view of the very general result of the exponential decay of the matrix product wavefunction at long distances, this conjecture would appear to be unlikely. In any event, it is highly plausible that there is a direct relationship between the threshold of exponential decay k_m and the entanglement of the wavefunction.

1.4.3 Relationship to the DMRG wavefunction

It was shown by Dukelsky *et al.* [50] that the the converged fixed point of infinite-size DMRG algorithm does not exactly correspond with the matrix product wavefunction and in particular the DMRG wavefunction is not exactly translationally invariant. The origin of this difficulty is the fact that two bare sites are added to the system at each step, so that each block has Nm degrees of freedom (where N is the number of basis states per site), whereas in the matrix product method [21],

there are only m degrees of freedom. This was interpreted in reference [50] as causing a shallow bound state to appear between the left and right halves of the system. A solution to this, proposed in [50] and carried over to the finite-size DMRG algorithm by Takasaki *et al.* [51], is to add a site to only the system block; no site is added to the environment block. This means that the environment block has only m degrees of freedom, thus as described previously (section 1.2), there will be at most only m non-zero eigenvalues of the reduced density-matrix. In particular, for each quantum number in the basis, the maximum number of states will be fixed. However, once the DMRG iterations have begun to converge, the number of states in each sector is fixed and the *equality* in Eq. (1.13) is satisfied. Thus, as long as enough ordinary DMRG iterations are done to fix the quantum numbers of the basis states, there is no reduction in the size of the basis when adding only one site at each iteration. A difficulty of the single-site scheme is that the truncation error is identically zero. The truncation error is typically used to obtain the scaling of the ground state energy to zero truncation error, because the energy is usually linear in the truncation error (with a small quadratic correction). But this cannot be done for the single-site algorithm, so the scaling must be done using m directly. The convergence issues are discussed further in section 1.6.

As a concrete example, table 1.1 shows some numerical data for the spin 1 Heisenberg chain, for the limit of small number of states kept. This shows the ground state energy density in the large lattice size limit for the standard DMRG and the modified DMRG with one site added per iteration (labeled $e^{2\text{ sites}}$ and $e^{1\text{ site}}$ respectively). The final column is the truncation error associated with the standard DMRG results. Also shown are energies calculated by the variational matrix product method (labeled e^{MP}) and some standard DMRG results from reference [50] (labeled $e^{\text{DMRG JD}}$). This table shows that when adding only a single site per iteration the energy density coincides with that of the matrix product method, to the accuracy of the calculation. The standard DMRG results in column 3, from reference [50], were intended to show that there is a significant accuracy advantage in adding only a single site at each iteration. However, there is a quite large disagreement between those DMRG results and that of the current thesis (column 5). After correspondence with one of the authors of this paper (T. Nishino), it has become clear that the DMRG results in [50] are in error. The DMRG results were obtained from an implementation of the Interaction-Round-a-Face (IRF) DMRG algorithm [52] (further discussed in section 2.3.3). It was thought by the authors of reference [50] that the algorithm used was equivalent to the standard DMRG algorithm with additional symmetries, but this is not the case and the actual algorithm

Table 1.1: Energy density of the spin 1 Heisenberg chain as a function of the number of states kept. $e^{\text{MP JD}}$ and $e^{\text{DMRG JD}}$ are from reference [50]. The exact energy density is $e = -1.4014845$ [53].

m	$e^{\text{MP JD}}$	$e^{\text{DMRG JD}}$	$e^{\text{1 site}}$	$e^{\text{2 sites}}$	$1 - P_m$
1	−1.333333	−1.333333	−1.3333333	−1.3333333	1.58×10^{-2}
2	−1.399659	−1.369077	−1.3996590	−1.3996237	4.06×10^{-4}
3	−1.401093	−1.392515	−1.4010933	−1.4010886	5.39×10^{-5}
4	−1.401380	−1.401380	−1.4013806	−1.4013798	1.63×10^{-5}
5	−1.401443	−1.401436	−1.4014447	−1.4014430	7.77×10^{-6}
6	−1.401474	−1.401468	−1.4014757	−1.4014756	1.35×10^{-6}

used corresponds to a different block structure[†].

Although this thesis shows that the accuracy advantage of the single-site DMRG is much smaller than that claimed by Dukelsky *et al.* [50], this does not completely eliminate the advantages of single-site DMRG. In particular, the single-site DMRG results in a wavefunction that is exactly translationally invariant. Figure 1.7 shows the energy of each bond for the DMRG wavefunction with one and two sites added per iteration. With the standard two-site algorithm, the wavefunction is far from being translationally invariant, with a deformation at the center of the chain interpreted by Dukelsky *et al.* [50] as a shallow bound state, although the deformation is several orders of magnitude smaller than was thought by Dukelsky *et al.* . With the single-site DMRG, the bond energy is exactly translationally invariant and is slightly lower (and hence better) than both the asymptotic and average bond energy of the standard (two-site) DMRG wavefunction. In addition, there is a large performance advantage to using a single added site, because the superblock Hamiltonian matrix has a much lower dimension. Indeed, even for $m = 2$, the difference in bond energy is rather small, so the improved performance is the main advantage of the single block DMRG, at least for the Heisenberg spin chain. For larger values of m, the bond energies given by the two algorithms converge rapidly.

Takasaki *et al.* [51] extended these results to the case of the finite-size algorithm. This work shows that it is also advantageous to add just a single site per iteration in the latter stages of the finite-size algorithm. When this is done, the finite-size algorithm has some interesting properties. The only states eliminated

[†]This is not an essential flaw, in principle any block structure that can be used in standard DMRG can also be used in IRF-DMRG.

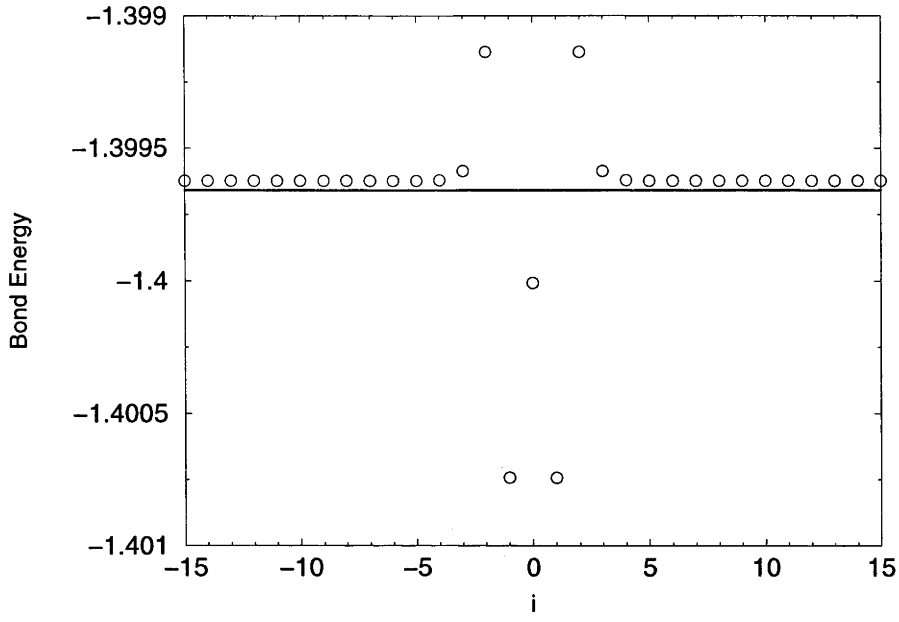

Figure 1.7: Bond energy $\langle \boldsymbol{S}_i \cdot \boldsymbol{S}_{i+1} \rangle$ as a function of lattice position for the DMRG wavefunction of the spin 1 Heisenberg chain with $m = 2$. The solid line is the bond energy of the translationally invariant wavefunction from the single block DMRG.

by the truncation have zero weight in the wavefunction, so the wavefunction is exactly represented after the truncation. This makes the wavefunction transform, Eq. (1.47) also exact. Because no states that have any weight in the wavefunction are ever lost, the variational principle implies that the new states introduced at each iteration can only ever reduce the energy. Thus the obtained ground state energy must monotonically decrease over the course of the DMRG sweep. It is also shown by Takasaki *et al.* [51] that the wavefunction converges to a fixed point that is independent of the position of the added site in the lattice. This is in sharp contrast to the behavior of the standard DMRG algorithm, where there is a large position dependence (further discussed in section 1.6.1). Again, the difference between properties calculated by the single-site variant and the standard finite-size algorithm goes to zero as m is increased, making the single-site finite-size DMRG less useful when a large number of states can be kept. However, similarly to the situation for the infinite-size algorithm, the single-site finite-size DMRG variant is surely useful from performance considerations alone. This has not been implemented for the main results in this thesis however. Additional work needs to be done to fully implement single-site DMRG. In particular, the convergence criteria discussed in section 1.6 would need substantial modification to work with this algorithm.

1.5 Two-Dimensional DMRG

There are several ways that the DMRG algorithm can be extended to higher dimensions. A conceptually simple approach is to replace a single DMRG site with an entire row of lattice sites. In this way the DMRG iterations proceed by sweeping across the $2D$ lattice from one side to the other, with one row being shifted from the left block to the right block (or *vice versa*) at each iteration. This scheme was implemented by M. S. L. du Croo de Jongh *et al.* [54] for the two-dimensional Ising model in a transverse field, for system sizes up to 30×6. Because a single 'DMRG site' is an entire row of the real-space lattice, it is relatively easy to make use of lattice symmetries. M. S. L. du Croo de Jongh *et al.* [54] utilized translation symmetry of the lattice rows, as well as spatial reflection and spin reflection. However the essential difficulty with this approach is that the dimension of the Hilbert space of the row of lattice sites that is added to the block at each iteration grows exponentially with the width of the row. For larger lattices this technique rapidly becomes prohibitively expensive. There are techniques in DMRG to deal with systems that have a large number of basis states per site, for example the four-block algorithm developed by R. J. Bursill [55] and the local reduction approach developed by C. Zhang *et al.* [17]. In the latter algorithm, only a small number of the basis states of the site are used at a time. For example, suppose that there are N basis states per site, but due to limited computational resources only m states can be included at a time, with $m \ll N$. At the first iteration, the wavefunction is obtained using only m states, chosen arbitrarily or perhaps using some information from previous steps to guess which are the most likely states. Then, $m/2$ say, of the highest weight states are kept and the other $m/2$ are discarded. The next set of $m/2$ basis states are then included in the calculation and the process repeats until all of the basis states have been used. The number of iterations required is $2N/m - 1$. Since N increases exponentially with the width of the lattice, the amount of computation required will also increase exponentially, hence only providing a minor improvement over the algorithm used in reference [54].

An alternative approach to extending DMRG to two dimensions is to add single lattice sites to the system, while following a connected one-dimensional path through the two-dimensional lattice. The original approach of S. Liang and H. Pang [56] is to map the system into a one-dimensional chain via a horizontal 'zipper', shown in Fig. 1.8. In the DMRG calculations on the two-dimensional $t - J$ model in chapter 4, a slightly modified scheme was used, shown in Fig. 1.9, which reduces the distance of the long-range interactions of the one-dimensional mapping, at the expense of having fewer nearest-neighbor interactions. It is not possible to

reflect the system block into an environment block of the proper geometry at each iteration, thus the finite-size DMRG algorithm must be used. The difficulty is how to construct the initial blocks for use in the finite-size algorithm. In principle, with enough computational resources this does not matter, as the finite size algorithm will converge to the ground state in the large m limit regardless of the initial state of the system at the start of the finite sweeps. However the rate of convergence definitely depends strongly on the initial condition, thus the way the initial blocks are constructed is rather important in practice. In the work of Liang and Pang [56], two schemes were tried for constructing the initial blocks. In the first scheme, they performed infinite-size DMRG on a one-dimensional chain as usual, up to a size $L_x \times L_y$ and then turned on additional couplings required to make the lattice two-dimensional. In the second scheme, they calculated several low-lying eigenstates of a one-dimensional chain of size $L_x + 1$ and used these states to prepare the environment block. Another approach was used by T. Xiang [13] in a momentum space formulation of the two-dimensional Hubbard model. Because different lattice sizes have different permissible k points, the lattice size needs to be fixed in both directions before the calculation is started. Xiang used the Wilson numerical renormalization-group to build the initial blocks for the calculation. This is roughly equivalent to DMRG where there is no interaction between the left and right blocks. In this case the eigenstates of the reduced density-matrix coincide with the eigenstates of the block Hamiltonian. Noack and White [41] used an improved method whereby the hybrid finite-infinite DMRG algorithm (see section 1.2.2) was used to maintain the overall size of the system at a multiple of the row size of the lattice. Thus the system grows by complete rows at a time, even though only two bare sites are used at each iteration.

Unfortunately, the computational effort of this scheme is not significantly better than the approach of adding a lattice row at a time. In particular, Liang and Pang [56] found that the number of states required to achieve a given accuracy increases exponentially with the lattice size. For the sample model of non-interacting spinless fermions, they found that the required number of states scales as $m \propto \alpha^L$, with $\alpha \simeq 3.9$. Generalizing this result to non-square lattices, they concluded that the required number of states depends on the number of contact points (*i.e.* the length of the interface) between the left and right blocks. The zipper configuration in Fig. 1.8 minimizes the number of contact points to $L_x + 1$, independent of L_y. This matches the general behavior of the row algorithm of du Croo de Jongh *et al.* [54], in that the computational effort increases exponentially with the width of the system, but is only polynomial in the length. This would appear to be a fundamental limitation

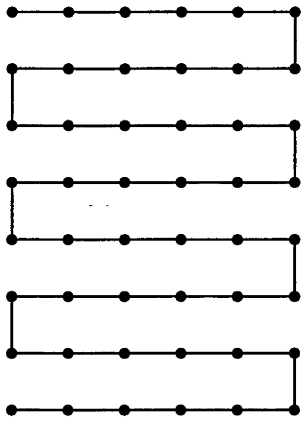

Figure 1.8: A two-dimensional lattice is mapped to a one-dimensional chain along the solid line. Interactions between nearest neighbor sites in the vertical direction become long range interactions in the one-dimensional mapping.

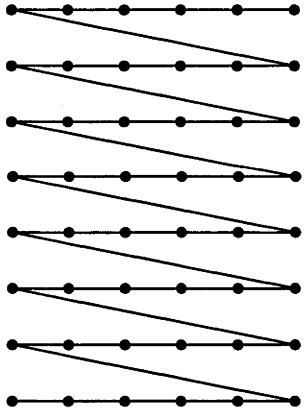

Figure 1.9: An alternative mapping that reduces the maximum distance of the long-range interactions on the one-dimensional chain.

of DMRG when applied to two-dimensional systems. The wavefunction in a DMRG calculation is inherently a one-dimensional matrix product, described by Eq. (1.58), with correlations between sites decreasing exponentially as the distance between the sites increases. In a one-dimensional system with short range interactions this does not present a significant problem. However, a two-dimensional system, when it is mapped onto a one-dimensional chain, contains long range interactions that join sites at distances proportional to the lattice size. A truly two-dimensional generalization of the matrix product wavefunction is possible, where the truncation

operator T is represented by a higher rank tensor, with one index per nearest-neighbor site. Higher dimensional generalizations is an active area of research (see for example the two-dimensional tensor product formulation of Nishino *et al.* [57]), however formulating a DMRG-like algorithm to calculate such a wavefunction would seem to be a formidable problem. However, despite these difficulties it is possible to treat two-dimensional systems of a somewhat larger size than is practical in an exact diagonalization. With well-optimized software and fast computers, it is possible to obtain reasonable results for modest size lattices.

Liang and Pang [56] found that the converged ground state was independent of the method of constructing the blocks. However this is not true in general as it is possible, if the number of states kept is too small, that the DMRG self-consistently converges to an incorrect state. This is a much bigger problem in two-dimensional calculations where it may not be possible to keep enough states to obtain a ground state that is independent of the initial conditions. This is especially noticeable if the ground state is not uniform, but has, *e.g.* a striped phase. This effect was noticed in the two-dimensional $t-J$ model with half-periodic, half-open boundary conditions, by Scalapino and White [58] and also in the calculations done for this thesis [11] (described in chapter 4).

Recently, Xiang *et al.* [12] suggested a modification of the usual 'zipper' mapping, proposing a scheme that allows a lattice of size $L \times L$ to be built from the DMRG blocks used to construct an $(L-1) \times (L-1)$ lattice. This is an important advance because the scheme can be applied iteratively to construct a good wavefunction for an arbitrarily large system, which can then be used as the initial state for finite-size sweeps. While this paper came too late to apply this technique to the two-dimensional DMRG calculations presented in chapter 4 of this thesis, it is well worth some investigation; in particular the claim that the approach is significantly more accurate than other two-dimensional DMRG algorithms in use [12]. The basic idea is that the two-dimensional system is mapped onto a one-dimensional chain with a diagonal mapping. In this way the system size can be increased while re-using blocks from smaller lattice sizes. This is illustrated in Fig. 1.10, which shows the initial block configuration up to size 3×3. These blocks can then be used to construct a 4×4 system as illustrated in Fig. 1.11. At the first step of each lattice size, the two added sites are at diagonally opposite corners of the lattice. This is not a major complication, however the wavefunction transformation Eq. (1.47) would need appropriate modifications for this block structure.

After $L-2$ iterations, the two added sites are adjacent and the DMRG iterations proceed as usual. Xiang *et al.* [12] have tested the algorithm on the two-

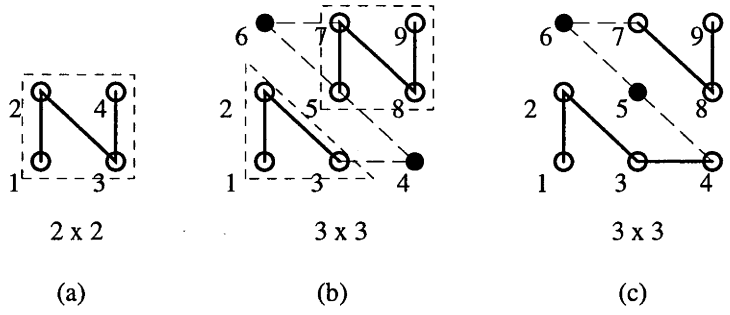

Figure 1.10: The configuration used to construct a 3×3 lattice from the initial 2×2 lattice, figure 3 from reference [12]. The solid circles are the locations of the bare DMRG sites. The numbers specify the order of the sites in the one-dimensional mapping. (a) is the 2×2 lattice at the first iteration. (b) shows how the 3×3 lattice is constructed from two 2×2 lattices. (c) shows how the added sites are moved into the correct sequence in the one-dimensional mapping.

dimensional spin 1/2 Heisenberg chain for lattice sizes up to 12×12. Undoubtedly the algorithm produces an excellent starting wavefunction for the finite-size iterations once the final lattice size is reached, greatly accelerating the computation. However, Xiang *et al.* [12] also claim that this algorithm gives significantly more accurate results than the horizontal zipper scheme. This is supported by some calculations of the ground state energy, which are reproduced in table 1.2. We only give the results for square lattices here; the original paper also includes calculations for diagonal lattices, but there seems to be no essential difference between the two as far as the accuracy of the DMRG is concerned. This table shows that the energy per bond obtained by the new algorithm is somewhat lower (and therefore better) than the energy obtained by the horizontal zipper scheme. Moreover the table implies that the improvement in energy grows substantially as the lattice size is increased. This is surprising, because the accuracy of two-dimensional DMRG calculations is expected to depend strongly on the length of the interface between the two blocks. For the horizontal zipper, the length of this interface is a minimum, at $L+1$ bonds. On the other hand, the diagonal zipper has up to $2L$ bonds connecting the two blocks. Once the calculation has converged, the ground state energy should be determined only by the configuration of the blocks, *ceteris paribis* and not on the the method used to construct the initial state. The method used to construct the $L \times L$ lattice should have no effect on the final accuracy, as long as the calculation has properly converged. Thus any real improvement in accuracy must arise from the

form of the mapping onto the one-dimensional chain.

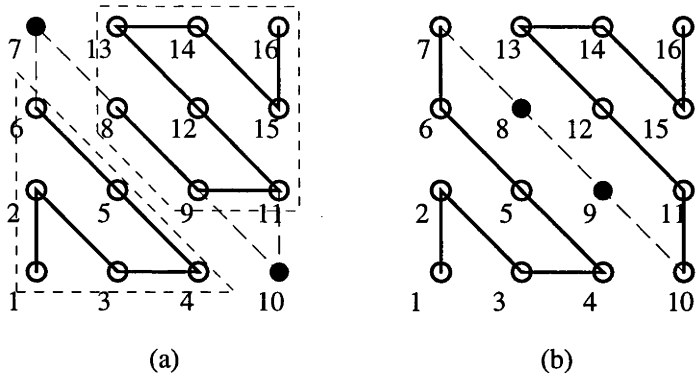

Figure 1.11: The configuration used to construct a 4×4 lattice from the 3×3 lattice, figure 4 from reference [12].

The DMRG algorithm used in reference [12] appears to be, apart from the modified mapping onto the one-dimensional chain, equivalent to the DMRG algorithm used in this thesis, *i.e.* with the same number of states kept essentially identical results are obtained. This alternative mapping is a rather simple modification to make, thus we have calculated, using the author's DMRG program, the ground state energy per bond for the horizontal and diagonal zipper algorithms, as well for the modified horizontal zipper shown in figure 1.9. By an extrapolation of the energy from between 400 and 500 states kept, an estimate of the true energy per bond has also been obtained (the methodology for this extrapolation is described in section 1.6). This data appears in table 1.3. The modified horizontal zipper gives results which are uniformly better than the standard horizontal zipper scheme, but the differences so small that it was not worth including the results in table 1.3, therefore only the energies produced by diagonal and horizontal algorithms are shown. The fractional error in the energy per bond in table 1.3 shows that there is a noticeable improvement in the diagonal zipper scheme, but the actual improvement is rather small. By measuring the difference between the energies of the diagonal and horizontal zipper algorithms without any comparison to the true ground state energy, the data in table 1.2 incorrectly suggests that the accuracy of the diagonal zipper compared with the horizontal zipper, increases as the lattice size is increased. In fact, the improvement in the relative error in the energy appears to be essentially independent of the lattice size and amounts to around one binary digit or less of accuracy.

Table 1.2: Comparison of the ground state energy per bond for the Heisenberg model on a square lattice of size L^2 and open boundary conditions, from reference [12]. E_d is the energy obtained by the diagonal mapping onto a 1D chain used in the new algorithm of Xiang [12] and E_h is the energy obtained from the conventional horizontal mapping.

L	m	E_d	E_h	$\frac{E_h - E_d}{\lvert E_h \rvert}$
6	50	-0.361972	-0.361919	1.5×10^{-4}
8	50	-0.352040	-0.351149	2.6×10^{-3}
10	50	-0.344292	-0.341389	8.4×10^{-2}
12	50	-0.337374	-0.332574	1.4×10^{-2}
6	100	-0.362096	-0.362089	1.9×10^{-5}
8	100	-0.353213	-0.353057	4.3×10^{-4}
10	100	-0.347043	-0.345771	1.3×10^{-3}
12	100	-0.341588	-0.338833	8.0×10^{-3}

Table 1.3: Energy per bond of the 2D Heisenberg model calculated using the author's DMRG program. E_g is an estimate of the true ground state energy per bond, extrapolated to $m \to \infty$. Not enough results were calculated for the 12×12 diagonal mapping to be able to perform the extrapolation for that case.

		Diagonal mapping		Horizontal mapping	
L	m	E_d	$\frac{E_d - E_g}{\lvert E_g \rvert}$	E_h	$\frac{E_h - E_g}{\lvert E_g \rvert}$
6	50	−0.361972476	3.8×10^{-4}	−0.361917718	5.4×10^{-4}
	100	−0.362096242	4.7×10^{-5}	−0.362088528	6.8×10^{-5}
	500	−0.362113079	6.1×10^{-8}	−0.362113056	1.2×10^{-7}
	∞	−0.362113101	–	−0.362113100	–
8	50	−0.352042	4.7×10^{-3}	−0.351147	7.3×10^{-3}
	100	−0.353213	1.5×10^{-3}	−0.353059	2.0×10^{-3}
	500	−0.353720	4.5×10^{-5}	−0.353719	4.9×10^{-5}
	∞	−0.353736	–	−0.353737	–
10	50	−0.34430	1.4×10^{-2}	−0.34129	2.3×10^{-2}
	100	−0.34705	6.3×10^{-3}	−0.34576	1.0×10^{-2}
	500	−0.34902	6.3×10^{-4}	−0.34898	7.5×10^{-4}
	∞	−0.34925	–	−0.34924	–
12	50	−0.3374	2.5×10^{-2}	−0.3335	3.7×10^{-2}
	100	−0.3416	1.1×10^{-2}	−0.3388	2.1×10^{-2}
	500	−0.3456	1.9×10^{-3}	−0.3452	3.0×10^{-3}
	∞	–	–	−0.3462	–

1.6 Convergence

The DMRG algorithm is, like most numerical calculations, subject to both random and systematic errors. The systematic errors are errors that affect the quantities in predictable ways. The error caused by the truncation of the block states falls into this category, at least for some quantities such as the energy. This error can be compensated for by calculating the scaling of $E(m)$, the ground state energy as a function of the number of states kept, as $m \to \infty$. Random errors arise from sources of error which are too hard to systematically compensate for, due to intrinsic limitations (such as hardware limitations on precision) or algorithmic truncation, whereby a convergence criteria is used to stop an iterative solver once some predetermined accuracy has been achieved. In the latter case, the magnitude of the error is usually controllable, by modifying the convergence criteria for more or less accuracy of the final result. Examples of random error in the DMRG algorithm are the accuracy of the superblock diagonalization and numerical errors in the density-matrix diagonalization. In the case of random errors, the best that can be hoped for is to calculate sôme reasonable bounds on the magnitude of the error. This section starts with a discussion of the random and systematic errors that occur in DMRG, leading to a discussion of the convergence criteria used in this thesis, both for the superblock ground state eigensolver and the convergence of the DMRG sweeps themselves. The usual approach, in a small DMRG calculation, is to fix the number of states m at each sweep from the outset. However, for calculating accurate ground state energies across a significant parameter range, with many separate DMRG runs, this is far from optimal. If the number of sweeps used is not enough to obtain a converged energy, the run needs to be repeated with a larger number of states. This requires a manual inspection of the energy of each sweep to check the convergence, for every DMRG run. On the other hand, if a conservatively large number of sweeps is used to ensure convergence a lot of CPU time will be wasted if the energy converges quickly for some parameter values. For example, in the studies on the Kondo lattice model, Fig. 3.4 in chapter 3, summarizes the result of 450 DMRG runs alone, the entire study comprises many thousands of DMRG runs. In the Kondo lattice study, much time was wasted in the early months following misleading paths suggested by DMRG calculations that later turned out to have insufficient accuracy or were simply not properly converged.

It is of interest to know how fast the calculation is expected to converge for a particular error bound. In the case of DMRG this is primarily determined by the rate of decay of the reduced density-matrix eigenvalues. In extreme cases, for example the AKLT model, only one state needs to be kept to obtain the exact

ground state. In a more typical one-dimensional calculation, an exact result is not possible but the reduced density-matrix eigenvalues decay exponentially fast, such that extremely small truncation errors are obtained, while keeping a reasonable number of states in the basis. In the case of a two-dimensional model, the behavior is typically more pathological, with the truncation error for a fixed number of states depending strongly on the size of the lattice.

1.6.1 Random errors

The energy as a function of iteration number can vary considerably in the finite DMRG method. In the early days of DMRG this was a cause for concern, however it turns out that the variation in energy across a sweep is rather small compared with the energy variance caused by the truncation of the basis. Figure 1.12 shows the ground state energy for seven complete DMRG sweeps for the Kondo lattice. This form of energy variation is typical of a DMRG calculation. Each sweep uses 300 states kept, using the $SO(4)$ algorithm described in chapter 2. There are two obvious sources of error displayed in this figure. Most striking is the variation in energy across the sweep, the standard deviation of the energy[†] being $\sigma_E = 2.1 \times 10^{-7}$. Also, the average energy across the sweep is itself decreasing, probably exponentially. The approach used in this thesis is to define $E(m)$ to be the average energy across the sweep and treat the variance in energy as a random error. Since DMRG is a variational method, it would also be valid to take the minimum energy of the sweep, however as will be seen later, such a choice has no effect on the overall calculation once all errors are taken into account.

The second source of error shown in Fig. 1.12 is lack of convergence of the DMRG sweeps themselves. Over the seven sweeps, the average energy of the sweep decreases $\sim 10^{-6}$, with only a slow leveling out. There are several ways to measure the energy difference between two successive sweeps. Perhaps the simplest measure is the difference between the average energies of two successive sweeps. However, this is prone to false positives, where the average energy happens to nearly coincide even though the iterations are not near to convergence. This was the cause of several failed runs, where by chance the automatic convergence criteria was met, but visual inspection of the energy revealed the calculation was far from convergence. Once the DMRG sweeps have converged the energy at each iteration should match closely the energy at the equivalent iteration of the previous sweep, to very high accuracy.

[†]This number also includes a contribution from the tolerance of the eigensolver, which is also of order 10^{-7}. This is a rather conservative estimate however, the true error attributable to the eigensolver is probably much less than this.

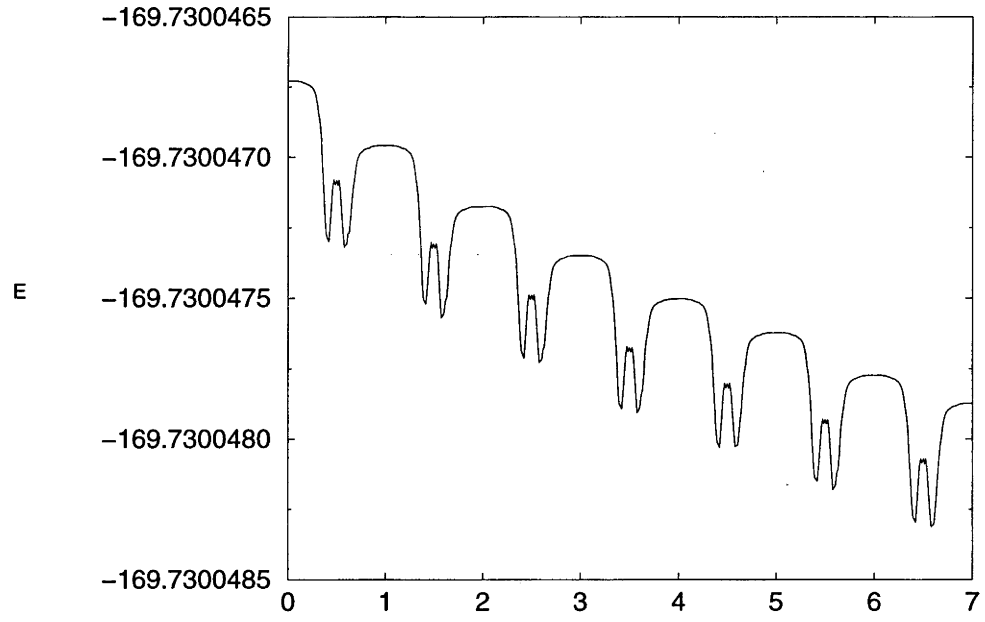

Figure 1.12: Energy at each iteration, for 7 complete DMRG sweeps of the Kondo Lattice model, 80 site lattice with electron density $n = 0.8$ coupling $J/t = 2.9$ and 300 states kept.

To take this into account an improved measure of the difference in energy between two sweeps was used, which we call the *sweep correlation error*,

$$\sigma_S = \left(\frac{\sum_i (E_i - E_i')^2}{N} \right)^{1/2} . \tag{1.72}$$

Here E_i and E_i' are the energies at the i^{th} step of two successive DMRG sweeps. For the data in Fig. 1.12 the correlation error decreases from 2.9×10^{-7}, between the first two sweeps shown, to 1.6×10^{-7} between the last two sweeps. This is very close to the difference between the average energy of the last two sweeps, which is 1.33×10^{-7}. Indeed, for perfect correlation between two sweeps, the sweep correlation error will be exactly equal to the energy difference. Assuming that the average energy of the sweep converges to the fixed point exponentially, the deviation in energy from the fixed point will be proportional to the energy difference and hence also to the correlation error. For the example in Fig. 1.12, an exponential fit to the average energy gives the fixed point at -169.73004881. The difference between the average energy at the final sweep in Fig. 1.12 and the extrapolated fixed point is 8.5×10^{-7}, around 5 times larger than the sweep correlation error.

One can conceive a convergence criteria based on performing an exponential fit to the average sweep energy and stopping when the error of the fit is smaller than some pre-determined tolerance. However this is a rather complex procedure and

it would probably take some effort to make a robust convergence criteria, without wasting CPU cycles, based on the direct fit. Instead, in this thesis we make use of the fact that the sweep correlation error will be proportional to the difference between the average energy of the current sweep and the extrapolated fitted energy. By checking the sweep correlation error directly against the given tolerance, we obtain a much simpler convergence criteria, which should give similar results. This is at the expense of the tolerance having a small model dependent (and parameter dependent) component, which has to be determined heuristically. The tolerance of choice is given by the error in the average sweep energy σ_E. Thus, the convergence criteria used can be summarized as stop when

$$\sigma_S \leq \text{const} \cdot \sigma_E \,, \tag{1.73}$$

where the constant is an estimate of the exponential decay in the fit. For the data presented in Fig. 1.12, the ideal constant would be 1/5, making the contribution to the error from the fit equal to the contribution of the error in the average sweep energy. Very good results are also achieved with a somewhat looser tolerance however. For most of the results presented in this thesis a constant of $0.5 - 1.0$ was found to be adequate; this is a trade-off between accuracy and the number of sweeps that need to be performed.

1.6.2 Systematic errors

As we have seen, the truncation of the operators in DMRG introduces a systematic error into the wavefunction that causes a deviation from the exact energy. Since this effect is dependent upon m, there is hope that the systematic error can be eliminated by a suitable scaling to $m \to \infty$.

We write the wavefunction at step i of the finite algorithm as a linear combination of the component of the wavefunction that is kept, $|\kappa_i\rangle$ and the truncated part $|\tau_i\rangle$. The mix of the two states is given by the sum of the reduced density matrix eigenvalues at step i, P_m^i.

$$|\psi_i\rangle = \sqrt{P_m^i}|\kappa_i\rangle + \sqrt{1 - P_m^i}|\tau_i\rangle \,. \tag{1.74}$$

The weight of the discarded states at each step is just the truncation error $(1 - P_m^i)$. Thus it is natural to expect that the difference between the exact energy and the energy obtained by the DMRG will be proportional to the cumulative truncation error $1 - P_m = \sum_i (1 - P_m^i)$ over the sweep[†]. This has become a standard calculation

[†]It is usual in the literature to quote a 'typical' truncation error at one particular iteration, rather than the cumulative truncation error over an entire sweep. There is little justification for this however.

in finite-size DMRG. It has also been noted in the literature that there is a small quadratic dependence on the truncation error, so that a better fit is obtained by

$$E(m) = E_0 + \alpha R_m + \beta R_m^2 \,, \tag{1.75}$$

where E_0 is the exact energy and α and β are parameters of the fit. For convenience, we write $R_m = 1 - P_m$. In most calculations, β is small enough that, to the accuracy of the overall calculation, it can be neglected. Indeed, it is possible that the quadratic dependence is a numerical artifact, due to the tendency for the calculation to take longer to converge when more states are kept; this is still an open question. The fit parameters are also highly model and parameter dependent. In general, it is only possible to attempt the fit Eq. (1.75) when the energy is calculated for several different values of m while all other parameters are kept fixed. Legeza and Fáth [59] showed that as the parameters of a model are varied, the magnitude of the error in the energy can change considerably even if the truncation error changes very little and *vice versa*. A typical scaling of the error to $m \to \infty$ appears in Fig. 1.13. The number of states kept m is, from left to right, 400, 380, 360, 340, 320. This example is taken from the Kondo lattice model calculations discussed in detail in chapter 3 of this thesis; only the numerical convergence features are discussed in this section. The parameters in this case are 60 site lattice, electron density per site $n = 0.8$, total spin $s = 0^{\dagger}$, Kondo coupling $J = 1.65$ and electron hopping $t = 1$. The extrapolated energy is shown for both the linear and quadratic fit. The difference between the linear and quadratic fit is rather small, of the order $\sim 6 \times 10^{-7}$, but this is still statistically significant.

An alternative measure of the deviation from the exact result is given by the difference in energy before and after the truncation of the wavefunction. As far as we know, this quantity has not been studied outside of this thesis. The *truncated energy* at step i of the sweep is defined by

$$E_t^i = (1 - R_m^i) \langle \kappa_i | H | \kappa_i \rangle - \langle \psi_i | H | \psi_i \rangle \,. \tag{1.76}$$

Expanding $|\psi_i\rangle$ into the kept and truncated parts gives

$$E_t^i(m) = -R_m^i \langle \tau_i | H | \tau_i \rangle - 2\sqrt{R_m^i (1 - R_m^i)}\, |\langle \kappa_i | H | \tau_i \rangle| \,. \tag{1.77}$$

This is linear in the truncation error R_m^i to an extremely high accuracy. The deviation from linearity from the $\sqrt{R_m^i(1 - R_m^i)}$ factor is reduced significantly because the off-diagonal matrix element of the Hamiltonian, $\langle \kappa_i | H | \tau_i \rangle$ will itself be very

[†]This is in fact an excited state, the ground state at this coupling being ferromagnetic with total spin $s = 6$. But this is unimportant for the convergence properties of the calculation.

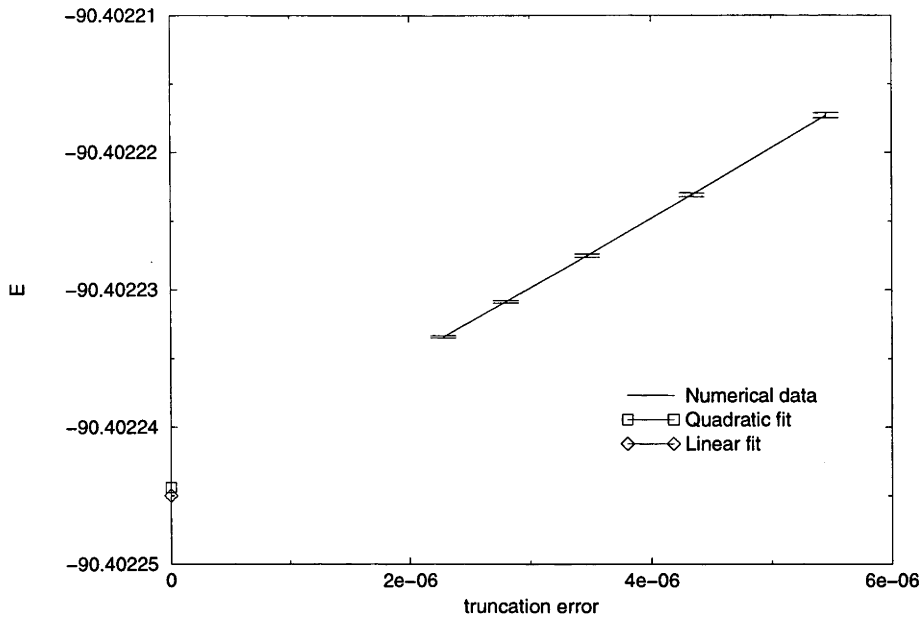

Figure 1.13: The energy as a function of the truncation error for a typical calculation for the Kondo lattice model, at filling $n = 0.8$ and coupling $J = 1.65$, $t = 1$.

small. Thus the cumulative truncated energy is also a suitable candidate for constructing the fit to $m \to \infty$. The advantage of the truncated energy over the standard truncation error, is that for all cases we have looked at, the coefficient of the linear term is very close to unity, *i.e.*

$$E(m) = E_0 + E_t(m) + \beta' E_t(m)^2 \,. \tag{1.78}$$

If Eq. (1.78) were to hold exactly, this would be an extremely useful result because it would imply that $E(m) - E_t(m)$ is a variational upper bound on the exact energy. Figure 1.14 shows $E(m) - E_t(m)$ as a function of $E_t(m)$, for the Kondo Lattice with the same parameters as in Fig. 1.13. Of particular interest is the vertical scale in this figure. The worst data point, with 320 states kept, is within 1.5×10^{-6} of the extrapolated exact energy, an order of magnitude better than in Fig. 1.13. Unfortunately, we have not been able to prove Eq. (1.78). By assuming that the DMRG iterations have converged to the point where the kept component of the wavefunction $|\kappa_i\rangle$ is identical for every iteration across the sweep[†], $|\kappa_i\rangle = |\kappa\rangle \forall i$, it is possible to construct a variational wavefunction as a linear combination of $|\kappa\rangle$ and $|\tau_i\rangle$,

$$|\Psi\rangle = a|\kappa\rangle + \sum_i b_i |\tau_i\rangle \,. \tag{1.79}$$

[†]This is unlikely to be true, to the necessary accuracy.

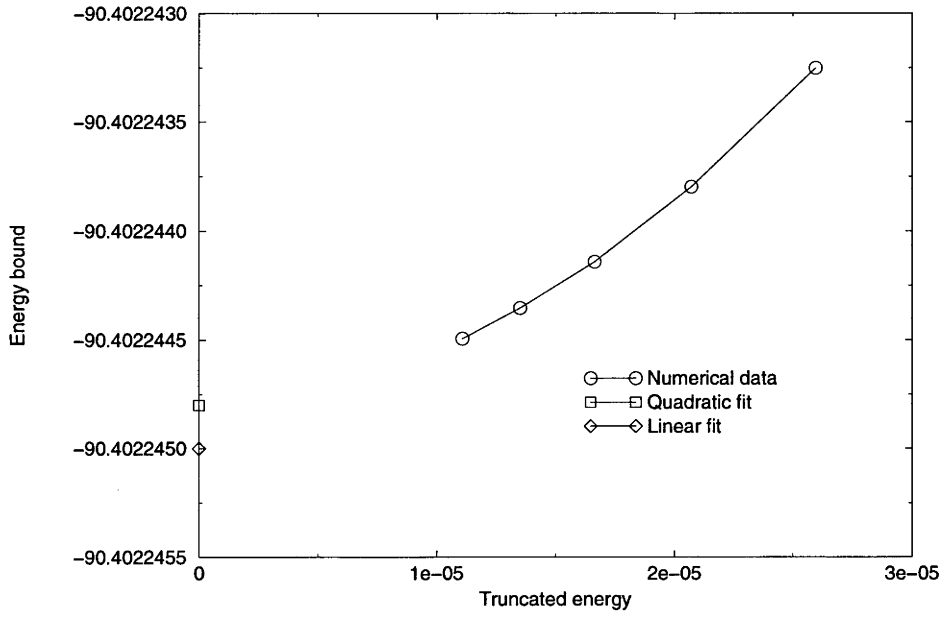

Figure 1.14: The hypothesized energy variational bound as a function of the truncated energy, for the Kondo lattice model, at filling $n = 0.8$ and coupling $J = 1.65$, $t = 1$.

Here a and b_i are variational parameters. As a first step to calculating the energy of this state, an approximation is required to eliminate some matrix elements that are expected to be small and would be very difficult to calculate from within the DMRG algorithm,

$$\langle \tau_i | H | \tau_j \rangle = 0 \ , \quad \text{if } i \neq j \ . \tag{1.80}$$

These matrix elements would be extremely difficult to calculate because normally $|\tau_i\rangle$ and $|\tau_j\rangle$ never exist in the same basis. By definition, $|\tau_i\rangle$ is a member of the subspace that is thrown away at the end of the i^{th} iteration. Transforming the subspace of truncated states for later iterations would require an exponentially increasing number of basis states. Since these terms will be small and in addition the coefficient of this matrix element in the energy of the state would be of order of the truncation error R_m, this approximation is well justified. If we require that the energy of this state can be calculated from *only* the truncated energy $E_t^i(m)$ and the energy of the converged state, $E_\kappa = \langle \kappa | H | \kappa \rangle$, enough constraints on a and b_i appear that the energy can be calculated. Unfortunately, the resulting variational energy is not a lower bound, but has an additional factor of $(1 - R_m)$,

$$E_\Psi = (1 - R_m)(E_\kappa - E_t(m)) \ . \tag{1.81}$$

This energy is higher than E_κ, so this trial wavefunction is not useful.

An alternative approach is to calculate more matrix elements. The remaining matrix elements are very easy to calculate with DMRG,

$$c_i = \langle \kappa | H | \tau_i \rangle \ , \tag{1.82}$$

$$d_i = \langle \tau_i | H | \tau_i \rangle \ . \tag{1.83}$$

This allows the construction of an eigenvalue sub-problem, where the form of the matrix is

$$\begin{pmatrix} E_\kappa & c_1 & c_2 & c_3 & \cdots \\ c_1^* & d_1 & 0 & 0 & \\ c_2^* & 0 & d_2 & 0 & \\ c_3^* & 0 & 0 & d_3 & \\ \vdots & & & & \ddots \end{pmatrix} . \tag{1.84}$$

If the original assumption on the nature of the converged wavefunction $|\kappa\rangle$ is correct, the lowest eigenvalue of this matrix is a variational upper bound on the energy and indeed is the best variational bound that could be calculated without calculating additional matrix elements. This matrix has been solved numerically for some sample cases; the lowest eigenvalue is always less than the usual DMRG variational bound thus it is a potentially useful measure. However in all the cases we have looked at the eigenvalue is somewhat larger than $E_\kappa - E_t$, so this variational state is not the one that was sought. This suggests that either the numerically determined scaling relation of Eq. (1.78) is an unfortunate coincidence of the particular models and DMRG algorithm that have been studied, or that the assumption of the convergence of $|\kappa\rangle$ is not justified.

In early sweeps where few states are kept and the wavefunction is not well converged, there is little reason to calculate the superblock eigenvector to more accuracy than is given by the truncated energy. Indeed, it is possible that calculating the eigenvector to a high precision in the early sweeps exacerbates the tendency of DMRG to self-consistently converge to an incorrect state. In this case, reducing the tolerance of the eigensolver is likely to lead to the DMRG state having a larger overlap with the true ground state and thus better convergence properties in the later stages of the calculation. In any event, when a fixed tolerance for the eigensolver is used, the bulk of the CPU time is spent when the number of states kept is small, primarily because the accuracy of the start vector, transformed from the previous step using the procedure described in section 1.3.2, is not as good when the truncation error is large. There is little point calculating an extremely precise eigenstate when most of the precision is lost at the truncation. Thus, we set the tolerance of the eigensolver at step i directly from the truncated energy of the previous

step, E_t^{i-1}. When the number of states is increased in a steady fashion, this scheme results in roughly a constant number of iterations of the eigensolver, substantially independent of the number of states kept. In some circumstances however, the number of iterations required by the eigensolver fluctuates significantly. We interpret this as the DMRG "tunneling" between two competing low-lying states, which cross in energy as m is increased. This interpretation is supported by the typically large number of energy level crossings observed in the lowest energy states of different symmetry sectors, even away from a phase transition. This is shown, for example, in Fig. 3.19, Fig. 3.20 and Fig. 3.21 in chapter 3. There are also known limitations of the Davidson and Jacobi-Davidson eigensolver algorithms, where for some specific circumstances the convergence of the eigenvector is extremely slow. However improvements to the algorithm to combat these problems are possible [60–62] and this is an active area if research in numerical mathematics. The particular structure of the superblock Hamiltonian matrix in DMRG suggests that a variant of the Jacobi-Davidson algorithm specifically tailored for this structure might be possible, although as far as we know there has not yet been any work on eigensolvers that is specific to DMRG[†].

For the single-site DMRG algorithm discussed in section 1.4, the truncation error and truncated energy are identically zero. Hence an alternate scaling relation would need to be developed for this case.

1.6.3 Scaling of density-matrix eigenvalues

The accuracy of the DMRG method for a given number of states kept is determined by the rate of decay of the density-matrix eigenvalues. Early DMRG calculations on one-dimensional systems suggested that these eigenvalues decay exponentially [43], although it wasn't until several years later that this was demonstrated by the explicit calculation of the density-matrix spectra for some non-critical integrable models, by Peschel, Kaulke and Legeza [65]. The procedure for calculating the density matrix spectra starts by relating the quantum system to the corresponding two-dimensional classical system. Nishino [66] showed that the density matrices then become partition functions of strips with a cut and these can, in turn, be expressed as products of corner transfer matrices [67]. For integrable models, the spectra of the corner transfer matrices is known in the thermodynamic limit to have the form $w_n \sim \exp(-\alpha n)$, with integer n. Provided that the correlation length ξ is much smaller than the strip width or chain length L, the same should hold for the

[†]Details of the Lanczos algorithm have been used to facilitate the calculation of dynamical properties [63,64], but this is unrelated to convergence.

reduced density-matrix eigenvalues ρ_n.

For a two-dimensional system, numerous studies have found that the number of states m needed to maintain a fixed accuracy grows exponentially with the width of the system [54, 56]. In reference [56], this behavior was derived explicitly from the behavior of non-interacting chains. Consider a toy model of M one-dimensional chains, forming a ladder of width M, in the limit of small interaction between each chain. The basis for this system can be written simply as a tensor product of the basis for each chain. If m states are needed to obtain the desired accuracy for a single chain, the basis for M chains has dimension m^M. This result was put on a firmer footing by Chung and Peschel [68], who obtained the exact density-matrix spectra for a two-dimensional system of coupled harmonic oscillators. This system is integrable in any number of dimensions, allowing the direct calculation of the reduced density matrices as an exponential in the bosonic operators of the normal coordinates of the system. This calculation gives a lot of insight into the behavior of the DMRG algorithm in both one and two dimensions, so it is worth outlining some of their calculation. The Hamiltonian studied by Chung and Peschel [68] was

$$H = \frac{1}{2}\sum_i (-\frac{\partial^2}{\partial u_i^2} + \omega_0^2 u_i^2) + \sum_{i,j} \frac{1}{2} k_{ij}(u_i - u_j)^2 \,, \tag{1.85}$$

where u_i is the coordinate of the i^{th} oscillator and w_0 its frequency. The masses are all equal to unity and the oscillators are coupled by springs of strength k_{ij}. This is immediately solvable by a transformation to the normal coordinates, giving the form of the solution (written here in the original coordinates),

$$\phi(u_1, u_2, \ldots) = \exp\left[-\frac{1}{2}\sum_{i,j} A_{ij} u_i u_j\right] . \tag{1.86}$$

The total density-matrix is then $|\phi\rangle\langle\phi|$. By integrating out part of the coordinates, the reduced density-matrix is obtained,

$$\rho = C \exp\left[-\sum_j \epsilon_j b_j^\dagger b_j\right] , \tag{1.87}$$

for bosonic operators $b_j^\dagger$ and b_j. The summation j is over all kept sites. The energies ϵ_j are derived from the A_{ij} matrix. It was shown by Peschel and Chung [69] that for a chain with nearest-neighbor coupling k and oscillator frequency $\omega_0 = 1 - k$, the ϵ_j for half of the system in the thermodynamic limit are given by

$$\epsilon_j = (2j - 1)\,\epsilon, \qquad j = 1, 2, \ldots , \tag{1.88}$$

where

$$\epsilon = \pi \frac{I(\sqrt{1-k^2})}{I(k)} . \tag{1.89}$$

Here $I(k)$ is the complete elliptic integral of the first kind. This result is also valid for finite systems, provided that the size is large compared with the correlation length.

Next, Chung and Peschel [68] repeated this analysis for a two-dimensional square lattice of oscillators with nearest-neighbor couplings k_x and k_y. This can be reduced to a one-dimensional problem by transforming the columns to normal coordinates. The corresponding normal frequencies are

$$\omega(q)^2 = \omega_0^2 + 2k_y(1 - \cos q) \tag{1.90}$$

where the vertical momenta q for open boundary conditions and M sites is given by $q = \pi x/M$, for $x = 1, 2, \cdots, (M-1)$.

If the columns are then coupled, the different momenta do not mix, thus for each value of q, a horizontal chain of the form Eq. (1.85) results, where the oscillator frequency is $\omega(q)$ and the coupling is k_x. This gives the energies similarly to Eq. (1.88) and Eq. (1.89), as

$$\epsilon_j(q) = (2j-1)\,\epsilon(q), \qquad j = 1, 2, \ldots , \tag{1.91}$$

with

$$\epsilon(q) = \pi \frac{I(\sqrt{1-k(q)^2})}{I(k(q))} , \tag{1.92}$$

$$k(q) = \frac{k_x}{k_x + \omega(q)} . \tag{1.93}$$

This gives an analytic expression for the spectrum. The actual eigenvalues ρ_n of the reduced density-matrix are obtained by specifying the occupation numbers of the bosonic single particle levels $\epsilon_j(q)$. From the resulting spectra, Chung and Peschel [68] derived an asymptotic formula,

$$\rho_n \sim \exp\left[-\frac{3}{2\pi^2}\lambda \ln^2 n\right] , \tag{1.94}$$

where λ is a parameter that is inversely proportional to the width M of the system,

$$\lambda = \frac{2\,\epsilon(q=0)}{M} . \tag{1.95}$$

Thus the $1/M$ behavior of the exponent is verified. The actual eigenvalues for the case $k_x = k_y = 1$, for a variety of widths M are shown in Fig. 1.15, reproduced

from reference [68]. It is clear from this figure that the accuracy of the numerical calculation inevitably decreases rapidly as the system size is increased. Increasing the strength of the interaction helps to some extent, as the energies ϵ (and therefore λ) increase with k_y, but this does not remove the essential $1/M$ dependence in the exponent.

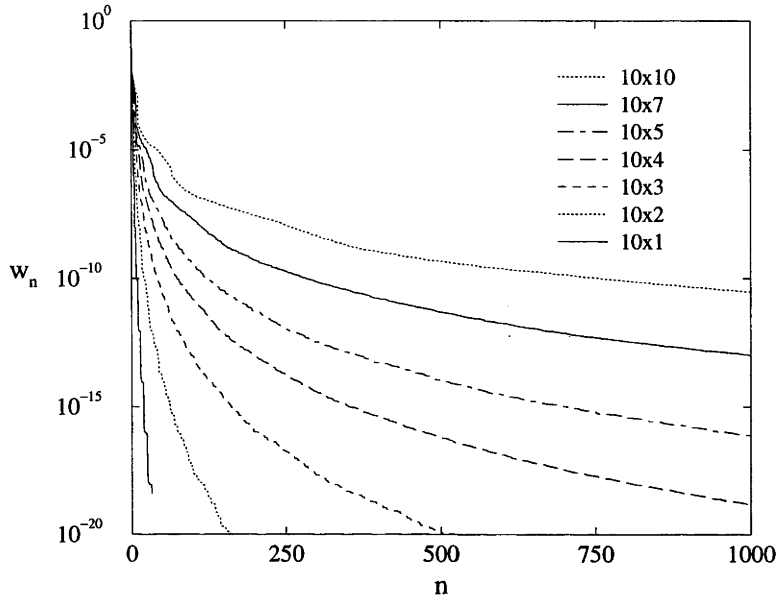

Figure 1.15: Density matrix eigenvalues w_n for systems of different widths M. Originally figure 3 from reference [68]

The calculation of Chung and Peschel [68] also provides some insight into the accuracy of periodic boundary conditions versus open boundary conditions. The loss of accuracy when periodic boundary conditions are used was noted early [70] and can be seen explicitly in the calculation of Chung and Peschel [68]. For periodic boundary conditions, both the left and the right boundaries of each block contain interactions with the other block. If the density-matrix is calculated for such a half-ring, for small energies ϵ_j the same values appear as in the open boundary case, but each value appears *twice*. The reason for this is the form of the eigenstates of the density-matrix, which for small ϵ_j are concentrated near the boundary of the left and right blocks. The two sets of reduced density-matrix states, each approximately localized at the point of contact with the opposite block, are approximately independent for small ϵ_j. Thus the situation is similar to that of a ladder of two weakly coupled chains, where $O(m^2)$ states are required to achieve the same accuracy as that of a single chain with m states kept.

Recently, another calculation by Chung and Peschel [71] obtained exact density-

matrix spectra for a system of non-interacting fermions, with a gapless excitation spectrum. The results were similar to the previous results for the bosonic system of coupled oscillators, although in the gapless case the density-matrix eigenvalues decay even slower, but only by a constant factor. In this work, Chung and Peschel [71] also investigated the reduced density-matrix spectra for different shapes of blocks, including the diagonal mapping used in the two-dimensional algorithm of Xiang *et al.* [12] and found no essential difference between any block structure.

To confirm these results for the density-matrix spectra for the DMRG program used in this thesis, the density-matrix spectra for the one-dimensional Hubbard model at half filling have been calculated, with both open and periodic boundary conditions. This is shown in Fig. 1.16. Except for the tail for very large n, the eigenvalues follow closely $\rho_n \propto \exp(-\alpha n^{1/3})$. This is in general agreement with the results of Peschel *et al.* [65], who considered both the anisotropic XXZ Heisenberg spin chain and the Ising model in a transverse field. Interestingly, the rapidly decreasing tail for large n shown in Fig. 1.16 also appears in finite-size corner transfer matrix spectra [72, 73], however this feature was not seen by Peschel *et al.* [65]. Rather, they found a tail that tends in the *opposite* fashion, such that the last few eigenvalues decrease in magnitude slower than exponential[†].

Finally, we note that the potential for two-dimensional *momentum space* calculations remains mostly un-investigated[‡]. The calculation by Xiang on the two-dimensional Hubbard model [13] produced mixed results, however in the 5 years since that calculation, several optimizations to the DMRG algorithm have been devised (*cf.* section 1.3) and a more recent algorithm could produce somewhat better accuracies. While it seems likely that in one dimension, momentum space DMRG is less accurate than real-space calculations, this does not mean that the asymptotic behavior for two-dimensional systems is necessarily worse in momentum space than real-space. In addition, momentum space calculations have the advantage that al-

[†]This data is close to the limit of the precision so this result may not be significant; in principle it should be possible to calculate the density-matrix eigenvalues to around the square of the machine precision (around 10^{-30}), since the values of the wavefunction vector are of order $\sqrt{\rho_n}$ but actually achieving this precision would require special effort which is pointless in practice as density-matrix eigenvalues smaller than the machine precision (around 10^{-15}) have negligible effect on the calculation.

[‡]During the final stages of preparing this thesis, a preprint by Nishimoto *et al.* [14] appeared, detailing (Abelian) momentum-space calculations for the one- and two-dimensional Hubbard models. While they show that momentum-space calculations in one-dimension are less accurate than real-space, even with periodic boundary conditions, the results are more promising for higher dimensions, where unlike real-space calculations, the accuracy of momentum-space calculations does not dramatically decrease as the dimension of the lattice is increased.

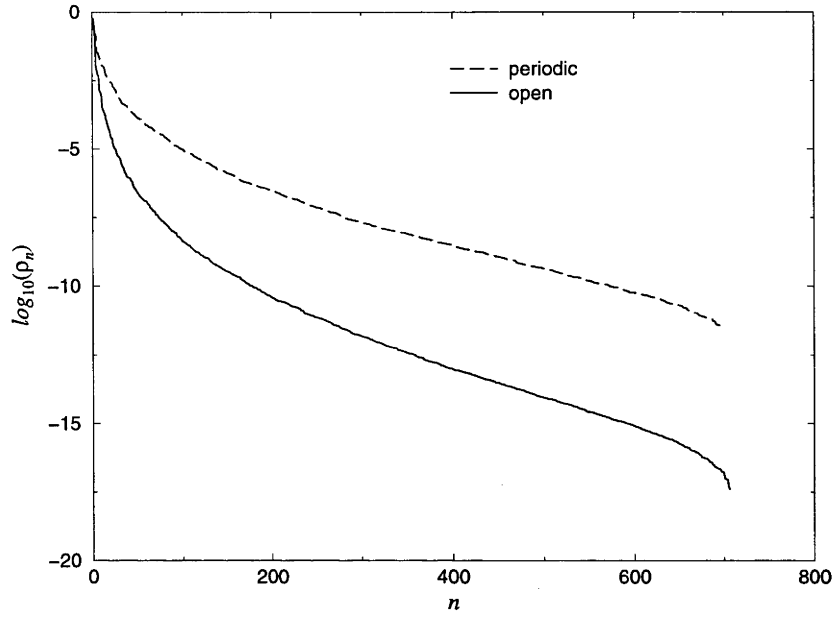

Figure 1.16: The density-matrix spectra for the one-dimensional Hubbard model at half-filling, $U/t = 1$ and 200 states kept, for open and periodic boundary conditions.

ternative boundary conditions, *e.g.* periodic or anti-periodic, are easy to apply and do not involve the dramatic loss of accuracy of open vs periodic boundary conditions in real-space calculations. Given that all DMRG algorithms based around the one-dimensional matrix product state (*cf.* section 1.4) probably inevitably require an exponential number of states kept in a two-dimensional calculation, the lattice sizes are extremely limited no matter what choice of basis is used. In these circumstances, where the system sizes are not significantly larger than what could be achieved with exact diagonalization, it is generally far preferable to use periodic boundary conditions.

Chapter 2

The non-Abelian Density-Matrix Renormalization-Group

For physical reasons, as well as numerical, it would be useful to be able to construct block states that are eigenstates of the total spin operator, $\boldsymbol{S}\cdot\boldsymbol{S}$. In principle, this can be done for all Hamiltonians that commute with the operators S^z, S^y, S^z. Using eigenstates of S^z only, the Hilbert space of some given j^z state contains total spin states for all values of $j = j^z, j^z+1, j^z+2, \ldots$. This makes it difficult to calculate any properties in the vicinity of a ferromagnetic phase transition, because whenever states of different total spin are numerically near-degenerate, the DMRG wavefunction will end up as a mixture of states. This can make first order phase transitions appear to be second order. It is also very difficult to calculate the energy increase from a ferromagnetic ground state to an excited state of smaller spin, as targeting a smaller value of j^z will result in a degenerate copy of the ferromagnetic ground state. A work around is to add a term λS^2 to the Hamiltonian, where λ is some scale factor. It is relatively easy to calculate the matrix elements required for this. If λ and j^z are chosen appropriately, an arbitrary total spin state can be forced to be the ground state. Thus, if sufficient numerical accuracy can be achieved, the properties of the system in any total spin sector of the Hilbert space can be obtained. However, it is difficult to achieve enough numerical accuracy to obtain good results from this technique; it has been attempted in some studies (for example, the $t-t'-U$ Hubbard model [74] and the $d-p$ and periodic Anderson models [8]), but with limited success.

Unfortunately it is not possible to simply append the total spin quantum number j to the labels of the block states and apply the DMRG algorithm otherwise unchanged. Consider the form of the wavefunction matrix in the superblock basis, when total spin labels j_a and j_b are added to the left and right block basis states respectively (to reduce the number of superscripts j^z is denoted by m from

now on; this should cause no confusion with the number of kept basis states, also conventionally denoted m),

$$|\Psi\rangle = \sum_{j_a,m_a,\alpha,j_b,m_b,\beta} \psi^{j_a m_a(\alpha)}_{j_b,m_b(\beta)} |j_a m_a(\alpha)\rangle \otimes |j_b m_b(\beta)\rangle \ . \tag{2.1}$$

Constructing eigenstates of total spin from the tensor product basis requires using the Clebsch-Gordan transformation,

$$|jm\rangle = \sum_{j_a,j_b,m_a,m_b} C^{j_a\ j_b\ j}_{m_a m_b m} |j_a m_a\rangle \otimes |j_b m_b\rangle \ , \tag{2.2}$$

where $C^{j_a\ j_b\ j}_{m_a m_b m}$ is the Clebsch-Gordan coefficient. The summation of j_a and j_b is over all spins such that

$$|j_a - j_b| \leq j \leq j_a + j_b \ , \tag{2.3}$$

where j is the total spin of the superblock target state. Hence unlike the previous case where only j^z is used, ψ is not block diagonal with respect to the total spin quantum number and is instead banded, with a bandwidth of $2j+1$. This implies that the reduced density-matrix, $\psi\psi^\dagger$, is not block diagonal either. This means that the truncation operator would mix up the total spin states and beyond the first truncation the total spin label could not be used. As a first fix to this problem, we apply a constraint so that the states kept in the truncated basis are forced to be eigenstates of total spin. This procedure was first described by the author in references [75,76]. Adding the constraint $S^2|\phi\rangle = j(j+1)|\phi\rangle$ for some half integer j and re-calculating the form of the density-matrix Eq. (1.17), gives

$$\rho^{(j_a,m_a)}_{\alpha'\alpha} = \sum_{j_b,m_b,\beta} \psi^{j_a m_a(\alpha')}_{j_b m_b(\beta)} \psi^{j_a m_a(\alpha)*}_{j_b m_b(\beta)} \ , \tag{2.4}$$

which is block diagonal with respect to the block total spin j_a, as well as the z-component of spin m_a. This matrix is made up of just those elements of the original density-matrix Eq. (1.17) that are block diagonal with respect to total spin, neglecting all elements that are not block diagonal. By expanding ψ in the tensor product basis via Eq. (2.2), we can see that $\rho^{(j_a,m_a)}_{\alpha'\alpha}$ is independent of the value of m_a. This is required to preserve the usual relationship

$$S^+|j_a, m_a, (\alpha)\rangle = \sqrt{(j-m)(j+m+1)}\,|j_a, m_a+1, (\alpha)\rangle \ , \tag{2.5}$$

which is required for the application of the Clebsch-Gordan transformation. Thus the density-matrix needs be calculated for each distinct value of j_a, but only for a single, arbitrary, value of m_a.

This provides a method whereby a specific total spin value can be targeted by DMRG, with the corresponding performance speed-up arising from the smaller Hilbert space. However this approach suffers from several problems. Despite the results of the calculation being independent of the z-component of spin, it is still necessary to use this label on all of the block states. The conservation of total spin implies that there exists many constraints on the matrix elements for different z-components of spin, however this formulation does not utilize this and every possible matrix element needs to be stored. This is rather expensive in memory, especially for large values of spin. In addition, the Clebsch-Gordan transformation Eq. (2.2) is computationally non-negligible. This transformation needs to be carried out several times each iteration, when adding a site to each block, when constructing the superblock and the inverse transform has to be calculated to write the superblock wavefunction in the tensor product basis prior to the construction of the density-matrix. There is a solution to both these problems, but first we review some required theory which is essential to the formulation. First we review briefly some of the basic theory of group representations and characters, leading to the definition of the Clebsch-Gordan coefficients for arbitrary finite groups and compact Lie groups. Then the theory of $SU(2)$ rotational invariance is introduced so that the important Wigner-Eckart theorem for irreducible tensor operators in $SU(2)$ can be stated. This approach has the advantage that the coupling coefficients of $SU(2)$ have somewhat simpler properties than the general case, however it is clear from the construction that the formulation carries over to other symmetries. We then calculate a concrete matrix representation of the $SU(2)$-invariant fermionic algebra, leading directly into the construction of the $SU(2)$-invariant DMRG algorithm itself in section 2.3. After a discussion of the generalization to arbitrary symmetries and the relationship between the current DMRG algorithm and previously published work in the field, we demonstrate the algorithm for the Hubbard model with $SU(2)$ symmetry (section 2.4) and $SO(4)$ symmetry (section 2.5). Finally, section 2.6 discusses the potential applications for the non-Abelian formulation with respect to spatial symmetries of a lattice.

2.1 Group Representations

This section contains a brief review of the principles of the theory of linear representations of some compact groups (specifically finite groups and compact Lie groups), including group characters and the Clebsch-Gordan coefficients. This is all standard theory, found in many textbooks, for example part I of Serre's book [77]

contains a good introduction to representations and characters of finite groups, Miller's book [78] contains an extremely thorough treatment of the basic theory with particular reference to applications in physics and van der Waerden's book [79] is rigorous but also very readable. Cornwell's book [80,81] is a thorough exposition of group theory in physics and one of the few 'classic' books on group theory in physics that is recent enough to contain the generalized Wigner–Eckart theorem. While the properties of quantum angular momentum and the Lie group $SU(2)$ were well established soon after the development of quantum mechanics itself, the generalization of the mathematical theory to other symmetry groups is more recent and indeed remains the focus of much current research.

2.1.1 Basic definitions and theorems

Definition *Representation of a group* $\boldsymbol{G}$

If there exists a homomorphic mapping of a group $\boldsymbol{G}$ onto a group of non-singular $d \times d$ matrices $\Gamma(T)$, $T \in \boldsymbol{G}$, with matrix multiplication as the group operation, then the group of matrices $\Gamma(T)$ forms a $d-$dimensional representation Γ of $\boldsymbol{G}$. To save later confusion, the dimension of the matrices of the representation Γ is referred to as the *degree* d of the representation; as we shall see later this is quite separate from the dimension of the relevant Hilbert in the DMRG algorithm. Clearly, the identity element of $\boldsymbol{G}$ must map onto the $d \times d$ identity matrix, so that $\Gamma(I) = I_d$.

Let $\phi_1, \phi_2, \ldots, \phi_d$ be the basis of a $d-$dimensional complex inner product space V, called the *carrier space*. For each $T \in \boldsymbol{G}$, define the linear operator $\Phi(T)$ acting on this basis by

$$\Phi(T)\phi_n = \sum_{m=1}^{d} \Gamma(T)_{mn}\phi_m \quad n = 1, 2, \ldots, d\,. \tag{2.6}$$

Two representations Γ and Γ' are *equivalent* if there exists a non-singular matrix S which generates a similarity transform $\Gamma'(T) = S^{-1}\Gamma(T)S$, for each $T \in \boldsymbol{G}$. As all 1×1 matrices commute, if $d = 1$ then $\Gamma' T = \Gamma T$ for all $T \in \boldsymbol{G}$ and for every 1×1 non-singular matrix S. Thus two representations of degree one are either identical or not equivalent.

For degree $d \geq 2$ the situation is not so simple and in general a similarity transform will produce an equivalent representation Γ' whose matrices are different from those of Γ.

A *unitary representation* of a group $\boldsymbol{G}$ is a representation Γ in which all the matrices $\Gamma(T)$ are unitary. An important theorem, proven in *e.g.* [80], states that if $\boldsymbol{G}$ is a *finite* group or a *compact* Lie group, then *every* representation of $\boldsymbol{G}$ is

equivalent to a unitary representation. Thus it is assumed from now on that all representations are unitary.

Definition *Reducible representation of a group* $\boldsymbol{G}$

A representation of a group $\boldsymbol{G}$ is *reducible*[†] if it is equivalent to a representation Γ which has the partitioned form

$$\Gamma(T) = \begin{bmatrix} \Gamma_{11}(T) & \mathbf{0}_{12} \\ \mathbf{0}_{21} & \Gamma_{22}(T) \end{bmatrix}, \tag{2.7}$$

for every $T \in \boldsymbol{G}$, where $\Gamma_{11}(T)$, $\Gamma_{22}(T)$ and the zero matrices $\mathbf{0}_{12}$ and $\mathbf{0}_{21}$ have dimensions $s_1 \times s_1$, $s_2 \times s_2$, $s_1 \times s_2$ and $s_2 \times s_1$ respectively. By applying the group operation to this form, it is easily shown that Γ_{11} and Γ_{22} are themselves representations of $\boldsymbol{G}$, of degree s_1 and s_2 respectively.

Definition *Irreducible representation of a group*

A representation of a group $\boldsymbol{G}$ is said to be *irreducible* if it is not reducible.

This definition implies that an irreducible representation *cannot* be transformed by a similarity transform into the block-diagonal form of Eq. (2.7). Thus it is clear that any unitary representation Γ can be decomposed as

$$\Gamma = n_1\Gamma^1 \oplus n_2\Gamma^2 \oplus \ldots \oplus n_k\Gamma^k = \bigoplus_{p=1}^{k} n_p\,\Gamma^p, \tag{2.8}$$

where Γ^p is irreducible and n_p specifies the *multiplicity* of the p^{th} irreducible representation.

The basic theorem used in identifying irreducible representations is Schur's Lemma. This states that if Γ is a irreducible representation of the group $\boldsymbol{G}$ of degree d and B is a $d \times d$ matrix such that $\Gamma(T)B = B\Gamma(T)$ for every $T \in \boldsymbol{G}$, then B must be a multiple of the identity matrix. A corollary of this theorem is that every irreducible representation of an Abelian group has degree one. Conversely, if every irreducible representation of a group $\boldsymbol{G}$ is of degree one, then $\boldsymbol{G}$ is Abelian. This corollary is of particular importance in this thesis, because as shown later, the original formulation of DMRG breaks down whenever the symmetry group contains one or more representations of degree $d > 1$.

Another important corollary of Schur's Lemma is the orthogonality theorem for matrix representations, which applies to both finite groups and compact Lie groups.

[†]In general a representation that is reducible only implies that it can be transformed by a similarity transformation into a upper-triangular form and the ability to transform the representation into block-diagonal form requires the stronger condition of *complete reducibility*. However this distinction is not required here, as any *unitary* reducible representation is completely reducible; see *e.g.* [80] for a proof.

Suppose that Γ^p and Γ^q are two unitary irreducible representations of a group $\boldsymbol{G}$, which are not equivalent if $p \neq q$ (but which are identical if $p = q$). Then

$$\frac{1}{g}\sum_{T\in\boldsymbol{G}} \Gamma^p(T)^*_{jk}\Gamma^q(T)_{st} = \frac{1}{d_p}\delta_{pq}\delta_{js}\delta_{kt} \,, \tag{2.9}$$

where g is the order of $\boldsymbol{G}$ and d_p is the degree of Γ^p.

Similarly, if $\boldsymbol{G}$ is a compact Lie algebra then the summation can be replaced by an integration over the group,

$$\int_{\boldsymbol{G}} \Gamma^p(T)^*_{jk}\Gamma^q(T)_{st}\, dT = \frac{1}{d_p}\delta_{pq}\delta_{js}\delta_{kt} \,. \tag{2.10}$$

2.1.2 Group characters

Although equivalent representations have essentially the same content, there is a large amount of arbitrariness associated with the explicit form of the matrices. The group characters provide a set of quantities that are the same for *all* equivalent representations. Furthermore, for finite groups and compact Lie groups, the characters *uniquely* determine the representations, up to equivalence.

Definition *The character of a representation*
Suppose that Γ is a representation of a group $\boldsymbol{G}$, with degree d. Then the *character* of the group element $T \in \boldsymbol{G}$ is

$$\chi(T) = \mathrm{tr}\,\Gamma(T) = \sum_{j=1}^{d} \Gamma(T)_{jj} \,. \tag{2.11}$$

The set of characters corresponding to a representation is called the *character system* of the representation.

Since $\Gamma(I) = I_d$, for the identity element of $\boldsymbol{G}$, it follows that $\chi(I) = d$.

An important theorem states that, if $\boldsymbol{G}$ is a finite group or a compact Lie group, then a necessary and sufficient condition for two representations to be equivalent is that they have identical character systems. The characters therefore provide a set of quantities that are unchanged by similarity transforms. There is an orthogonality theorem for the group characters, that is analogous to the group representation orthogonality theorem. Let $\chi^p(T)$ and $\chi^q(T)$ be the characters of two irreducible representations of a finite group $\boldsymbol{G}$ of order g, these representations assumed to be inequivalent if $p \neq q$. Then

$$\frac{1}{g}\sum_{T\in\boldsymbol{G}} \chi^p(T)^*\chi^q(T) = \delta_{pq} \,. \tag{2.12}$$

Similarly, if $\boldsymbol{G}$ is a compact Lie group, the summation can be replaced by a group integral,

$$\int_{\boldsymbol{G}} \chi^p(T)^* \chi^q(T)\, dT = \delta_{pq} \,. \tag{2.13}$$

The following theorem provides a hint at the usefulness of the group characters. The number of times n_p that an irreducible representation Γ^p (or a representation equivalent to Γ^p) appears in a reducible representation Γ is given, for a finite group, by

$$n_p = \frac{1}{g} \sum_{T \in \boldsymbol{G}} \chi(T) \chi^p(T)^* \,, \tag{2.14}$$

where $\chi^p(T)$ and $\chi(T)$ are the characters of Γ^p and Γ respectively. For a compact Lie group, this generalizes to

$$n_p = \int_{\boldsymbol{G}} \chi(T) \chi^p(T)^*\, dT \,. \tag{2.15}$$

This n_p is the multiplicity of the irreducible representation in the decomposition of Eq. (2.8).

A straightforward corollary of this theorem, is that a necessary and sufficient condition for a representation Γ of a finite group $\boldsymbol{G}$ to be irreducible is

$$\frac{1}{g} \sum_{T \in \boldsymbol{G}} |\chi(T)|^2 = 1 \,. \tag{2.16}$$

The corresponding result for a compact Lie group is

$$\int_{\boldsymbol{G}} |\chi(T)|^2\, dT = 1 \,. \tag{2.17}$$

There are two theorems that often (but not always) are sufficient to uniquely determine the degrees of the inequivalent irreducible representations for a finite group. Firstly, for a finite group $\boldsymbol{G}$, the sum of the squares of the degrees of the inequivalent irreducible representations is equal to the order of $\boldsymbol{G}$. Secondly, for a finite group $\boldsymbol{G}$, the number of inequivalent irreducible representations is equal to the number of conjugacy classes of $\boldsymbol{G}$.

For compact Lie groups, the number of inequivalent irreducible representations is infinite but countable. This implies that the irreducible representations of a compact Lie group can be specified by a parameter that takes only *integral* values (or a set of parameters taking integral values, if more convenient). This means that it is practical to use group representation theory in a numerical calculations; without this theorem it would be impossible in general to label an irreducible representation using a digital computer.

Of importance in quantum mechanics is the notion of the direct product of representations. If Γ^p and Γ^q are two unitary irreducible representations of a group $\boldsymbol{G}$, with degree d_p and d_q respectively, then the set of matrices defined by

$$\Gamma(T) = \Gamma^p(T) \otimes \Gamma^q(T) \,, \tag{2.18}$$

for all $T \in \boldsymbol{G}$, forms a unitary representation of $\boldsymbol{G}$ of degree $d_p d_q$. The character $\chi(T)$ of this representation is given by

$$\chi(T) = \chi^p(T)\chi^q(T) \,. \tag{2.19}$$

In general, the representation $\Gamma^p \otimes \Gamma^q$ is reducible, even if Γ^p and Γ^q are themselves irreducible. Suppose that a similarity transformation C is applied to the representation $\Gamma^p \otimes \Gamma^q$ to give an equivalent representation that is a direct sum of unitary irreducible representations and the unitary irreducible representation Γ^r of $\boldsymbol{G}$ appears n^r_{pq} times in this sum. This can be written as

$$C^{-1}\left(\Gamma^p \otimes \Gamma^q\right) C = \bigoplus_r n^r_{pq} \Gamma^r \,. \tag{2.20}$$

The right-hand side of Eq. (2.20) is called the *Clebsch-Gordan* series for $\Gamma^p \otimes \Gamma^q$. The theorem given previously on the multiplicity of the irreducible representations gives, for the Clebsch-Gordan series of a finite group,

$$n^r_{pq} = \frac{1}{g} \sum_{T \in \boldsymbol{G}} \chi^p(T)\chi^q(T)\chi^r(T)^* \,, \tag{2.21}$$

the corresponding result for a compact Lie group being

$$n^r_{pq} = \int_{\boldsymbol{G}} \chi^p(T)\chi^q(T)\chi^r(T)^* \, dT \,. \tag{2.22}$$

Thus the Clebsch-Gordan series is determined solely by the characters. Clearly, as $\Gamma^p \otimes \Gamma^q$ is a representation of degree $d_p d_q$ we have,

$$d_p d_q = \sum_r n^r_{pq} d_r \,. \tag{2.23}$$

Let ϕ^p_j and ψ^q_k be basis functions for the carrier spaces of Γ^p and Γ^q respectively. Now given that n^r_{pq} is the number of times that the irreducible representation Γ^r appears in the Clebsch–Gordan series for $\Gamma^p \otimes \Gamma^q$, there must be n^r_{pq} linearly independent sets of basis functions for Γ^r formed by linear combinations of the products $\phi^p_j \psi^q_k$. Let these be denoted by $\theta^{r,\alpha}_l$, where $\alpha = 1, 2, \ldots, n^r_{pq}$ and $l = 1, 2, \ldots, d_r$. These basis functions can be written in the form

$$\theta^{r,\alpha}_l = \sum_{j=1}^{d_p} \sum_{k=1}^{d_q} \left({}^{pq}_{jk} \middle| {}^{r,\alpha}_{l} \right) \phi^p_j \psi^q_k \,. \tag{2.24}$$

The coefficients $\left(\begin{smallmatrix} pq \\ jk \end{smallmatrix} \middle| \begin{smallmatrix} r,\alpha \\ l \end{smallmatrix}\right)$ are the generalized *Clebsch–Gordan coefficients* of the group $\boldsymbol{G}$. They can be regarded as forming a $d_p d_q \times d_p d_q$ non-singular matrix, the rows being labeled by the pairs (j,k) and the columns by the triple (r,α,l). This is the matrix C in Eq. (2.20).

The inverse of Eq. (2.24) can be written,

$$\phi_j^p \psi_k^q = \sum_{j=1}^{d_p} \sum_{k=1}^{d_q} \left(\begin{smallmatrix} \alpha,r \\ l \end{smallmatrix} \middle| \begin{smallmatrix} pq \\ jk \end{smallmatrix}\right) \theta_l^{r,\alpha} \,. \tag{2.25}$$

The coefficients $\left(\begin{smallmatrix} \alpha,r \\ l \end{smallmatrix} \middle| \begin{smallmatrix} pq \\ jk \end{smallmatrix}\right)$ again form a $d_p d_q \times d_p d_q$ non-singular matrix, but this time the rows are labeled by the triple (r,α,l) and the columns by the pair (j,k). This is the matrix C^{-1} of Eq. (2.20).

As $\Gamma^p \otimes \Gamma^q$ is unitary and the Clebsch–Gordan expansion on the right hand of Eq. (2.20) is unitary, it is possible to choose C to be unitary also, which implies that

$$\left(\begin{smallmatrix} \alpha,r \\ l \end{smallmatrix} \middle| \begin{smallmatrix} pq \\ jk \end{smallmatrix}\right) = \left(\begin{smallmatrix} pq \\ jk \end{smallmatrix} \middle| \begin{smallmatrix} r,\alpha \\ l \end{smallmatrix}\right)^* . \tag{2.26}$$

The conventional notation for the Clebsch–Gordan coefficients of $SU(2)$, as C_{jkl}^{pqr} is possible because for the $SU(2)$ case, the multiplicity of the irreducible representation, n_{pq}^r is always ≤ 1 for every r, thus all non-vanishing coefficients have $\alpha = 1$ so this label is redundant. In addition, a purely real representation of $SU(2)$ is possible, so that there is no need to distinguish between the Clebsch–Gordan coefficient and its (complex–conjugated) inverse. These properties mean that the Clebsch-Gordan coefficients for $SU(2)$ are comparatively easy to use in a calculation, compared with some other Lie groups. Appendix B lists some formulas and symmetry relations for the $SU(2)$ coupling coefficients that are used in this thesis.

The condition $n_{pq}^r \leq 1$, if it holds on the group $\boldsymbol{G}$, gives a significant simplification to the problem of finding an explicit form for the Clebsch–Gordan coefficients. As a first step, we note that the product of two Clebsch-Gordan coefficients can be written in terms of the group characters [80],

$$\sum_{\alpha=1} n_{pq}^r \left(\begin{smallmatrix} pq \\ st \end{smallmatrix} \middle| \begin{smallmatrix} r,\alpha \\ u \end{smallmatrix}\right) \left(\begin{smallmatrix} pq \\ jk \end{smallmatrix} \middle| \begin{smallmatrix} r,\alpha \\ l \end{smallmatrix}\right)^* = \frac{d_r}{g} \sum_{T \in \boldsymbol{G}} \Gamma^p(T)_{sj} \Gamma^q(T)_{tk} \Gamma^r(T)_{ul}^* \,. \tag{2.27}$$

For a compact Lie-algebra the corresponding result is

$$\sum_{\alpha=1} n_{pq}^r \left(\begin{smallmatrix} pq \\ st \end{smallmatrix} \middle| \begin{smallmatrix} r,\alpha \\ u \end{smallmatrix}\right) \left(\begin{smallmatrix} pq \\ jk \end{smallmatrix} \middle| \begin{smallmatrix} r,\alpha \\ l \end{smallmatrix}\right)^* = d_r \int_{\boldsymbol{G}} \Gamma^p(T)_{sj} \Gamma^q(T)_{tk} \Gamma^r(T)_{ul}^* \, dT \,. \tag{2.28}$$

There is a large degree of arbitrariness in the Clebsch-Gordan coefficients, even if they are assumed to be unitary. Consider first the case $n_{pq}^r = 1$. If the Clebsch-

Gordan coefficients $\binom{pq}{jk}\big|^{r,1}_{l}\big)$ satisfy Eq. (2.27), then for any real number w independent of j, k and l, the coefficients

$$\left(\binom{pq}{jk}\big|^{r,1}_{l}\right)' = e^{iw}\left(\binom{pq}{jk}\big|^{r,1}_{l}\right), \tag{2.29}$$

also satisfy Eq. (2.27). That is, the Clebsch-Gordan coefficients contain an arbitrary phase factor whose choice depends on p, q and r and is entirely a matter of convention. If $n^r_{pq} > 1$, the situation is even more complicated. In this case, the coefficients defined by

$$\left(\binom{pq}{jk}\big|^{r,\alpha}_{l}\right)' = \sum_{\beta=1}^{n^r_{pq}} s_{\alpha\beta}\left(\binom{pq}{jk}\big|^{r,\beta}_{l}\right), \tag{2.30}$$

where s is any $n^r_{pq}\times n^r_{pq}$ unitary matrix, also satisfy Eq. (2.27). Thus the arbitrariness of the coefficients is increased from a single phase factor to a $n^r_{pq}\times n^r_{pq}$ unitary matrix.

When $\boldsymbol{G}$ is a finite group and $n^r_{pq} = 1$, Eq. (2.27) provides a direct way of evaluating the Clebsch-Gordan coefficients. Firstly, choose a set of j, k, l such that

$$\frac{d_r}{g}\sum_{T\in\boldsymbol{G}} \Gamma^p_{jj}\Gamma^q_{jj}\Gamma^r T^*_{ll}, \tag{2.31}$$

is non-zero. From Eq. (2.27), it is clear that this number must be real and positive. Adopting the phase convention that $\binom{pq}{jk}\big|^{r,1}_{l}\big)$ is real and positive, Eq. (2.27) implies that

$$\left(\binom{pq}{jk}\big|^{r,1}_{l}\right) = \left[\frac{d_r}{g}\sum_{T\in\boldsymbol{G}} \Gamma^p T_j j \Gamma^q(T)_{kk}\Gamma^r(T)^*_{ll}\right]^{1/2}. \tag{2.32}$$

Then for *all* $s = 1, 2, \cdots, d_p$, $t = 1, 2, \cdots, d_q$ and $u = 1, 2, \cdots, d_r$, we have

$$\left(\binom{pq}{st}\big|^{r,1}_{u}\right) = \frac{(d_r/g)^{1/2}\sum_{T\in\boldsymbol{G}}\Gamma^p(T)_{sj}\Gamma^q(T)_{tk}\Gamma^r(T)^*_{ul}}{\left[\sum_{T\in\boldsymbol{G}}\Gamma^p(T)_{jj}\Gamma^q(T)_{kk}\Gamma^r(T)^*_{ll}\right]^{1/2}}. \tag{2.33}$$

Although this formula generalizes in the obvious way for a compact Lie group, it is much easier to use Lie-algebraic methods to determine the Clebsch-Gordan coefficients in this case. This procedure is outlined in the next section for the case of $SU(2)$. In principle, the calculation of the Clebsch-Gordan coefficients for a compact Lie group is straightforward, if tedious (see *e.g.* chapter 16 of reference [81]); however direct formulas suitable for use in numerical computations are less easy to obtain, especially in the non-multiplicity-free case (when one or more of the $n^r_{pq} > 1$), such as $SU(3)$.

2.2 Angular Momentum

In classical mechanics, the angular momentum $\boldsymbol{L}$ of a particle is defined to be the moment of the momentum,

$$\boldsymbol{L} = \boldsymbol{r} \times \boldsymbol{p}, \tag{2.34}$$

where $\boldsymbol{r}$ and $\boldsymbol{p}$ are the position and linear momentum respectively. Angular momentum is an *additive* quantity, like linear momentum and the total angular momentum of a system is defined to be the sum $\boldsymbol{L}_{\text{total}} \equiv \sum_\alpha \boldsymbol{L}_\alpha$ of the constituent angular momenta.

Extending this definition to quantum mechanics, the position and momentum become operators, satisfying the commutation relation $[r^j, p^j] = i\hbar\delta_{ij}$. It follows that the angular momentum operator obeys the commutation relation

$$\left[L^i, L^j\right] = ie_{ijk}L^k\,, \tag{2.35}$$

where e_{ijk} is the *Levi-Cevita* totally antisymmetric tensor and we choose units $\hbar \equiv 1$.

Given that the motion of each particle is, in the absence of interactions, independent of the motion of all other particles, it follows immediately that the position and momentum operators for different particles mutually commute,

$$[r^i_\alpha\,,\, r^j_\beta] = [r^i_\alpha\,,\, p^j_\beta] = [p^i_\alpha\,,\, p^j_\beta] = 0\,, \quad \alpha \neq \beta\,. \tag{2.36}$$

The total angular momentum operator $\boldsymbol{L} = \sum_\alpha \boldsymbol{L}_\alpha$, as well as the angular momentum of each particle, $\boldsymbol{L}_\alpha$, obey the same commutation relation Eq. (2.35).

There are two distinct ways of proceeding to characterize the properties of $\boldsymbol{L}$; either using the differential form of the operators, or in an approach pioneered by Born, Heisenberg and Jordan [82], convert the problem into a finite-dimensional matrix eigenvalue problem. This latter approach reveals that the *complete* structure of the angular momentum operators can be calculated from the algebraic relations Eq. (2.35) alone, which define the Lie algebra $SO(3)$, locally isomorphic to $SU(2)$. This is important, because the *spin* vector $\boldsymbol{S}$ obeys identical commutation relations, but without the differential form of the orbital angular momentum. Thus, we can proceed to review the properties of an arbitrary angular momentum $\boldsymbol{J}$, which we define as any quantity that satisfies

$$\left[J^i, J^j\right] = ie_{ijk}J^k\,. \tag{2.37}$$

This approach encompasses orbital angular momentum, spin, or any other quantity that obeys this algebra.

As a first step to calculating the structure of the algebra, we note that the operator $J^2 = J_x^2 + J_y^2 + J_z^2$, commutes with $\boldsymbol{J}$,

$$[J^2\,,\,\boldsymbol{J}] = 0\,. \tag{2.38}$$

Thus it is possible to simultaneously diagonalize $\boldsymbol{J}^2$ and at most *one* of the set J^i, conventionally the choice is to diagonalize J^z. Thus the eigenvalue problem is formulated,

$$\begin{aligned} J^2|j^{2\prime},j^{z\prime}\rangle &= j^{2\prime}|j^{2\prime},j^{z\prime}\rangle\,, \\ J^z|j^{2\prime},j^{z\prime}\rangle &= j^{z\prime}|j^{2\prime},j^{z\prime}\rangle\,, \end{aligned} \tag{2.39}$$

where $j^{2\prime}$ and $j^{z\prime}$ are (assuming that the J^i can be put in Hermitian form) real numbers and $j^{2\prime}$ is positive. The next step is to construct two non-Hermitian operators

$$J^{\pm} = J^x \pm iJ^y\,, \tag{2.40}$$

which satisfy the commutation relations

$$\begin{aligned} [J^2\,,\,J^{\pm}] &= 0\,, \\ [J^z\,,\,J^{\pm}] &= \pm J^{\pm}\,, \\ [J^+\,,\,J^-] &= 2J^z\,. \end{aligned} \tag{2.41}$$

By virtue of these commutation relations, one finds that, if $J^+|j^{2\prime},j^{z\prime}\rangle \neq 0$, then

$$J^2(J^+|j^{2\prime},j^{z\prime}\rangle) = j^{2\prime}(J^+|j^{2\prime},j^{z\prime}\rangle)\,, \tag{2.42}$$

and

$$J^z(J^+|j^{2\prime},j^{z\prime}\rangle) = (j^{z\prime}+1)(J^+|j^{2\prime},j^{z\prime}\rangle)\,. \tag{2.43}$$

Similarly, if $J^-|j^{2\prime},j^{z\prime}\rangle$ is non-zero, it is also a simultaneous eigenstate, with eigenvalues of $j^{2\prime}$ and $j^{z\prime}-1$. This behavior, of increasing or decreasing the eigenvalue of J^z, gives the operators J^+ and J^- the names *raising* and *lowering* operators respectively. The raising and lowering processes must terminate. This is easy to prove given the norm of $J^+|j^{2\prime},j^{z\prime}\rangle$,

$$\langle j^{2\prime},j^{z\prime}\,|\,J^-J^+\,|\,j^{2\prime},j^{z\prime}\rangle = (j^{2\prime}-j^{z\prime}(j^{z\prime}+1))\langle j^{2\prime},j^{z\prime}|j^{2\prime},j^{z\prime}\rangle\,. \tag{2.44}$$

For the norm to be non-negative, one must have $j^{2\prime}-j^{z\prime}(j^{z\prime}+1) \geq 0$. Thus $j^{z\prime}$ cannot be raised indefinitely, but there must be some $j^{z\prime}_{\max}$ such that $|j^{2\prime},j^{z\prime}_{\max}\rangle \neq 0$, but $J^+|j^{2\prime},j^{z\prime}_{\max}\rangle = 0$. Therefore $j^{2\prime} = j^{z\prime}_{\max}(j^{z\prime}_{\max}+1)$. Similarly, the norm of $J^-|j^{2\prime},j^{z\prime}\rangle$ must be positive, which implies that the lowering process also must terminate such that there exists a $j^{z\prime}_{\min}$ such that $|j^{2\prime},j^{z\prime}_{\min}\rangle \neq 0$ but $J^-|j^{2\prime},j^{z\prime}_{\min}\rangle = 0$. From this it follows that $j^{2\prime} = j^{z\prime}_{\min}(j^{z\prime}_{\min}-1)$.

The fact that the process must terminate above and below quantizes the eigenvalues of J^2 and J^z. To see why, one repeatedly applies the raising operator to $|j^{2\prime}, j^{z\prime}\rangle$. At some point this terminates, so we have, for some non-negative integer k, $(J^+)^k|j^{2\prime}, j^{z\prime}\rangle \neq 0$, but $(J^+)^{k+1}|j^{2\prime}, j^{z\prime}\rangle = 0$. Similarly, there exists some non-negative integer l such that $(J^-)^l|j^{2\prime}, j^{z\prime}\rangle \neq 0$ but $(J^-)^{l+1}|j^{2\prime}, j^{z\prime}\rangle = 0$. Then $j^{z\prime}_{\max} = j^{z\prime} + k$, $j^{z\prime}_{\min} = j^{z\prime} + l$ and $j^{2\prime} = (j^{z\prime} + k)(j^{z\prime} + k + 1) = (j^{z\prime} - l)(j^{z\prime} - l - 1)$. This requires that we have

$$\begin{aligned} j^{z\prime} &= \tfrac{l-k}{2} , \\ j^{2\prime} &= \left(\tfrac{k+l}{2}\right)\left(\tfrac{k+l}{2}+1\right) , \\ j^{z\prime}_{\max} &= \tfrac{k+l}{2} , \\ j^{z\prime}_{\min} &= -\tfrac{k+l}{2} . \end{aligned} \tag{2.45}$$

This implies the existence of a set of eigenkets of J^2,

$$\begin{aligned} &|j^{2\prime}, j^{z\prime}\rangle , J^+|j^{2\prime}, j^{z\prime}\rangle, \ldots, (J^+)^k|j^{2\prime}, j^{z\prime}\rangle, \\ &J^-|j^{2\prime}, j^{z\prime}\rangle, \ldots, (J^-)^j|j^{2\prime}, j^{z\prime}\rangle . \end{aligned} \tag{2.46}$$

The eigenvalues of J^z corresponding to these kets are

$$\begin{aligned} &j^{z\prime}, j^{z\prime}+1, \ldots, j^{z\prime}+k = j^{z\prime}_{\max}, \\ &j^{z\prime}-1, \ldots, j^{z\prime}-l = j^{z\prime}_{\min} . \end{aligned} \tag{2.47}$$

The standard way of enumerating these results is to introduce $j = (k+l)/2$ and let m denote any number in the set $\{j, j-1, \ldots, -j\}$. Then $|jm\rangle$ denotes a normalized simultaneous eigenket of J^2 and J^z, with eigenvalues

$$\begin{aligned} J^2|jm\rangle &= j(j+1)|jm\rangle , \\ J^z|jm\rangle &= m|jm\rangle . \end{aligned} \tag{2.48}$$

Hence $2j$ is a non-negative integer and m ranges from $-j$ to $+j$ in steps of unity. By virtue of the Hermiticity of $\boldsymbol{J}$, these states are orthogonal,

$$\langle j'm'|jm\rangle = \delta_{j'j}\delta_{m'm} . \tag{2.49}$$

The action of $J^\pm$ on these basis states is now easily calculated,

$$\begin{aligned} J^+|jm\rangle &= \sqrt{(j-m)(j+m+1)}\,|jm+1\rangle , \\ J^-|jm\rangle &= \sqrt{(j+m)(j-m+1)}\,|jm-1\rangle . \end{aligned} \tag{2.50}$$

This gives, with Eq. (2.48), the matrix elements of $\boldsymbol{J}$,

$$\begin{aligned} \langle j'm'\,|\,J^\pm\,|\,jm\rangle &= \sqrt{(j\mp m)(j\pm m+1)}\,\delta_{j'j}\delta_{m',m\pm1} , \\ \langle j'm'\,|\,J^z\,|\,jm\rangle &= m\delta_{j'j}\delta_{m'm} . \end{aligned} \tag{2.51}$$

These matrices are block-diagonal with respect to j, thus we can label each block as $\boldsymbol{J}^{[j]}$, a $(2j+1)\times(2j+1)$-dimensional matrix. Given an arbitrary angular momentum operator $\boldsymbol{J}$, it can be decomposed into a direct sum of blocks,

$$\boldsymbol{J} = \bigoplus_j n_j \, \boldsymbol{J}^{[j]} \,, \tag{2.52}$$

where n^j is the multiplicity of block $\boldsymbol{J}^{[j]}$ in $\boldsymbol{J}$.

A rotation of angle θ about some axis given by the unit vector $\hat{n}$ is given by the unitary matrix

$$U(\theta\hat{n}) \equiv e^{-i\theta\hat{n}\cdot\boldsymbol{J}} \,, \tag{2.53}$$

which, given the expansion Eq. (2.52), reduces to the study of the matrices

$$D^j(\theta\hat{n}) \equiv e^{-i\theta\hat{n}\cdot\boldsymbol{J}^{[j]}} \,, \tag{2.54}$$

where the matrix elements of the representation D^j are given by

$$D^j_{m'm}(\theta\hat{n}) = \langle\, jm' \,|\, e^{-i\theta\hat{n}\cdot\boldsymbol{J}^{[j]}} \,|\, jm \,\rangle \,. \tag{2.55}$$

The action of $U(\theta\hat{n})$ on the eigenket $|\,jm\rangle$ is then given by

$$\begin{aligned} U(\theta\hat{n})|\,jm\rangle &= \sum_{m'} |\,jm'\rangle\langle jm'|U(\theta\hat{n})|\,jm\rangle \\ &= \sum_{m'} D^j_{m'm}(\theta\hat{n})|\,jm'\rangle \,. \end{aligned} \tag{2.56}$$

2.2.1 The Wigner-Eckart theorem

Suppose that a system has a rotational symmetry and hence can be completely described in terms of a basis set of eigenstates of total angular momentum, $|\,jm(\alpha)\rangle$. The label (α) denotes all other quantum numbers that are *not* associated with angular momentum. Consider now an arbitrary operator T that acts on the system. This can be described completely by the set of matrix elements

$$\{\, \langle\, j'm'(\alpha') \,|\, T \,|\, jm(\alpha) \,\rangle \,\} \,. \tag{2.57}$$

The physical probabilities associated with these probability amplitudes must necessarily be invariant with respect to arbitrary transformations of the coordinate frame. Thus $|\langle\, j'm'(\alpha') \,|\, T \,|\, jm(\alpha) \,\rangle|^2$ is an invariant. The implications of this constraint can be summarized by a fundamental theorem on symmetry due to Wigner [83],

The invariance of the physical probability $|\langle\, j'm'(\alpha') \,|\, T \,|\, jm(\alpha) \,\rangle|^2$ *under a symmetry implies that either (a) the probability amplitude, Eq. (2.57) is invariant,*

or (b) the probability amplitude transforms under the symmetry into its complex conjugate.

Wigner showed that the latter case corresponds to time reversal, thus in the case of rotational symmetry the amplitude itself is invariant, hence

$$\langle\, j'm'(\alpha') \,|\, T \,|\, jm(\alpha) \,\rangle = \text{invariant to rotations of coordinates.} \tag{2.58}$$

This is valid for all possible basis states, so it follows directly that it is also true for arbitrary vectors in the Hilbert space,

$$\langle\, \psi \,|\, T \,|\, \phi \,\rangle = \text{invariant to rotations of coordinates,} \tag{2.59}$$

for arbitrary vectors $|\phi\rangle$ and $\langle\psi|$. The action of a rotation $U = \exp(-i\theta\hat{n}\cdot\boldsymbol{J})$ on the ket $|\phi\rangle$ is

$$|\phi\rangle \to |\phi'\rangle = U|\phi\rangle\,, \tag{2.60}$$

with a corresponding unitary transformation on the bra vector,

$$\langle\psi| \to \langle\psi'| = \langle\psi|U^{-1}\,. \tag{2.61}$$

The statement of the invariance Eq. (2.59) now takes the form

$$\langle\, \psi \,|\, T \,|\, \phi \,\rangle = \langle\, \psi' \,|\, T' \,|\, \phi' \,\rangle\,, \tag{2.62}$$

which implies

$$\langle\, \psi \,|\, T \,|\, \phi \,\rangle = \langle\, \psi \,|\, U^{-1}T'U \,|\, \phi \,\rangle\,, \tag{2.63}$$

from which one obtains

$$T' = UTU^{-1}\,. \tag{2.64}$$

Under an infinitesimal transformation $U = \exp(-i\,\delta\theta\,\hat{n}\cdot\boldsymbol{J})$, T transforms as

$$T' = T - i\,\delta\theta\,\hat{n}\cdot[\boldsymbol{J}\,,\,T]\,, \tag{2.65}$$

thus

$$\delta T \equiv T' - T = -i\,\delta\theta\,\hat{n}\cdot[\boldsymbol{J}\,,\,T]\,. \tag{2.66}$$

The appearance of a commutator with the angular momentum operators motivates the definition of an *irreducible tensor operator* of rank J ($J = 0, \frac{1}{2}, 1, \cdots$). An irreducible tensor operator of rank J, denoted $\boldsymbol{T}^{[J]}$, is a set of linear operators $\left\{T^{[J]}_M : M = -J, -J+1, \cdots, J\right\}$, where the commutator action with the angular momentum $\boldsymbol{J}$ is

$$\begin{aligned}
[J^+\,,\,T^{[J]}_M] &= \sqrt{(J-M)(J+M+1)}\,T^J_{M+1}\,,\\
[J^-\,,\,T^{[J]}_M] &= \sqrt{(J+M)(J-M+1)}\,T^J_{M-1}\,,\\
[J^z\,,\,T^{[J]}_M] &= M\,T^J_M\,.
\end{aligned} \tag{2.67}$$

The components $T^{[J]}_M$ are referred to as the *projections* of the irreducible tensor operator $\boldsymbol{T}^{[J]}$.

From this definition it is easy to derive the action of the rotation $U(\theta\hat{n})$ on $\boldsymbol{T}^J$,

$$U(\theta\hat{n})\, T^{[J]}_M\, U^{-1}(\theta\hat{n}) = \sum_{M'} D^J_{M'M}(\theta\hat{n})\, T^{[J]}_{M'} . \tag{2.68}$$

This is exactly analogous to the transformation of a ket vector, Eq. (2.56).

Curiously, the operator $\boldsymbol{J}$, in the usual from $\boldsymbol{J} = (J^x, J^y, J^z)$ does *not* itself transform as an irreducible tensor operator. The reason is that, in this form $\boldsymbol{J}$ transforms according to the vector representation of $SO(3)$, whereas the definition Eq. (2.67) applies to a rank J representation of $SU(2)$. The two algebras are locally isomorphic, the correspondence given by

$$\begin{aligned} J^1_{-1} &= -J^- \\ J^1_0 &= J^z/\sqrt{2} \\ J^1_1 &= J^+ . \end{aligned} \tag{2.69}$$

In this form, $\boldsymbol{J}^1$ is an irreducible tensor operator of rank 1.

The importance of irreducible tensor operators is demonstrated by the *Wigner-Eckart* theorem,

When written in an angular momentum basis, each matrix element of an irreducible tensor operator is a product of two factors, a purely angular momentum dependent factor (the "Clebsch-Gordan" coefficient) and a factor that is independent of the projection quantum numbers (the "reduced matrix element").

The reduced matrix elements, being independent of the projection quantum number, act on a different basis set and are denoted with the unusual notation $\|j(\alpha)\rangle$. The explicit relationship between the two basis sets is is given by the Clebsch-Gordan coefficients,

$$\langle\, j'm'(\alpha') \,|\, T^{[J]}_M \,|\, jm(\alpha)\,\rangle = \langle\, j'(\alpha') \,\|\, \boldsymbol{T}^J \,\|\, j(\alpha)\,\rangle C^{j\ J\ j'}_{mMm'} , \tag{2.70}$$

where the reduced matrix element $\langle\, j'(\alpha') \,\|\, \boldsymbol{T}^J \,\|\, j(\alpha)\,\rangle$ is defined by

$$\langle\, j'(\alpha') \,\|\, \boldsymbol{T}^J \,\|\, j(\alpha)\,\rangle = \sum_{mM} C^{j\ J\ j'}_{mMm'} \langle\, j'm'(\alpha') \,|\, T^{[J]}_M \,|\, jm(\alpha)\,\rangle . \tag{2.71}$$

The value of m' is arbitrary here, as long as $-j' \le m' \le j'$, as the summation over m and M gives a coefficient that is independent of m'. Alternatively, one can sum over all m' and divide by $2j'+1$,

$$\langle\, j'(\alpha') \,\|\, \boldsymbol{T}^{[J]} \,\|\, j(\alpha)\,\rangle = \frac{1}{2j'+1} \sum_{mMm'} C^{j\ J\ j'}_{mMm'} \langle\, j'm'(\alpha') \,|\, T^{[J]}_M \,|\, jm(\alpha)\,\rangle . \tag{2.72}$$

The importance of the Wigner-Eckart theorem is that it establishes a clear separation between the geometric (group-theoretic) aspects of an operator, given by the Clebsch-Gordan coefficients and the essential physics, given by the reduced matrix elements. This is a very important principle, which can be carried further to describe the coupling of tensor operators in a manifestly $SU(2)$-invariant way.

2.2.2 Coupling of tensor operators

Consider two operators $\boldsymbol{S}^{[k_1]}$ and $\boldsymbol{T}^{[k_2]}$, each of which is an irreducible tensor operator with respect to the total angular momentum $\boldsymbol{J}$. Thus each of the sets of operators $\left\{S_{\mu_1}^{[k_1]}\right\}$ and $\left\{T_{\mu_2}^{[k_2]}\right\}$ obey the commutation relations given by Eq. (2.67). We generalize the usual matrix product to the coupling of irreducible tensor operators by introducing the symbol

$$\left[\boldsymbol{S}^{[k_1]}\times\boldsymbol{T}^{[k_2]}\right]^{[k]}, \tag{2.73}$$

to denote the set of operators with components

$$\left[\boldsymbol{S}^{[k_1]}\times\boldsymbol{T}^{[k_2]}\right]_{\mu}^{[k]}, \quad \mu = -k, -k+1, \ldots, k\,. \tag{2.74}$$

These are defined by a coupling of the components $S_{\mu_1}^{[k_1]}$ and $T_{\mu_1}^{[k_1]}$, given by

$$\left[\boldsymbol{S}^{[k_1]}\times\boldsymbol{T}^{[k_2]}\right]_{\mu}^{[k]} \equiv \sum_{\mu_1\,\mu_2} C^{k_1\,k_2\,k}_{\mu_1\,\mu_2\,\mu} S_{\mu_1}^{[k_1]} T_{\mu_1}^{[k_1]}\,. \tag{2.75}$$

The proof that $\left[\boldsymbol{S}^{[k_1]}\times\boldsymbol{T}^{[k_2]}\right]^{[k]}$ is indeed a irreducible tensor operator of rank k follows from the action under a rotation, Eq. (2.68).

The application of the Wigner-Eckart theorem to this operator gives

$$\langle\, j'm'(\alpha') \,|\, \left[\boldsymbol{S}^{[k_1]}\times\boldsymbol{T}^{[k_2]}\right]_{\mu}^{[k]} \,|\, jm(\alpha)\,\rangle = \langle\, j'(\alpha') \,\|\, \left[\boldsymbol{S}^{[k_1]}\times\boldsymbol{T}^{[k_2]}\right]^{[k]} \,\|\, j(\alpha)\,\rangle C^{j\;k\;j'}_{m\mu m'}\,. \tag{2.76}$$

Expanding $\left[\boldsymbol{S}^{[k_1]}\times\boldsymbol{T}^{[k_2]}\right]_{\mu}^{[k]}$ with Eq. (2.75), gives, after a couple of lines of algebra,

$$\begin{aligned}
&\langle\, j'(\alpha') \,\|\, \left[\boldsymbol{S}^{[k_1]}\times\boldsymbol{T}^{[k_2]}\right]^{[k]} \,\|\, j(\alpha)\,\rangle \\
&\quad = (-1)^{j+j'+k} \sum_{(\alpha'')j''} \left[(2j''+1)(2k+1)\right]^{\frac{1}{2}} \left\{ \begin{array}{ccc} j' & k_1 & j'' \\ k_2 & j & k \end{array} \right\} \\
&\qquad \times \langle\, j'(\alpha') \,\|\, \boldsymbol{S}^{[k_1]} \,\|\, j''(\alpha'')\,\rangle \langle\, j''(\alpha'') \,\|\, \boldsymbol{T}^{[k_2]} \,\|\, j(\alpha)\,\rangle\,,
\end{aligned} \tag{2.77}$$

where the coefficients $\{\cdots\}$ are the Wigner $6j$ coefficients, defined as a sum over

four Clebsch-Gordan coefficients,

$$(-1)^{j+j'+k}[(2j''+1)(2k+1)]^{\frac{1}{2}}\left\{\begin{array}{ccc} j' & k_1 & j'' \\ k_2 & j & k \end{array}\right\} \equiv \sum_{\mu_1\,\mu_2\,\mu\,m\,m''} C^{k_1\,k_2\,k}_{\mu_1\,\mu_2\,\mu}C^{j\;\;k\,j'}_{m\,\mu\,m'}C^{j''\;\;k_1\,j'}_{m''\;\mu_1\,m'}C^{j\;\;k_2\,j''}_{m\,\mu_2\,m''}\,. \tag{2.78}$$

m' may be chosen arbitrarily in this result, given $-j' \leq m' \leq j'$. This gives the reduced matrix elements of the coupling $[\boldsymbol{S}^{[k_1]}\times\boldsymbol{T}^{[k_2]}]^{[k]}$ directly from the reduced matrix elements of $\boldsymbol{S}^{[k_1]}$ and $\boldsymbol{T}^{[k_2]}$ in a form that is, after the calculation of the $6j$ coefficients, independent of the projection numbers. The existence of more than one choice of the rank k in the coupling means that it is not possible, in general, to define uniquely a multiplication operator. This means that the set of irreducible tensor operators on the space of reduced matrix elements does not form an algebra, but can instead be interpreted as a generalization of an algebra whereby there are many 'multiplication' operators. An additional complication is that this generalized 'algebra' is non-associative. Applying Eq. (2.77) to the coupling of three operators $[[\boldsymbol{S}\times\boldsymbol{T}]\times\boldsymbol{U}]$ and $[\boldsymbol{S}\times[\boldsymbol{T}\times\boldsymbol{U}]]$ gives

$$[\boldsymbol{S}^{[k_1]}\times[\boldsymbol{T}^{[k_2]}\times\boldsymbol{U}^{[k_3]}]^{[k_{23}]}]^{[k]} = (-1)^{2k}\sum_{k_{12}}\sqrt{2k_{12}+1}\left\{\begin{array}{ccc} k_1 & k_2 & k_{12} \\ k_3 & k & k_{23} \end{array}\right\} \times[[\boldsymbol{S}^{[k_1]}\times\boldsymbol{T}^{[k_2]}]^{[k_{12}]}\times\boldsymbol{U}^{[k_3]}]^{[k]}\,. \tag{2.79}$$

Proof of this follows from the definition Eq. (2.75) and the symmetry properties of the Clebsch-Gordan coefficients. Alternatively, it can be proven from the properties of the $6j$ coefficients alone, by using the Biedenharn-Elliott identity [84].

The mathematical properties of the coupling of tensor operators can be put on a more concrete footing by using the *unit tensor operator* formulation described at length in Biedenharn and Louck [85]. When written in terms of unit tensor operators, the coupling forms an associative, non-Abelian algebra called the *Wigner-Racah algebra.* However, with this formulation the operator product of two unit tensors does not in general transform irreducibly. In practice, as we shall see later, we are usually interested in coupling two tensor operators to an irreducible tensor. Thus if the Wigner-Racah formulation was used, the most common operation would be the product of unit tensor operators followed by a projection onto some irreducible component. This destroys the associativity properties of the product operation, so it is not clear that this formulation provides any advantage for the purposes of this thesis.

A special case of the coupling law Eq. (2.77) that is particularly relevant to the DMRG algorithm is when the operators act on different spaces, such that they have

a tensor product form

$$\begin{aligned} S^{[k_1]}_{\mu_1} &= T^{[k_1]}_{\mu_1}(1) \otimes I(2) \,, \\ T^{[k_2]}_{\mu_2} &= I(1) \otimes T^{[k_2]}_{\mu_2}(2) \,. \end{aligned} \tag{2.80}$$

Here $I(i)$ denotes the identity operator and $\boldsymbol{T}^{[k_i]}(i)$ is an irreducible tensor operator with respect to the angular momentum $\boldsymbol{J}(i)$ of part i of a two-part physical system ($i = 1, 2$). The total angular momentum of the system is $\boldsymbol{J} = \boldsymbol{J}(1) + \boldsymbol{J}(2)$. In this case, we write the coupling as $[\boldsymbol{S}^{[k_1]} \times \boldsymbol{T}^{[k_2]}]^{[k]} \equiv [\boldsymbol{T}^{[k_1]}(1) \otimes \boldsymbol{T}^{[k_2]}(2)]^{[k]}$. Repeated application of the Wigner-Eckart theorem to these tensor operators gives, after some algebra,

$$\begin{aligned} &\langle\, j' \,(j'_1 j'_2 \alpha'_1 \alpha'_2) \,\|\, [\boldsymbol{T}^{[k_1]}(1) \otimes \boldsymbol{T}^{[k_2]}(2)]^{[k]} \,\|\, j \,(j_1 j_2 \alpha_1 \alpha_2) \,\rangle \\ &= \begin{bmatrix} j_1 & j_2 & j \\ k_1 & k_2 & k \\ j'_1 & j'_2 & j' \end{bmatrix} \langle\, j'_1 \,(\alpha'_1) \,\|\, \boldsymbol{T}^{[k_1]}(1) \,\|\, j_1 \,(\alpha_1) \,\rangle \langle\, j'_2 \,(\alpha'_2) \,\|\, \boldsymbol{T}^{[k_2]}(2) \,\|\, j_2 \,(\alpha_2) \,\rangle \,, \end{aligned} \tag{2.81}$$

where

$$\begin{bmatrix} j_1 & j_2 & j \\ j_1 & k_2 & k \\ j'_1 & j'_2 & j' \end{bmatrix} \equiv [(2j'_1 + 1)(2j'_2 + 1)(2j + 1)(2k + 1)]^{\frac{1}{2}} \begin{Bmatrix} j_1 & j_2 & j \\ k_1 & k_2 & k \\ j'_1 & j'_2 & j' \end{Bmatrix} , \tag{2.82}$$

and the term in curly brackets is the Wigner $9j$ coefficient, which can be defined as a summation over $6j$ coefficients [84],

$$\begin{aligned} \begin{Bmatrix} j_1 & j_2 & j \\ k_1 & k_2 & k \\ j'_1 & j'_2 & j' \end{Bmatrix} \equiv\ & (-1)^{j_1+j_2+j+k_1+k_2+k+j'_1+j'_2+j'} \sum_{j''} (-1)^{2j''} (2j'' + 1) \\ & \times \begin{Bmatrix} j' & k_1 & j'' \\ k_2 & j & k \end{Bmatrix} \begin{Bmatrix} j' & j'_2 & j'_1 \\ j_1 & k_1 & j'' \end{Bmatrix} \begin{Bmatrix} j'' & j_1 & j'_2 \\ j_2 & k_2 & j \end{Bmatrix} . \end{aligned} \tag{2.83}$$

The coupling law Eq. (2.81) has immediate applications to numerical blocking techniques, where a common task is to obtain the matrix elements of operators acting on the complete system given the matrix elements of the constituent blocks.

2.2.3 Properties of irreducible tensor operators

An important class of irreducible tensor operators are those that are *rotational invariants*, that is, operators that transform under a rotation as

$$U(\theta \hat{n})\, T^{[J]}_M\, U^{-1}(\theta \hat{n}) = T^{[J]}_M \,. \tag{2.84}$$

It follows immediately from Eq. (2.66) that T must commute with $\boldsymbol{J}$ and hence T must transform as a rank-0 tensor. The converse is also immediate from Eq. (2.67); *all* rank-0 tensors are rotational invariants. In this case, the Wigner-Eckart theorem Eq. (2.70) simplifies dramatically, to

$$\langle j'm'(\alpha') \,|\, T_0^0 \,|\, jm(\alpha) \rangle = \langle j'(\alpha') \,\|\, \boldsymbol{T}^0 \,\|\, j(\alpha) \rangle \, \delta_{j'j} \delta_{m'm} \Delta_{jm} \,, \tag{2.85}$$

where Δ_{jm} is unity if $-j \leq m \leq j$ and zero otherwise. Thus, a rotational invariant operator is block diagonal with respect to j and m and the matrix elements are independent of the projection m.

For higher rank tensors, the properties of the Clebsch-Gordan coefficients imply that the reduced matrix is block-banded and the permissible non-zero matrix elements are between elements $|j'(\alpha')\rangle$ and $|j(\alpha)\rangle$, with $j' = j + \Delta J$ and the allowed values of ΔJ are

$$\Delta J = J, J-1, \ldots, -J \,. \tag{2.86}$$

The matrix elements of $\boldsymbol{J}$ itself were derived in Eq. (2.51), which gives the reduced matrix elements

$$\langle j'(\alpha') \,\|\, \boldsymbol{J}^{[1]} \,\|\, j(\alpha) \rangle = \sqrt{j(j+1)} \, \delta_{j'j} \, \delta_{\alpha'\alpha} \,. \tag{2.87}$$

The construction of the coupled tensor operators $[\boldsymbol{S}^{[k_1]} \times \boldsymbol{T}^{[k_2]}]^{[k]}$ leads to a natural way of constructing a rotational invariant,

$$[\boldsymbol{S}^{[K]} \times \boldsymbol{T}^{[J]}]_0^{[0]} = \sum_M \frac{(-1)^{J-M}}{(2J+1)^{\frac{1}{2}}} \, S_M^{[J]} \, T_{-M}^{[J]} \,. \tag{2.88}$$

This can be written, apart from the unimportant J-dependent pre-factor, as a trace over M, by recasting $\boldsymbol{T}^{[J]}$ as a *conjugate irreducible tensor operator* $\bar{\boldsymbol{T}}^{[J]}$,

$$\bar{T}_M^{[J]} \equiv (-1)^{J-M} T_{-M}^{[J]} \,. \tag{2.89}$$

Thus, if $\boldsymbol{S}^{[J]}$ and $\bar{\boldsymbol{T}}^{[J]}$ denote tensor and conjugate tensors respectively, then the quantity

$$\sum_M S_M^J \bar{T}_M^{[J]} \,, \tag{2.90}$$

is a rotational invariant.

The transform properties of this operator are different to that of $T_M^{[J]}$, in that the transform coefficients are the complex conjugate of the rotation matrix elements,

$$U(\theta\hat{n}) \, \bar{T}_M^{[J]} \, U^{-1}(\theta\hat{n}) = \sum_{M'} D_{M'M}^{J*}(\theta\hat{n}) \, \bar{T}_{M'}^{[J]} \,. \tag{2.91}$$

The usual definition of the Hermitian conjugate is equivalent to taking the complex conjugate of the transpose. In the case of irreducible tensor operators, such a definition is not completely satisfactory, because it is easy to show that such an operator transforms as a conjugate irreducible tensor. In the DMRG code it would be desirable to only have one species of tensor operators; the appearance of conjugate tensors, with different transformation rules and coupling coefficients, is an unnecessary complication. Thus in this thesis, we use an alternate definition of the *Hermitian conjugate* $T^{\dagger[J]}$, such that it transforms as an ordinary tensor operator,

$$\langle j'm'(\alpha') \,|\, T^{\dagger[J]}_{M} \,|\, jm(\alpha) \rangle = (-1)^{J-M} \langle jm(\alpha) \,|\, T^{[J]}_{-M} \,|\, j'm'(\alpha') \rangle^* \,. \tag{2.92}$$

This amounts to taking, in addition to the usual Hermitian conjugate, the tensor conjugate given in Eq. (2.89). This notation is equivalent to that used in reference [86], but is different to the notation of reference [84]. The advantage of the current notation is that the reduced matrix elements of the Hermitian conjugate of an operator can be written directly in terms of the reduced matrix elements of the original operator,

$$\langle j'(\alpha') \,\|\, \boldsymbol{T}^{\dagger[J]} \,\|\, j(\alpha) \rangle = (-1)^{J+j-j'} \sqrt{\frac{2j+1}{2j'+1}} \langle j(\alpha) \,\|\, \boldsymbol{T}^{[J]} \,\|\, j'(\alpha') \rangle^* \,. \tag{2.93}$$

Unfortunately the notation is somewhat confusing and it is very important to distinguish the conjugate of a tensor (which transforms as a conjugate irreducible tensor) and the Hermitian conjugate of a tensor (which transforms as an ordinary irreducible tensor). However with this definition of Hermitian conjugation, we can do everything with ordinary irreducible tensors and we no longer need to deal with conjugate irreducible tensors at all.

An interesting feature of the Hermitian conjugation operation is that applying Hermitian conjugation twice does not in all cases give the original operator, but instead

$$(\boldsymbol{T}^{\dagger[J]})^{\dagger} = (-1)^{2J} \boldsymbol{T}^{[J]} \,. \tag{2.94}$$

Thus for tensors that transform as half-integral representations, an additional minus sign appears and the Hermitian conjugation needs to be applied *four* times to recover the original operator. Even rank tensors can also have unfamiliar properties with respect to Hermitian conjugation. For example, the total angular momentum $\boldsymbol{J}^{[1]}$ itself is skew-Hermitian, $\boldsymbol{J}^{\dagger[1]} = -\boldsymbol{J}^{[1]}$.

The commutation relations between irreducible tensor operators needs to be generalized, in particular the rank of the coupled tensors does make a difference. We define the generalized commutator by

$$\left[\boldsymbol{S}^{[k_1]}, \boldsymbol{T}^{[k_2]}\right]^{[k]} = \left[\boldsymbol{S}^{[k_1]} \times \boldsymbol{T}^{[k_2]}\right]^{[k]} - \left[\boldsymbol{T}^{[k_2]} \times \boldsymbol{S}^{[k_1]}\right]^{[k]} , \tag{2.95}$$

and the anticommutator by

$$\left\{ \boldsymbol{S}^{[k_1]} , \boldsymbol{T}^{[k_2]} \right\}^{[k]} = [\boldsymbol{S}^{[k_1]} \times \boldsymbol{T}^{[k_2]}]^{[k]} + [\boldsymbol{T}^{[k_2]} \times \boldsymbol{S}^{[k_1]}]^{[k]} . \tag{2.96}$$

2.2.4 Tensor formulation of the fermionic algebra

In this section, the algebra of the operators corresponding to a system of fermions is re-cast into irreducible tensor form. The usual algebra for a system of fermions is given by annihilation operators $c_{\sigma,i}$ and creation operators $c^{\dagger}_{\sigma,i}$, of $z-$component of spin σ acting on site i. Spin $\frac{1}{2}$ is assumed, with σ taking values of $\uparrow$ and $\downarrow$. These operators obey the anti-commutation relations

$$\{c^{\dagger}_{\sigma,i} , c_{\tau,j}\} = \delta_{\sigma\tau}\delta_{ij} , \tag{2.97}$$

$$\{c^{\dagger}_{\sigma,i} , c^{\dagger}_{\tau,j}\} = \{c_{\sigma,i} , c_{\tau,j}\} = 0 . \tag{2.98}$$

The operator n_i, defined by

$$n_i = c^{\dagger}_{\uparrow,i} c_{\uparrow,i} + c^{\dagger}_{\downarrow,i} c_{\downarrow,i} , \tag{2.99}$$

gives the number of particles at site i, as a consequence of the commutation relations

$$\begin{array}{rcl} [n_i , c_{\sigma,i}] & = & -c_{\sigma,i} \\ [n_i , c^{\dagger}_{\sigma,i}] & = & c^{\dagger}_{\sigma,i} . \end{array} \tag{2.100}$$

The total spin at each site is defined through the Pauli spin matrices,

$$\boldsymbol{S}_i = \frac{1}{2} \sum_{\sigma,\tau} c^{\dagger}_{\sigma,i} \boldsymbol{\sigma}_{\sigma\tau} c_{\tau,j} , \tag{2.101}$$

and we choose the usual representation of the spin matrices,

$$\begin{array}{rcl} \sigma^x & = & \begin{pmatrix} 0 & 1 \\ 1 & 0 \end{pmatrix} , \\ \sigma^y & = & \begin{pmatrix} 0 & -i \\ i & 0 \end{pmatrix} , \\ \sigma^z & = & \begin{pmatrix} 1 & 0 \\ 0 & -1 \end{pmatrix} . \end{array} \tag{2.102}$$

It follows that the creation and annihilation operators obey commutation relations with respect to the spin operators,

$$\begin{array}{rcl} [S^z , c_{\uparrow,i}] & = & -\frac{1}{2} c_{\uparrow,i} , \\ [S^z , c_{\downarrow,i}] & = & \frac{1}{2} c_{\downarrow,i} , \end{array} \tag{2.103}$$

Assuming that there is no orbital component, the total angular momentum $\boldsymbol{J}$ is equal to the total spin $\boldsymbol{S}$. Thus it is clear that the creation and annihilation operators can be re-cast as rank $\frac{1}{2}$ tensors (spinors),

$$\begin{aligned} \boldsymbol{c}_i^{[1/2]} &= \begin{pmatrix} c_{-1/2,i} \\ c_{1/2,i} \end{pmatrix} , \\ \boldsymbol{c}_i^{\dagger[1/2]} &= \begin{pmatrix} c_{-1/2,i}^\dagger \\ c_{1/2,i}^\dagger \end{pmatrix} . \end{aligned} \tag{2.104}$$

Direct comparison between the commutation relations Eq. (2.103) and those of a irreducible tensor operator Eq. (2.67) gives a possible identification

$$\begin{aligned} c_{-1/2,i} &= c_{\uparrow,i} \\ c_{1/2,i} &= c_{\downarrow,i} \\ c_{-1/2,i}^\dagger &= -c_{\downarrow,i}^\dagger \\ c_{1/2,i}^\dagger &= c_{\uparrow,i}^\dagger , \end{aligned} \tag{2.105}$$

We have chosen the sign in the first two relations for $\boldsymbol{c}^{[1/2]}$ and chosen to set $\boldsymbol{c}^{\dagger[1/2]} = (\boldsymbol{c}^{[1/2]})^\dagger$, which then gives the final two relations for $\boldsymbol{c}^{\dagger[1/2]}$, via Eq. (2.93). This means that $(\boldsymbol{c}^{\dagger[1/2]})^\dagger = -\boldsymbol{c}^{[1/2]}$.

For a single site, the commutation relations imply that the complete set of basis states is four-dimensional. The usual notation for the basis states is $\{|0\rangle, |\uparrow\rangle, |\downarrow\rangle, |\uparrow\downarrow\rangle\}$, but here we want to use the notation more applicable to the irreducible tensor formulation, $|jm(\alpha)\rangle$. Taking the non-$SU(2)$ label α to be the number of particles n is sufficient to distinguish all the basis states,

$$\begin{aligned} |0\rangle &\rightarrow |0,0,(0)\rangle \\ |\uparrow\rangle &\rightarrow |1/2,1/2,(1)\rangle &&= c_\uparrow^\dagger|0\rangle \\ |\downarrow\rangle &\rightarrow |1/2,-1/2,(1)\rangle &&= c_\downarrow^\dagger|0\rangle \\ |\uparrow\downarrow\rangle &\rightarrow |0,0,(2)\rangle &&= c_\uparrow^\dagger c_\downarrow^\dagger|0\rangle . \end{aligned} \tag{2.106}$$

With respect to this basis, the matrix elements of the operators $c_\uparrow$ and $c_\downarrow$ are

$$\begin{aligned} c_\uparrow &= \begin{pmatrix} 0 & 1 & 0 & 0 \\ 0 & 0 & 0 & 0 \\ 0 & 0 & 0 & 1 \\ 0 & 0 & 0 & 0 \end{pmatrix} , \\ c_\downarrow &= \begin{pmatrix} 0 & 0 & 1 & 0 \\ 0 & 0 & 0 & -1 \\ 0 & 0 & 0 & 0 \\ 0 & 0 & 0 & 0 \end{pmatrix} . \end{aligned} \tag{2.107}$$

The matrix elements of $c^\dagger_\uparrow$ and $c^\dagger_\downarrow$ are the (ordinary) Hermitian conjugate of these.

The reduced basis $||j(\alpha)\rangle\rangle$ corresponding to this set is three-dimensional,

$$\begin{aligned} &||0,(0)\rangle\rangle \\ &||1/2,(1)\rangle\rangle &&= \boldsymbol{c}^{\dagger[1/2]}\,||0,(0)\rangle\rangle \\ &||0,(2)\rangle\rangle &&= \tfrac{1}{\sqrt{2}}[\boldsymbol{c}^{\dagger[1/2]}\times\boldsymbol{c}^{\dagger[1/2]}]^{[0]}\,||0,(0)\rangle\rangle\,. \end{aligned} \tag{2.108}$$

In this basis, the reduced matrix form of $\boldsymbol{c}^{[1/2]}$ is given by

$$\boldsymbol{c}^{[1/2]} = \begin{pmatrix} 0 & \sqrt{2} & 0 \\ 0 & 0 & 1 \\ 0 & 0 & 0 \end{pmatrix}\,. \tag{2.109}$$

The matrix elements of the creation operator are then given from the definition of the Hermitian conjugate of an irreducible tensor operator and are

$$\boldsymbol{c}^{\dagger[1/2]} = \begin{pmatrix} 0 & 0 & 0 \\ 1 & 0 & 0 \\ 0 & -\sqrt{2} & 0 \end{pmatrix}\,. \tag{2.110}$$

By using the coupling law between tensors acting on separate parts of a system, Eq. (2.81), the matrix elements of $\boldsymbol{c}_i^{\dagger[1/2]}$ (and arbitrary combinations of $\boldsymbol{c}_i^{\dagger[1/2]}$ acting on different sites) can be constructed in the basis of eigenstates of total spin of the complete system.

The generalized commutation relations, applied to the spinor form of the operators, are

$$\begin{aligned} \left\{\boldsymbol{c}_i^{\dagger[1/2]}, \boldsymbol{c}_j^{[1/2]}\right\}^{[0]} &= \tfrac{1}{\sqrt{2}}\delta_{ij}\,, \\ \left\{\boldsymbol{c}_i^{\dagger[1/2]}, \boldsymbol{c}_j^{[1/2]}\right\}^{[1]} &= 0\,, \end{aligned} \tag{2.111}$$

$$\begin{aligned} \left\{\boldsymbol{c}_i^{[1/2]}, \boldsymbol{c}_j^{[1/2]}\right\}^{[0]} &= -2\sqrt{2}\delta_{ij}\,\boldsymbol{\eta}_i^{[0]}\,, \\ \left\{\boldsymbol{c}_i^{[1/2]}, \boldsymbol{c}_j^{[1/2]}\right\}^{[1]} &= 0\,. \end{aligned} \tag{2.112}$$

$$\begin{aligned} \left\{\boldsymbol{c}_i^{\dagger[1/2]}, \boldsymbol{c}_j^{\dagger[1/2]}\right\}^{[0]} &= 2\sqrt{2}\delta_{ij}\,\boldsymbol{\eta}_i^{\dagger[0]}\,, \\ \left\{\boldsymbol{c}_i^{\dagger[1/2]}, \boldsymbol{c}_j^{\dagger[1/2]}\right\}^{[1]} &= 0\,, \end{aligned} \tag{2.113}$$

Here $\boldsymbol{\eta}_i^{[0]}$ and $\boldsymbol{\eta}_i^{\dagger[0]}$ are the η-pairing operators [87], which transform as $SU(2)$ scalars† and annihilate and create a double occupied site respectively,

$$\begin{aligned} \boldsymbol{\eta}_i^{[0]} &= c_\downarrow c_\uparrow &&= -\tfrac{1}{\sqrt{2}}[\boldsymbol{c}_i^{[1/2]}\times\boldsymbol{c}_i^{[1/2]}]^{[0]}\,, \\ \boldsymbol{\eta}_i^{\dagger[0]} &= c_\uparrow^\dagger c_\downarrow^\dagger &&= \tfrac{1}{\sqrt{2}}[\boldsymbol{c}_i^{\dagger[1/2]}\times\boldsymbol{c}_i^{\dagger[1/2]}]^{[0]}\,. \end{aligned} \tag{2.114}$$

†Later we shall see that the operators η^+ and η^- actually transform as components of a vector operator with respect to an additional $SU(2)$ pseudospin symmetry.

The unusual square root factors appearing in the coupling of tensor operators are a consequence of the orthonormality conditions on the Clebsch-Gordan coefficients Eq. (B.3); in principle these factors can be adjusted by a different choice of normalization.

Re-casting the number operator n_i in tensor form shows that, as expected, it transforms as a rotational invariant,

$$n_i = \boldsymbol{n}_i^{[0]} = \sqrt{2}\left[\boldsymbol{c}_i^{\dagger[1/2]} \times \boldsymbol{c}_i^{[1/2]}\right]^{[0]} . \tag{2.115}$$

The spin operator is given by the triplet coupling

$$\boldsymbol{S}_i^{[1]} = \left[\boldsymbol{c}_i^{\dagger[1/2]} \times \boldsymbol{c}_i^{[1/2]}\right]^{[1]} . \tag{2.116}$$

As shown earlier, this operator is skew-Hermitian, with reduced matrix elements given by Eq. (2.87). The members of the multiplet are

$$\boldsymbol{S}_i^{[1]} = \begin{pmatrix} S_{-1}^{[1]} \\ S_0^{[1]} \\ S_1^{[1]} \end{pmatrix} = \begin{pmatrix} c_\downarrow^\dagger c_\uparrow \\ \left[c_\uparrow^\dagger c_\uparrow - c_\downarrow^\dagger c_\downarrow\right]/\sqrt{2} \\ -c_\uparrow^\dagger c_\downarrow \end{pmatrix} . \tag{2.117}$$

Coupling $\boldsymbol{S}^{[1]} \times \boldsymbol{S}^{[1]}$ into a rotational invariant gives the total spin S^2 operator, with an additional normalization factor similar to the case in Eq. (2.115),

$$S_i^2 = -\sqrt{3}\left[\boldsymbol{S}_i^{[1]} \times \boldsymbol{S}_i^{[1]}\right]^{[0]} = \sqrt{3}\left[\boldsymbol{S}_i^{\dagger[1]} \times \boldsymbol{S}_i^{[1]}\right]^{[0]} . \tag{2.118}$$

Including the identity operator I, the set of rotational invariants $\{I, N, S^2, \eta, \eta^\dagger\}$ form a linearly independent set for *all* rotational invariants that can be constructed out of the basis states of a single site. The subset $\{I, N, S^2\}$ forms a linearly independent set of all rotational invariants acting on a single site that also preserve particle number.

2.3 Non-Abelian DMRG

This section describes the non-Abelian DMRG algorithm itself, the generalization of the $SU(2)$ case to an arbitrary compact symmetry and the relationship between the non-Abelian algorithm and previous work on rotationally invariant DMRG algorithms.

2.3.1 Construction

Now that we have seen how to manipulate irreducible tensor operators, it is straightforward to recast the DMRG algorithm into this form. Once the single site

operators have been expressed in terms of the reduced basis, the tensor product of a block operator with a single site operator becomes a projection onto an irreducible component of the tensor product coupling, given by Eq. (2.81). The construction of the superblock Hamiltonian as a block-sparse matrix described in section section 1.3.1 is essentially the same except for the $9j$ coefficient that appears as a multiplicative factor for each set of quantum numbers. Because the Hamiltonian is always a rotational invariant, by definition it transforms as the identity representation, for which the Clebsch-Gordon coefficients are trivial. The interaction terms in the Hamiltonian, Eq. (1.36) for the coupling of the left block operator $\boldsymbol{M}^{\boldsymbol{A}[k_1]}$ of rank k_1 and right block operator $\boldsymbol{M}^{\boldsymbol{B}[k_2]}$ of rank k_2[†] becomes

$$([[\boldsymbol{M}^{\boldsymbol{A}[k_1]} \times \boldsymbol{M}^{\boldsymbol{B}[k_2]}]^{[0]}]\boldsymbol{\psi}^{[j]})_{j_1' j_2'} = \sum_{j_1 j_2} \left(\boldsymbol{M}^{\boldsymbol{A}[k_1]}{}_{j_1' j_1} \boldsymbol{\psi}^{[j]}{}_{j_1 j_2} \left(\boldsymbol{M}^{\boldsymbol{B}[k_2]}{}_{j_2' j_2} \right)^\dagger \right) \begin{bmatrix} j_1 & j_2 & j \\ k_1 & k_2 & 0 \\ j_1' & j_2' & j \end{bmatrix}, \tag{2.119}$$

where the interaction is a coupling of a rank k_1 operator and a rank k_2 operator and the target state is the $D(j)$ representation of $SU(2)$. As in the original formulation of Eq. (1.36), for each set of quantum number labels (j_1', j_1, j_2', j_2), the components of the left block operator $\boldsymbol{M}^{\boldsymbol{A}[k_1]}{}_{j_1' j_1}$, right block operator $\boldsymbol{M}^{\boldsymbol{B}[k_2]}{}_{j_2' j_2}$ and wavefunction $\boldsymbol{\psi}^{[j]}{}_{j_1' j_2'}$ are in general dense matrices. Thus, the additional multiplicative factor arising from the $9j$ coefficient is of no consequence since multiplying a matrix by a constant factor is $O(n^2)$ operations, whereas the matrix-matrix multiply is $O(n^3)$ operations. In fact, the ability to scale the matrix-matrix multiply by a real number is already present in the optimized Basic Linear Algebra Subroutines (BLAS) package [88] used in the DMRG software, thus as long as the $9j$ coefficient itself can be calculated quickly, the $9j$ factor has negligible effect on the computation time of the superblock Hamiltonian matrix-vector multiply.

Once the wavefunction $\boldsymbol{\psi}^{[j]}{}_{j_1 j_2}$ has been obtained, the reduced density-matrix needs to be calculated. Clearly this must be a rotational invariant operator, transforming as the identity representation of the symmetry algebra. Since the $9j$ coefficients for the identity representation are trivial, this is essentially unchanged from the original construction, being

$$\boldsymbol{\rho}^{[0]}{}_{j_1' j_1} = \sum_{j_2} \boldsymbol{\psi}^{[j]}{}_{j_1' j_2} \left(\boldsymbol{\psi}^{[j]}{}_{j_1 j_2} \right)^\dagger. \tag{2.120}$$

The transformation of the wavefunction from one step to use as the initial vector of the next step, described for the original DMRG formulation in section 1.3.2 is

[†]For semi-simple Lie algebras, the allowable representations from the Clebsch-Gordan expansion implies $k_1 = k_2$. For finite groups, k_1 must be the inverse of k_2.

modified somewhat by the rotational invariant formulation because the procedure involves a basis transformation of the form $|\alpha_n\rangle \otimes |s_{n+1}\,\beta_{n+2}\rangle \rightarrow |\alpha_n\,s_{n+1}\rangle \otimes |\beta_{n+2}\rangle$. In terms of the quantum numbers of the states, assuming $|\alpha_n\rangle$, $|s_{n+1}\rangle$ and $|\beta_{n+2}\rangle$ having quantum number labels j_1, j_2 and j_3 respectively, the transformation is $\|j_1(j_2j_3)j_{23}; j\rangle \rightarrow \|(j_1j_2)j_{12}j_3; j\rangle$. This requires the $6j$ coefficients [84], giving

$$\begin{aligned} \|j_1(j_2j_3)j_{23}; j\rangle \;=\; & \sum_{j_{12}} \frac{(-1)^{j_1+j_2+j_3+j}}{\sqrt{(2j_{12}+1)(2j_{23}+1)}} \begin{Bmatrix} j_1 & j_2 & j \\ j_3 & j_{12} & j_{23} \end{Bmatrix} \\ & \times \;\; \|(j_1j_2)j_{12}j_3; j\rangle \,. \end{aligned} \tag{2.121}$$

It turns out that the algorithm, as presented above, is significantly less efficient when the target state transforms as any spin j greater than zero. To see why this happens, consider the structure of the superblock wavefunction in matrix form, $\psi^{[j]}{}_{j_1j_2}$. In the case of $j = 0$, the only non-zero matrix elements are for $j_1 = j_2$, which means that $\psi^{[0]}{}_{j_1j_2}$ can (after a trivial reordering of indices) be put in block-diagonal form. However, if $j > 0$, the allowed matrix elements are all j_1 and j_2 such that $|j_1 - j_2| \leq j \leq j_1 + j_2$. This means that in the $j > 0$ case the wavefunction matrix is banded, with a bandwidth of $2j+1$. This drastically increases the number of allowed non-zero elements in the wavefunction matrix, which amounts to an increase in the dimension of the superblock Hilbert space. For small j, this is an $(2j + 1)$-fold increase in the dimension of the superblock Hilbert space, which has a disastrous effect on the computation time. There is a solution to this problem, which was inspired by the solution to the corresponding problem in IRF-DMRG [52] (see section 2.3.3 below) and suggested by Nishino Tomotosi. Targeting a state of spin j is equivalent to adding a non-interacting spin of magnitude j coupled to the spin of the system and then targeting the identity $j = 0$ representation. This non-interacting spin can be inserted anywhere in the lattice; if the spin is added between the left and right blocks then the resulting construction is formally equivalent to that of targeting the spin j state directly. However, a much more efficient choice is to put the non-interacting spin at one end of the lattice. This means that at every step of the finite-size algorithm the identity $j = 0$ state can be targeted, with the corresponding improvement in the dimension of the superblock basis. With the original method of targeting the states, the performance of the non-Abelian DMRG algorithm degrades rapidly as the target spin is increased. With the non-interacting spin formulation, the performance actually improves as the target spin is increased, as would be expected by the reduced overall size of the Hilbert space for higher spin.

However, placing the non-interacting spin at one edge of the lattice necessarily breaks the reflection symmetry of the system, so it is no longer possible to use

reflection symmetry at the mid point of the lattice. In addition, it would appear to preclude an efficient non-Abelian infinite-size DMRG algorithm, as in this case the magnitude of the non-interacting spin would need to be a function of the lattice size.

Even using the finite-size algorithm, it is necessary in general to target states of non-zero spin during the build sweep. For large spin j, all of the spin states in the initial four site block will have spin greater than zero, therefore the $j = 0$ sector of the Hilbert space is empty. The solution is to gradually reduce the spin of the target state such that it starts high and becomes zero once the lattice reaches full size. That is, if the overall target state is spin j and lattice size L, then the target state j_T at lattice size l is

$$j_T = j(1 - l/L)\,, \tag{2.122}$$

rounded to the nearest permissible (integer or half-integer) value.

To summarize, the complete algorithm for the 'infinite-size' case is listed in table 2.1. The differences from the DMRG algorithm as originally published [43] are: (1) The targeting of the appropriate symmetry sector is done via a non-interacting spin of magnitude j positioned at the left end of the lattice (site 0), rather than projecting onto a z-component of spin sector of the superblock basis. (2) This algorithm does not use reflection symmetry about the midpoint of the lattice, since that symmetry is broken by the non-interacting spin. (3) The coupling law for irreducible tensor operators Eq. (2.81) is used instead of the ordinary matrix direct product. (4) The final target state must be specified at the beginning of the iterations, which makes this algorithm useless for anything other than constructing the initial blocks for the 'finite-size' algorithm.

In this algorithm, the left block consisting of sites 0 (the non-interacting spin), $1, 2, \ldots, n$ is denoted A_n and the right block consisting of sites $n, n+1, \ldots, L$ is denoted B_n. The notation for the truncation operators is the same as in section 1.3.2; ${}^{L}T^{n}$ denotes the truncation operator acting on left sites $0, 1, \ldots, n$ and ${}^{R}T^{n}$ denotes the truncation operator acting on right sites $n, n+1, \ldots, L$.

Table 2.2 describes the 'finite-size' algorithm for non-Abelian symmetries. This algorithm only describes a right-moving sweep; the left-moving sweep is the exact mirror image of this algorithm.

Table 2.1: 'Infinite-size' algorithm with $SU(2)$ symmetry, for target system size of L sites and total spin j.

1. *Setup:* Construct the reduced basis and matrix elements for each site in the lattice using the Wigner-Eckart theorem Eq. (2.72).
2. Make a single block consisting of a one-dimensional basis of a single spin j.
3. Make the initial blocks. The initial left block A_1 consists of two sites, the non-interacting spin and the first actual lattice site, coupled via Eq. (2.81). The initial right block B_L consists of a single site. Initially the system size is $l = 2$, not counting the non-interacting spin.
4. *Start of iterations:* Add one site to each block, using the coupling rule Eq. (2.81). This adds two sites to the complete system, $l \to l + 2$.
5. Form the superblock Hamiltonian matrix (in block-sparse form) again using the coupling Eq. (2.81) in the subspace of spin $(1 - l/L)$, rounded to the nearest permissible half-integer.
6. Diagonalize the Hamiltonian to find one (or more) of the low energy eigenvectors.
7. Form the reduced density-matrix for the left and right blocks separately, using Eq. (2.120).
8. Diagonalize each density-matrix to find the eigenvalues and eigenvectors. Discard all but the largest m eigenvalues and associated eigenvectors of each density-matrix and construct left and right truncation operators to change basis to the kept density-matrix eigenstates. This gives the truncation operators ${}^{L}T^{l/2}$ and ${}^{R}T^{L-l/2+1}$.
9. (Optional) Diagonalize the Hamiltonian for the left and right blocks in the truncated basis and use the resulting eigenstates as the new basis rather than the reduced density-matrix eigenstates (*cf.* section 1.3.4).
10. Apply the left and right truncation operators to each operator that will be needed to construct the superblock Hamiltonian for $l + 2$ sites. This gives the truncated blocks $A_{l/2}$ and $B_{L-l/2+1}$.
11. Store the left and right block operators and truncation operators for later use in the 'finite-size' sweeping.
12. *Repeat:* Go to step 4, until the current lattice size l is equal to the desired length L.

Table 2.2: 'Finite-size' algorithm with $SU(2)$ symmetry, for L sites and target state j.

1. *Setup:* Use the 'infinite-size' algorithm to obtain left and right blocks up to sizes $L/2$. Let $n = L/2$ be the number of sites in the left block (not counting the non-interacting spin site).
2. *Start of iterations:* Add one site to the left block using the coupling rule Eq. (2.81), to form $A_n \otimes s_{n+1}$.
3. Retrieve the right block B_{n+3} stored previously and add a site to it to form the block $s_{n+2} \otimes B_{n+3}$.
4. Transform the wavefunction from the $A_{n-1} \otimes s_n \otimes s_{n+1} \otimes B_{n+2}$ basis to the $A_n \otimes s_{n+1} \otimes s_{n+2} \otimes B_{n+3}$ basis, using section 1.3.2 and Eq. (2.121). This requires the truncation operator ${}^{R}T_{n+2}$ stored previously.
5. Form the superblock Hamiltonian matrix (in block-sparse form) using the coupling Eq. (2.81) in the subspace of spin zero (the identity representation of the symmetry algebra).
6. Diagonalize the Hamiltonian to find one (or more) of the low energy eigenvectors.
7. Form the reduced density-matrix for the left block only.
8. Diagonalize the left density-matrix. Discard all but the largest m eigenvalues and associated eigenvectors and construct the left truncation operator ${}^{L}T_{n+1}$ to change basis to the kept density-matrix eigenstates.
9. (Optional) Diagonalize the left block Hamiltonian in the truncated basis and use the resulting eigenstates as the new basis, rather than the reduced density-matrix eigenstates.
10. Apply the left truncation operator to form the truncated block A_{n+1}.
11. Store the left block and truncation operator for later use.
12. *Repeat:* Increment $n \to n+1$ and go to step 2 until $n = L-2$.

2.3.2 General formulation

We have seen how to construct the DMRG algorithm for $SU(2)$ symmetry. However as shown in section 2.1, the Clebsch-Gordan coefficients and hence the Wigner-Eckart theorem and associated coupling laws, apply to arbitrary finite groups and compact Lie groups. In fact, the Wigner-Eckart theorem can be proven for more general conditions [89] and the analogous coupling laws can be formulated for *e.g.* quantum groups and supersymmetry. For example, $SO(4)$ symmetry is particularly easy, because $SO(4)$ is locally isomorphic to $SU(2) \times SU(2)$. Thus, every representation of $SO(4)$ can be labeled by two half-integer quantum numbers, written as $D(i,j) \equiv D(i) \times D(j)$, where $D(i)$ and $D(j)$ are irreducible representations of $SU(2)$. This means that the $6j$ and $9j$ coupling coefficients used in Eq. (2.81) and Eq. (2.121) are simply the product of two $SU(2)$ coefficients,

$$\left\{ \begin{array}{ccc} (a_1,a_2) & (b_1,b_2) & (c_1,c_2) \\ (d_1,d_2) & (e_1,e_2) & (f_1,f_2) \end{array} \right\}_{SO(4)} \equiv \left\{ \begin{array}{ccc} a_1 & b_1 & c_1 \\ d_1 & e_1 & f_1 \end{array} \right\}_{SU(2)} \times \left\{ \begin{array}{ccc} a_2 & b_2 & c_2 \\ d_2 & e_2 & f_2 \end{array} \right\}_{SU(2)}, \tag{2.123}$$

and

$$\left[\begin{array}{ccc} (a_1,a_2) & (b_1,b_2) & (c_1,c_2) \\ (d_1,d_2) & (e_1,e_2) & (f_1,f_2) \\ (g_1,g_2) & (h_1,h_2) & (i_1,i_2) \end{array} \right]_{SO(4)} \equiv \left[\begin{array}{ccc} a_1 & b_1 & c_1 \\ d_1 & e_1 & f_1 \\ g_1 & h_1 & i_1 \end{array} \right]_{SU(2)} \times \left[\begin{array}{ccc} a_2 & b_2 & c_2 \\ d_2 & e_2 & f_2 \\ g_2 & h_2 & i_2 \end{array} \right]_{SU(2)}. \tag{2.124}$$

This formulation encompasses *all* symmetries that can be used in DMRG, including the Abelian symmetries used in the original formulation. For an Abelian symmetry, the $6j$ and $9j$ coefficients are simple enough that they are rarely written explicitly. For example, the $9j$ coefficients of a $U(1)$ symmetry of, *e.g.* particle-number, are

$$\left[\begin{array}{ccc} n_1 & n_2 & n \\ N_1 & N_2 & N \\ n_1' & n_2' & n' \end{array} \right]_{U(1)} = \delta_{n_1',N_1+n_1} \delta_{n_2',N_2+n_2} \delta_{n',n+N} \delta_{n,n_1+n_2} \delta_{N,N_1+N_2} \delta_{n',n_1'+n_2'}. \tag{2.125}$$

If this set of $9j$ coefficients is used in Eq. (2.81), the coupling reduces to the ordinary matrix direct product and the original formulation of DMRG is recovered exactly.

2.3.3 Relationship to previous work

There have been previous attempts to explicitly include $SU(2)$ rotational invariance into the DMRG algorithm. The most successful previous algorithm is the interaction-round-a-face DMRG (IRF-DMRG) algorithm introduced by Sierra and Nishino [52]. In this method, the vertex Hamiltonian is first transformed into an IRF model [67] and then a variant of DMRG is applied to the IRF Hamiltonian. The IRF model can be chosen such that it explicitly factors out the symmetry group. The resulting Hamiltonian matrix elements are, in principle, identical to those given by the non-Abelian formulation. Using the IRF-DMRG algorithm, Sierra and Nishino studied the spin 1 Heisenberg chain using $SU(2)$ symmetry and and the XXZ chain using quantum group $SU_q(2)$ symmetry [52]. Later, the IRF-DMRG was applied to the spin 1 and spin 2 Heisenberg chains by Tatsuaki [90]. However, the IRF-DMRG algorithm is complicated by the necessity to calculate the Boltzmann weights for each interaction term in the Hamiltonian. Without a special effort to factorize the coupling coefficients, the number of non-trivial IRF weights increases rather quickly as the magnitude of the spins in the system is increased and for a larger symmetry group. Thus, as far as we know, the IRF-DMRG has not been applied to any more complex models, such as the fermionic models treated in this thesis.

Sakamoto and Kubo [7] describe a different method of constructing eigenstates of $SU(2)$. This algorithm requires estimating the total spin of the ground state, calculating the wavefunction for every possible z-component of spin and then constructing the $SU(2)$ invariant density-matrix,

$$\rho_{i'i} = \frac{1}{2j+1} \sum_{m=-j}^{j} \psi_{i'j}(m)\psi^*_{ij}(m)\,, \tag{2.126}$$

where $\psi_{ij}(m)$ is the ground state wavefunction with z-component of total spin m. The description given by Sakamoto and Kubo [7] is not clear on how $\psi_{ij}(m)$ is actually obtained for each value of m. In principle, given $\psi_{ij}(m)$ for a single value of m, all other components can be calculated by successive applications of the S^+ and S^- operators. This is a trivial calculation for eigenstates of total spin. However, in that case it is not necessary to perform the summation in Eq. (2.126), as the density-matrix will contain the same elements independent of m. There is also no mention of projecting the superblock Hilbert space onto a given total spin sector, in fact the description of the algorithm explicitly states that the total spin is determined *after* obtaining the wavefunction, implying that the diagonalization is performed in a state of fixed z-component of spin only. So it is not clear what the advantage of this algorithm is, or the magnitude of the efficiency gain, if any.

2.4 The Hubbard Model

The Hubbard model [91,92] was introduced as an attempt to describe d-electron correlations in transition metals and has since seen many different applications, for example it has been suggested as a realistic (albeit simplified) model of the Cu-O planes in high T_c superconductors [23] (*cf.* chapter 4). The Hamiltonian is

$$H = \sum_{i,j,\sigma} t_{ij} c^\dagger_{i,\sigma} c_{j,\sigma} + U \sum_i \left[\left(n_{i,\uparrow} - \frac{1}{2} \right) \left(n_{i,\downarrow} - \frac{1}{2} \right) + \frac{1}{4} \right] , \tag{2.127}$$

which consists of two contributions, a hopping integral t_{ij} which is usually taken to be translationally invariant and acting between nearest-neighbors only, *i.e.* $t_{ij} = -t$ for i, j nearest-neighbors and zero otherwise and an on-site term of strength U, representing the effective screened Coulomb interaction. The important component of this interaction term is $U n_{i,\uparrow} n_{i,\downarrow}$, which gives an energy penalty (in the $U > 0$ case) for each double-occupied site. The other components appearing in the interaction are irrelevant in the current case, being a constant (depending on the number of lattice sites) and a term proportional to the total number of electrons (*i.e.* a chemical potential). Since the number of electrons commutes with H, this is a good quantum number in the DMRG calculations thus it is not necessary to explicitly add a chemical potential; the number operator can simply be replaced by its eigenvalue resulting in a trivial energy shift. The reason for writing the interaction in this form (rather than simply $U \sum_i n_{i,\uparrow} n_{i,\downarrow}$) will become clear in section 2.5.

The Hubbard model has been shown to be integrable in one dimension [93] which makes the model useful for testing the efficiency and accuracy of numerical algorithms, although the numerical solution is useful in its own right for the calculation of quantities which are not so easy to determine from the exact solution.

The $SU(2)$-invariant matrix representation of the fermionic algebra was determined in section 2.2.4. All that remains is to construct the interaction term and the $SU(2)$-invariant form of the Hamiltonian Eq. (2.127). In the full single site basis of Eq. (2.106), the operator $(n_{i,\uparrow} - \frac{1}{2})(n_{i,\downarrow} - \frac{1}{2}) + \frac{1}{4}$ has the matrix elements

$$\left(n_{i,\uparrow} - \frac{1}{2} \right) \left(n_{i,\downarrow} - \frac{1}{2} \right) + \frac{1}{4} = \frac{1}{2} \begin{pmatrix} 1 & 0 & 0 & 0 \\ 0 & 0 & 0 & 0 \\ 0 & 0 & 0 & 0 \\ 0 & 0 & 0 & 1 \end{pmatrix} . \tag{2.128}$$

The application of the Wigner-Eckart theorem Eq. (2.70) gives the reduced matrix

elements in the basis of Eq. (2.108),

$$\left[\left(n_{i,\uparrow}-\frac{1}{2}\right)\left(n_{i,\downarrow}-\frac{1}{2}\right)+\frac{1}{2}\right]^{[0]}=\frac{1}{2}\begin{pmatrix}1&0&0\\0&0&0\\0&0&1\end{pmatrix}. \tag{2.129}$$

Putting all of this together, the $SU(2)$-invariant Hamiltonian reads

$$\begin{aligned}H &= -\sqrt{2}t\sum_{<i,j>}\left(\left[\boldsymbol{c}_{1/2}^{\dagger[i]}\times\boldsymbol{c}_{1/2}^{[j]}\right]^{[0]}+\text{h.c.}\right)\\ &\quad +U\sum_i\left[\left(n_{i,\uparrow}-\frac{1}{2}\right)\left(n_{i,\downarrow}-\frac{1}{4}\right)+\frac{1}{4}\right]^{[0]}.\end{aligned} \tag{2.130}$$

Conventional DMRG studies of a system such as the Hubbard model use the $U(1)\times U(1)$ basis of number of particles N and z-component of total spin s^z. The $SU(2)$-invariant DMRG algorithm allows the z-component of the total spin to be replaced by the total spin s itself, giving a much larger symmetry group, $U(1)\times SU(2)$. Table 2.3 compares the accuracy and efficiency of the DMRG calculation when these two basis sets are used, for the Hubbard model at half-filling, for a 60 site lattice with $t=U=1$. This data was calculated on a desktop machine with an Athlon 500MHz processor. For the case of half-filling, the degree of the representation of the block basis is equal to the number of states that would need to be kept in the $U(1)\times U(1)$ basis to achieve the same accuracy. Each basis state of total spin j in the $U(1)\times SU(2)$ basis corresponds to $2j+1$ basis states of the $U(1)\times U(1)$ basis. This appears as the well-known $(2j+1)$-fold degeneracy in the density-matrix eigenvalues [43] of the original DMRG algorithm.

Table 2.3 shows that the use of the $SU(2)$-invariant algorithm results in almost two orders of magnitude improvement in the fractional error in the energy and in the cumulative truncation error. There is an increase in the CPU time per sweep, however most of the variance in CPU time is due to different numbers of matrix-vector multiplies being performed by the eigensolver. The CPU time for each matrix-vector multiply is nearly identical irrespective of the choice of symmetry group.

Table 2.4 shows the accuracy and efficiency of the $U(1)\times U(1)$ and $U(1)\times SU(2)$ algorithms when targeting a state of higher spin, in this case $s=5$ (or $s^z=5$, in the case of the $U(1)\times U(1)$ algorithm). The data for the $U(1)\times SU(2)$ basis was obtained by targeting the spin 5 state directly, *without* using the non-interacting spin. Thus, while there is a small accuracy improvement, the CPU time per sweep is much larger, because the dimension of the superblock Hilbert space is significantly bigger for the same number of block states. The loss of efficiency is corrected

Table 2.3: Comparison of $U(1) \times U(1)$ and $U(1) \times SU(2)$ basis for the ground state of the half-filled Hubbard model for a 60 site lattice, at $t = U = 1$. Columns are the basis used, number of states kept m, degree of the group representation d, energy E, fractional error in the energy, cumulative truncation error over the sweep $1 - \sigma$, CPU time in seconds per sweep.

basis	m	d	E	$(E - E_g)/\lvert E_g \rvert$	$1 - \sigma$	CPU
$U(1) \times U(1)$	100	200	−61.7484986435	5.2×10^{-5}	5.3×10^{-4}	10
$U(1) \times U(1)$	200	200	−61.7514641444	4.5×10^{-6}	4.8×10^{-5}	41
$U(1) \times U(1)$	300	300	−61.7516910404	7.9×10^{-7}	8.8×10^{-6}	110
$U(1) \times SU(2)$	100	226	−61.7515581914	2.9×10^{-6}	3.1×10^{-5}	15
$U(1) \times SU(2)$	200	468	−61.7517319907	1.3×10^{-7}	1.4×10^{-6}	64
$U(1) \times SU(2)$	300	716	−61.7517389831	1.4×10^{-8}	1.5×10^{-7}	158

by using a non-interacting spin to force the target state into the singlet sector as described previously. The resulting algorithm produces the data shown in table 2.5. The difference in energy between the two forms of targeting the state using the $U(1) \times SU(2)$ basis is extremely small, which indicates that the additional superblock states that occur in the direct targeting method have negligible effect on the variational energy, while substantially reducing the computational efficiency.

For the higher spin states of Hubbard model, the accuracy improvement arising from the $SU(2)$-invariant algorithm is rather small. The improvement is much more significant in the vicinity of a ferromagnetic phase transition, where many states of different total spin are numerically near-degenerate and the ability to target directly a single sector of total spin substantially reduces the density of low-lying eigenstates of the superblock Hamiltonian. This is apparent in the Kondo lattice calculations in chapter 3.

Table 2.4: Comparison of the $U(1) \times U(1)$ and $U(1) \times SU(2)$ basis for the lowest spin 5 excited state for the half-filled Hubbard model on a 60 site lattice with $t = U = 1$. The $U(1) \times SU(2)$ were obtained by directly targeting the spin 5 state (no non-interacting spin).

basis	m	E	$(E - E_g)/\|E_g\|$	$1 - \sigma$	CPU
$U(1) \times U(1)$	100	-59.5701792131	4.0×10^{-5}	3.9×10^{-4}	11
$U(1) \times U(1)$	200	-59.5723270633	3.6×10^{-6}	3.8×10^{-6}	41
$U(1) \times U(1)$	300	-59.5725015232	6.3×10^{-7}	6.8×10^{-5}	102
$U(1) \times SU(2)$	100	-59.5702795890	3.8×10^{-5}	3.9×10^{-4}	26
$U(1) \times SU(2)$	200	-59.5723402180	3.3×10^{-6}	3.7×10^{-5}	90
$U(1) \times SU(2)$	300	-59.5725035338	5.9×10^{-7}	6.8×10^{-6}	207

Table 2.5: Energy and CPU time using the $U(1) \times SU(2)$ basis for the lowest spin 5 excited state for the half-filled Hubbard model on a 60 site lattice with $t = U = 1$, using a non-interacting spin to target the appropriate symmetry sector.

basis	m	E	$(E - E_g)/\|E_g\|$	$1 - \sigma$	CPU
$U(1) \times SU(2)$	100	-59.5702385716	3.9×10^{-5}	3.8×10^{-4}	14
$U(1) \times SU(2)$	200	-59.5723344203	3.4×10^{-6}	3.6×10^{-6}	47
$U(1) \times SU(2)$	300	-59.5725027479	6.1×10^{-7}	6.7×10^{-6}	113

2.5 SO(4) Example

In 1990, C. N. Yang and S. C. Zhang [94] showed that the Hubbard model contains an additional symmetry group, known as *pseudospin*. To obtain this symmetry, one notices that the Hamiltonian Eq. (2.127) is invariant under a particle-hole transformation of the *e.g.* down spins only,

$$\begin{aligned} c_{i,\downarrow}^\dagger &\to \bar{c}_{i,\downarrow}^\dagger = (-1)^i c_{i,\downarrow}, \\ c_{i,\downarrow} &\to \bar{c}_{i,\downarrow} = (-1)^i c_{i,\downarrow}^\dagger. \end{aligned} \tag{2.131}$$

The staggered phase ensures that the hopping term connecting nearest-neighbor sites is preserved. More generally, the hopping term remains invariant if and only if the lattice is *bipartite*, with hopping only from one partition of lattice sites to the other partition.

Since the Hamiltonian is invariant under the transformation Eq. (2.131), for any operator X that commutes with H, the image under the transformation, $\bar{X}$, must also commute with H. In particular, this applies to the operators S^+, S^- and S^z. This is useful because the image of these operators under the transformation Eq. (2.131) results in a new set of operators generating an additional $SU(2)$ symmetry,

$$\begin{aligned} Q_i^+ &= \bar{S}^+ = (-1)^i c_{i,\uparrow}^\dagger c_{i,\downarrow}^\dagger, \\ Q_i^- &= \bar{S}^- = (-1)^i c_{i,\downarrow} c_{i,\uparrow}, \\ Q_i^z &= \bar{S}^z = \tfrac{1}{2}(n_{i,\uparrow} + n_{i,\downarrow} - 1). \end{aligned} \tag{2.132}$$

The *pseudospin* operators[†] Q^+, Q^-, Q^z all mutually commute with S^+, S^- and S^z, which means that the 6 quantities generate the algebra $SU(2) \times SU(2)$, which is locally isomorphic to $SO(4)$. The pseudospin symmetry is a generalization of the $U(1)$ particle number symmetry. Indeed, the z-component of pseudospin is related to the particle number N by

$$N = L + 2Q^z. \tag{2.133}$$

Particle-hole symmetry corresponds to pseudospin reflection $Q^z \to -Q^z$. The pseudospin operators are closely related to the η-pairing operators defined in section 2.2.4 and are important in superconductivity [87, 95, 96].

On a single site of the Hubbard model, pseudospin symmetry places the empty- and double-occupied states into a multiplet of degree 2, with pseudospin 1/2 and spin zero. The singly-occupied states in the spin 1/2 multiplet have zero pseudospin and are essentially unchanged from the $U(1) \times SU(2)$ case. These two multiplets

[†]In the literature, it is common to denote the pseudospin vector by I^+, I^- and I^z. However, to avoid confusion with the identity operator I, the pseudospin vector is denoted Q^+, Q^-, Q^z in this thesis.

have the quantum numbers of the *holon* and *spinon* respectively [97]. Thus the pseudospin gives a particularly useful construction for demonstrating spin-charge separation of the one-dimensional model.

The additional $SU(2)$ symmetry label means that there are now two spin indices on every operator and basis state, which we write as $[q, s]$ for pseudospin q and spin s. This places the $\boldsymbol{c}^{[i]}_{1/2}$ and $\boldsymbol{c}^{\dagger[i]}_{1/2}$ into a single operator with two spinor indices[†], $\boldsymbol{c}^{[1/2,1/2]}_i$, transforming as the $D(1/2,1/2)$ representation of $SO(4)$.

Choosing an ordering of reduced basis states ($\|0,1/2\rangle$, $\|1/2,0\rangle$) (respectively the spinon and holon), a concrete matrix representation of $\boldsymbol{c}^{[1/2,1/2]}_i$ can be obtained,

$$\boldsymbol{c}^{[1/2,1/2]}_i = \begin{cases} \begin{pmatrix} 0 & \sqrt{2} \\ \sqrt{2} & 0 \end{pmatrix}, & \text{if } i \text{ even;} \\ \begin{pmatrix} 0 & -\sqrt{2} \\ \sqrt{2} & 0 \end{pmatrix}, & \text{if } i \text{ odd.} \end{cases} \tag{2.134}$$

This operator is skew-Hermitian. It is important to note that the generators of pseudospin $SU(2)$ Eq. (2.132) do *not* commute with the spatial reflection operator R. This is because spatial reflection flips sites from the even sublattice onto the odd sublattice and *vice versa* . Spatial reflection is only possible with the simultaneous exchange of odd and even sublattices. Applying separately either spatial reflection or exchange of sublattice, violates pseudospin symmetry. For example, suppose that there existed a unitary transformation R that transforms as a rotational invariant with respect to $SO(4)$ and has the effect of flipping the sublattice at some arbitrary site i. Such an operator would have the effect of interchanging the sign of the creation/annihilation operator Eq. (2.134), giving

$$R \begin{pmatrix} 0 & \sqrt{2} \\ \sqrt{2} & 0 \end{pmatrix} R^{-1} = \begin{pmatrix} 0 & -\sqrt{2} \\ \sqrt{2} & 0 \end{pmatrix} . \tag{2.135}$$

It is easy to see that there is no such operator.

The coupling $\boldsymbol{C}^{[1/2,1/2]}_i \times \boldsymbol{C}^{[1/2,1/2]}_i$ has three irreducible representations, $[0,0]$, $[0,1]$ and $[1,0]$. These are

$$\begin{aligned} [\boldsymbol{c}^{[1/2,1/2]}_i \times \boldsymbol{c}^{[1/2,1/2]}_i]^{[0,0]} &= -1 , \\ [\boldsymbol{c}^{[1/2,1/2]}_i \times \boldsymbol{c}^{[1/2,1/2]}_i]^{[0,1]} &= -\boldsymbol{S}^{[0,1]}_i , \\ [\boldsymbol{c}^{[1/2,1/2]}_i \times \boldsymbol{c}^{[1/2,1/2]}_i]^{[1,0]} &= -\boldsymbol{Q}^{[1,0]}_i . \end{aligned} \tag{2.136}$$

[†]Despite the superficial similarity, this has very little in common with a Dirac bispinor. Although the degree of the representation is the same, bipinors transform as the $D(1/2,0)\oplus D(0,1/2)$ representation.

Table 2.6: Energy and CPU time for the $SO(4)$ basis for the ground state of the half-filled Hubbard model for a 60 site lattice, at $t = U = 1$. *cf.* table 2.3.

basis	m	d	E	$(E - E_g)/\lvert E_g \rvert$	$1 - \sigma$	CPU
$SO(4)$	100	526	−61.7517351742	7.6×10^{-8}	8.4×10^{-7}	18
$SO(4)$	200	1136	−61.7517397636	1.4×10^{-9}	1.5×10^{-8}	71
$SO(4)$	300	1766	−61.7517398448	9.9×10^{-11}	1.0×10^{-9}	133

The last two projections are respectively the spin and pseudospin operators at site i. In the $SO(4)$ reduced basis, the Hubbard interaction term in 2.127 becomes proportional to the number of holons and is given by

$$U\sum_i \left[\left(n_{i,\uparrow} - \frac{1}{2}\right)\left(n_{i,\downarrow} - \frac{1}{4}\right) + \frac{1}{4}\right]^{[0,0]} = \frac{U}{2}\sum_i n_i^h\,, \tag{2.137}$$

where the number of holons at site i, n_i^h, is a rotational-invariant operator given by

$$n_i^h = \begin{pmatrix} 0 & 0 \\ 0 & 1 \end{pmatrix}\,. \tag{2.138}$$

The number of spinons, n_i^s, has a similar form,

$$n_i^s = \begin{pmatrix} 1 & 0 \\ 0 & 0 \end{pmatrix}\,, \tag{2.139}$$

and these two operators satisfy the identity

$$n_i^h + n_i^s = 1\,. \tag{2.140}$$

Thus the Coulomb interaction can be written using many different combinations of the n^h and n^s operators.

Using pseudospin $SO(4)$ symmetry gives an additional accuracy improvement over the $U(1) \times SU(2)$ basis. This is shown in table 2.6, for the half-filled Hubbard model with the same parameters as table 2.3. The use of non-Abelian symmetries gives an improvement of three orders of magnitude in the fractional error in the energy and the cumulative truncation error with 100 states kept, extending to almost four orders of magnitude for 300 states kept.

The results for the spin 5 excited state with the $SO(4)$ algorithm appear in table 2.7. Again there is a significant accuracy improvement compared with the $U(1) \times SU(2)$ algorithm shown in table 2.5.

Table 2.7: Energy and CPU time for the $SO(4)$ basis for the lowest spin 5 excited state for the half-filled Hubbard model on a 60 site lattice with $t = U = 1$. *cf.* table 2.5.

basis	m	E	$(E - E_g)/\|E_g\|$	$1 - \sigma$	CPU
$SO(4)$	100	-59.5723497975	3.2×10^{-6}	3.4×10^{-5}	16
$SO(4)$	200	-59.5725312667	1.3×10^{-7}	1.4×10^{-6}	64
$SO(4)$	300	-59.5725381253	1.4×10^{-8}	2.2×10^{-7}	148

In the large-U limit of the Hubbard model, the energy penalty for each holon in the system implies that the number of holons is minimized, *i.e.* given a band filling specified by q^z, the total pseudospin will be $q = |q^z|$. Thus in this case it is sufficient to label the states by q^z alone, so that the $SU(2)$ pseudospin reduces to $U(1)$. The basis states can be labeled by the number of holons, $n^h = 2|q^z|$ and the total spin s. The reduced basis consists of two states $\|1,0\rangle$ transforming as the one-dimensional $D(1,0)$ representation and $\|0,1/2\rangle$ transforming as the two-dimensional $D(0,1/2)$ representation of $U(1) \times SU(2)$. The total degree of the single site basis has been reduced from four states to three, as the pseudospin up and down states, corresponding to double-occupied and empty sites respectively, become formally equivalent. The physical choice for positive $U \to \infty$ is to take the $\|1,0\rangle$ state to represent the empty site, eliminating all double-occupied sites from the model.

An equivalent choice of basis is to take the $U(1)$ quantum number to be the number of spinons, rather than the number of holons. This is equivalent because of the identity $n_i^h + n_i^s = 1$, shown previously. With this choice, the two reduced single site basis elements are notated $\|0,0\rangle$ and $\|1,1/2\rangle$.

2.6 Spatial Symmetries

Previous momentum-space calculations using DMRG [13,14] have utilized translation symmetry of the lattice, generated by the translation operator T, so that the basis states transform as irreducible representations of C_L, the cyclic group of order L. This group is Abelian, so the formulation of the DMRG algorithm is essentially the same as the real-space case, except that for the models under consideration (as far as we know, all studies of the DMRG in momentum space have consid-

ered the Hubbard model), the momentum-space Hamiltonian contains many more terms. The lattice sites of the momentum-space formulation can be labeled by the momentum, $k = 2\pi h/L$, for h an integer with $0 \leq h < L$.

The full symmetry group of a lattice is generally bigger than just C_L, even in the one-dimensional case. The addition of spatial-reflection (parity) P extends the symmetry group, since there are now two generators P and T, with

$$\begin{aligned} T^L &= 1\,, \\ P^2 &= 1\,, \\ PTP &= T^{-1}\,. \end{aligned} \tag{2.141}$$

This is the dihedral group D_L, of order $2L$ and the relation $PTP = T^{-1}$ implies that it is non-Abelian. The properties of this group are discussed in practically any book on group theory (*e.g.* [77, 78, 80]). The set of $2L$ elements in the group is $\{T, T^2, \ldots, T^L = 1, PT, PT^2, \ldots, PT^L = P\}$. The irreducible representations are slightly different when L is even versus L odd; here we consider only the case of L even. There are four irreducible representations of degree 1, obtained by setting T and P to be ± 1 in all possible ways. This corresponds to the states of total momentum $k = 0, \pi$, with parity $p = \pm 1$. All other representations are degree two. Let $k = 2\pi h/L$, for h an arbitrary integer. A representation of D_L is given by

$$\begin{aligned} \Gamma^k(T^n) &= \begin{pmatrix} \cos kn & \sin kn \\ -\sin kn & \cos kn \end{pmatrix}\,, \\ \Gamma^k(P) &= \begin{pmatrix} 1 & 0 \\ 0 & -1 \end{pmatrix}\,. \end{aligned} \tag{2.142}$$

It is easy to verify by direct calculation, that this is indeed a representation for all integers h. It depends only on the momentum k modulo 2π, moreover Γ^k and Γ^{-k} are isomorphic, hence we may assume that $0 \leq k \leq \pi$ (equivalent to $0 \leq h \leq L/2$). The extreme cases $k = 0$ and $k = \pi$ are *reducible* and are equivalent to the direct sum of the parity ± 1 representations described previously. On the other hand, for $0 < k < \pi$, it is easy to show that the representation Γ^k is *irreducible*. Thus, the representations found so far are the four representations of degree 1, labeled by (k, p) with $k = 0, \pi$, $p = \pm 1$ and $L/2 - 1$ representations of degree 2, labeled by (k), with $k = 2\pi h/L$ for h an integer, $0 < h < L/2$. The sum of the squares of their degrees is $4 \times 1 + (L/2 - 1) \times 4 = 2L$, which is the order of the group. Thus we have found *all* of the irreducible representations.

Note that the number of irreducible representations and hence the number of distinct sites of the momentum-space lattice, has been reduced from L to $L/2 + 2$. This reduction in the number of lattice sites arises from the symmetry group being

non-Abelian and it reflects the two-fold degeneracy of states with momentum k and $-k$, when $k \neq 0, \pi$. The two-fold degeneracy does not occur when $k = 0$ or $k = \pi$ and instead the parity becomes a good quantum number, with $p = \pm 1$. Thus, non-Abelian lattice symmetries have a rather different effect to the continuous spin and pseudospin $SU(2)$ symmetries considered previously. The reduction in the number of lattice sites by a factor of ~ 2, coupled with the reduction in the dimension of the Hilbert space due to momentum and parity conservation, is undoubtedly beneficial to the accuracy of the algorithm. However, placing momenta k and $-k$ into the same multiplet has the effect doubling the degree of the representation of the single-site basis. This serves to *increase* the dimension of the superblock Hamiltonian, acting against the reduction in dimension due to momentum and parity conservation. It is not yet clear how this trade-off will affect the efficiency of the DMRG algorithm. It would seem however that, as the size of the lattice symmetry group is increased, the degree of the single-site basis increases rapidly. For example, for a two-dimensional square lattice with periodic boundary conditions in both directions, the symmetry group is rather large, with four generators $\{T_x, T_y, P_x, R_{xy}\}$, corresponding to translation in the x and y direction, spatial reflection in the x direction and rotation 90 degrees about the z-axis (spatial reflection in the y direction is equivalent to the combination $R_{xy} P_x R_{xy}^{-1}$). The lowest symmetry point has degree 8, which implies that for a DMRG calculation using this symmetry group, at the low symmetry points a single site in the DMRG lattice would represent 8 different momenta, as now points $\{(k_x, k_y), (k_x, -k_y), (-k_x, k_y), (-k_x, -k_y), (k_y, k_x), (k_y, -k_x), (-k_x, k_y), (-k_x, -k_y)\}$ are all included in the same multiplet. Thus, the degree of the site basis would be very large, *i.e.* even in the simplest case of only two basis states per momenta, the single site basis would have, for some lattice sites, degree $2^8 = 256$. Because many of the basis states have degree $d > 1$ the actual number of states will be much less than the total degree, but only by a factor of the order of order d, which still implies that the number of basis states increases exponentially as additional non-Abelian lattice symmetries are included in the calculation. The trade-off between increasing the number of good quantum numbers versus increasing the dimension of the single-site basis needs to be fully investigated before large-scale calculations using non-Abelian lattice symmetries are attempted.

Chapter 3

The Kondo Lattice Model

The Kondo lattice model is one of the canonical models used to study impurity effects in strongly correlated electron systems and has been the subject of intense study for many years. The Kondo lattice model describes the interaction between a band of conduction electrons (c-electrons) and a lattice of localized magnetic moments, *e.g.* f-electrons. In this chapter, the the ground state phases of the one-dimensional Kondo lattice are presented, focusing on the antiferromagnetic coupling regime $J/t > 0$, starting with previously known results and then the numerical DMRG results which show the existence of a previously unrecognized ferromagnetic region at intermediate coupling. In the final section, this new phase is shown to also exist in the periodic Anderson model.

3.1 Introduction

The Kondo lattice model is a special case of a general two-band electron system with inter-band interactions. Like the Hubbard model, the Kondo lattice contains pseudospin symmetry, so this discussion of the properties of the Kondo lattice is carried out from this point of view. The assumptions from which the Kondo lattice model can be derived are: (i) There is at most one localized f-electron at each lattice site. In the pure Kondo lattice, there is always one f-electron at each site, but in general it may be a fraction of the sites, to model dilute Kondo impurities. The original version of the Kondo model had only a single f-electron (now known as the single-impurity Kondo model) and was the subject of the famous work by Wilson using the numerical renormalization group [30]. (ii) The only interactions are between the f- and c-electrons on each site. There are no inter-site interactions. The motivation for this assumption is mostly to simplify the model, without losing essential physics. In any real system, there will be dipolar and exchange interactions between the localized electrons, however given that there is only one localized

electron per site, such interactions are necessarily between nearest neighbor sites or even longer range. Thus these interactions are expected to be much smaller than the intra-site interaction between the f- and c-electrons. By a similar argument, all inter-site $c-c$ and $c-f$ interactions are also neglected. In some parameter regimes these interactions are likely to be important, for example in the heavy fermion alloys (*cf.* section 3.2.2).

Given that each $f-$band site contains only a single spin with zero pseudospin, there is only *one* choice of non-trivial interaction between the $c-$ and $f-$electrons that does not break $SO(4)$ symmetry, namely a spin-spin interaction, giving the Hamiltonian

$$H = -t\sum_{i,\sigma}^{L-1}(c^\dagger_{i,\sigma}c_{i+1,\sigma} + \text{h.c.}) + J\sum_{i=1}^{L} \boldsymbol{S}^c_i \cdot \boldsymbol{S}^f_i \ , \tag{3.1}$$

where $t > 0$ is the usual kinetic parameter and $\boldsymbol{S}^c_i$, $\boldsymbol{S}^f_i$ are the spin operators at site i for the c- and f-electrons respectively. A single site of the Kondo lattice is thus the tensor product of a Hubbard-type site and a spin, giving an 8 dimensional representation transforming under $SO(4)$ rotations as $D(0,0) \oplus D(0,1) \oplus D(1/2,1/2)$. The complete set of states is given in table 3.1. The interaction is diagonal in this basis, as the site reduced basis states are also eigenstates of $\boldsymbol{S}^c \cdot \boldsymbol{S}^f$. Thus the energy of each basis state is also listed. In this chapter, except when explicitly stated otherwise, hopping $t = 1$ is assumed.

The Kondo lattice model can be derived as a limiting case of the more general periodic Anderson model (also known as the Anderson lattice model), for which the Hamiltonian is

$$\begin{aligned} H = & -t\sum_{<i,j>,\sigma}(c^\dagger_{i,\sigma}c_{j,\sigma} + \text{H.c.}) + U\sum_i f^\dagger_{i,\uparrow}f_{i,\uparrow}f^\dagger_{i,\downarrow}f_{i,\downarrow} \\ & +\epsilon_f\sum_{i,\sigma} f^\dagger_{i,\sigma}f_{i,\sigma} + V\sum_{i,\sigma}(c^\dagger_{i,\sigma}f_{i,\sigma} + \text{H.c.}) \ . \end{aligned} \tag{3.2}$$

Here, $c^\dagger_{i,\sigma}$, $c_{i,\sigma}$ are the creation and annihilation operators for a conduction-band electron of spin σ at site i, $f^\dagger_{i,\sigma}$, $f_{i,\sigma}$ are the creation and annihilation operators for a localized band of electrons (typically f- or d-electrons), $U > 0$ is the on-site Coulomb repulsion between f-electrons, ϵ_f is the energy of the localized electrons and V is the hybridization between the c- and f-band. The hybridization term makes the periodic Anderson model superficially different from the Kondo lattice model, in which the f-electrons are fixed at their lattice sites and $\langle c^\dagger_{i,\sigma}f_{i,\sigma}\rangle$ is strictly zero. Schhrieffer and Wolff [98] showed that this difference is in fact superficial only and that the periodic Anderson model reduces to the Kondo lattice model in the local moment regime. The local moment regime has the f level ϵ_f below the Fermi

Table 3.1: Basis states of a single site of the Kondo lattice model. The notation for the reduced basis is $\|q,s\rangle$ of pseudospin q and spin s. As there is at most one basis state of a given set of quantum numbers, these labels are enough to completely specify the basis. c-electrons are denoted by $\{\uparrow,\downarrow\}$, f-electrons by $\{\Uparrow,\Downarrow\}$.

State	Energy	q	s	degree	Projections	q^z	s^z
$\|\|0,0\rangle$	$-3J/4$	0	0	1	$(\|\uparrow\Downarrow\rangle - \|\downarrow\Uparrow\rangle)/\sqrt{2}$	0	0
$\|\|0,1\rangle$	$J/4$	0	1	3	$\|\downarrow\Downarrow\rangle$	1	-1
					$(\|\uparrow\Downarrow\rangle + \|\downarrow\Uparrow\rangle)/\sqrt{(2)}$	0	0
					$\|\uparrow\Uparrow\rangle$	0	1
$\|\|1/2,1/2\rangle$	0	1/2	1/2	4	$\|\Downarrow\rangle$	$-1/2$	$-1/2$
					$\|\Uparrow\rangle$	$-1/2$	1/2
					$\|\uparrow\downarrow\Downarrow\rangle$	1/2	$-1/2$
					$\|\uparrow\downarrow\Uparrow\rangle$	1/2	1/2

energy and $\epsilon_f + U$ above the Fermi energy. Thus the ground state has a single f-electron at each site and double occupation of the f-band sites is suppressed by the strong Coulomb repulsion U. Under the symmetric condition

$$\epsilon_f = -\frac{U}{2}\,, \tag{3.3}$$

the energy of an unoccupied f-band site is the same as the energy of a double occupied f-band site and the system has $SO(4)$ pseudospin symmetry. By performing a perturbative expansion of the Hamiltonian Eq. (3.2) with respect to V, Schhrieffer and Wolff [98] showed that the Kondo lattice model is recovered, with an antiferromagnetic exchange interaction inversely proportional to U, given by

$$J_{\text{eff}} = \frac{8V^2}{U}\,. \tag{3.4}$$

Therefore the limit of strong Coulomb interaction corresponds to the weak coupling limit of the Kondo lattice model and conversely the weak Coulomb interaction corresponds to the Kondo lattice with strong coupling. It must be remembered however that for small U, the periodic Anderson model is no longer in the local moment regime and the Schhrieffer-Wolff transformation is not applicable.

3.2 Applications to Real Materials

The Kondo lattice describes materials in which the main interactions are between two distinct types of particles; localized electrons, of which the only relevant property is the magnetic moment and itinerant conduction electrons. This situation is realized in two important classes of materials, manganese oxide perovskites, in which there usually exists a mixture of Mn^{3+} and Mn^{4+} ions and the so-called *heavy fermion* compounds, which contain rare-earth or actinide elements such that atomic-like f-electrons interact with a conduction band. Although these materials are not one-dimensional, so far the Kondo lattice model has proven to be substantially intractable in two and three dimensions. While there is great hope of making progress toward the numerical solution of the model in higher dimensions (especially in two dimensions), in the near future, the study of the one-dimensional case remains the most important and practical theoretical tool for modeling these materials.

3.2.1 Manganese oxide perovskites and colossal magnetoresistance

The manganese oxide perovskites have the form $R_{1-x}A_xMnO_3$, where R is La, Nd or Pr is a trivalent rare earth element and A is Ca, Sr, Ba, Cd, Pb is divalent and usually an alkaline earth. These materials have a rich phase diagram with several generic low-temperature phases [99]. At low doping $x \lesssim 0.2$, there is a spin-cantered insulating state. This is often followed by a small region of $\Delta x \sim 0.05$, which is ferromagnetic insulator. For $0.2 \lesssim x \lesssim 0.5$, the materials are ferromagnetic metals. These materials have, in recent years, attracted renewed interest due to the discovery of colossal magnetoresistance (CMR) [100]. The magnetoresistance is

$$\frac{\Delta\rho}{\rho(0,T)} = \frac{\rho(H,T) - \rho(0,T)}{\rho(0,T)} , \tag{3.5}$$

where $\rho(H,T)$ is the resistivity in an applied magnetic field H at temperature T. The magnetoresistance undergoes a $\sim 1,000$-fold reduction in thin films of manganese oxide compounds near the Curie temperature in the metallic ferromagnetic phase. The great interest is stimulated by the potential applications in magnetic recording heads. Even more recently, ARPES measurements of the Fermi surface of $La_{1.2}Sr_{1.8}Mn_2O_7$ by Chaun *et al.* [101] found evidence for a pseudogap, long suspected to play a critical role in high-temperature superconductivity and indications of a striped phase.

The relevance of the Kondo lattice to manganese oxide perovskites arises from the properties of the $3d$ shell electrons in Mn. In the undoped $RMnO_3$ compounds,

the manganese atoms are triply ionized and contain four $3d$ electrons in the outer shell. In the perovskite lattice the $3d$ band splits and Mn^{3+} has the following configuration [102]: Three electrons occupy the lower three-fold degenerate localized t_{2g} orbitals and one electron is in an upper two-fold degenerate delocalized e_g orbital. Upon doping the trivalent rare earth R with a divalent element A, such as an alkaline earth, electrons are stripped from the Mn atoms resulting in a mixture of Mn^{3+} and Mn^{4+} ions. The latter are missing the e_g electron. A very strong Hund's rule coupling forces alignment of the spins of the localized t_{2g} electrons and these act as the localized moments in the Kondo lattice model. The delocalized e_g electrons form the conduction band. Since there are in fact three t_{2g} electrons the localized spin is $3/2$, so the application of the Kondo lattice model to these materials requires approximating the localized spins to be $1/2$, rather than $3/2$. The coupling between the localized electrons and the delocalized e_g orbitals is again via Hund's rule. This favors strong ferromagnetic alignment, corresponding to $J < 0$ and $|J|/t > 1$. Of potential importance is electron-phonon effects in these materials. These are ignored in the Kondo lattice model, which may result in the model being unable to reproduce critical properties of the real materials. It is argued by Millis *et al.* [103–105] that it is necessary to include the electron-phonon coupling induced by a Jahn-Teller splitting of the Mn^{3+} ions. However, this issue is still open, although it would seem likely that phonon effects play some role [101]. As far as the author knows, a striped phase has never been observed in the Kondo lattice model, but it has been suggested by Nagaev [106] that impurity models such as the Kondo and Anderson lattices are in fact natural candidates for stripe formation, more so than other models such as Hubbard or $t - J$. A solution of the two-dimensional Kondo lattice model in the appropriate parameter regime would be of critical importance in clarifying these issues.

3.2.2 Rare earth and actinide compounds

One broad class of compounds with interesting strong interaction effects are the heavy fermion materials, characterized by a very small energy scale which gives a Fermi-liquid-like state at low temperatures. This small energy scale, typically only a few tens of Kelvins, manifests most prominently in the specific heat C and the spin susceptibility χ. The linear coefficient of the specific heat C/T is extremely large compared with that of conventional metals, by two or three orders of magnitude. The spin susceptibility is similarly enhanced, but the Wilson ratio of these two quantities remains of order unity. Therefore it is possible to accommodate this behavior in the standard Fermi-liquid picture by taking the quasiparticle mass m^* to be two

or three orders of magnitude larger than the bare electron mass, thus the quasiparticles are named *heavy fermions*. Heavy fermion materials exhibit a large diversity of ground states, including magnetically ordered states ($CeAl_2$ and U_2Zn_{17}), novel (non-BCS) superconductivity ($CeCu_2Si_2$ and UBe_{13}) and ground states which are neither magnetically ordered nor superconducting ($CeAl_3$ and UAl_2). The heavy fermion systems contain two different types of electrons. One is a set of conduction electrons in s- p- or d-orbitals that move through the lattice forming broad bands. The other set is electrons in inner f-orbitals. The electrons keep their essentially atomic character even in the periodic lattice, thus they hybridize with the conduction electrons only weakly. As a consequence the electron-electron interaction between f-electrons on the same ion is the largest energy scale of the system, followed by Hund's rule coupling. The situation is realized by one ionic configuration, f^n say, which has lower energy than the other f configurations, such that the energy of the f^n electrons lies completely below the energy of the conduction band, which is in turn below the energy of the other f states. By neglecting orbital degeneracy and all interactions between c- and f-electrons not on the same site, this can be modeled by the periodic Anderson model. The configuration of the energy levels puts this in the Kondo regime.

A related class of compounds that have attracted great interest in the last decade are the Kondo insulators. The Kondo insulators are semiconductors containing rare-earth or actinide elements and are characterized by a very small excitation gap, of the order of a few meV, much smaller than ordinary semiconductors where the gap is of the order $\sim 1eV$. The Kondo insulators are reviewed in references [107] and [108].

3.3 Single-Impurity Limit

The Kondo lattice model can be considered an extension of the single impurity model. The single-impurity model has a single localized spin interacting with the conduction electrons at a single site only. This is described by the Hamiltonian

$$H_{1\text{ imp}} = -t \sum_{<i,j>,\sigma}^{L} (c^\dagger_{i,\sigma} c_{j,\sigma} + \text{h.c.}) + J \boldsymbol{S}^c_0 \cdot \boldsymbol{S}^f_0 \,. \tag{3.6}$$

An antiferromagnetic coupling $J > 0$ is assumed. Historically, study of the single impurity model preceded that of the lattice case[†] and $H_{1\text{ imp}}$ is now well understood,

[†]although Frölich and Nabarro [109] considered the lattice case in 1940 as a model of magnetic ordering of nuclear spins

to the point of an exact solution via the *Bethe ansatz* [110, 111]. Thus, this section is merely a brief outline of the large body of work that has been obtained on this model, concentrating on features that are of relevance to the lattice case. The book by Hewson [112] contains a thorough discussion and list of references on the various types of calculations that have been performed on the single-impurity model.

Interest in the single-impurity model arose from the famous Kondo effect; the anomalous increase in the resistivity of dilute magnetic alloys as the temperature T decreases to $T \to 0$. In simple metals the resistivity decreases monotonically as the temperature is lowered, because the main contribution to the resistivity for low temperatures is from electron-phonon scattering, which decreases as T^5 for small T. In metals with dilute magnetic impurities, such as iron in gold, the resistivity is not monotonic with temperature, but has a resistance minimum before rising again as $T \to 0$. A breakthrough in understanding this phenomena was achieved by Kondo [113], who calculated the resistivity of $H_{1\text{ imp}}$ to third order in the coupling J, by diagrammatic perturbation theory. He found that at third order, the interaction leads to spin scattering of the conduction electrons with the magnetic impurity, giving a $-\log T$ contribution to the resistivity. This explained well the behavior of the resistance in the vicinity of the minimum and the temperature scale of this resistance minimum became known as the Kondo temperature T_K. The scattering off the magnetic impurity leads to a sharp increase in the density of states at the Fermi surface, known as the Kondo resonance.

Since $\log T$ diverges as $T \to 0$, it is clear that the perturbation theory fails at temperatures much lower than T_K. Thus, while Kondo's calculation provided the first understanding of the effect of dilute magnetic impurities, the method could not access the low temperature regime. The problem of finding a solution valid as $T \to 0$ became known as the Kondo problem. This was essentially solved in the 1970's by Wilson's numerical renormalization group. This numerical algorithm was the precursor to DMRG and is described in more detail, although from a numerical perspective, in the introduction to DMRG in chapter 1. The results of the Wilson numerical renormalization calculation show that as the Kondo temperature T_K is approached, the initially small antiferromagnetic coupling $J > 0$ becomes large and the conduction electrons form a magnetically neutral singlet with the localized spin, quenching the magnetic impurity. The resistance minimum then reflects the formation of strongly-coupled screening clouds of conduction electrons around each magnetic impurity.

The correctness of the scaling approach was confirmed in 1980 with the discovery of an exact solution to $H_{1\text{ imp}}$ by Andrei [110] and Vigman [111] using the *Bethe*

ansatz. The exact solution verified that the single-impurity model contains only a single energy scale T_K below the conduction electron bandwidth, which measures the energy for the quenching of the localized spin via singlet formation with the conduction electrons. The form of the Kondo temperature is

$$T_K \propto \exp\left[-\frac{1}{\rho(\epsilon_F)J}\right] , \tag{3.7}$$

where the density of conduction electron states at the Fermi surface is

$$\rho(\epsilon_F) = 2\sum_k \delta(\epsilon(k) - \epsilon(k_F)) . \tag{3.8}$$

As a result of the existence of only one energy scale, the low temperature thermodynamic properties of the model are universal functions of T/T_K. For a summary of these properties, see appendix K of reference [112].

It remains unclear as to what extent these results apply to the Kondo lattice model. Many aspects of the single-impurity model have no clear analogue in the lattice case. The most important of these is the extent of the Kondo screening cloud. When the conduction electrons screen the localized spin, the scaling arguments suggest that the screening cloud extends over a scale $\xi_K \sim v_F/k_B T_K$, where v_F is the Fermi velocity of the electrons. Since T_K is generally of the order of tens of Kelvins, the screening cloud extends over thousands of lattice spacings. This cannot occur in the lattice case, because the conduction electrons are never separated from a localized spin. This is the 'exhaustion principle', first noted by Nozières [114]; there are not enough conduction electrons (or alternatively there are too many holons) to be able to screen all of the localized spins, so the extent of the screening cloud per localized spin is less than one lattice spacing, thus is clearly a localized effect and qualitatively very different from the single impurity case. Nevertheless there have been several attempts to define a 'Kondo temperature' for the lattice model which, similarly to the single-impurity case, measures the energy scale for the formation of spin singlets around the localized spins. In the weak coupling regime of the lattice model, the electrons are much more delocalized and the possibility exists that there is a second energy scale T^* that signifies the onset of a coherent state over the whole lattice. This energy scale does not exist in the single-impurity model. Most of the work in this direction has been on the Kondo lattice in three dimensions, or dynamical mean-field calculations (infinite dimensions), *e.g.* references [115–117] and references cited therein.

3.4 Exactly Solved Limits

The Kondo lattice has been studied extensively for well over two decades, however despite the intense effort, rigorous results are relatively few. Generally speaking, methods developed for the single-impurity Kondo model are impossible, as in the case of the Bethe Ansatz solution [110,111], or involve uncontrolled approximations. Primary examples of the latter are $1/N$ expansions, slave-boson methods and Gutzwiller projections. Reference [118] contains a detailed discussion and many references for these approaches. These methods have been moderately successful in describing the formation of a coherent band of quasiparticles in the three-dimensional model, as observed in the heavy fermion compounds. While the various methods developed on the basis of the single-impurity model appear to capture some of the essential physics of the lattice problem, it is *a priori* unclear as to which aspects of the various solutions are reliable and which are not. In particular, there is not yet a consensus on the ground state phase diagram.

The mean-field calculation of Doniach [22] in 1977, for the model in three dimensions, indicated a ferromagnetic phase at weak coupling and a paramagnetic phase at strong coupling. For the one-dimensional case, the many mean-field and slave-boson calculations produced mixed results (for a review, see reference [119] and references cited therein). Initial Monte Carlo results by Troyer and Würtz [120] suggested that the weak coupling regime is *paramagnetic*, with a transition to a ferromagnetic ground state as the coupling J is increased. This was contrary to the intuitive picture at the time, which suggested that for strong coupling, Kondo singlet formation would suppress ferromagnetic order. Since this work, some rigorous results supplemented by several numerical calculations, give substantial agreement on most of the broad features of the phase diagram. Before proceeding to present the results of the numerical calculations, it is useful to summarize what is known rigorously about the lattice model. Section 3.4.1 contains a brief discussion of results for the one dimensional Kondo lattice with a half-filled conduction band. Qualitatively, the main properties of the phase diagram for finite doping are specified by the behavior in the low conduction electron density limit and the strong coupling $J \to \pm\infty$ limit. These limits are exactly solvable and are described in sections 3.4.2 and 3.4.3 respectively.

3.4.1 Half-filling

The Kondo lattice with half-filled conduction band is thought in some circles to be a good effective model for the Kondo insulators (see, for example references [121]

and [122]). As mentioned in section 3.2.2, the Kondo insulators are semiconductors with a very small gap, arising from hybridization between singly-occupied localized f-orbitals and a half-filled conduction band [107, 108]. There are however doubts as to whether the Kondo insulators are in the local moment regime [30, 112], and hence some question as to whether the Kondo lattice is applicable, or whether the periodic Anderson model should be used instead.

Half-filling is defined by $n = N_e/L = 1$, where N_e is the number of conduction electrons and L is the number of lattice sites. This corresponds to z-component of pseudospin $q^z = 0$, thus the ground state is also a pseudospin singlet. A theorem on the ground state of the half-filled Kondo lattice model is rigorously proven in references [123] and [124]:

In any dimension, the Kondo lattice on a bipartite lattice has, for $J > 0$ a unique ground state that is a spin singlet. For ferromagnetic coupling $J < 0$ the same conclusion holds as long as the number of sites in each sublattice is the same.

In addition, in the large J limit (either positive or negative) there is a spin gap. Thus the ground state of the half-filled lattice forms a spin-liquid. The properties of the ground state are different in the $J > 0$ and $J < 0$ cases, so it is convenient to consider them separately.

At large antiferromagnetic coupling $J \to \infty$ the ground state is trivial and comprises L Kondo singlets, for a total ground state energy $E \to -3JL/4$. The lowest energy spin excitation requires flipping a Kondo singlet into a Kondo 'triplet', for an increase in energy of J. The lowest energy charge excitation requires moving an electron from one site to another, forming two holons (or a holon and an anti-holon) and two f-spins. These can couple either as (pseudo-)spin triplets or singlets; the charge gap corresponds to the pseudospin triplet and spin singlet case, but the energies of all these states are degenerate in the large J limit. However, it is proven later in section 3.4.3 that the large J limit is ferromagnetic in a perturbative sense to leading order in t/J, hence the pseudospin triplet and spin triplet state actually has lower energy than the pseudospin triplet and spin singlet state. The persistence of both the spin and charge gaps down to $J \to 0$ was initially suggested by a mapping onto the Hubbard model via real-space renormalization by Jullien and Pfeuty [125] and has since been examined by exact diagonalization [126] and DMRG [121] and further supported by approximate analytic techniques; Gutzwiller-projected mean-field solutions [122] and a mapping of the Kondo lattice model to a nonlinear sigma model with a semi-classical approximation for the localized spins [127]. At strong coupling the gap is linear in J, while taking an exponential form $\Delta E \sim e^{-a/J}$ for small J.

For large ferromagnetic coupling $J \to -\infty$, substantially less work has been done. Exact diagonalization results coupled with finite-size scaling show that there exists a gap for $J < 0$, however the nature of the gap is quite different. Unlike the $J > 0$ case, $J \to -\infty$ leads to a ground state made up of Kondo triplets. Electron hopping necessarily breaks the Kondo triplets leading to an increase in energy of $J/2$, thus the leading effective interaction must instead be of a spin exchange type. Indeed, at strong coupling the ground state is a Haldane phase; instead of the spin gap increasing as $J \to -\infty$ it decreases [126].

3.4.2 Low density

The case of one electron in the Kondo lattice was solved exactly by Sigrist *et al.* in 1991 [128] (see also the review in reference [118]), for the case of antiferromagnetic coupling $J > 0$. This section contains an outline of this proof. A general basis state for a single c-electron in a lattice of L sites can be written in the form

$$|j, \sigma; \sigma_1, \ldots, \sigma_L\rangle = \sigma |j, \sigma\rangle \otimes |\sigma_1, \ldots, \sigma_L\rangle \,, \tag{3.9}$$

where $|j, \sigma\rangle$ denotes a conduction electron of spin σ at site j and $|\sigma_1, \ldots, \sigma_L\rangle$ is a basis state for the localized spins. Due to the spin symmetry of the Kondo lattice, it is sufficient to take a single value, say M, for the z-component of total spin. The overall factor of σ is a phase factor which is positive if the conduction spin is up ($\sigma = +1$) and negative if the conduction spin is down ($\sigma = -1$). The purpose of this phase factor is to make the off-diagonal matrix elements of the Hamiltonian in this basis all non-positive, to allow the application of the Perron-Fronebius theorem. The application of the Hamiltonian to this basis state gives

$$\begin{aligned} H|j, \sigma; \sigma_1, \sigma_2, \ldots, \sigma_L\rangle \;=\; & -t \sum_a |j + a, \sigma; \sigma_1, \sigma_2, \ldots, \sigma_L\rangle \\ & + \frac{1}{4} J \sigma \sigma_j |j + a, \sigma; \sigma_1, \sigma_2, \ldots, \sigma_L\rangle \\ & - \frac{1}{4} J (1 - \sigma\sigma_j) |j, -\sigma; \sigma_1, \ldots, -\sigma_j, \ldots, \sigma_L\rangle \,, \end{aligned} \tag{3.10}$$

where the sum $\sum_a$ is taken over the nearest neighbors of j. The successive application of the Hamiltonian to a basis state will ultimately connect all basis states, *i.e.* for two arbitrary basis states $|a\rangle$ and $|b\rangle$ there always exists an integer n such that $\langle a | H^n | b \rangle \neq 0$. With the non-positivity property, this gives sufficient conditions to apply the Perron-Fronebius theorem, which states that the lowest energy eigenstate $|\psi_g(M)\rangle$ has a strictly positive wavefunction in this basis and is nondegenerate.

To calculate the value of the total spin of the state $|\psi_g(M)\rangle$, it is sufficient to construct a reference wavefunction $|\phi\rangle$ with a given total spin which has finite overlap, $\langle\phi|\psi_g(M)\rangle \neq 0$. The choice of wavefunction used by Sigrist *et al.* [128] is

$$|\phi((L-1)/2)\rangle = |j,\uparrow;\downarrow,\uparrow,\uparrow,\cdots,\uparrow\rangle + |j,\downarrow;\uparrow,\uparrow,\uparrow,\cdots,\uparrow\rangle \,. \tag{3.11}$$

This state represents a Kondo singlet at site 1 with all other localized spins aligned parallel, for z-component of spin equal to the total spin, which is $(L-1)/2$. The repeated application of S^- to this state, to make the z-component of spin equal to the z-spin of the ground state M, yields

$$\begin{aligned} |\phi(M)\rangle &= (S^-)^{(L-1)/2-M}|\phi((L-1)/2)\rangle \\ &= [(L-1)/2-M]! \\ &\quad \times \sum_{\sigma_2+\sigma_3+\ldots+\sigma_L=M} \Big(|j,\uparrow;\downarrow,\sigma_2,\ldots,\sigma_L\rangle + |j,\downarrow;\uparrow,\sigma_2,\ldots,\sigma_L\rangle\Big) \,. \end{aligned} \tag{3.12}$$

This is a non-zero vector, hence $\langle\phi(M)|\psi_g(M)\rangle \neq 0$ and $|\phi(M)\rangle$ has finite overlap with the ground state. This proves that the total spin of the ground state is $s = \frac{1}{2}(L-1)$.

Given that the total spin of the ground state of the Kondo lattice with a single electron is known, the exact form of the wavefunction is not difficult to obtain [128]. Choosing the z-component of spin to be maximal, the ground state can be written as

$$|\phi\rangle = \sum_{i=1}^{L}\left(A^i c^\dagger_{i\downarrow} + \sum_{j=1}^{L} B^{ij} c^\dagger_{i\uparrow} S^-_j\right)|\mathrm{FM}\rangle \,, \tag{3.13}$$

where A^i and B^{ij} are yet to be determined coefficients and $|\mathrm{FM}\rangle$ is the ferromagnetic state of zero conduction electrons and all localized spins up. The spin of this state is enforced by requiring $S^+|\phi\rangle = 0$.

Operating on $|\phi\rangle$ with the Hamiltonian gives an eigenvalue equation for A^i and B^{ij},

$$\begin{aligned} EA^i &= -t\textstyle\sum_a A^{i+a} - \frac{1}{4}JA^i + \frac{1}{2}JB^{ii} \,, \\ EB^{ij} &= -t\textstyle\sum_a B^{i+a,j} + \frac{1}{2}J\delta_{ij}A^i - \frac{1}{4}J(2\delta_{ij}-1)B^{ij} \,, \end{aligned} \tag{3.14}$$

where the summation $\sum_a$ is over nearest neighbor sites of site i. These equations can be solved in momentum space by taking the Fourier transforms

$$\begin{aligned} \tilde{A}^K &= \tfrac{1}{\sqrt{L}}\textstyle\sum_{j=1}^{L} A^i e^{-iKj} \,, \\ \tilde{B}^{Kq} &= \tfrac{1}{L}\textstyle\sum_{j,l=1}^{L} B^{jl} e^{-iKj-iq(j-l)} \,. \end{aligned} \tag{3.15}$$

Here K is the total momentum and is a good quantum number. The energy eigenvalues E_K are given by the solutions of

$$F(E_K) = -\frac{E_K - \epsilon_K + J/2}{E_K - \epsilon_K - J/4}\,, \tag{3.16}$$

with

$$F(E) \equiv \frac{1}{L}\sum_q \frac{J}{2E - \epsilon_q - J/2}\,. \tag{3.17}$$

The corresponding wavefunctions can be determined by

$$\tilde{B}^{Kq} = -\frac{1}{\sqrt{L}}\frac{E - \epsilon_q - J/4}{E - \epsilon_{K+q} - J/4}\tilde{A}^K\,, \tag{3.18}$$

with the normalization condition $|\tilde{A}^K|^2 + \sum_q |\tilde{(B)}^K|^2 = 1$.

The analysis by Sigrist *et al.* [128] revealed that the ground state has zero total momentum, $K = 0$ and for every momentum the wavefunction describes a bound state, *i.e.* a massive spin polaron.

3.4.3 Strong coupling

In the doped case (corresponding to non-zero pseudospin), the large J limit has been studied extensively. Taking $J = \infty$, the only states that survive are, from table 3.1, the Kondo singlet $\|0,0\rangle$ and the holon-spin $\|1/2,1/2\rangle$. If two Kondo singlet sites were to instead form two holons (*i.e.* an unoccupied c-electron site and a double occupied c-electron site), there would be an energy penalty of $3J/2$. Thus for large coupling J, the number of holons will the the minimum possible *i.e.* $2q$, since it is energetically favorably for any additional holons to instead form into Kondo singlets. This reduces the effective symmetry of the pseudospin down to $U(1)$. Thus we can replace the pseudospin at site i with the number of holons at site i, n_i^h, with $n_i^h = 2q_i$. Then the total pseudospin is given by the total number of holons, $q = \frac{1}{2}\sum_i n_i^h$. This gives the two basis states, written in $U(1) \times SU(2)$ form of holon number and spin, as $\|0,0\rangle$ and $\|1,1/2\rangle$. These basis states are identical to those of the $U = \infty$ Hubbard model discussed in chapter 2. In fact, it was shown by Lacroix [129] that the Kondo lattice can be mapped rigorously to the Hubbard model in this case, where the localized spins are represented as fermions. The Hamiltonian reads

$$H = \frac{t}{2}\sum_{i,\sigma} \tilde{f}_{i,\sigma}^\dagger \tilde{f}_{i+1,\sigma} + \text{H.c.} + \frac{3J}{4}\sum_i (1 - n_i)\,, \tag{3.19}$$

where the fermion operators $\tilde{f}_{i,\sigma}^\dagger$ and $\tilde{f}_{i,\sigma}$ satisfy the constraint $n_i = \tilde{f}_{i,\sigma}^\dagger \tilde{f}_{i,\sigma} \leq 1$, *i.e.* no double occupancy. An empty site of this Hubbard model corresponds to a

Kondo singlet and a site occupied by a spin corresponds to an empty site (thus an unpaired f spin) of the Kondo lattice. Because of the lack of double occupancy and only nearest-neighbor hopping, the electrons in the $U = \infty$ Hubbard model can never move past one another; given an ordering of electrons, say from left to right, that ordering is preserved by the action of the Hamiltonian. In addition there are no spin-flip interactions; therefore the spin degrees of freedom are completely degenerate and can be specified separately from the charge degrees of freedom [130]. Such a state of N fermions can be specified as a product of a charge wavefunction and a spin wavefunction,

$$\begin{aligned} |\Psi_N;(\sigma_1,\sigma_2,\ldots,\sigma_N)\rangle &= |N\rangle \otimes |\sigma_1,\sigma_2,\ldots,\sigma_N\rangle \\ &= \textstyle\sum_{i_1<i_2<\ldots<i_N} A_{i_1,i_2,\ldots,i_N} \tilde{f}^\dagger_{i_1,\sigma_1} \tilde{f}^\dagger_{i_2,\sigma_2} \cdots \tilde{f}^\dagger_{i_N,\sigma_N} |0\rangle \ . \end{aligned} \tag{3.20}$$

The vacuum state $|0\rangle$ corresponds to the half-filled lattice of all Kondo-singlets.

The complete spin degeneracy does not persist away from the $J = \infty$ case and it was shown by Sigrist *et al.* [131] (see also [118]) using a perturbative expansion with respect to t/J, that the spin degeneracy is lifted and the ground state is completely polarized with total spin $s = (L - N)/2$. This corresponds to the spin being equal to the pseudospin. Note that 'completely polarized' here means polarized with respect to the available basis states, being just the Kondo singlet and the holon-spin. This is not the *maximal* spin state, which would have every spin aligned and spin $s = (L+N)/2$. However spin $s = (L-N)/2$ is the largest spin that can be the ground state for large J/t. This is because increasing the spin beyond $(L - N)/2$ requires flipping one or more Kondo singlet states into Kondo triplets. This gives an increase in energy of J, similarly to the gap in the half-filled case discussed earlier. In fact, the proof of the spin gap at half filling extends readily to a gap between $E_g(q, s = q)$ and $E_g(q, s = q + 1)$. The existence of a gap between lowest states of two spin sectors does not imply that there is a true gap in the excitation spectrum however. There will only be a true gap if J is larger than the energy of all the singlet excitations.

This result for strong coupling was later extended by Yanagisawa and Harigaya [132], who proved a similar result for the partially filled Kondo lattice when a strong Hubbard conduction band on-site Coulomb repulsion is added to the standard Hamiltonian of Eq. (3.1). As the Coulomb repulsion $U \to \infty$, the ground state of the extended Kondo lattice is fully polarized with spin $s = (L - N)/2$ for all couplings $J > 0$. For $J < 0$, the ground state is again ferromagnetic, but with maximal spin $s = (L + N)/2$. In the case of $J > 0$, this result is easy to understand from the mapping onto the Hubbard model discussed above. The Hubbard U term adds an energy penalty $U/2$ to each holon in the system. Thus it is again

energetically favorable for any excess holons to instead form Kondo singlets so the number of holons is the minimum possible. Thus the mapping onto the Hubbard model proceeds exactly as in the large J case.

3.5 Effective Interactions In The Kondo Lattice Model

There are some parameter regimes in which the dominant interaction processes can be identified. The results presented in this thesis show that, unfortunately, the number of such regimes is smaller than previously thought. At weak coupling $|J/t| \ll 1$, second order perturbation theory gives an effective Ruderman-Kittel-Kasuya-Yodida (RKKY) interaction [133–135]. This is an effective interaction between the localized spins which is mediated by the conduction electrons. The derivation is discussed in section 3.5.1. Kondo singlet formation, the dominant effect in the single-impurity model, was the focus of much early work on the lattice model. However the extent of the similarities between Kondo singlet formation in the single impurity model and the lattice model is not clear. Certainly, the *mechanism* of Kondo singlet formation in the single impurity model, responsible for the Kondo screening cloud, is not present in the lattice case. Of more importance is the double-exchange interaction, which was recognized as early as 1951 to be of importance in the perovskite manganese oxides [136], but has only recently been discussed in relation to the Kondo lattice [137,138].

3.5.1 RKKY

At $J = 0$, both the conduction electrons and the localized spins in the Kondo lattice are non-interacting. Thus the wavefunction separates into a tensor product of the conduction band wavefunction and the localized spin wavefunction. There is complete 2^L-fold degeneracy in the localized spin state, which is expected to be broken perturbatively when J is increased from 0. The wavefunction, written as a product of the free electron ground state $|0\rangle$ and an arbitrary spin state, is $|\Psi\rangle = |0\rangle \otimes |\sigma\rangle$, where $|\sigma\rangle = \sum_{\sigma_1,\sigma_2,\ldots,\sigma_L} \psi^{\sigma}_{\sigma_1,\sigma_2,\ldots,\sigma_L} |\sigma_1\sigma_2\ldots\sigma_L\rangle$ is the wavefunction for the localized spins. Treating the interaction with the localized spins as a perturbation H_{KL} to the free electron Hamiltonian H_0, the application of Rayleigh-Schrödinger perturbation theory gives,

$$E = E_0 + \langle\, \Psi \,|\, H_{\mathrm{KL}} \,|\, \Psi \,\rangle - \sum_{n\neq 0} \frac{|\langle n|\langle\, \sigma \,|\, H_{\mathrm{KL}} \,|\, 0 \,\rangle|\sigma\rangle|^2}{E_n - E_0} + \cdots , \qquad (3.21)$$

where $|n\rangle$ are the non-interacting excited states, with $H_0|i\rangle = E_i|i\rangle$. The only excited states giving non-vanishing matrix elements are those of the form $|n\rangle = c^\dagger_{ck\sigma}c_{ck'\sigma'}|0\rangle$, with $|k'| < k_F < |k|$. To second order, this gives,

$$\begin{aligned} E &= E_0 + \textstyle\sum_{ij} J_{\mathrm{RKKY}}(i-j)\langle\,\sigma\,|\,\boldsymbol{S}_i\cdot\boldsymbol{S}_j\,|\,\sigma\,\rangle\ , \\ J_{\mathrm{RKKY}}(i-j) &= \frac{J^2}{2L^2}\sum_{|k'|<k_F<|k|\le\pi/a}\frac{e^{i(k'-k)(i-j)a}}{\epsilon(k)-\epsilon(k')} \end{aligned} \tag{3.22}$$

where L is the lattice size, with lattice constant a. This implies that the complete 2^L-fold degeneracy of the localized spins at $J = 0$ is lifted perturbatively so that the localized spins order so as to minimize E, giving an effective interaction between the localized spins at sites i and j of $J_{\mathrm{RKKY}}(i-j)$, called the *RKKY* interaction [133–135].

The form of Eq. (3.22) is generic to any dimension. However the summation over k and k' is significantly different depending on the dimension. This calculation is carried out in reference [139], with the results

$$J_{\mathrm{RKKY}}(r) = \begin{cases} \frac{m_e J^2}{2\pi}[\mathrm{Si}(2k_Fr) - \frac{\pi}{2}] & 1D\ , \\ \frac{m_e k_F^2 J^2}{8\pi}[J_0(k_Fr)Y_0(k_Fr) + J_1(k_Fr)Y_1(k_Fr)] & 2D\ , \\ \frac{m_e k_F J^2}{16\pi^3 r^3}[\cos(2k_Fr) - \frac{\sin(2k_Fr)}{2k_Fr}] & 3D\ , \end{cases} \tag{3.23}$$

where $r = |i-j|a$ is the distance between lattice sites i and j. The special functions in Eq. (3.23) are the sine integral Si and the first and second kind Bessel functions of order n, J_n and Y_n respectively.

Ordering of localized moments with wavevector $2k_F$ is characteristic of the RKKY interaction in any dimension. In three dimensions, the interaction decreases at large distances as r^{-3}. In two dimensions, the interaction also decreases at large distances because of the $1/r$ asymptotic behavior of the Bessel functions. In one dimension however, the interaction diverges. The Fourier component of J_{RKKY} at wavevector k is given by

$$J_{\mathrm{RKKY}}(k) = \frac{1}{2\pi}\int_{-\infty}^{\infty} J_{\mathrm{RKKY}}(r)e^{ikr}\,dk\ . \tag{3.24}$$

From the 1D form of the real-space interaction, the form of the momentum-space interaction is

$$J_{\mathrm{RKKY}}(k) \propto \frac{1}{k}\ln\left|\frac{2k_F+k}{2k_F-k}\right|\ , \tag{3.25}$$

which has a logarithmic divergence at $2k_F$. This divergence is typical of perturbation theory applied to one-dimensional systems. While the ordering of the localized moments is still expected to be predominantly at wavevector $2k_F$, it is not possible

to use the RKKY interaction itself to describe this ordering; since the interaction diverges there is no lower bound to the ground state energy, even for arbitrarily small J. Thus it is necessary to go beyond perturbation theory to properly account for the weak coupling regime of the Kondo lattice model in one dimension. The results from bosonization [137, 140] give RKKY-like behavior, with dominant $2k_F$ modulations superimposed on an incoherent background. This behavior fits well with previous numerical results at weak coupling [28, 39] as well as the numerical results presented in this thesis.

3.5.2 Double exchange

Double-exchange ordering was introduced by Zener [136] to describe ferromagnetism in the manganese oxide perovskites. Zener considered the Mn oxide compounds $La_{1-x}A_xMnO_3$, with $0 < x < 1$ and A = Ca, Sr or Ba. The compound contains Mn^{3+} and Mn^{4+} ions, in concentrations $1-x$ and x respectively. For $x = 0$ the compounds are insulating, while for moderate doping $x \gtrsim 0.2$ they are metallic ferromagnets. Zener proposed that the close connection between ferromagnetism and conduction in these materials can be accounted for by supposing that the e_g electrons in Mn^{3+} ions can hop to vacant e_g orbitals on neighboring Mn^{4+} ions. Since hopping electrons tend to preserve their spin and Hund's rule coupling strongly favors alignment of the e_g spin with that of the localized t_{2g} electrons (*cf.* section 3.2.1), this hopping should favor a ferromagnetic alignment of the t_{2g} electrons on neighboring Mn ions. Since the hopping of the e_g electrons occurs through an intermediate O^{2-} ion, Zener called this the double-exchange interaction. The name is somewhat unfortunate, as the interaction is not an exchange in the usual sense, but it simply reflects the tendency of hopping electrons to preserve their spin.

A microscopic derivation of the double-exchange interaction was given by Anderson and Hasegawa [141] for the two-site Kondo lattice with ferromagnetic coupling $J < 0$, which models the Hund's rule coupling of the Mn oxides. However, double-exchange operates regardless of the sign of the coupling; the fact that the electrons align parallel or antiparallel to the localized spins at each site is irrelevant to the preservation of spins while hopping. It is the latter which forces the localized spins to align. The first hints of this are in Anderson and Hasegawa's original work [141], where they noticed that the sign of the coupling was largely irrelevant to the ferromagnetic ordering within a semi-classical approximation for the localized spins. In the $SO(4)$-symmetric basis, the matrices of the two-site Kondo lattice are very small so it is worthwhile exploring in full detail. The three reduced basis states of a single site of the Kondo lattice are given in table 3.1, with the basis transforming under

$SO(4)$ rotations as the representation $D(0,0) \oplus D(0,1) \oplus D(1/2,1/2)$ of degree 8. For two sites, the Clebsch-Gordan series expansion gives the representation

$$\begin{aligned}[D(0,0) \oplus D(0,1) \oplus D(1/2,1/2)] \otimes [D(0,0) \oplus D(0,1) \oplus D(1/2,1/2)] \\ = \; 3D(0,0) \oplus 4D(0,1) \oplus 4D(1,0) \oplus D(1,0) \oplus 4D(1/2,1/2) \\ \oplus 2D(1/2,3/2) \oplus D(0,2) \oplus D(1,1) \; .\end{aligned} \tag{3.26}$$

Thus there are 8 $SO(4)$ symmetry sectors of the two site Kondo lattice and the largest subspace is 4 dimensional. This could be reduced further, *e.g.* by using spatial reflection, but 4×4 matrices are not hard to deal with so this step is hardly worthwhile. The complete set of basis states is given in table 3.2. The one electron sector comprises all states that can be constructed from a single holon and either a Kondo triplet or a Kondo singlet. This is of course degenerate (via particle-hole symmetry) with the 3 electron sector. Two spin states are possible; a Kondo singlet coupled with a holon has spin $1/2$, transforming as the $D(1/2,1/2)$ representation and a Kondo triplet coupled with a holon gives both a spin $1/2$ state ($D(1/2,1/2)$ representation) and a spin $3/2$ state ($D(1/2,3/2)$ representation). To simplify the notation of table 3.1, we denote the Kondo singlet, Kondo triplet and holon states by $\|S\rangle$, $\|T\rangle$ and $\|H\rangle$ respectively. The correspondence with the previous notation is

$$\begin{aligned} \|S\rangle &= \|0,0\rangle \; , \\ \|T\rangle &= \|0,1\rangle \; , \\ \|H\rangle &= \|1/2,1/2\rangle \; . \end{aligned} \tag{3.27}$$

Consider first the the ferromagnetic $(1/2,3/2)$ sector. The complete Hamiltonian is

$$H_{(1/2,3/2)} = -t\Big(\|HT\rangle\langle TH\| + \|TH\rangle\langle HT\|\Big) + \frac{J}{4}\Big(\|HT\rangle\langle HT\| + \|TH\rangle\langle TH\|\Big) \; , \tag{3.28}$$

or, in matrix form,

$$H_{(1/2,3/2)} = \begin{pmatrix} J/4 & -t \\ -t & J/4 \end{pmatrix} \; . \tag{3.29}$$

This is trivially diagonalizable, with eigenvalues $J/4 + t$ and $J/4 - t$. The eigenstates correspond respectively to antisymmetric and symmetric states with respect to spatial reflection. The ground state eigenvector is

$$\|\Psi_0\rangle = \frac{1}{\sqrt{2}}(\|HT\rangle + \|TH\rangle) \; , \tag{3.30}$$

corresponding to the ground state eigenvalue of $E_{0,J<0} = J/4 - t$. This is the prototypical state for double-exchange ordering; a holon moves through a Kondo triplet background, preserving the spin (and indeed the pseudospin) at each hop.

Table 3.2: Basis states of the two-site Kondo lattice. The dimension is the number of distinct states in each symmetry sector and the degree of the representation is the degeneracy of each state.

(q, s) Sector	Degree	Dimension	States
$(0, 0)$	1	3	$\|\|SS\rangle$ $\|\|TT\rangle$ $\|\|HH\rangle$
$(0, 1)$	3	4	$\|\|ST\rangle$ $\|\|TS\rangle$ $\|\|TT\rangle$ $\|\|HH\rangle$
$(1, 0)$	3	1	$\|\|HH\rangle$
$(1/2, 1/2)$	4	4	$\|\|SH\rangle$ $\|\|HS\rangle$ $\|\|TH\rangle$ $\|\|HT\rangle$
$(1/2, 3/2)$	8	2	$\|\|HT\rangle$ $\|\|TH\rangle$
$(0, 2)$	5	1	$\|\|TT\rangle$
$(1, 1)$	9	1	$\|\|HH\rangle$

Now consider the $(1/2, 1/2)$ sector, where the spin is a minimum. Using the ordering of basis vectors specified in table 3.2, the Hamiltonian is

$$H_{(1/2,1/2)} = \begin{pmatrix} -3J/4 & -t/2 & 0 & -\sqrt{3}t/2 \\ -t/2 & -3J/4 & \sqrt{3}t/2 & 0 \\ 0 & \sqrt{3}t/2 & J/4 & -t/2 \\ -\sqrt{3}t/2 & 0 & -t/2 & J/4 \end{pmatrix} . \tag{3.31}$$

The four eigenvalues are $E = -\frac{J}{4} \pm \frac{1}{2}\sqrt{J^2 \pm Jt + 4t^2}$. For $J < 0$, the lowest energy state is $E_{1,J<0} = -\frac{J}{4} - \sqrt{J^2 - Jt + 4t^2}$, which is always higher than the lowest energy state in the $(1/2, 3/2)$ sector, of $E_{0,J<0} = J/4 - t$.

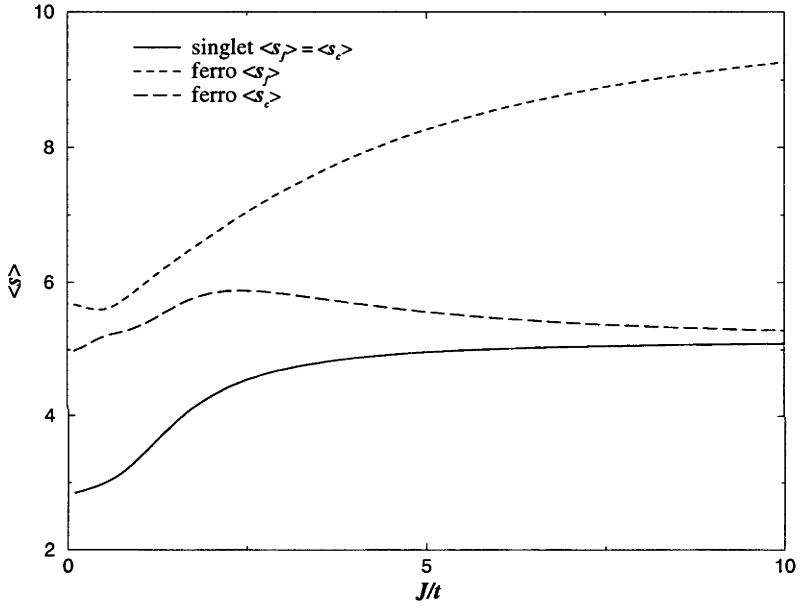

Figure 3.1: The expectation value of the total spin for the conduction band and the f-spins for antiferromagnetic coupling $J > 0$, for a 60 site lattice at filling $n = 0.7$. The ferromagnetic state has total spin $s = 9$.

For antiferromagnetic coupling $J > 0$, the situation is obscured because for only two sites the spin of the completely polarized ferromagnetic state of spin $(L - N)/2$ is only $1/2$, coinciding with the minimum possible spin. Instead, Fig. 3.1 shows the expectation value of the total spin, given by $s(s+1) = \langle \boldsymbol{S} \cdot \boldsymbol{S} \rangle$, of the conduction band and the f-spins separately, for the fully polarized ferromagnetic state and the singlet state of the Kondo lattice for 60 sites with filling $n = 0.7$. For these parameters, the fully polarized state has total spin $s = 9$. When the spin of the complete system is a singlet, the spin of the conduction electrons must be the same magnitude but aligned antiparallel with the spin of the f-spins. The important aspect of this figure

is that the spin of the conduction band and the f-spins considered separately, rapidly increases as the Kondo coupling is turned on, so that even for the ferromagnetic state the conduction electrons are predominantly aligned antiparallel to the f-spins. Thus the picture of double exchange for antiferromagnetic coupling $J > 0$ is of conduction electrons aligned parallel with each other, but antiparallel to the background of ferromagnetic f-spins.

3.5.3 Kondo singlet formation

It is clear that the *mechanism* of Kondo singlet formation, responsible for the large conduction-electron screening cloud in the single-impurity model, is absent in the lattice case. Indeed, the similarities of the strong coupling limit between $J \to \infty$ and $J \to -\infty$ (which extends to a large region of the phase diagram discussed in section 3.6) suggests that Kondo singlet formation is not an important effect *per se* in the lattice model, but rather the importance lies in the side-effect of localization of the conduction electrons. This localization also occurs in the case of ferromagnetic coupling $J < 0$, except here it is due to Kondo *triplet* formation, rather than Kondo singlets. However, it is apparent from the numerically obtained phase diagram (see section 3.7.2), that the RKKY interaction and double-exchange are insufficient by themselves to describe all of the phases of the Kondo lattice model. These additional effective interactions have not yet been characterized.

3.6 Phase diagram from bosonization

The bosonization technique is useful for a large class of one-dimensional systems. The essential idea is that the fermionic fields are represented in terms of collective density operators that satisfy bosonic commutation relations. This mapping is exact down to a short wavelength cutoff α, of the order $\alpha \sim k_F^{-1}$, which is of the order of the mean distance between electrons. The utility of this approach lies in the general property of bosonic Hamiltonians, being generally much easier to handle than fermionic Hamiltonians. Thus it is *relatively* simple to apply, for example, a unitary transformation to simplify a bosonic Hamiltonian. Bosonization as it is currently used in one-dimensional strongly correlated electron systems was first introduced by Bloch [142] and Tomonaga [143] and further developed by Mattis and Lieb [144], Coleman [145], Luther and Peschel [146], Mandelstam [147] and Heidenreich *et al.* [148]. The bosonization solution of the Kondo lattice, by Honner and Gulácsi [137, 149] was the first analytic work to rigorously establish the phase diagram and provide a non-perturbative explanation of the $2k_F$ correlations in the

RKKY regime without the divergences that plague the perturbative approach. This is the most far reaching analytic calculation on the Kondo lattice model to date, so it is worth the describing broad features of the derivation and solution. We make no attempt at providing a detailed description of the bosonization technique; instead many excellent tutorials exist in the literature, *e.g.* references [150–152], which serve as the background to this section.

Bosonization of a lattice system begins by constructing the density operators in momentum space, corresponding to right-moving (+) and left-moving (-) collective excitations of charge (ρ) and spin (σ) about the Fermi points $+k_F$ and $-k_F$,

$$\begin{aligned}
\rho_+(k) &= \sum_{\sigma,0<k'\leq\pi/a} c^\dagger_{k'-\frac{k}{2},\sigma} c_{k+\frac{k}{2},\sigma} \,, \\
\rho_-(k) &= \sum_{\sigma,-\pi/a<k'\leq 0} c^\dagger_{k'-\frac{k}{2},\sigma} c_{k+\frac{k}{2},\sigma} \,, \\
\sigma_+(k) &= \sum_{\sigma,0<k'\leq\pi/a} \sigma c^\dagger_{k'-\frac{k}{2},\sigma} c_{k+\frac{k}{2},\sigma} \,, \\
\sigma_-(k) &= \sum_{\sigma,-\pi/a<k'\leq 0} \sigma c^\dagger_{k'-\frac{k}{2},\sigma} c_{k+\frac{k}{2},\sigma} \,.
\end{aligned} \tag{3.32}$$

These densities satisfy the bosonic algebra

$$\begin{aligned}
[\rho_r(k)\,,\,\rho_{r'}(k')] &= \delta_{r,r'}\,\delta_{k,-k'}\,\tfrac{rkL}{2\pi} \,, \\
[\sigma_r(k)\,,\,\sigma_{r'}(k')] &= \delta_{r,r'}\,\delta_{k,-k'}\,\tfrac{rkL}{2\pi} \,.
\end{aligned} \tag{3.33}$$

When $k = 0$, the densities correspond to the number of right-movers and left-movers respectively. In order to simplify the notation somewhat, it is conventional in bosonization to give a separate notation for the number operators, normalized with respect to the non-interacting ground state $|0\rangle$,

$$N^\nu_\pm = \nu_\pm(0) - \langle\, 0 \,|\, \nu_\pm(0) \,|\, 0 \,\rangle \,, \tag{3.34}$$

where $\nu = \rho, \sigma$ denotes charge and spin respectively.

The density fluctuations with a wavelength shorter than α are excluded by a cut-off function $\Lambda_\alpha(k)$, a typical cutoff function would be, *e.g.* a Gaussian $\Lambda_\alpha(k) = \exp(-\alpha^2 k^2/2)$. We can now define the Bose fields themselves:

$$\begin{aligned}
\phi_\nu(j) &= \tfrac{\pi j a}{L}(N^\nu_+ + N^\nu_-) - i\textstyle\sum_{k\neq 0}\tfrac{\pi}{kL}[\nu_+(k) + \nu_-(k)]\Lambda_\alpha(k)e^{ikja} \\
\theta_\nu(j) &= \tfrac{\pi j a}{L}(N^\nu_+ - N^\nu_-) - i\textstyle\sum_{k\neq 0}\tfrac{\pi}{kL}[\nu_+(k) - \nu_-(k)]\Lambda_\alpha(k)e^{ikja} \,.
\end{aligned} \tag{3.35}$$

Here a is the lattice spacing and j is an integer label of the real space lattice sites. The derivatives of the Bose fields are notated $\partial_x\psi_\nu(j)$, which is shorthand for $\partial_x\psi_\nu(x/a)$ evaluated at $x = ja$.

In the one-dimensional Kondo lattice, the conduction band may be bosonized but not the localized spins [137]. This is because the spins are strictly localized and their Fermi velocity vanishes. Substituting the definition of the Bose fields into the Hamiltonian of the Kondo lattice gives,

$$\begin{aligned} H &= \frac{v_F a}{4\pi}\sum_{j,\nu}\{[\partial_x\theta_\nu(j)]^2+[\partial_x\phi_\nu(j)]^2\} \\ &+\frac{Ja}{2\pi}\sum_j[\partial_x\phi_\sigma(j)]S_j^z \\ &+A\frac{Ja}{2\alpha}\sum_j\{\cos[\phi_\sigma(j)]+\cos[2k_Fja+\phi_\rho(j)]\}(e^{-i\theta_\sigma(j)}S_j^+ + \text{h.c.}) \\ &-A\frac{Ja}{2\alpha}\sum_j\sin[\phi_\sigma j]\sin[2k_Fja+\psi_\rho j]S_j^z\ , \end{aligned} \tag{3.36}$$

where A is a dimensionless constant that depends on the cutoff function $\Lambda_\alpha(k)$.

The bosonized Hamiltonian generates the same behavior as the original Hamiltonian provided that the conduction electrons are not too strongly localized. In particular, this Hamiltonian does not describe directly Kondo singlet formation. The Bose representation of the spin-flip terms responsible for Kondo singlet formation is reliable only at long wavelengths, describing the properties of spin-flip interactions only at large distances from the site of the scattering localized spin. This provides a good description at weak couplings, but as is usual for bosonization, this may be insufficient when the coupling is strong enough that the electrons become trapped on-site by the localized spin. Indeed, this perhaps accounts for why some of the features of the phase diagram obtained numerically by the author do not appear in the bosonization solution (*cf.* section 3.7.2).

It is important to note that the $SO(4)$ spin and pseudospin symmetry has been explicitly broken in the bosonized Hamiltonian Eq. (3.36). This is due to use use of Abelian bosonization, which breaks the $SU(2)$ rotation symmetry down to $U(1)$ for both the spin and pseudospin symmetries [150]. While the Hamiltonian Eq. (3.36) commutes with S^2, it does *not* commute with S^+, S^- and S^z, the generators of $SU(2)$, therefore the degeneracy of the ground state for spin $s > 0$ is broken and the Abelian bosonization explicitly picks out the state for which the z-component of spin is a maximum.

To simplify the Hamiltonian, Honner and Gulácsi next applied a unitary transformation to change the basis such that the conduction electron spin degrees of freedom are coupled directly to the localized spins. The transformation used was

$H \to \tilde{H} = e^{-S} H e^{S}$, where

$$S = i\frac{Ja}{2\pi v_F}\sum_j \theta_\sigma(j) S_j^z \,. \tag{3.37}$$

The transformation can be carried out exactly, without the use of a perturbative expansion, giving the transformed Hamiltonian $\tilde{H}$,

$$\begin{aligned}
\tilde{H} \;=\; & \frac{v_F a}{4\pi}\sum_{\nu j}\{[\partial_x\theta_\nu(j)]^2 + [\partial_x\phi_\nu(j)]^2\} \\
& -\frac{J^2a^2}{4\pi^2 v_F}\sum_{j,l}\left\{\int_0^\infty dk\, \cos[k(j-l)a]\Lambda_\alpha^2(k)\right\} S_j^z S_l^z \\
& +A\frac{Ja}{2\alpha}\sum_j\{\cos[K(j)+\phi_\sigma(j)] + \cos[2k_F ja + \phi_\rho(j)]\} \\
& \quad \times \left(e^{-i(1+Ja/2\pi v_F)\theta_\sigma(j)} S_j^+ + \text{h.c.}\right) \\
& -A\frac{Ja}{\alpha}\sum_j\{\sin[K(j)+\phi_\sigma(j)]\sin[2k_F ja + \phi_\rho(j)]S_j^z \,.
\end{aligned} \tag{3.38}$$

The function $K(j)$ is related to the commutator of the spin Bose fields,

$$K(j) = i\frac{Ja}{2\pi v_F}\sum_l [\phi_\sigma(j)\,,\,\theta_\sigma(l)]S_l^z \,. \tag{3.39}$$

This is highly non-local. At distances $ja \gg \alpha$, $[\phi_\sigma(j)\,,\,\theta_\sigma(l)] \to \text{sign}(j)i\pi$, thus $K(j)$ effectively adds all the localized spins to the right of site j and subtracts all the localized spins to the left of site j. Honner and Gulácsi [137] showed that $K(j)$ vanishes in the ferromagnetic phase and essentially measures the amount of disorder.

The second term in the transformed Hamiltonian Eq. (3.38) represents a non-perturbative effective interaction between the localized spins, which originates from the forward scattering part of $(J/2)\sum_j(n_{j\uparrow} - n_{j\downarrow})S_j^z$ in the Kondo lattice Hamiltonian. The interaction is independent of the sign of J and is the only term in the transformed Hamiltonian that is of order J^2, thus this term is expected to dominate the ordering of the localized spins as J increases. Honner and Gulácsi [137] showed that the interaction is ferromagnetic for all choices of cutoff function; thus it satisfies all the properties of double-exchange, discussed in section 3.5.2. For reasonable choices of cutoff function, the integral in the second term of Eq. (3.38) can be evaluated showing that the interaction is short-ranged and is well approximated by taking the nearest neighbor form $-\mathcal{J}\sum_j S_j^z S_{j+1}^z$, where

$$\mathcal{J} = \frac{J^2a^2}{2\pi^2 v_F}\int_0^\infty dk\, \cos(ka)\Lambda_\alpha^2(k) \,. \tag{3.40}$$

An effective Hamiltonian for the localized spins is obtained from Eq. (3.38), by taking appropriately chosen expectation values for the conduction electron Bose fields. Since the Bose fields enter only at order J in the transformed Hamiltonian, Honner and Gulácsi [137] approximated these fields by their non-interacting $J = 0$ expectation values†

$$\langle \phi_\sigma(j) \rangle \;=\; \langle \theta_\sigma(j) \rangle \;=\; 0\,. \tag{3.41}$$

This completely eliminates the conduction electron Bose fields and gives an effective Hamiltonian for the localized spins only,

$$\begin{aligned} H_{\text{eff}} \;=\; & -\mathcal{J} \sum_j S_j^z S_{j+1}^z \\ & + A \frac{Ja}{\alpha} \sum_j \{\cos[K(j)] + \cos[2k_F ja]\} S_j^x \\ & - A \frac{Ja}{\alpha} \sum_j \{\sin[K(j)] \sin[2k_F ja]\} S_j^z \,. \end{aligned} \tag{3.42}$$

The remainder of this section is devoted to a survey of the properties of this effective Hamiltonian.

Since the ferromagnetic double-exchange coupling $\mathcal{J}$ is of order J^2, it is immediate from Eq. (3.42) that H_{eff} describes ferromagnetic ordering of the localized spins for strong coupling $J/t \gg 1$ for all fillings $n < 1$. As described previously, $K(j)$, defined in Eq. (3.39) vanishes whenever the ground state is ferromagnetic, thus the destruction of ferromagnetic ordering at weak coupling is governed by the second term in Eq. (3.42) and the effective Hamiltonian takes the form of a transverse-field Ising chain in the phase transition regime. Thus the Kondo lattice undergoes a quantum ferromagnetic to paramagnetic phase transition at a filling dependent critical coupling J_c. A great deal is known about the transverse-field Ising chain, in particular the critical line for the transition is known [153–155], which then gives the critical line of the Kondo lattice [137],

$$\frac{J_c}{t} = \frac{8\pi^2 A \sin(\pi n/2)}{\alpha \int_0^\infty dk \, \cos(ka) \Lambda_\alpha^2(k)} \,. \tag{3.43}$$

The renormalization group analysis [154,155] of the Ising chain with a transverse field features a Griffiths phase, where anomalous clusters of double-exchange ordered localized spins survive into the paramagnetic region and similarly, disordered regions of paramagnetism survive into the ferromagnetic phase. These regions are due to

†In the light of the numerical results presented in section 3.7, it has become apparent that this approximation is not reliable near to half-filling. This is discussed in section 3.7.2.

the incommensurability of the conduction band filling with respect to the lattice of localized spins and the consequent inability of the conduction band to either totally order or totally disorder the localized spins as the transition is crossed. Although these anomalous regions are very dilute, they dominate the low-energy properties of the spin chain. Strictly speaking, an incommensurate filling is not possible to obtain in a numerical study of a finite lattice. Similar effects could perhaps occur due to, *e.g.* open boundary conditions or simply from numerical truncation, causing small deviations in the density and wavelength of the correlations. However numerical perturbations will only lead into an anomalous region if it is energetically favorable for the finite system to undergo a slight phase separation, into a region of incommensurate filling in the anomalous phase, with a compensating region of different phase. However the numerical results for antiferromagnetic coupling $J > 0$ show no sign of any instability toward phase separation. There is a phase separated region for $J < 0$ observed numerically [156], but it appears unrelated to the Griffiths phase.

Fig. 3.2 shows the phase diagram from reference [137]. The critical line was constructed by fitting Eq. (3.43) to the numerical data that was available at the time.

3.7 Numerical Results

This section details the DMRG results obtained by the author for the antiferromagnetic $J > 0$ Kondo lattice model. The focus is on the region between quarter-filling and half-filling, where comparatively little is known. After describing the construction of the $SO(4)$-invariant Hamiltonian, the obtained phase diagram is presented, focusing on the newly discovered intermediate coupling ferromagnetic region. The order of the phase transitions has been a controversial issue for several years, with analytic results suggesting that the transition should be second order, but conflicting numerical results suggesting a first order transition. Some progress toward clarifying these issues is presented in section 3.7.3. The nature of the ground state, specifically the location of the Fermi surface (in one dimension, this 'surface' reduces to the two Fermi points $+k_F$ and $-k_F$), has been the focus of recent studies on the Kondo lattice. This is discussed in section 3.7.4, followed by a discussion of the Luttinger liquid parameters in section 3.7.5. Clearly, without a rigorous error analysis any numerical study is at best a suggestive guide and at worst dangerously misleading. The justification of the presented numerical results is discussed in section 3.7.6.

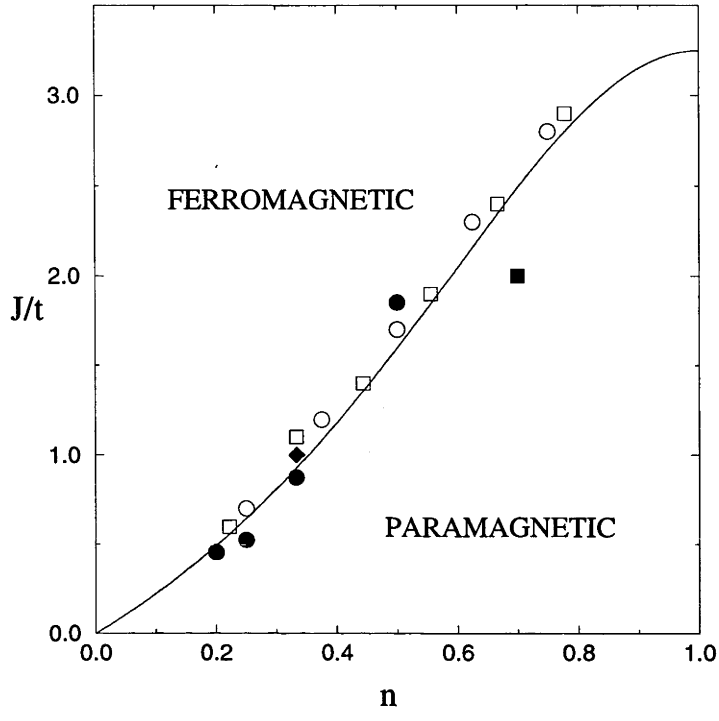

Figure 3.2: The phase diagram of the Kondo lattice model for antiferromagnetic coupling $J > 0$, as determined by bosonization [137]. The fitting of the parameters is from numerical data; open circles and squares are exact diagonalization data from reference [157], the solid square is Monte Carlo data from reference [120], the solid diamond and solid circles are DMRG data from references [39] and [28] respectively.

3.7.1 Construction of the $SO(4)$ Hamiltonian

The construction of the DMRG algorithm for the Kondo lattice model with $SO(4)$ symmetry proceeds essentially the same as that for the Hubbard model, described in chapter 2. Written in terms of the conduction band creation/annihilation operator at the i^{th} site $\boldsymbol{c}_i^{[1/2,1/2]}$, conduction band spin operator $\boldsymbol{S}_{c,i}^{[0,1]}$ and localized spin operator $\boldsymbol{S}_{f,i}^{[0,1]}$, the Hamiltonian of the Kondo lattice model with open boundary conditions reads

$$H = 2t \sum_{i=1}^{L-1} [\boldsymbol{c}_i^{[1/2,1/2]} \times \boldsymbol{c}_{i+1}^{[1/2,1/2]}]^{[0,0]} - \sqrt{3} J \sum_{i-1}^{L} [\boldsymbol{S}_{c,i}^{[0,1]} \times \boldsymbol{S}_{f,i}^{[0,1]}]^{[0,0]} . \tag{3.44}$$

The number of $SO(4)$ basis elements is, from table 3.1 described previously, just three, so the single site operators are represented as 3×3 matrices. Choosing a

mapping of the basis state kets onto vectors in $\mathbb{R}^3$,

$$\begin{aligned} \|0,0\rangle &\equiv (1,0,0)\,, \\ \|0,1\rangle &\equiv (0,1,0)\,, \\ \|1/2,1/2\rangle &\equiv (0,0,1)\,, \end{aligned} \tag{3.45}$$

the single site operators can be written in explicit form. The matrix elements of $\boldsymbol{c}_i^{[1/2,1/2]}$ are, from the Wigner-Eckart theorem Eq. (2.70),

$$\boldsymbol{c}_i^{[1/2,1/2]} = \begin{cases} \begin{pmatrix} 0 & 0 & \sqrt{2} \\ 0 & 0 & \sqrt{2} \\ -\sqrt{2}/2 & \sqrt{3/2} & \end{pmatrix}, & \text{if } i \text{ even;} \\ \begin{pmatrix} 0 & 0 & \sqrt{2} \\ 0 & 0 & \sqrt{2} \\ \sqrt{2}/2 & -\sqrt{3/2} & \end{pmatrix}, & \text{if } i \text{ odd.} \end{cases} \tag{3.46}$$

This explicitly takes into account the bipartite lattice and the choice of signs ensures the Hermiticity of $[\boldsymbol{c}_i^{[1/2,1/2]} \times \boldsymbol{c}_{i+1}^{[1/2,1/2]}]^{[0,0]}$. Similarly to the case of the Hubbard model, $[\boldsymbol{c}_i^{[1/2,1/2]} \times \boldsymbol{c}_j^{[1/2,1/2]}]^{[0,0]}$ is Hermitian if sites i and j are in different sub-lattices and skew-Hermitian if sites i and j are in the same sub-lattice.

Since the spin interaction term is a sum of operators acting only on a single site, it is not necessary to use the separate $\boldsymbol{S}_{c,i}^{[0,1]}$ and $\boldsymbol{S}_{f,i}^{[0,1]}$ operators, but instead this term is absorbed into the local single site Hamiltonian H_i^{local}, which, in our choice of site basis, has the form

$$H_i^{\text{local}} = \begin{pmatrix} -3J/4 & 0 & 0 \\ 0 & J/4 & 0 \\ 0 & 0 & 0 \end{pmatrix}. \tag{3.47}$$

These two operators are enough to completely specify the Hamiltonian of the Kondo lattice. In contrast, the Hamiltonian written using $U(1)$ symmetries requires more operators, $c_{\uparrow,i}^\dagger$, $c_{\downarrow,i}^\dagger$, $c_{\uparrow,i}$ and $c_{\downarrow,i}$. So although the construction of the DMRG algorithm is more complicated, with various $6j$ and $9j$ symbols entering into the generic construction of the algorithm, the model-dependent operators, represented by the reduced matrices Eq. (3.46) and Eq. (3.47) are actually simplified, in the sense that we have gone from five operators over an eight dimensional basis, to two operators over a three dimensional basis.

3.7.2 Numerical phase diagram

The phase diagram calculated from the DMRG appears in Fig. 3.3. The solid curve is a fitting of the critical line from the bosonization result of Eq. (3.43). The

location of the paramagnetic/ferromagnetic phase transitions was determined by calculating the lowest energy state in two or more total spin sectors and determining the critical coupling of the crossover point. The most striking feature of this phase diagram is the previously unrecognized regions of ferromagnetism in the intermediate coupling regime close to half filling. As far as we know, this region has not been predicted by any analytic calculations. On reviewing the older numerical calculations, hints of this region can be seen but the results were discarded by the respective authors as numerical instability. The exact diagonalization study by Tsunetsugu, Sigrist and Ueda [157] found ferromagnetism at $J/t = 1.5$ at filling $n = 0.75$, but the calculation was coarse grained enough that this was the only data point that falls within the intermediate coupling ferromagnetic region. Shibata, Ueda, Nishino and Ishii [158] noted that their DMRG calculations for 10 and 20 site clusters indicated a region of ferromagnetism at $1.6 < J/t < 1.8$ at filling $n = 0.9$, but they do not report any ferromagnetism for larger lattices, nor did they comment on the physical origin of this phase. The recent review by Tsunetsugu, Sigrist and Ueda [118] makes no mention of ferromagnetism for intermediate coupling near half-filling. Indeed, this paper makes the bold claim that the one dimensional ground state phase diagram was completely known, a claim that was repeated in a later work by Shibata and Ueda [159], again without mentioning the intermediate coupling ferromagnetism.

Since the intermediate coupling ferromagnetism has only previously been seen in very small systems, it is natural to question whether this constitutes a finite size effect. In a thermodynamic system the conduction band forms a continuum, whereas in a finite size system, the conduction band states are necessarily gapped (although the gap is very tiny for even a moderate size lattice), which could potentially introduce distortions in the phase diagram. Figure 3.4 shows the energy difference between the lowest energy state in every spin sector, from $0 \leq s \leq q$, for a 60 site lattice with $q = 9$, corresponding to filling $n = 0.7$. The baseline is the $s = 9$ state, so the ground state is fully polarized ferromagnetic when all the energy differences are positive and less than fully polarized (or paramagnetic) when the energy differences are negative. The $s = 9$ state was chosen as the baseline because the numerical error in the energy is smaller for this state (*cf.* section 3.7.6). This clearly shows four different regimes. From the bosonization and the small J/t perturbative expansion, the degeneracy of the spin states at $J = 0$ is expected to be lifted by corrections of order $(J/t)^2$. The obtained numerical results do not extend to very weak coupling, but the results down to $J/t = 0.5$ are consistent with this. However, the excitation energy to the ferromagnetic state reaches a maximum at

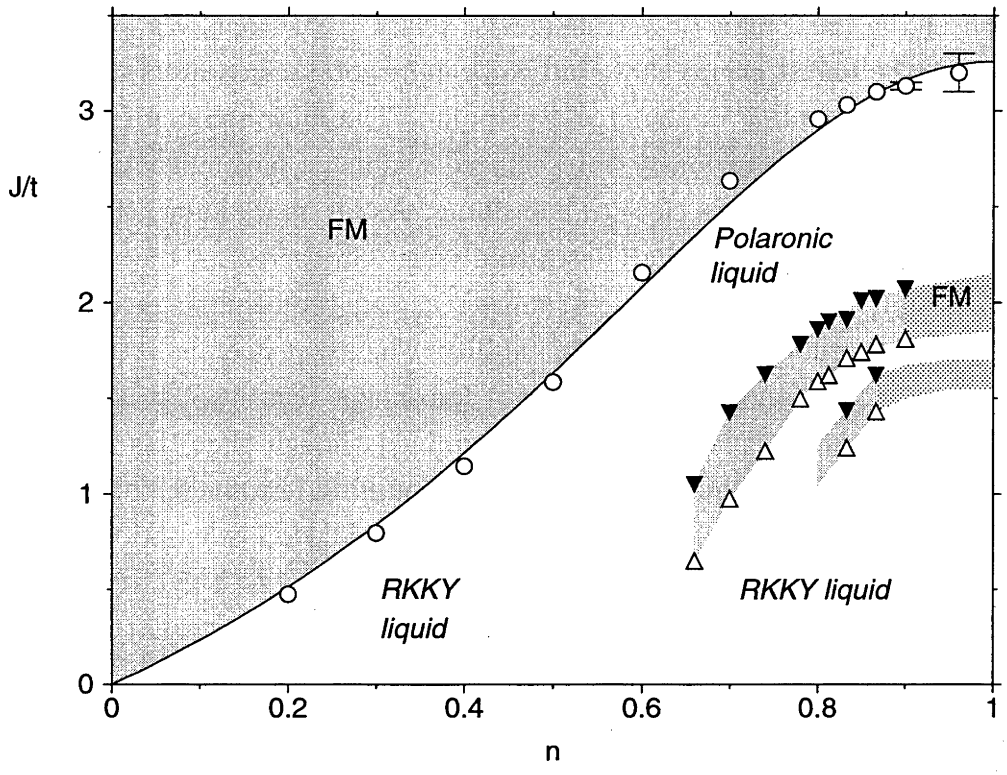

Figure 3.3: The phase diagram of the Kondo lattice model for antiferromagnetic coupling $J > 0$.

a relatively low $J/t \sim 0.65$ and then rapidly decreases again. Thus it is clear that the weak coupling regime does not extend to very large J/t. This is supported by Fig. 3.5. This figure shows the kinetic energy T and 'internal energy' U, which is defined by

$$U = J\frac{\partial E}{\partial J} = J\sum_{i=1}^{L}\langle \boldsymbol{S}_i^c \cdot \boldsymbol{S}_i^f \rangle \,. \tag{3.48}$$

The internal energy has an asymptotic large J/t value of $U \to \frac{3}{4}J(L-2q)$, where the conduction electrons localize and form Kondo singlets of energy $3J/4$, leaving $2q$ unpaired f-spins that have zero internal energy. Fig. 3.5 shows that the internal energy is close to the asymptotic large J/t value even for relatively small coupling, indicating that virtually all of the conduction electrons have condensed into Kondo singlets. Thus it is no surprise that the weak coupling regime only survives for fairly small coupling J. What is more surprising is that for slightly larger coupling, the system becomes ferromagnetic. This is unlikely to be caused by double exchange; the total spin of the conduction electrons alone is rather small, unlike in the double exchange regime where the conduction electrons align spin parallel, but antiparallel to the f-spins. This phase does perhaps fit into the bosonization picture however.

The original calculation of Honner and Gulácsi [137] approximated the conduction band Bose fields by the non-interacting $J = 0$ value, justified by expectation that these terms in the bosonized Hamiltonian will become irrelevant at both weak and strong coupling (*cf.* section 3.6). The available numerical data at the time did not indicate that there was interesting physics in the intermediate coupling regime, so that it was thought that this approximation was completely satisfactory. If the spin Bose fields are instead taken to be the expectation value of the regular sine-Gordon model, which was found by Zachar, Kivelson and Emery [160] as an effective model of the Kondo lattice in the large density limit, the effective Hamiltonian is [161]

$$\begin{aligned} H_{\text{eff}} &= -\frac{J^2\mathcal{A}}{2\pi^2 v_F}\sum_j S_j^z S_{j+1}^z \\ &\quad +2J\mathcal{B}\sum_j \left\{1-\left(\frac{\langle\Phi_\sigma\rangle_{\text{sG}}^2}{2}\right)\left(1+\frac{J}{2\pi v_F}\right)^2+\cos(2k_F j)\right\} S_j^x \,, . \end{aligned} \tag{3.49}$$

where $\langle\Phi_\sigma\rangle_{\text{sG}}^2$ is the expectation value of the spin density of the sine-Gordan model and $\mathcal{A}$ and $\mathcal{B}$ are cutoff functions arising from the bosonization. The intermediate coupling ferromagnetic region can be modeled by this Hamiltonian, however there are more parameters that are undetermined from the bosonization than was the case for the original effective Hamiltonian in Eq. (3.42). This gives an extremely wide variety of possible phase transitions, so this effective Hamiltonian is not useful without a lot of numerical data to fit the undetermined parameters.

A finite-size scaling of the gap between the ferromagnetic ground state and the paramagnetic singlet state, for a point in the middle of the intermediate coupling ferromagnetic phase at $J/t = 1.1$ and filling $n = 0.7$, appears in Fig. 3.6. This shows that the energy of the singlet state is always higher than the ground state energy and that this almost certainly persists to the thermodynamic limit. The energy gap is expected to scale linearly with the lattice size, although there are clearly deviations, presumably due to the open boundary and relatively small lattice sizes. Unfortunately, for larger lattices, $L \gtrsim 120$ in this case, it is difficult to calculate the energies with enough accuracy.

For larger coupling, $1.4 \leq J/t \leq 2.6$ in Fig. 3.4, the ground state is again paramagnetic and in this region the DMRG is numerically very stable. The spin excitations here have been calculated with enough accuracy to obtain reliably the spin susceptibility, which is discussed in section 3.7.5. Above the critical J/t bounding this paramagnetic region, double-exchange dominates and the system is in the strong coupling ferromagnetic phase.

At larger filling, above $n \gtrsim 0.8$, a *third* ferromagnetic region appears. The first signs of this phase are apparent in the magnitude of the spin excitations at $n = 0.8$,

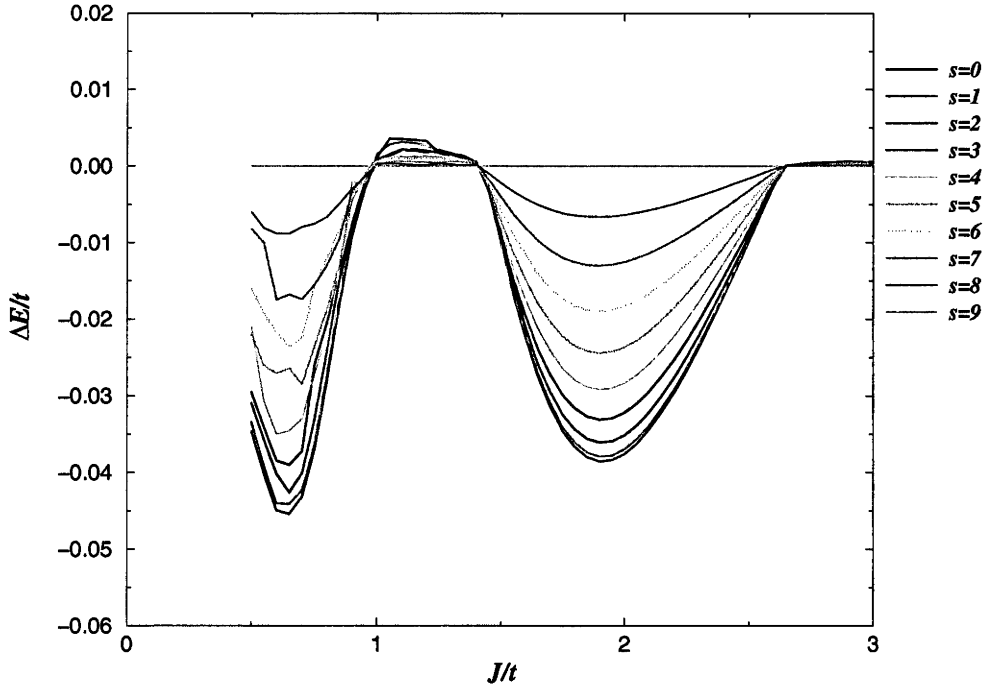

Figure 3.4: The energy difference between each spin state, relative to the energy of the fully polarized ferromagnetic state, for a 60 site lattice at $q = 9$, corresponding to a filling of $n = 0.7$.

shown in Fig. 3.7. There is a quite pronounced reduction in the magnitude of the spin excitations and there is also a level crossing between the $s = 1$ and $s = 2$ states at $1.05 < J/t < 1.25$, suggesting that the ground state here is a partially polarized ferromagnet. However, although the numerical accuracy in this region is enough that the feature in the spin excitation energy is significant, the difference in energies of the neighboring $s = 0$ and $s = 1$ states is more sensitive to error (*cf.* section 3.7.6). Above filling $n = 5/6$, the third ferromagnetic region is fully polarized. Fig. 3.8 shows the difference between the energy states of different spin for a 60 site lattice with $q = 5$, corresponding to filling $n = 5/6$. At this filling, the third ferromagnetic region is extremely pronounced, with the excitation energy to the singlet spin state being comparatively big, much bigger than the spin excitation energy in the second ferromagnetic phase.

3.7.3 Order of the phase transitions

The order of the phase transition in the Kondo lattice has long been a source of controversy. The bosonization results [137] suggest that, via the mapping onto the transverse Ising chain, the phase transition should be second order, with the

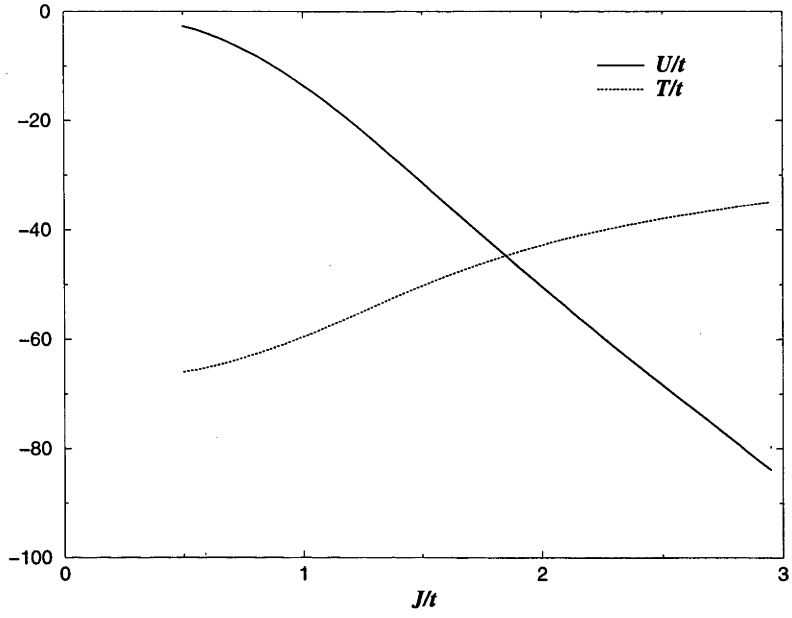

Figure 3.5: The kinetic and internal energies of the 60 site system with $q = 9$.

ground state magnetization M obeying

$$M = \left(\frac{J - J_c}{J_c} \right)^{\delta} , \tag{3.50}$$

for $J > J_c$. The exponent δ varies with the filling. However, early numerical studies were inconclusive with respect to the order of the transition. The exact diagonalization study by Tsunetsugu *et al.* [157] found a partially polarized ground state at low electron density, but not at higher fillings. Fig. 3.9 shows the ground state spin as a function of the coupling, in the vicinity of the phase transition for a 40 site lattice at quarter filling, $n = 1/2$. This shows that the second derivative of the energy with respect to the magnetization, $\partial^2 E/\partial M^2$, is always positive and hence the transition is second order. The energy levels near the transition are numerically close to degeneracy, so this is a rather sensitive calculation. A 40 site lattice is the largest that could be solved with enough accuracy to be able to determine the energy difference between the spin states. However, the sign of $\partial^2 E/\partial M^2$ is most unlikely to change as a function of the lattice size. The numerical results are not accurate enough to attempt calculating the critical exponent δ in Eq. (3.50), but it would not take a huge increase in computation time to do this, at least for moderately small lattices. There is a small instability in Fig. 3.9, where the energy for even values of the spin s is slightly lower than the energy for odd values of the spin, which is most likely a finite size effect. The dotted lines in the figure interpolate between

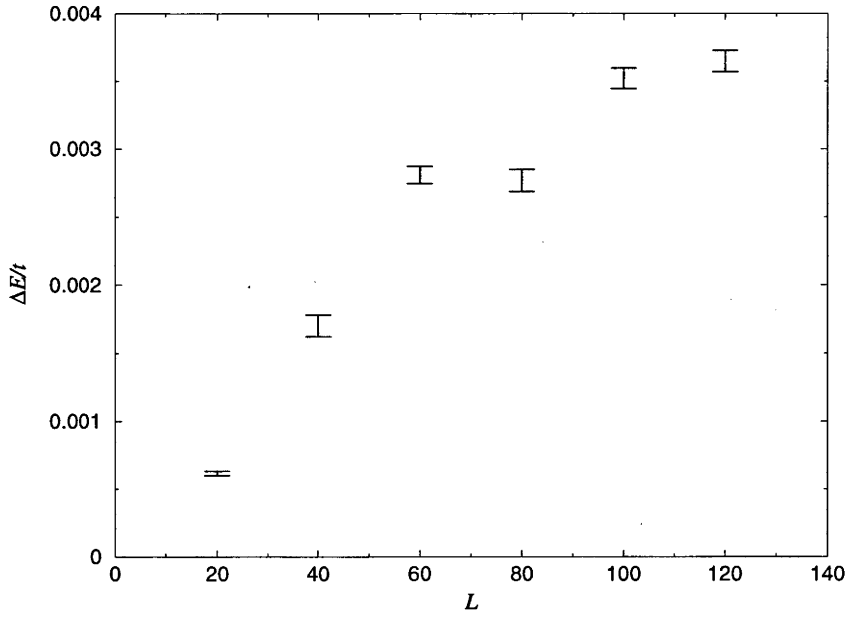

Figure 3.6: The energy difference between the ferromagnetic ground state and the singlet excited state as a function of the lattice size, for $J/t = 1.1$ and filling $n = 0.7$.

neighboring spin energies to minimize this instability.

The order of the phase transitions in the intermediate coupling ferromagnetic regime has not been determined. The calculations used to determine the phase diagram are not accurate enough to determine the sign of $\partial^2 E/\partial M^2$ in the vicinity of the phase transitions, however the numerical evidence would tend to support all phase transitions being second order. This is also supported by the bosonization results using the sine-Gordon spin expectation values for the Bose fields, discussed in section 3.7.2

3.7.4 Fermi surface sum rules

The location of the Fermi points in the one-dimensional Kondo lattice model has been a controversial issue for several years. The early exact diagonalization study by Tsunetsugu *et al.* [157] suggested that in the weak coupling regime, the model describes a paramagnetic Luttinger liquid and hence the dominant spin and charge correlations are at $2k_F$, where k_F is the Fermi wave number, found to be given by the conduction electrons only, *i.e.* $k_F = k_{F_{\text{small}}} \equiv \pi n_c/2$. However, the Kondo lattice can be derived in the appropriate limits from the periodic Anderson model, which is conventionally assumed to have a 'large' Fermi surface, such that the f-spins are included. If this picture also applies to the Kondo lattice, then the

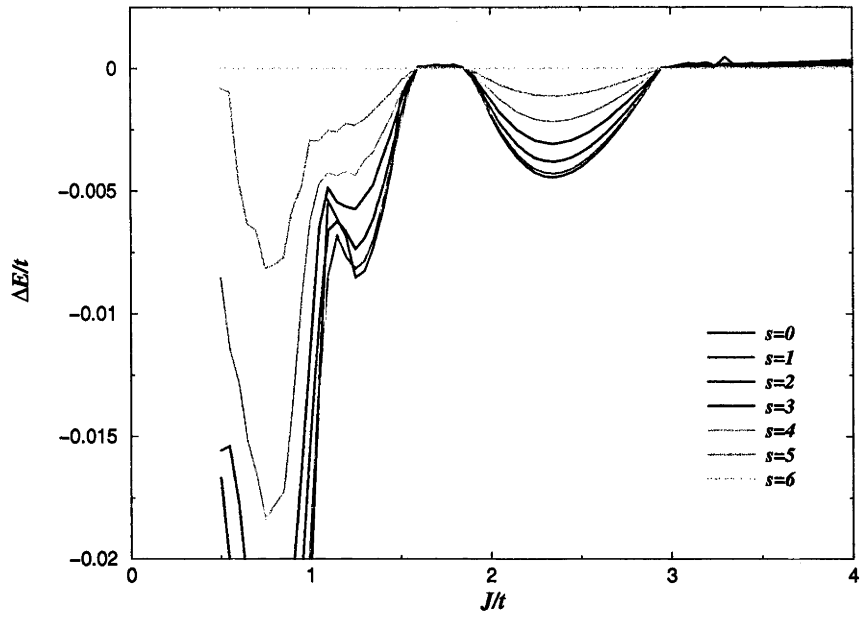

Figure 3.7: The energy difference between each spin state, relative to the energy of the fully polarized ferromagnetic state, for a 60 site lattice at $q = 6$, corresponding to a filling of $n = 0.8$. The strong coupling ferromagnetic phase occurs above the critical coupling $J/t \simeq 2.95$. There is a second region of fully polarized ferromagnetism at $1.60 < J/t < 1.85$. Between $1.05 < J/t < 1.25$ there is a partially polarized ground state.

Fermi surface should be given by $k_F = k_{F_{\text{large}}} \equiv \pi(n_c + 1)/2$.

A later study by Moukouri and Caron [39] examined the Kondo lattice at density $n_c = 0.7$ and found agreement with the 'small' Fermi surface picture, even away from the weak coupling regime. This was also the conclusion of a Monte Carlo study by Troyer and Würtz [120]. However, Ueda, Nishino and Tsunetsugu [162] found that the Kondo lattice, with the addition of a frustrated next-nearest neighbor hopping, has a large Fermi surface. It remains uncertain as to the extent that this result applies when the next-nearest neighbor hopping is removed. In particular, the additional term changes the phase diagram quite substantially, with the strong coupling regime being an additional paramagnetic phase, rather than the usual ferromagnetic phase. Ueda *et al.* only found a large Fermi surface in the strong coupling paramagnetic regime with the next-nearest neighbor hopping added, but they suggested that the two paramagnetic phases may be adiabatically connected, in which case it is likely that the Fermi surface is large throughout the whole of the phase diagram. Even if this is true, the addition of the next-nearest neighbor hopping breaks the $SO(4)$ symmetry and the bipartite structure of the Kondo lattice, which is expected to have a significant effect.

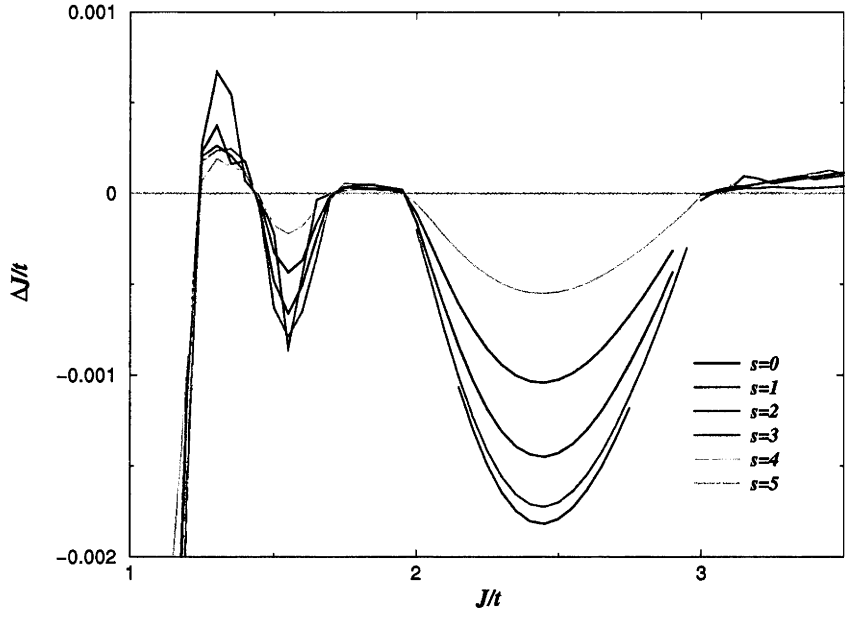

Figure 3.8: The energy difference between each spin state, relative to the energy of the fully polarized ferromagnetic state, for a 60 site lattice at $q = 5$, corresponding to a filling of $n = 5/6$. There are three distinct regions of fully polarized ferromagnetism.

The large Fermi surface picture was given further strength by a second study by Moukouri and Caron [163], this time for the Kondo lattice with an additional direct $f - f$-spin interaction J_H. An antiferromagnetic coupling was used to stabilize the paramagnetic state for larger values of the Kondo coupling J, where the f-spin structure factor and the conduction electron momentum distribution both indicated a large Fermi surface. However the results for weak coupling were not clear; the density fluctuations introduced in the infinite-size DMRG algorithm (*cf.* section section 1.2.1) effectively made this region numerically inaccessible. The conclusion, that the Fermi surface is large for the pure Kondo lattice with $J_H = 0$, is dependent on the assumption that the strong and weak coupling paramagnetic phases of the Kondo lattice model are adiabatically connected. Further studies of Friedel oscillations in the pure Kondo lattice model, by Shibata *et al.* [158] placed the existence of a large Fermi surface in the strong coupling end of the paramagnetic region beyond doubt, however little has been said by these authors on the weak coupling regime. In particular, if the hypothesis of reference [158], that the Fermi surface of the Kondo lattice is always large, then an additional mechanism is needed to explain the $2k_{F_{\text{small}}}$ correlations which are observed both numerically and in bosonization calculations [137]. It is notable that while reaching the conclusion that the Fermi

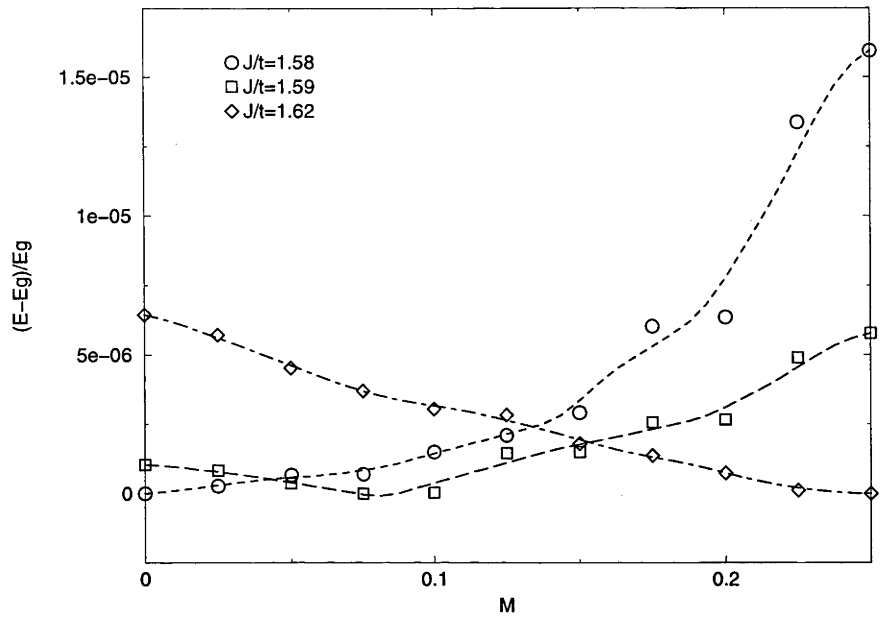

Figure 3.9: The magnetization per site $M = s/L$, as a function of the coupling J in the vicinity of the phase transition at quarter filling $n = 0.5$, for a 40 site lattice.

surface is always large, Shibata *et al.* [158] did not present any calculations for coupling below $J/t = 1.5$. In this work, Shibita *et al.* did find a ferromagnetic region at filling $n = 0.9$, between $1.6 \lesssim J/t \lesssim 1.8$, but made no comment on the physics of this phase, except for noting that it appears as a level crossing between the paramagnetic and fully polarized[†] ferromagnetic states [158], suggesting a first order transition. This observed ferromagnetic region was ignored in later papers by the same authors [118, 159].

In a finite size calculation, the Fermi wave number should appear as a finite gap in the conduction electron momentum distribution. In one dimension, the gap vanishes only in the thermodynamic limit, with a logarithmic size dependence. In the calculation for the Kondo lattice with the direct $f - f$ spin interaction [163], there is no evidence that such a gap opens at $k_{F_{\text{small}}}$ in the weak coupling regime. However, Moukouri and Caron used a fixed $J_H = 0.5$, so correspondence between the weak coupling regime $J/t \ll 1$ of this model and the weak coupling regime of the pure Kondo lattice with $J_H = 0$ is not clear. It is notable that Moukouri and Caron found no evidence for a ferromagnetic region at intermediate coupling, however this is not such as surprise as several other numerical studies failed to see this phase[‡]. Another possibility that requires further investigation is that the

[†]with $s = (L - N)/2$

[‡]The threshold of accuracy required to observe the intermediate coupling ferromagnetism is

intermediate coupling regime is unstable with respect to the added $f - f$ spin interaction.

The current results indicate that the dominant correlations are at $2k_{F_{\text{small}}}$ in the weak coupling paramagnetic phase, in agreement with most previously published results that have examined this regime (for example references [28, 163]), with the exception of the Friedel oscillation results for $J/t = 1.5$ at filling $n = 0.9$, where a large Fermi surface was found [158]. Thus the Friedel oscillation calculations are in disagreement with the spin correlation calculations at this point. The current results suggest that the large Fermi surface appears only above the intermediate coupling ferromagnetic region. Some numerical data of the conduction electron momentum distribution and f-spin structure factor for a range of couplings at filling $n = 0.6$ appear in Fig. 3.10. This shows the crossover from $2k_{F_{\text{small}}} = 0.6\pi$ correlations for small coupling to $2k_{F_{\text{large}}} = 0.4\pi$ for stronger coupling, together with the appearance of a feature at $k_{F_{\text{large}}}$ in the conduction band momentum distribution.

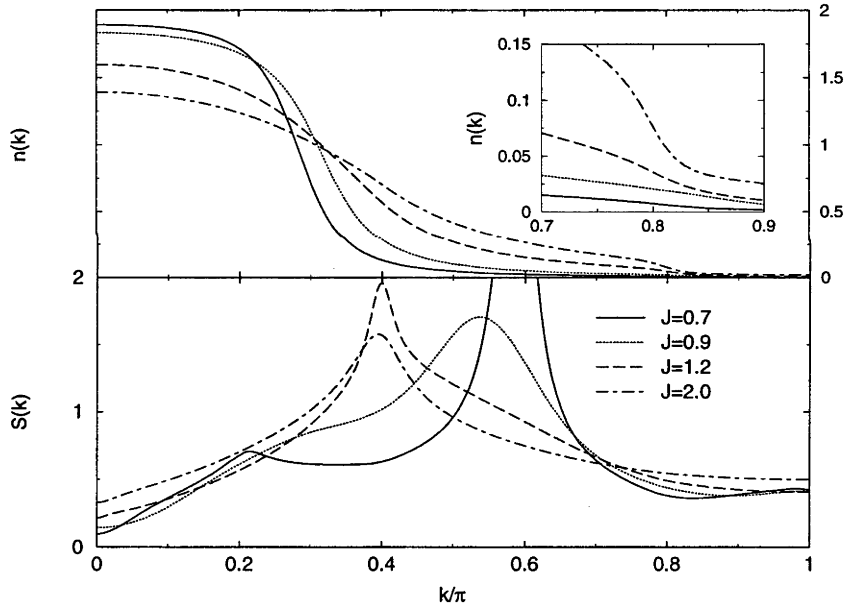

Figure 3.10: Conduction band momentum distribution $n(k)$ and f-spin structure factor $S(k)$ for the Kondo lattice at filling $n = 0.6$. The inset shows the appearance of a feature at $k_{F_{\text{large}}}$ for stronger coupling.

The importance of this controversy resides in the application of the Luttinger theorem [164] in one-dimension. This theorem says that the volume inside the Fermi surface is invariant as the interaction strength changes, as long as the number of particles does not change. This theorem has been proven under rather general con-

discussed in section 3.7.6.

ditions for three dimensions and the applicability of the theorem to one-dimension has been the focus of much interest for many years. The theorem was proven by Luttinger by demonstrating that the correction to the volume vanishes order by order in the perturbative expansion [164]. Clearly, this proof breaks down in the presence of non-perturbative effects, typical in a one-dimensional system.

In 1997, Yamanaka, Oshikawa and Affleck [165] presented a proof of the Luttinger theorem applicable to a wide range of one-dimensional models, including the Kondo lattice. At this time, it appeared that the weight of evidence suggested that the Fermi surface of the Kondo lattice is always large, even in the weak coupling regime. The current results, indicating that there is a large region of ferromagnetism at intermediate coupling cast a doubt over this result, as the Luttinger theorem is not required to hold across a phase transition. Thus it remains possible that the Fermi surface is small in the weak coupling regime and changes discontinuously to a large Fermi surface as the coupling j is increased. This however remains conjecture. The appearance of multiple intermediate ferromagnetic phases further complicates the picture. The properties of the 'nested' paramagnetic phase(s) in the intermediate coupling regime and in particular the nature of the dominant correlations and the Fermi surface, has not yet been investigated.

3.7.5 Luttinger liquid parameters

The spin-1/2 Luttinger liquids have gapless spin and charge excitations, characterized by the velocity v_k and correlation exponent K_k, with $k = \sigma$ for the spin, $k = \rho$ for the charge degrees of freedom. In the paramagnetic region where the ground state is a spin singlet, the spin $SU(2)$ symmetry fixes the correlation exponent K_σ to be unity [150]. The low-energy physics of a Luttinger liquid is completely determined by these parameters. In particular, the spin and charge susceptibilities are given by

$$\chi_\sigma = \frac{2}{\pi v_\sigma}, \tag{3.51}$$

$$\chi_\rho = \frac{2}{\pi v_\rho}. \tag{3.52}$$

The asymptotic forms of the density-density and spin-spin correlation functions are [150]

$$\langle n(0)n(x)\rangle \sim A_1 \cos(2k_F x)x^{-(1+K_\rho)} + A_2 \cos(4k_F x)x^{-4K_\rho}, \tag{3.53}$$

$$\langle \boldsymbol{S}(0)\cdot\boldsymbol{S}(x)\rangle \sim \cos(ref2k_F x)x^{-(1+K_\rho)}, \tag{3.54}$$

In the Luttinger model, when K_ρ is small ($\leq 1/3$) the $4k_F$ charge density wave oscillations dominate over the $2k_F$ ones. For larger K_ρ (corresponding to weaker coupling), the $2k_F$ correlations dominate. Shibata and Ueda [159] examined charge density Friedel oscillations induced by the open boundary conditions and spin density Friedel oscillations induced by a magnetic field applied at the edges of the lattice. The asymptotic form of the Fridel oscillations is expected to be the same as the correlation functions [159]. Thus, with a careful numerical fit, Shibata and Ueda were able to determine K_ρ in a small region of the phase diagram. In addition, the spin and charge susceptibilities are relatively easy to calculate, which in combination allows the spin and charge velocities to be determined, via Eq. (3.51) and Eq. (3.52). The calculated K_ρ from Shibata and Ueda [159] appears in Fig. 3.11. This data is somewhat surprising. The limiting case of $K_\rho \to 1/2$ as $J \to \infty$ is clear as in this limit the Kondo lattice maps onto the $U = \infty$ Hubbard model (*cf.* section 3.4.3), where the correlation exponent is given by the spinless fermion value of $K_\rho = 1/2$. What is surprising is that the exponent decreases as the coupling strength decreases. This means that the effective repulsive interaction between the conduction electrons *increases* in strength as the coupling J is reduced. For $J = 0$, the conduction band is non-interacting, giving $K_\rho = 1$. The expected behavior in the weak coupling regime would be (by analogy with the Hubbard model) for K_ρ to converge continuously to the non-interacting value as $J \to 0$.

The momentum distribution function of a Luttinger liquid is given by [150]

$$n(k) \sim \frac{1}{2} - A_1 \mathrm{sign}(\mathrm{k} - \mathrm{k_F})|\mathrm{k} - \mathrm{k_F}|^\alpha - \mathrm{A_2}(\mathrm{k} - \mathrm{k_F}) \,, \tag{3.55}$$

where the exponent α is

$$\alpha = (K_\rho + 1/K_\rho - 2)/4 \,. \tag{3.56}$$

The data in Fig. 3.11 suggests that, at the lower boundary of the large Fermi surface regime, $\alpha = 1$ and thus the singularity in the momentum distribution disappears [159]. Whether this behavior continues into the weak coupling regime is an interesting issue that has not yet been resolved.

No new data has been obtained in this thesis for the correlation exponent K_ρ. The method used by Shibata and Ueda [159] to obtain the spin Friedel oscillations violates spin $SU(2)$ symmetry and the presence of large short-range corrections to the asymptotic behavior of the correlations makes a direct fit difficult. However, an independent check of the data in Fig. 3.11 is obviously important. The spin and charge susceptibilities have been calculated however. The spin susceptibility in the large Fermi surface regime at filling $n = 0.7$ appears in Fig. 3.12. This agrees with the limited data published by Shibata and Ueda [159], reproduced in table

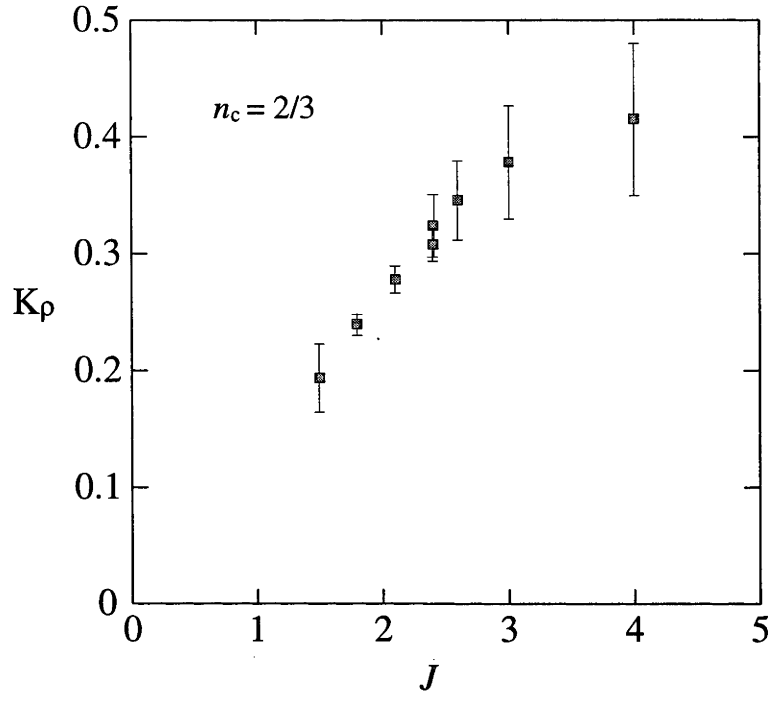

Figure 3.11: Correlation exponent K_ρ for filling $n = 2/3$ and $t = 1$. Fig. 11 of reference [159].

3.3 for filling $n = 2/3$. Unfortunately, the data for $J/t = 1.5$, where the current results indicate that the spin susceptibility should be sharply increasing, were not given. The charge susceptibility at filling $n = 5/6$ is shown in Fig. 3.13. The non-interacting susceptibility, at $J = 0$ where $v_{\rho,\sigma} \to v_F$, is also shown. It appears that the charge susceptibility for the Kondo lattice does converge smoothly in the $J \to 0$ limit. The asymptotic large J value should tend to the large U limit of the Hubbard model, where $v_\rho = 2t \sin(\pi n)$, giving in this case $\chi_\rho(U = \infty) = 0.6366$ at filling $n = 5/6$. This limiting behavior also looks quite plausible from the data in Fig. 3.13.

3.7.6 Error analysis

In the numerical calculations, the energies were calculated by an extrapolation to large number of states kept, based on sweeps of typically 400, 380, 360, 340, 320 states kept. For the calculation of the order of the phase transition, 500 states were kept. Fig. 3.14 shows the degree of the block representation as a function of the number of states kept, at the half-filled ground state of spin zero and pseudospin zero. In this case, the degree of the representation is equal to the number of block

Table 3.3: Luttinger liquid parameters of the one-dimensional Kondo lattice model at density $n = 2/3$. From Table I of reference [159].

J/t	K_ρ	v_σ	χ_σ	v_ρ	χ_ρ
1.5	0.19±0.03			0.30±0.06	0.42
1.8	0.24±0.02	0.014	46	0.41±0.06	0.38
2.0	0.27±0.02	0.011	56	0.48±0.06	0.36

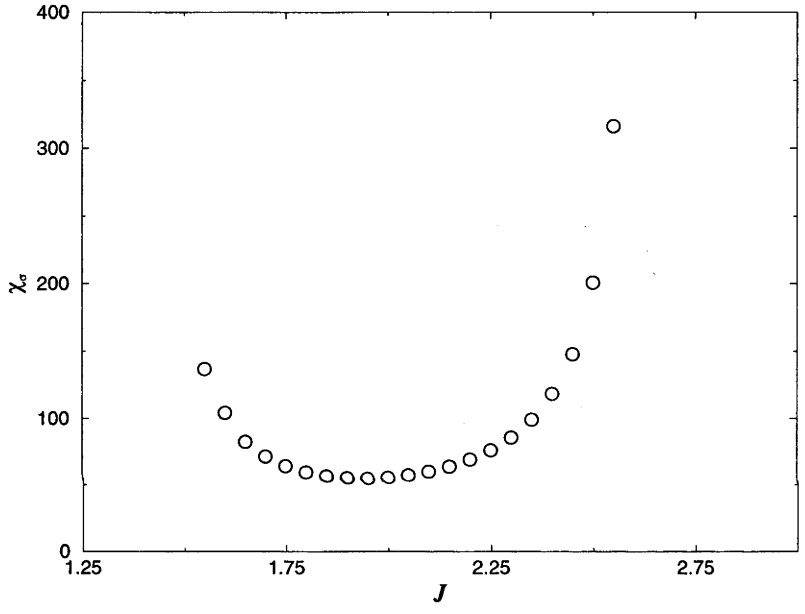

Figure 3.12: The spin susceptibility of the Kondo lattice model in the large Fermi surface regime at filling $n = 0.7$, calculated from a 60 site lattice.

states that would need to be kept in the Abelian $U(1) \otimes U(1)$ representation, used in all previous DMRG studies on the Kondo lattice model. For higher spin or pseudospin states, the *relative* advantage of the $SO(4)$ symmetry decreases linearly, until at the maximum possible spin and pseudospin the dimension of the Fock space is unity, independent of the choice of symmetry. The degree δ of the block basis as a function of the number of states kept m follows closely $\delta = 5.71m$, with a very small quadratic dependence. As the number of states kept is increased and states with smaller weight in the wavefunction are included in the basis, the spread of quantum numbers of the states increases. The distribution of quantum numbers is bounded below by the $[0, 0]$ representation of degree 1, but is not bounded above; this leads to the small quadratic dependence. The degree of the representations for

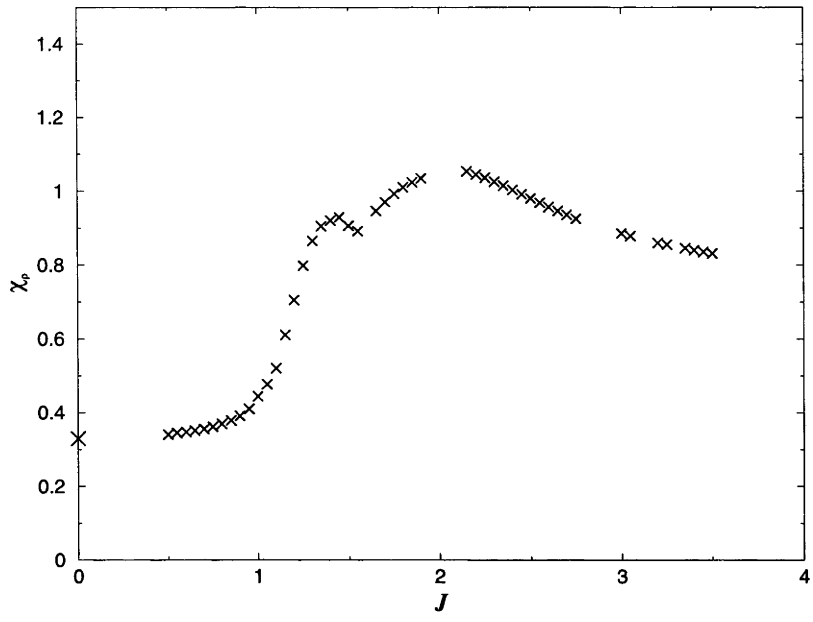

Figure 3.13: The charge susceptibility of the Kondo lattice model at filling $n = 5/6$, calculated from a 60 site lattice.

500 states kept indicates that this is equivalent to well over 3000 states kept using a $U(1) \otimes U(1)$ representation. By this measure, this is by far the most accurate DMRG study that the author is aware of. The largest number of states kept using an algorithm that is directly comparable with that used in this thesis is, as far as is known, 1500 states kept, in a study of the 2-leg Hubbard model [9].

Figures 3.15 and 3.16 show the estimated relative error in the energy, $\sigma_E/|E|$, as a function of the coupling J and spin s, for 60 site lattice and two values of pseudospin, $q = 5$ and $q = 9$. This corresponds to fillings $n = 25/30$ and $n = 7/10$ respectively. These figures show that the relative error depends mostly on the coupling J and is only weakly dependent on the spin s and pseudospin q. This strong dependence on the coupling J is in fact mostly an artifact of the convergence criteria discussed in section 1.6.1. It turns out that for small J, the estimated standard error in the energy of each sweep is comparatively big, implying that the tolerance used for convergence in Eq. (1.73) should be smaller in the weak coupling regime. However, enough accuracy has been achieved even in the weak coupling regime to be able to determine the phase diagram.

To be able to measure the total spin of the ground state, the error in the energy for each total spin s must be less than the energy difference between the spin states. Figures 3.17 and 3.18 show the estimated error in the energy, relative to the size of the largest energy gap between any two spin states, for the same parameter regimes

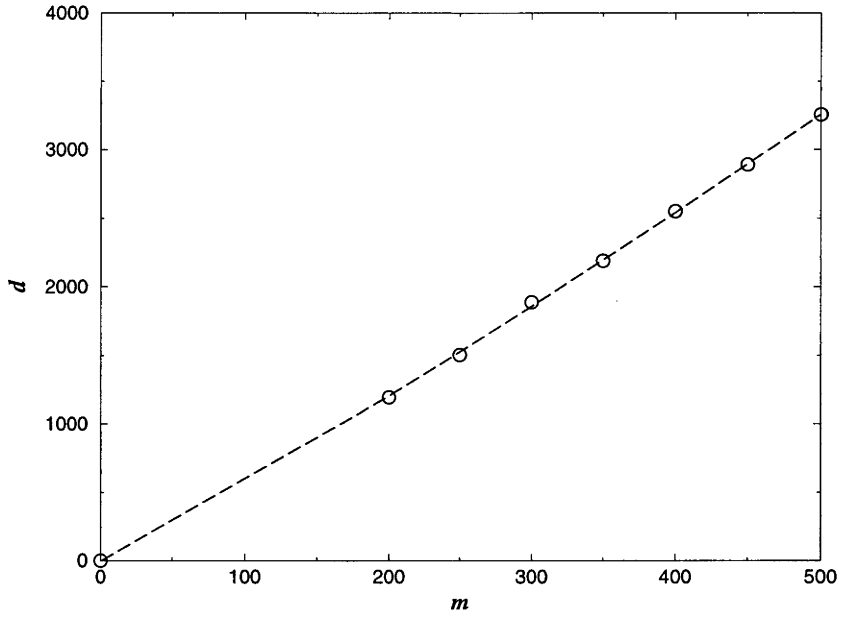

Figure 3.14: The degree of the block basis δ, as a function of the dimension of the basis m, for the singlet ground state of the half-filled Kondo lattice. For this target state, δ corresponds to the equivalent number of states that would need to be kept if $SO(4)$ symmetry was not used.

as in Fig. 3.15 and Fig. 3.16. In all parameter regimes, the error in the energy is less than the energy gap, thus these figures demonstrate that enough accuracy has been achieved in the numerical calculations to determine reliably the total spin of the ground state. Note that this does not mean however that the ground state spin can be determined *exactly* in all parameter regimes; this would require that σ_E is much smaller than the *minimum* energy difference between the spin states. In most of the phase diagram, the difference between lowest energy states of spin s and $s+1$ is of the same order of magnitude, independent of s (as long as $s \leq q$, as there is a finite gap for $s > q$, *cf.* section 3.4.3). However, near a paramagnetic-ferromagnetic phase transition the spin of the ground state becomes indeterminate, as by definition at the phase transition itself one (or more) total spin states will be degenerate. In the regions of Fig. 3.17 and Fig. 3.17 where $\sigma_E/|\Delta_s E|$ is close to unity, the ground state spin can only be determined to within ± 1 or so. This is only a small section of the parameter regime, in the weak- to intermediate-coupling regime close to half-filling. In all other parameter regimes, the absolute error in the total spin of the ground state is much less than one.

To see in more detail the rate of convergence of the DMRG algorithm, Fig. 3.19 shows the energy at each DMRG iteration for a typical point in the large Fermi

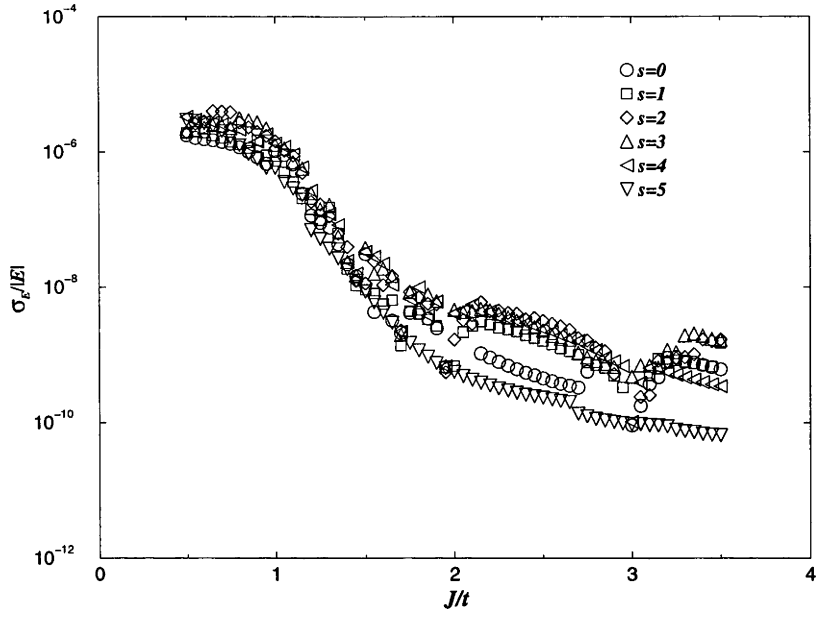

Figure 3.15: The relative error $\sigma_E/|E|$ as a function of the coupling J and spin s, for a 60 site lattice with pseudospin $q = 5$, corresponding to a filling of $n = 5/6$.

surface regime, at $J = 2.5$, for a 60 site lattice with $q = 4$ (equivalent to filling $n = 13/15$). This is the perhaps the most numerically stable regime in the phase diagram. In this set of calculations, the number of states kept m was increased gradually, in increments of 5 states, up to 400 states kept at sweep number 80. Then, m was maintained at 400 states until the convergence criteria described in section 1.6.1 was reached. This was then followed by sweeps of decreasing number of states kept, down to a minimum of $m = 320$. It is clear from Fig. 3.19 that this set of calculations has converged extremely well; the curves are extremely flat once the convergence criteria has been reached and the difference in converged energy as the number of states kept is changed is much smaller than the energy gap between the spin states. In this parameter regime, enough accuracy has been achieved to calculate reliably the spin susceptibility. However, although the number of states kept increases linearly until sweep number 80, the convergence of the energy is extremely non-linear. There is an energy level crossover between the $s = 0$ and $s = 1$ states, giving an incorrect ground state until a total of 53 sweeps have been performed. Most likely, this level crossover is due mostly to slower convergence of the spin $s = 0$ calculation, rather than a genuine crossover in the converged ground state as the number of states kept is increased. This convergence is in marked contrast to that described in the early DMRG studies. For example, reference [43]

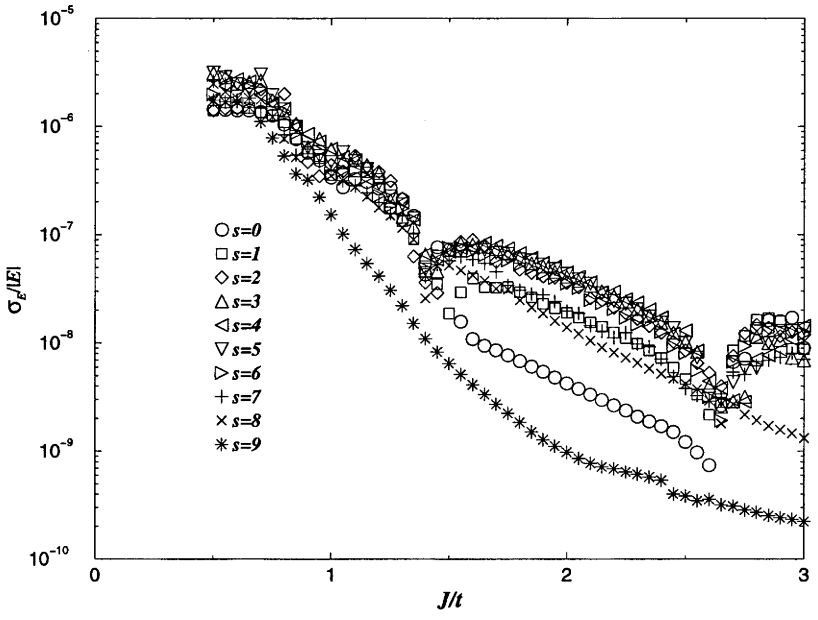

Figure 3.16: The relative error $\sigma_E/|E|$ as a function of the coupling J and spin s, for a 60 site lattice with pseudospin $q = 9$, corresponding to a filling of $n = 7/10$.

suggests that two or three sweeps is adequate for convergence and that it is sufficient to perform only a single sweep with the largest number of states kept. With the large scale DMRG calculations performed in recent years, it has become apparent that the convergence of DMRG in the asymptotic large m limit is completely different to the convergence of the early studies with relatively small numbers of states kept.

A rather different situation is shown in Fig. 3.20. This data is calculated at the same filling ($n = 13/15$), but this time at $J = 1.45$, in the third ferromagnetic region. The convergence in this region of the phase diagram is not nearly so good. The energy is still decreasing at sweep 80 when the maximum number of states kept is reached, thus this calculation is not as well converged as it should be. This is an artifact of the J dependence on the convergence criteria, discussed previously. In principle is not difficult to remedy this, at the expense of some additional CPU time[†]. There are multiple energy level crossings at around 300 states kept, to the point that until sweep 64, the ground state is completely different to the ground state at 400 states kept. The slope $\mathrm{d}E/\mathrm{d}m$ suggests that the converged energy decreases monotonically as the spin is decreased, consistent with a stable ferromagnetic ground state. A DMRG calculation stopping at less than 300 states kept[‡] would give the

[†]Assuming that the convergence would occur in a similar number of sweeps as in Fig. 3.19, the extra CPU time required for improved convergence would not be prohibitive.

[‡]This would be equivalent to around 1500 states in a $U(1) \otimes U(1)$ basis, which would place

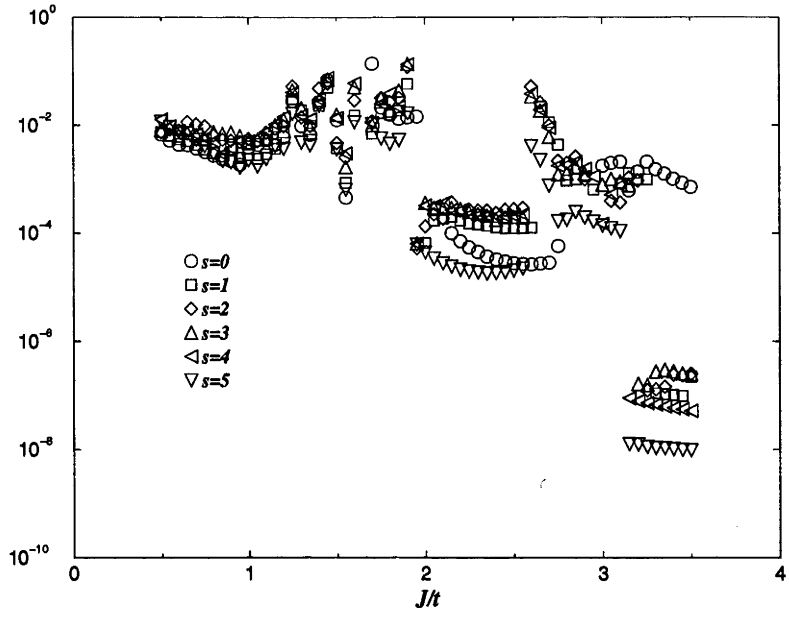

Figure 3.17: The standard error in the energy relative to the separation of the low lying spin states. This corresponds to the fractional error in the total spin. Lattice size is 60 sites, with pseudospin $q = 5$, corresponding to a filling of $n = 5/6$.

opposite conclusion, namely a stable paramagnetic state. This demonstrates the sensitivity of the calculation and explains why this ferromagnetic state has not been identified before in numerical studies. Indeed, if the number of states kept was a physical parameter, then this figure would indicate a first order phase transition! This figure was chosen as an example of particularly poor convergence, although it is still possible to infer the ground state phase from this calculation. The majority of calculations in the new ferromagnetic regions have much better convergence. A more typical example is illustrated in Fig. 3.21, here in the second ferromagnetic region for a 60 site lattice with pseudospin $q = 9$ (equivalent to filling $n = 7/10$) at $J = 1.1$. In this calculation, good convergence was achieved with a maximum of 340 states kept. Despite the superficial similarities with Fig. 3.20, the convergence is much better; the plateau where the energy remains constant for several sweeps around the $m = 340$ mark is a clear indication that the ground state wavefunction has converged well. Note that there are still energy level crossings prior to convergence.

such a calculation at or beyond the extreme limit of the capabilities of conventional DMRG with current generation computers.

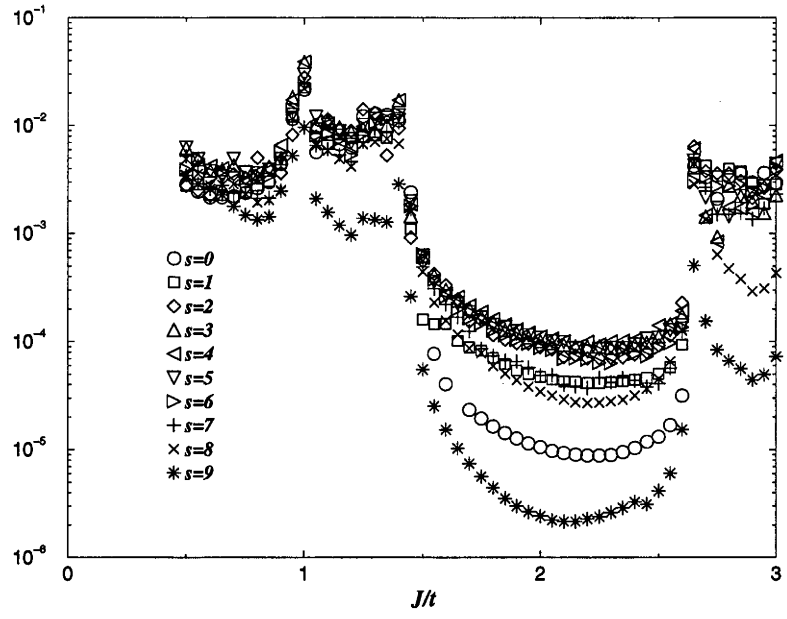

Figure 3.18: The standard error in the energy relative to the separation of the low lying spin states. Lattice size is 60 sites, with pseudospin $q = 9$, corresponding to a filling of $n = 7/10$.

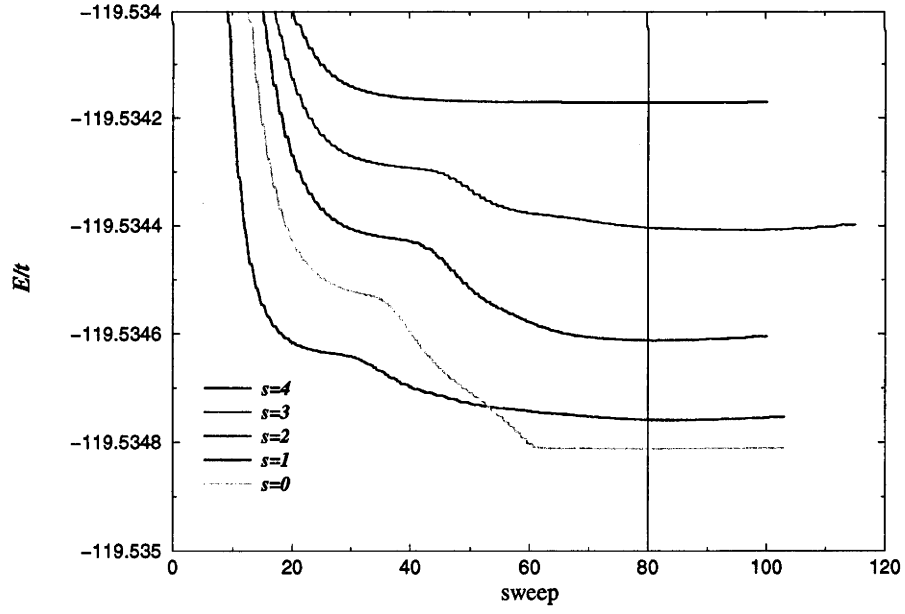

Figure 3.19: The energy at each DMRG iteration, for a 60 site lattice, $J = 2.5$ and $q = 4$, in the middle of the large Fermi surface region. The vertical bar denotes the point where the maximum of $m = 400$ states was reached. Thereafter, the number of states was decreased, down to $m = 320$ states kept.

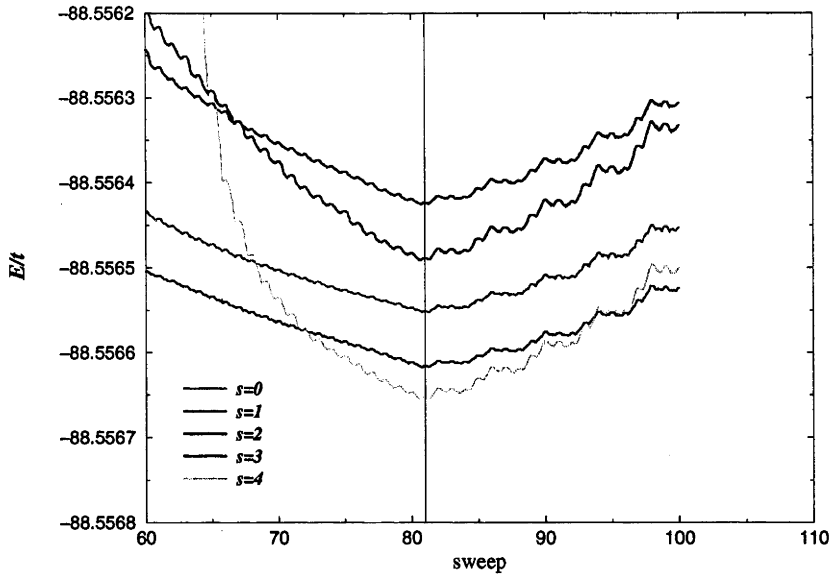

Figure 3.20: The energy at each DMRG iteration, for a 60 site lattice, $J = 1.45$ and $q = 4$, in the third ferromagnetic region. The vertical bar denotes the point where the maximum of $m = 400$ states was reached. Thereafter, the number of states was decreased, down to $m = 320$ states kept. This calculation is an example of the relatively poor convergence in the weak coupling regime.

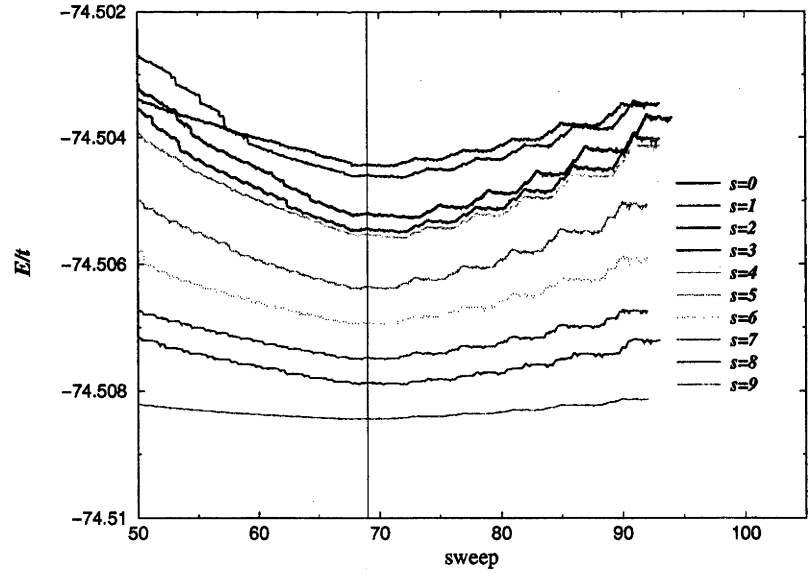

Figure 3.21: The energy at each DMRG iteration, for a 60 site lattice, $J = 1.1$ and $q = 9$, corresponding to a filling $n = 7/10$. The vertical bar denotes the point where the maximum of $m = 340$ states was reached. Thereafter the number of states was decreased, down to $m = 240$. The plateaus where convergence is reached for each value of m are clearly visible.

3.8 The Periodic Anderson Model

In section 3.1 it was described how the Kondo lattice model can be recovered as the limiting case of the symmetric periodic Anderson model in in the local moment regime. A naive application of the Schrieffer-Wolff transformation to the Kondo phase diagram of Fig. 3.3 yields, for the example case of $V = 0.75$, $t = 1$, the phase diagram shown in Fig. 3.22. The number of electrons in this figure refers to the total of the conduction plus f electrons, so in the local moment regime the density of electrons per site is $n_{\text{Anderson}} = n_{\text{Kondo}} + 1$, since the usual notation for the Kondo lattice model does not count the localized f-spins in the electron density. The Schrieffer-Wolff transformation does not apply outside the local moment regime, so there is no reason why this phase diagram should be accurate for either small U, or very close to quarter-filling [98]. Indeed, in 1993 Möller and Wolfe [119] used a slave boson treatment to show that in the strong coupling case (large U) near quarter filling there is a narrow band of antiferromagnetism and a phase transition to a ferromagnetic ground state at larger band filling. Later, Guerrero and Noack [166] studied the model using DMRG and showed that the small U region is paramagnetic. The phase diagram obtained by Guerrero and Noack is shown in Fig. 3.23. Here C denotes what Guerrero and Noack refer to as *complete* ferromagnetism, which has been denoted *fully polarized* ferromagnetism in this thesis, where all un-paired f-elecrons are aligned parallel for a state of spin $s = (2 - n)L/2$ and I denotes *incomplete* ferromagnetism, where the ground state is partially polarized with spin $s < (2 - n)L/2$. It was later shown by Guerrero and Noack [8] that the incomplete ferromagnetic regime is phase separated into domains of ferromagnetism in an antiferromagnetic background.

Notably, the additional region of ferromagnetism at intermediate coupling discovered in the Kondo lattice model is absent in the phase diagram of Fig. 3.23. The intermediate coupling ferromagnetism is also absent in a phase diagram calculated by the author using an early version of the DMRG software. This phase diagram appears in Fig. 3.24. This earlier program used $SU(2)$ spin symmetry, but not pseudospin symmetry. In addition, the number of states kept was, by contemporary standards, tiny at just $m = 20$. In the light of the discovery of intermediate coupling ferromagnetism in the Kondo lattice model, some additional results have been calculated for the periodic Anderson model for a few points surrounding the location of the intermediate ferromagnetic phase as determined by the Schrieffer-Wolff transformation. These results appear in table 3.4 and show that there is indeed an intermediate ferromagnetic region in this model.

A re-examination of the results used to calculate the phase diagram in Fig.

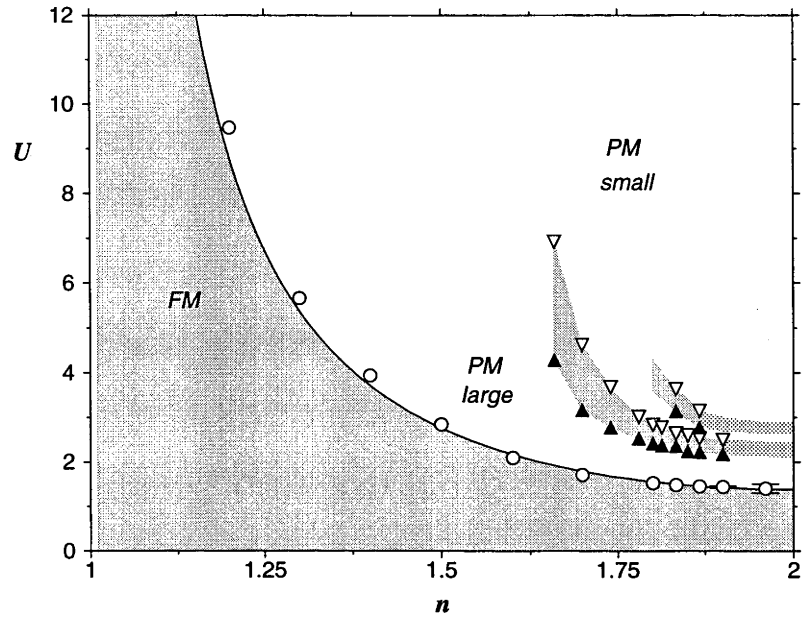

Figure 3.22: Naive application of the Schrieffer-Wolff transformation of the Kondo lattice phase diagram, for $V = 0.75$, $t = 1$. The transformation in fact breaks down for small U and close to quarter-filling ($n = 1$).

3.24 reveals the source of the incorrect determination of the ground state phase. With only 20 states kept, it was not possible to perform a rigorous scaling to zero truncation error. As described in section 3.7.6, it is rather common for there to be energy level crossings between the lowest energy states in different spin sectors as the number of states is increased. This probably explains why the ferromagnetism was missed in the studies of Guerrero and Noack [8, 166]. These calculations did not use $SU(2)$ symmetry, so the total spin of the ground state was determined by calculating the expectation value $\langle \boldsymbol{S} \cdot \boldsymbol{S} \rangle$. Given the tendency of DMRG to converge to a self-consistent excited state [11] (*cf.* section 1.5), it is likely that in the initial sweeps, where not many states are kept, the DMRG wavefunction was converging to the singlet state and not enough states were kept in later sweeps for the wavefunction to 'tunnel' into the higher spin state.

3.9 Summary

The extension of DMRG to non-Abelian symmetries allowed us to make use of spin and pseudospin symmetries inherent in the Kondo lattice and periodic Anderson models to make the most complete determination of the ground-state phase diagram yet obtained for these models. In particular, we have made sub-

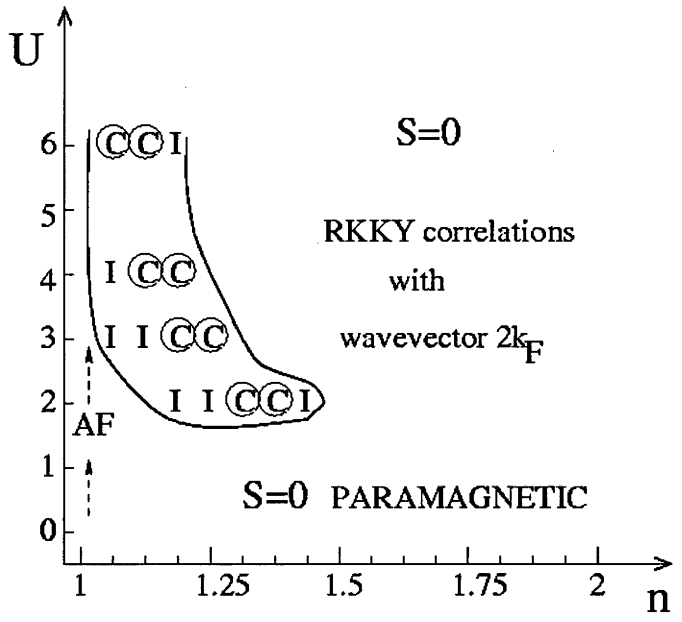

Figure 3.23: Phase diagram of the periodic Anderson model obtained from DMRG, from figure 3 of reference [166]. The parameters here are $t = 0.5$, $V = 0.375$. This corresponds to the parameters used in Fig. 3.22, where all parameters are divided by 2, *i.e.* $U = 1$ in this figure corresponds to $U = 2$ in Fig. 3.22.

stantial progress in mapping the boundaries of a previously unrecognized ferromagnetic regime for intermediate coupling strengths, for conduction band filling $0.5 < n < 1$. This ferromagnetic phase divides the weak coupling regime, characterized by RKKY-like spin correlations at wave number $n\pi$, from the "large Fermi surface regime", characterized by spin correlations at wave number $(n-1)\pi$.

The work by Yamanaka *et al.* [165] on the Luttinger theorem in one-dimension suggested that the Fermi point of the Kondo lattice model is fixed as the interaction strength is varied and is therefore 'large', since the large Fermi surface has previously been detected in numerical calculations (as far was we know, there have been no *analytic* calculations showing the existence of the large Fermi surface). However, this picture is inconsistent with the numerical data at weak coupling as well as the bosonization results and the weak coupling perturbative expansion[†], which all show backscattering correlations at $2k_{F_{\text{small}}}$ given by the conduction-band filling only. The intermediate coupling ferromagnetic regime potentially provides a resolution to this problem, if the proof of the Luttinger theorem does not apply across a phase

[†]Although the perturbative expansion must be seen as suggestive only, since the expansion diverges at second order.

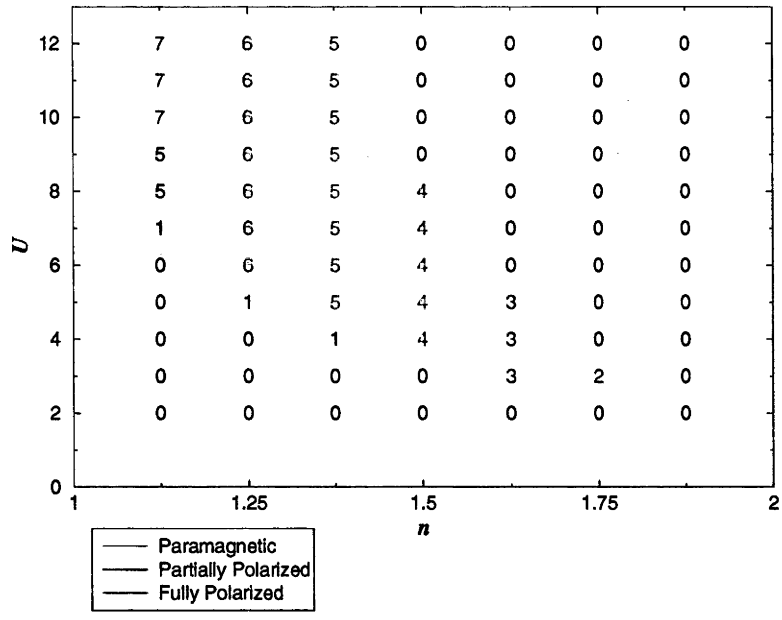

Figure 3.24: Phase diagram of the periodic Anderson model for $V = 1.5$, $t = 1$. By to the Schrieffer-Wolff transformation, there should be an intermediate coupling ferromagnetic region at the top right hand corner.

transition.

The general picture we have obtained is of physics governed by the formation of *spin polarons*. As the Kondo coupling is turned on, the conduction-band electrons couple weakly to the f-spins forming an extended cloud as the conduction electrons attempt to screen the f-spins. Since there are more f-spins than conduction electrons, the shielding is incomplete and the polarons are *locally* ferromagnetic. The paramagnetic phase at weak coupling is due to spiral correlations from the RKKY-like effective interaction. For stronger coupling, the conduction electrons bind tightly to the f-spins and it is no longer useful to talk in terms of separate conduction-band and f-spins. Rather, the relevant particles in the system are the Kondo singlet, Kondo triplet and the unpaired f-spins. These latter particles are effectively a bound state of a conduction-band holon and an f-spin. Presumably, backscattering interactions between the Kondo singlets and the holons lead to the $2k_{F_{\text{large}}}$ correlations characteristic of the large Fermi surface regime. For still higher couplings, the double-exchange mechanism dominates leading to an effective Hubbard model with perturbative ferromagnetic coupling between the unpaired f-spins.

The physics behind the intermediate coupling ferromagnetic region remains substantially unknown. The bosonization calculations allow for additional phases if the spin Bose fields are not well-approximated by the non-interacting values [161], but

Table 3.4: Energy for the lowest singlet and fully polarized ferromagnetic states of the periodic Anderson model, for a 60 site lattice with $V = 0.75$, $t = 1$. The fully polarized ferromagnetic state has spin $s = 9$ for density $n = 1.7$, and spin $s = 6$ for density $n = 1.8$. The intermediate ferromagnetic region is shown at $U = 4$ for density $n = 1.7$ and $n = 1.8$. These points are in the two branches of the intermediate ferromagnetic region shown in Fig. 3.22.

U	n	s	E
2.5	1.7	0	−164.646171
2.5	1.7	9	−164.638130
4	1.7	0	−202.397026
4	1.7	9	−202.397776
5.5	1.7	0	−243.548654
5.5	1.7	9	−243.527937
2.5	1.8	0	−167.486517
2.5	1.8	6	−167.486109
4	1.8	0	−206.016579
4	1.8	6	−206.016592

results in several parameters that must be determined from outside of the bosonization calculation and is in no way predictive. While the numerical calculations are extremely useful in obtaining the phase boundaries, without some guiding principle as to the physical origins of the intermediate coupling ferromagnetic region it is difficult to know what to look for in the numerical experiments. The author is of the opinion that an analytic derivation of the large Fermi surface correlations (*i.e.* an effective interaction that leads to $2k_{F_{\text{large}}}$ spin-spin correlations) would be extremely useful for the full explanation of the properties of the Kondo lattice. The numerical results indicate that the $k_{F_{\text{large}}}$ region is very robust, suggesting that the physics should be comparatively transparent. An analytic construction of the effective interactions in the intermediate coupling ferromagnetic region is likely to be harder to obtain, but surely some insight into this phase would arise from the crossover of the weak coupling effective interactions (known from the bosonization calculations [137]) and the large Fermi surface effective interactions.

Chapter 4

Two-Dimensional DMRG - the $t - J$ Model

Since the discovery of superconductivity in the rare-earth copper oxides [167], there has been a growing interest in strongly correlated electronic systems. The $t - J$ model proposed by Anderson [23] and Zhang and Rice [24] is an example of this interest. The theoretical predictions and implications of the model are possibly relevant and useful for a deeper understanding, particularly of the high temperature superconductors and more generally of the motion of holes in an antiferromagnet. Following the discovery of a low temperature striped phase in the underdoped cuprates [168–170], White and Scalapino [10] published numerical evidence using DMRG for a striped phase of the two-dimensional $t - J$ model. The numerical result generated much controversy, in part for the boundary conditions used, where obtaining sufficient numerical accuracy dictated periodic boundary conditions in only one direction and in the early results, a staggered magnetic field.

The motivation for studying the $t-J$ model in this thesis was to test the $SU(2)$-invariant DMRG for a two-dimensional model and in doing so, confirm the existence of the striped phase and uncover some more of the physics of the model.

4.1 The Physics of the $t - J$ Model

The cuprate superconductors share the perovskite structure of many novel compounds (for example the CMR materials). A canonical example, the YBCO compound, is illustrated in Fig. 4.1. By general consensus, research has focused on the two-dimensional Cu-O planes as being responsible for the superconducting properties. In principle then, the relevant model mirrors that of the Cu-O planes, of a square lattice with Cu atoms on the sites and O atoms on the links. The hopping is mainly between Cu and O, but other terms may well be relevant. For example,

a large overlap between the O atoms would lead to a direct hopping among them. Although physically this description is already much simplified, it is necessary, if theoretical progress is to be made, to further simplify the Hamiltonian. Anderson [23] suggested that a one-band Hubbard model encapsulates the basic physics. In the regime of large U/t, the Hubbard model further simplifies to the $t-J$ model, given by the Hamiltonian

$$H = -t \sum_{\langle i,j\rangle,\sigma} (c^{\dagger}_{i,\sigma} c_{j,\sigma} + \text{H.c.}) + J \sum_{\langle i,j\rangle} (\boldsymbol{S}_i \cdot \boldsymbol{S}_j - \frac{1}{4} n_i n_j) \,, \tag{4.1}$$

defined on the subspace of no double occupancy and $\langle i,j\rangle$ means summation over nearest neighbor pairs only. The single site operators act on the three dimensional basis of an empty site (hole), a single up spin and a single down spin.

This section discusses the derivation of the $t-J$ model as the strong-coupling limit of the Hubbard model, as well as efforts to derive the $t-J$ model directly from the Cu-O Hamiltonian. The known properties of the ground state phase diagram are then discussed.

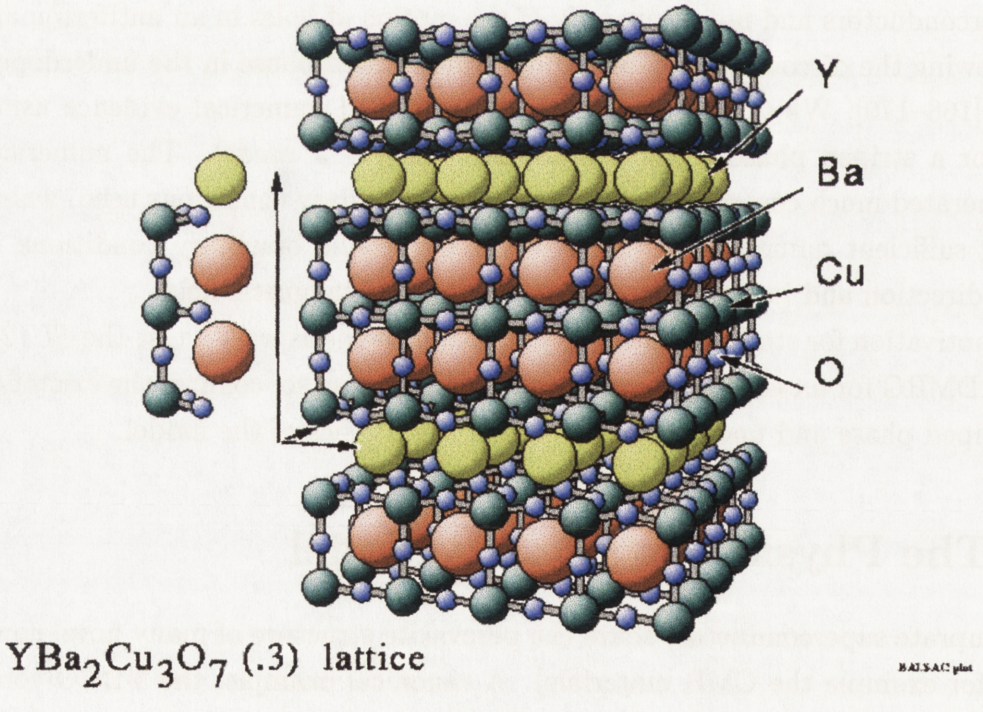

Figure 4.1: The perovskite structure of YBCO. Picture obtained from the *BALSAC* project [171].

4.1.1 Strong coupling limit of the Hubbard model

The $t-J$ model is an effective model of the large U Hubbard model, to second order in the perturbative expansion for small t/U. Starting from the Hubbard model and following the approach of Emery [172] (equivalent to the calculation of Chao *et al.* [173]), we write

$$H = H_0 + H_1 \,, \tag{4.2}$$

with

$$H_0 = U \sum_i n_{i,\uparrow} n_{i,\downarrow} \,, \tag{4.3}$$

$$H_1 = \sum_{i,j} t_{ij} c_i^\dagger c_j \,. \tag{4.4}$$

The hopping matrix t_{ij} is taken to be $t_{ij} = -|t|$, if i,j are nearest neighbor, $t_{ij} = 0$ otherwise. Emery [172] calculated the second order expansion for large attractive interaction, $U < 0$ and then showed that the same solution applies to the $U > 0$ model in a very simple way. For $U \to -\infty$, the H_0 component of the Hamiltonian describes real-space pairing of electrons on each site. For N electrons (assuming N is even) the ground state is degenerate, with every possible configuration of pairs having the same total energy $E_0 = NU/2$. Breaking a pair requires an energy gain of $|U|$. However the effect of the hopping term H_1 is to break such pairs, so it is clear that H_1 gives no contribution at first order. The singly occupied states are unoccupied, so every basis state has spin zero, reducing the $SO(4)$ symmetry down to the $SU(2)$ pseudospin symmetry only.

Let the various degenerate ground states of H_0 be denoted $|\alpha\rangle$. This basis is thus the set of states which contain *only* unoccupied or double occupied sites. If E is the energy of the perturbed ground state $|\psi\rangle$, then

$$(E - H_0)|\psi\rangle = H_1|\psi\rangle \,. \tag{4.5}$$

Multiplying the right hand side by $1 \equiv P + \sum_\alpha |\alpha\rangle\langle\alpha|$, where $P = 1 - \sum_\alpha |\alpha\rangle\langle\alpha|$ is the operator that projects out the unperturbed ground states, gives

$$(E - H_0)|\psi\rangle = PH_1|\psi\rangle + \sum_\alpha |\alpha\rangle\langle\,\alpha\,|\,H_1\,|\,\psi\,\rangle \,. \tag{4.6}$$

On multiplying both sides by $(E - H_0)^{-1}$ one obtains

$$|\psi\rangle = (E - H_0)^{-1} PH_1|\psi\rangle + \sum_\alpha |\alpha\rangle \frac{\langle\,\alpha\,|\,H_1\,|\,\psi\,\rangle}{E - E_0} \,. \tag{4.7}$$

This is equivalent to

$$|\psi\rangle = \sum_\alpha a_\alpha |\psi_\alpha\rangle \,, \tag{4.8}$$

where

$$|\psi_\alpha\rangle = (E - H_0)^{-1} P H_1 |\psi_\alpha\rangle + |\alpha\rangle \,, \tag{4.9}$$

and

$$a_\alpha = \frac{\langle \alpha \,|\, H_1 \,|\, \psi \rangle}{E - E_0} \,. \tag{4.10}$$

Expanding Eq. (4.9) to first order in $(E - H_0)^{-1} P H_1$ gives,

$$|\psi_\alpha\rangle = (E - H_0)^{-1} P H_1 |\alpha\rangle + |\alpha\rangle \,. \tag{4.11}$$

Now $H_1|\alpha\rangle$ is a state of one broken pair and thus has no overlap with any of the ground states $|\alpha\rangle$. Hence P has no effect on this state. H_1 breaks exactly one pair for an excitation energy of $-U$, so that

$$|\psi_\alpha\rangle = \left(\frac{H_1}{U} + 1\right) |\alpha\rangle \,. \tag{4.12}$$

substituting this into Eq. (4.10) gives

$$(E - E_0) a_\alpha = \frac{1}{U} \sum_{\alpha'} \langle \alpha \,|\, H_1^2 \,|\, \alpha' \rangle a_{\alpha'} \,, \tag{4.13}$$

which is a Schrödinger equation in the $|\alpha\rangle$ subspace with effective Hamiltonian H_1^2/U. Since the Hilbert space in which this effective Hamiltonian acts is the set of degenerate ground states $|\alpha\rangle$, the only non-zero matrix elements of $\langle \alpha \,|\, H_1^2 \,|\, \alpha' \rangle$ are those where the first application of H_1 transfers and electron of spin σ from site j to site i and the second application of H_1 either returns the electron to its original site, or transfers and electron of spin $-\sigma$ from site i to site j. Thus the effective Hamiltonian is

$$H_1' = -\frac{1}{|U|} \sum_{i,j,\sigma} t_{ij}^2 c_{i,\sigma}^\dagger c_{j,\sigma} c_{j,\sigma}^\dagger c_{i,\sigma} + c_{i,-\sigma}^\dagger c_{j,-\sigma} c_{j,\sigma}^\dagger c_{i,\sigma} \,. \tag{4.14}$$

This can be written in several equivalent ways, the most useful of which is to make use of the eta-pairing operators

$$\begin{aligned} \eta_i &= c_{i,\uparrow} c_{i,\downarrow} \,, \\ \eta_i^\dagger &= c_{i,\downarrow}^\dagger c_{i,\uparrow}^\dagger \,. \end{aligned} \tag{4.15}$$

Recall from section section 2.5, that the $\eta_i^\dagger$ and η_i are related to the q^+ and q^- components of the pseudospin vector operator by

$$\begin{aligned} q_i^+ &= (-1)^i \eta_i^\dagger \,, \\ q_i^i &= (-1)^i \eta_i \,. \end{aligned} \tag{4.16}$$

The z-component of this operator gives the number of particles,

$$q_i^z = \frac{1}{2}(n_{i,\uparrow} + n_{i,\downarrow} - 1) \,. \tag{4.17}$$

Writing the Hamiltonian Eq. (4.14) using these operators gives

$$H_1' = \frac{1}{|U|} \sum_{i,j} t_{ij}^2 \left(q_i^+ q_j^- + q_i^- q_j^+ + 2q_i^z q_j^z + 2s_i^z s_j^z - 1 \right) \,. \tag{4.18}$$

Because the only single site basis states are unoccupied and doubly occupied states, s_i^z vanishes on every site, so this term can be neglected. The constant term is also irrelevant. Thus the effective Hamiltonian is

$$H_1' = \frac{2}{|U|} \sum_{i,j} t_{ij}^2 \, \boldsymbol{q}_i \cdot \boldsymbol{q}_j \,. \tag{4.19}$$

Thus, the $U < 0$ Hubbard model in the strong coupling limit is equivalent to the Heisenberg spin chain. It is important to note here that the spins in the effective Heisenberg model do not correspond to the real spins in the Hubbard model, which make no appearance in the effective Hamiltonian Eq. (4.19), but rather to the charge pseudospin symmetry. The $z-$component of the spin in the effective Heisenberg model is effectively the number of electrons, and is given by $q^z = \sum_i (n_{i,\uparrow} + n_{i,\downarrow} - 1)$.

To apply this result to the $U > 0$ model, Emery [172] applied a canonical transformation consisting of a particle-hole transformation for the down spins only[†],

$$\begin{aligned} \bar{c}_{i,\downarrow} &= c_{i,\downarrow}^\dagger \\ \bar{c}_{i,\uparrow} &= c_{i,\uparrow} \,, \end{aligned} \tag{4.20}$$

This transforms the Hamiltonian into a model with the sign of the U term reversed,

$$\begin{aligned} \bar{H}_0 &= -U \sum_i \bar{n}_{i,\uparrow} \bar{n}_{i,\downarrow} + U \sum_i \bar{n}_{i,\uparrow} \,, \\ \bar{H}_1 &= -t \sum_{<i,j>} \left(\bar{c}_{i,\uparrow}^\dagger \bar{c}_{j,\uparrow} - \bar{c}_{i,\downarrow}^\dagger \bar{c}_{j,\downarrow} \right) \,. \end{aligned} \tag{4.21}$$

For $U > 0$, the coupling is now attractive, with the number of pairs being equal to the number of up spins of the original basis. The second order term in the perturbative expansion is now exactly the same as before, except now if the system is doped away from half filling, the first order term is not zero. Away from half-filling, the hopping H_1 breaks the degeneracy at first order by transferring an electron from

[†]This is similar to the transformation used to obtain the pseudospin operators from the ordinary spin operators, except that the staggered phase factor is missing. This causes the hopping term to have a spin-dependent amplitude.

a singly occupied site to an empty site. All other first order processes vanish due to the energy penalty U for transferring an electron from a singly occupied site to a doubly occupied site. Thus, the first order component of the Hamiltonian is PH_1P, where P now projects out all states that have a double occupied site,

$$P = 1 - \sum_i n_{i,\uparrow} n_{i,\downarrow} \,. \tag{4.22}$$

The second order component, $\bar{H}_1^2/U$ is

$$H_1' = \frac{2}{U} \sum_{i,j} t_{ij} \left(\boldsymbol{s}_i \cdot \boldsymbol{s}_j - q_i^z q_j^z \right) \,. \tag{4.23}$$

Away from half-filling, q_i^z does not vanish, so this term must be retained in Eq. (4.23). Thus the full effective Hamiltonian is

$$H' = -t \sum_{<i,j>,\sigma} \left(P c_{i,\sigma}^\dagger c_{j,\sigma} P + \text{H.c.} \right) - \frac{4t^2}{U} \sum_{<i,j>} \left(\boldsymbol{s}_i \cdot \boldsymbol{s}_j - q_i^z q_j^z \right) \,. \tag{4.24}$$

On expanding the pseudospin interaction, $q_i^z q_j^z = \frac{1}{4}(n_i n_j - n_i - n_j + 1)$, the usual $t-J$ Hamiltonian is obtained (aside from an irrelevant constant term and term proportional to the total number of electrons), with coupling

$$J_{\text{eff}} = \frac{4t^2}{U} \,. \tag{4.25}$$

This is valid for $U \gg t$, which implies that $J \ll t$.

Note that there are terms missing in Eq. (4.23) that arise in the large U Hubbard model away from half-filling, such as the three site interaction

$$c_{i,\sigma}^\dagger c_{j,\sigma} c_{j,\sigma'}^\dagger c_{k,\sigma'} \,, \tag{4.26}$$

and the four site interaction

$$c_{i,\sigma}^\dagger c_{j,\sigma} c_{k,\sigma'}^\dagger c_{l,\sigma'} \,. \tag{4.27}$$

However, these terms are usually neglected on the grounds that three and four site interactions are expected to be less important in understanding the magnetic correlations of the model, but the real effect of these terms is unclear [174].

4.1.2 Derivation as an effective model of CuO planes

Zhang and Rice [24] have presented a justification of the $t-J$ model as an effective model of the high temperature superconducting copper oxides from a very general starting point, valid away from the strict limit $J \ll t$ where the $t-J$

model is an effective Hamiltonian for the Hubbard model. It is generally agreed that the holes introduced into a superconductor reside primarily on the O sites and do not form Cu^{3+} ions; this suggests that a single-band model might be inadequate and two (or more) bands are necessary. However Zhang and Rice argue that the hybridization strongly binds a hole on each square of O atoms to the central Cu^{2+} ion forming a local singlet. This singlet then moves through the lattice of Cu^{2+} ions in a similar way to a spinless holon in the single band Hubbard model. The starting point of Zhang and Rice's calculation [24] is a Hamiltonian describing a single layer of square planar coordinated Cu and O atoms,

$$\begin{aligned} H &= \sum_{i,\sigma} \epsilon_d d^\dagger_{i,\sigma} d_{i,\sigma} + \sum_{k,\sigma} \epsilon_p p^\dagger_{k,\sigma} p_{k,\sigma} \\ &\quad + U \sum_i d^\dagger_{i,\uparrow} d_{i,\uparrow} d^\dagger_{i,\downarrow} d_{i,\downarrow} + \sum_{<i,k>,\sigma} V_{ik} d^\dagger_{i,\sigma} p_{k,\sigma} + \text{H.c.} \,. \end{aligned} \tag{4.28}$$

Here $d^\dagger_{i,\sigma}$ create Cu holes $(3d_{x^2-y^2})$ at site i and $p^\dagger_{k,\sigma}$ create O holes $(2p_x, 2p_y)$ at site k. The $< i,k >$ summation is over the four O sites k around each Cu site i. The hybridization matrix V_{ik} is taken to be the overlap of Cu and O holes. The symmetry of the wavefunctions gives the signs shown in Fig. 4.2. Taking these signs into account, the hybridization matrix can be written as

$$V_{ik} = (-1)^{M_{ik}} t_0 \,, \tag{4.29}$$

where t_0 is the amplitude of the hybridization, $M_{ik} = 0$, if $k = i - \frac{1}{2}\hat{x}$ or $i - \frac{1}{2}\hat{y}$ and $M_{ik} = 1$, if $k = i + \frac{1}{2}\hat{x}$ or $i + \frac{1}{2}\hat{y}$.

Consider one Cu ion surrounded by four O ions. A hole at an oxygen site can be in a symmetric or antisymmetric state with respect to the central copper ion. Both of these states may combine with the d-wave Cu hole to form either a singlet or a triplet state. To second order in perturbation theory about the atomic $(t = 0)$ limit, Zhang and Rice [24] showed that the singlet state has lowest energy, so it is then assumed that it is possible to work in the singlet subspace only, without losing any of the essential physics. Thus, a hole located on the oxygen site has been replaced by a spin singlet centered on the copper site. This is equivalent to removing one Cu spin-$\frac{1}{2}$ from the square lattice of Cu spins, giving an effective model of spins and holes on a square lattice. The oxygen ions are no longer explicitly present in the model. After some further calculations, Zhang and Rice [24] showed that the effective model is the $t-J$ model.

This reduction to the $t-J$ model is still controversial†. In particular, Emery and Reiter [175] argue that the resulting quasiparticles have both charge and spin,

†For a review, see reference [174] and references cited therein.

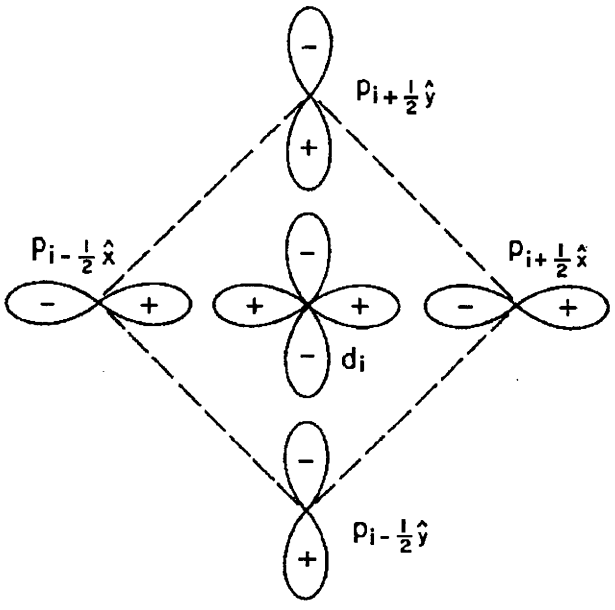

Figure 4.2: The sign of the wavefunction given the $3d_{x^2-y^2}$ symmetry of the Cu holes, and the $2p_x, 2p_y$ symmetry of the O holes. The unit length is the Cu-Cu distance. From reference [24].

in contrast to the Cu-O singlets that form the effective one-band $t-J$ model. Zaanen, Oleś and Horsch [176] studied the motion of a triplet carrier in a spin-$\frac{1}{2}$ background, which might occur if the singlet approximation of Zhang and Rice [24] does not strictly apply and found the properties to be completely different from the standard $t-J$ model.

4.1.3 Stripes versus phase separation

The $t-J$ model belongs to the class of systems which do not obey the condition of Perron-Frobenuis [177]. This condition states that if the off-diagonal elements of a matrix are all non-positive and if the matrix is not in a block diagonal form then the ground state eigenvalue is non-degenerate. In the case of the $t-J$ Hamiltonian the off-diagonal elements are not all non-positive. Thus the theorem can not be applied, which implies that the phenomenon of ground state level crossing is present [178]. As a direct consequence of this, the thermodynamic system is unstable against phase separation. Emery, Kivelson and Lin [179] showed that the model phase separates completely into hole-rich and no-hole phases.

Many experiments have found evidence for stripes[†] and stripes arise in a number

[†]For a recent review, see reference [180].

of different theories involving strong correlations [10,181–184]. The first direct evidence of the existence of a stripe ground state emerged from $t-J$ model calculations by White and Scalapino [10], with further calculations by the same authors [185,186] and Scalapino and White [58]. The reason the striped phase was found first in the $t-J$ model, rather than the Hubbard model, is that the $t-J$ model inherits all the exchange hole correlations resulting from the antiparallel spin correlations in the $U \to \infty$ limit. Hence if stripes do exist, they will be more robust in the $t-J$ model.

Stripes have been studied by a number of numerical techniques in the $t-J$ model, unfortunately resulting in conflicting conclusions. A major question is if stripes are part of the known phase separated regime of the $t-J$ model [187], or if they represent a different ground state phase.

In two dimensions, it was argued that phase separation corresponds to stripe formation [187]. Stripe formation is one of the most controversial issues in the study of high temperature superconductors, where there is a phase separation of the holes which is limited to short range by Coulomb forces.

4.2 The DMRG Algorithm

4.2.1 Construction of the $SU(2)$ invariant Hamiltonian

In matrix form, choosing basis vectors $(1,0)$ to be a hole and $(0,1)$ to be a spin, The operators relevant to the t-J model are

$$
\begin{aligned}
c^{[-1,1/2]} &= \begin{pmatrix} 0 & \sqrt{2} \\ 0 & 0 \end{pmatrix} \\
c^{\dagger[1,1/2]} &= \begin{pmatrix} 0 & 0 \\ 1 & 0 \end{pmatrix} \\
s^{[0,1]} &= \begin{pmatrix} 0 & 0 \\ 0 & \sqrt{3/4} \end{pmatrix} \\
n^{[0,0]} &= \begin{pmatrix} 0 & 0 \\ 0 & 1 \end{pmatrix} \\
p^{[0,0]} &= \begin{pmatrix} 1 & 0 \\ 0 & -1 \end{pmatrix},
\end{aligned}
$$

where we use square brackets to denote which representation of $U(1) \otimes SU(2)$ the operators transform as. $p^{[0,0]}$ is the usual parity matrix used to enforce the correct commutation relations on the DMRG matrix operators (*cf.* section 1.2.3.

We now write the Hamiltonian so that the operators transform as representations of the global symmetry group. For the $t-J$ model, this is

$$H = -\sqrt{2}t \sum_{\langle i,j \rangle} (c_i^{\dagger[1,1/2]} \cdot c_j^{[-1,1/2]} + \text{H.c.}) - \sqrt{3}J \sum_{\langle i,j \rangle} S_i^{[0,1]} \cdot S_j^{[0,1]} - \frac{1}{4} J \sum_{\langle i,j \rangle} n_i^{[0,0]} \cdot n_j^{[0,0]} . \tag{4.30}$$

Note that the interaction between two nearest neighbor sites (i,j) in the non-Abelian representation requires summing 4 distinct terms, $c_i^\dagger c_j$, $c_i c_j^\dagger$, $S_i S_j$ and $n_i n_j$. In the S^z basis used in all previous DMRG calculations on the $t-J$ model, there are 8 terms: $c_{\uparrow i}^\dagger c_{\uparrow j}$, $c_{\uparrow i} c_{\uparrow j}^\dagger$, $c_{\downarrow i}^\dagger c_{\downarrow j}$, $c_{\downarrow i} c_{\downarrow j}^\dagger$, $S_i^+ S_j^-$, $S_i^z S_j^z$, $S_i^- S_j^+$ and $n_i n_j$. Thus, although the matrix elements of the single site operators are more difficult to calculate using the non-Abelian formulation, there are correspondingly fewer matrix elements and operators required.

4.2.2 Boundary conditions

The DMRG algorithm was applied to the two-dimensional $t-J$ model by unrolling the two-dimensional lattice into a one dimensional model with long range interactions, following the 'zipper' approach described in section 1.5. The boundary conditions the same as those used by White [10]; periodic boundary conditions in the y direction and open boundary conditions in the (generally longer) x direction. Ideally, one would like to perform the calculations with periodic boundary conditions in both directions, but as described in section 1.6.3, this would substantially increase the number of states required. Although the resulting one dimensional zipper model is reflection symmetric at the midpoint of the lattice, it is difficult to make use of this symmetry due to the non-uniform nature of the ground state. As a DMRG sweep progresses from one end of the system toward the center point, the holes and spins tend to distribute themselves in a slightly asymmetric way between the left and right halves of the system so that, when the center point is reached, the left block basis is biased toward states that have too few holes and the right block basis is biased toward states that have too many holes (or *vice versa*). Enforcing reflection symmetry by using only one block plus its spatial reflection leads to a catastrophic reduction in the number of admissible superblock states and a corresponding jump in the energy at that DMRG iteration.

4.2.3 Initial conditions

While there are many possible ways to construct the initial blocks, we use the simple approach of constructing the initial blocks 'in place'; that is, starting from an

initial 4 site system consisting of the 2 extreme sites from the left and right ends of the zipper and adding two sites at a time, one from each end of the zipper, working toward the center of the system. This means that for most of the warm-up sweeps, there are no interaction terms between the left and right blocks. An alternative procedure is to rotate the system 90 degrees, so that the opposite ends of the zipper are connected on the periodic boundary. However this introduces many more interactions between the left and right blocks throughout the calculation, which impacts on the accuracy. With no interactions between the two blocks, the eigenstates of the block density matrix coincide with the eigenstates of the block Hamiltonian. Therefore, there will only be a single non-zero density matrix eigenvalue (more, if the ground state is degenerate). The effect is that, until the first inter-block interaction appears, $m-1$ of the block eigenstates are essentially random vectors. There are other methods of constructing the initial blocks [12, 41, 56] (*cf.* chapter 1 section 1.5), but the dominant effect in this case is not the inter-block interactions, but rather the initial density of holes. This can be specified by manipulating the target state as a function of system size. We have done this to obtain various initial conditions; a state with all holes uniformly distributed, a phase separated state and several random states. An important test of the validity of the obtained ground-state is that it is obtained independently of this initial condition.

4.3 Numerical Results

Calculations have been made for various lattice sizes, keeping up to 1200 basis states per block. Table 1 shows a comparison of the ground state energy as a function of the number of basis states kept, using the $U(1) \otimes U(1)$ and $U(1) \otimes SU(2)$ basis, for a typical point in the 'striped' regime [10]. The $SU(2)$ symmetry provides a saving of a factor of two in the number of block states required. However, even with 1200 states kept in the $U(1) \otimes SU(2)$ basis (equivalent to around 2500 states in the $U(1) \times U(1)$ basis), the achieved energy is around 0.25% higher than the estimated true ground state energy. This compares very poorly with the accuracies generally achieved by DMRG for one dimensional models.

In DMRG, the ground state wavefunction is iteratively improved, but only locally. This can lead to a situation where the DMRG converges self-consistently to an incorrect state, depending on the initial conditions and the details of the algorithm [58]. In many cases, for a small number of states (but still relatively large compared with traditional DMRG studies) we have observed qualitatively different DMRG wavefunctions, depending on how the initial build sweep is performed. We

Table 4.1: Comparison of $U(1)$ and $SU(2)$ bases for the number of states versus ground state energy of a 16×6 $t - J$ system with $J = 0.35$, $t = 1$, 8 holes and cylindrical boundary conditions. The results using the $U(1)$ basis are from reference (White and Scalapino 1999) We also include an estimate of the true energy, extrapolated to zero truncation error.

basis	m	E
$U(1)$	1000	-52.279
$SU(2)$	500	-52.284
$SU(2)$	800	-52.463
$SU(2)$	1200	-52.520
$-$	∞	-52.65 ± 0.05

have also observed different converged wavefunctions even with the same initial condition, simply by varying the the rate at which the number of basis states per block is increased as the DMRG sweeps progress. For example, for the calculation of the 16×6 system used in table 4.1, using 500 basis states in the $U(1) \otimes SU(2)$ basis, the ground state is most likely a two stripe configuration in agreement with [10]. However, if we increase the number of retained states at a faster rate so that it takes fewer sweeps to reach the final total, we actually obtain a three stripe configuration. It is not until the number of states is increased to 800 that the three stripe configuration moves out of this local minima and formed the two stripe configuration. Simply performing additional DMRG sweeps with 500 states is not effective in 'tunneling' between the two competing low lying states.

A possible way of dealing with the problem of competing low lying states is to compare the energies of the competing states, similarly to what was done for the different total spin symmetry sectors in determining the phase diagram of the Kondo lattice model in chapter 3. The problem with this approach is that DMRG only provides a variational upper bound on the energy and that the goodness of the variational energy (and therefore the truncation error associated with the DMRG state) can depend significantly on the nature of the ground state. This is exacerbated by the non-uniform nature of the ground state of the $t - J$ model. While extrapolation to zero truncation error (described in section 1.6) is relatively easy to do in a typical one-dimensional calculation, the number of states that need to be kept in a two-dimensional calculation makes this a very time consuming procedure and impractical in this case.

In this chapter, we only report results where we have a unique ground state, independent of the initial conditions (at least for the initial conditions we have used). However, the problem of multiple candidate ground states depending on the initial conditions deteriorates rather quickly as the system size increases. Indeed, one doesn't need to increase the system size too far before the DMRG fails to converge to a believable ground state at all, at least in a reasonable number of sweeps.

Fig. 4.3 shows, for the striped phase, the hole density along the x direction for a fixed number of holes (8), as the system size is increased. As the size grows, the stripes tend to move further apart while keeping approximately the same width, although it is difficult to make any real conclusions about the stripe width from this limited data. In particular, the indicated width of the fluctuations in the real space density may be much larger than the correlation width of the stripe itself, if the stripe is delocalized. This depends on how much effect the boundary conditions have in pinning the stripes. A better measure of the stripe width would come from the density-density correlation functions, however these have not yet been obtained.

Fig. 4.4 shows the effect of reducing the number of holes to 6, for the 16×6 case. The ground state shown here is curious in that it breaks spatial reflection symmetry (and thus cannot be the true ground state in the limit of larger number of states kept), but it does provide evidence that it is energetically favorable to form a 'normal' stripe of hole density 4/6 and one 'proto' stripe, of hole density 2/6, rather than two stripes of equal hole density, or a single stripe. This suggests, as with the results from Fig. 4.3, that that the thermodynamic hole density per stripe is a constant (which depends on J/t). There is nothing in the DMRG algorithm that forbids the formation of broken symmetry states such as the one seen in Fig. 4.4. The true ground state is likely to be very similar to either a symmetric or antisymmetric combination of the state shown in Fig. 4.4 and its spatial reflection. If the symmetric and antisymmetric states have very similar energy, then numerical mixing of the two states will favor the state which minimizes the variational energy for the given finite number of block states kept, which *ceteris paribis* occurs when most of the block states at each block size are in the same symmetry sector. Thus, it is favorable for all of the basis states to have a similar hole configuration, rather than half of the basis having the spatially reflected configuration as would be required if the wavefunction was an eigenstate of spatial reflection.

In Fig. 4.5, we attempt to find the optimal filling per stripe, by increasing the system size and number of holes by 50%, to a 24×6 lattice with 12 holes. Since we consistently obtain three stripes, this limits the hole density per unit length

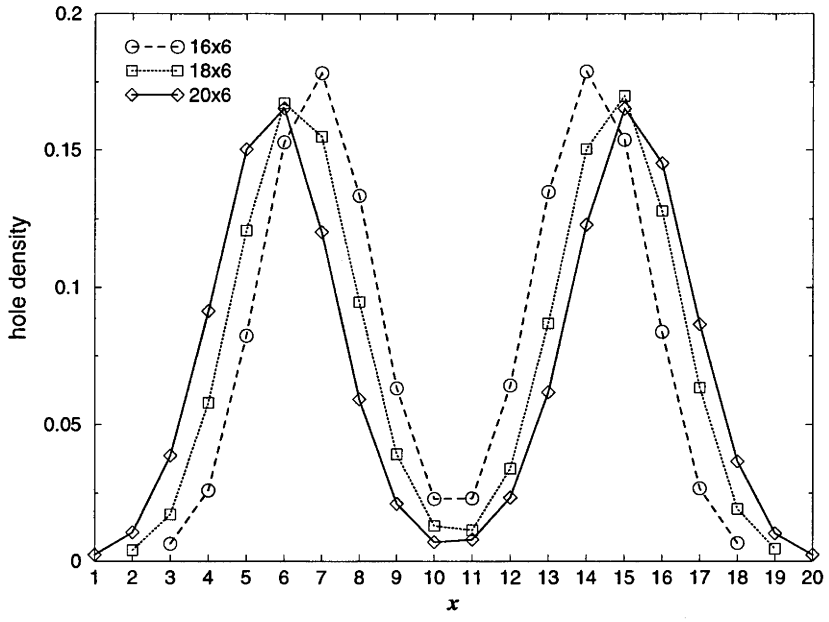

Figure 4.3: Hole density across the x direction of a $t - J$ lattice with 8 holes and $J/t = 0.35$, for lattice sizes 16×6, 18×6 and 20×6.

of the stripes to $0.5 < d < 1$. This is the largest system that we could study, while still being reasonably certain that the obtained ground state is substantially independent of the initial conditions. Thus, for these parameters and boundary conditions, the two dimensional $t - J$ model almost certainly has a striped ground state and doping the system changes the density of stripes while the number of holes per stripe remains constant. It is difficult, however, to extrapolate these results to make definite conclusions about the nature of the ground state of the $t - J$ model in the thermodynamic limit. Because of the half-periodic boundary conditions, the hole density is constant in the y direction. Therefore any fluctuation in the hole density across the system, pinned by the open boundary in that direction, will appear as a vertical stripe in these calculations, whether or not it is truly a 'stripe'. Other possible ground states of the thermodynamic $t - J$ model, such as diagonal stripes or antiferromagnetic bubbles, are not permitted by construction.

Another important point to note is that in the phase separated regime, the holes are attracted to the open boundary of the finite system. On the other hand, in the striped regime, the holes are repelled by the boundary. Thus the open boundary may well have a significant effect on the nature of the ground state that we observe and especially, on the critical value of J/t that separates stripe formation from phase separation.

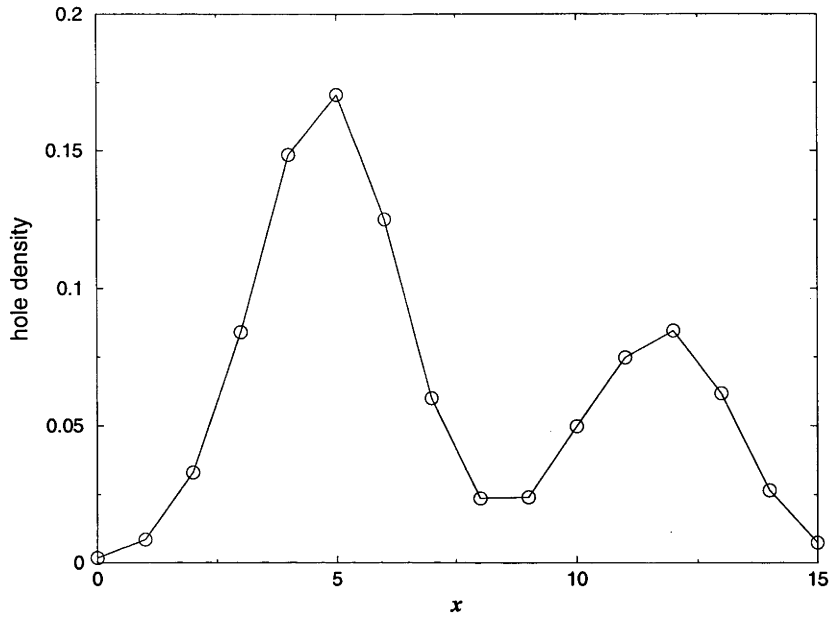

Figure 4.4: Hole density across the x direction of a 16×6 $t - J$ lattice, with 6 holes and $J/t = 0.35$.

4.4 The Physics of Stripes

This section describes some of the physical properties of stripes that are important for their theoretical description, with particular reference to aspects affecting the potential for numerical solutions. This is a very large area of condensed matter physics and there is no hope to fully cover the many ideas currently in the literature. It is only possible to give the merest overview here and point the interested reader to recent articles [106, 174, 188, 189] and references cited therein for a complete description. This section does however cover what appear to be the promising directions for future investigations from a numerical point of view.

4.4.1 Antiphase boundaries

It is important to emphasize that stripe formation always implies the presence of antiphase boundaries, *i.e.* antiphase domain walls in the antiferromagnet. In all approaches, antiphase boundaries are found in conjunction with stripes; from a simple mean-field calculations [181] to the more sophisticated quantum numerical approaches [10, 190–192]. From our numerical data we cannot conclude that the antiphase boundaries are a consequence of stripes or *vice versa* . What we are certain of, is that the presence of the antiphase boundaries is a clear evidence of stripe existence. This favors the earlier observation that stripes are different from

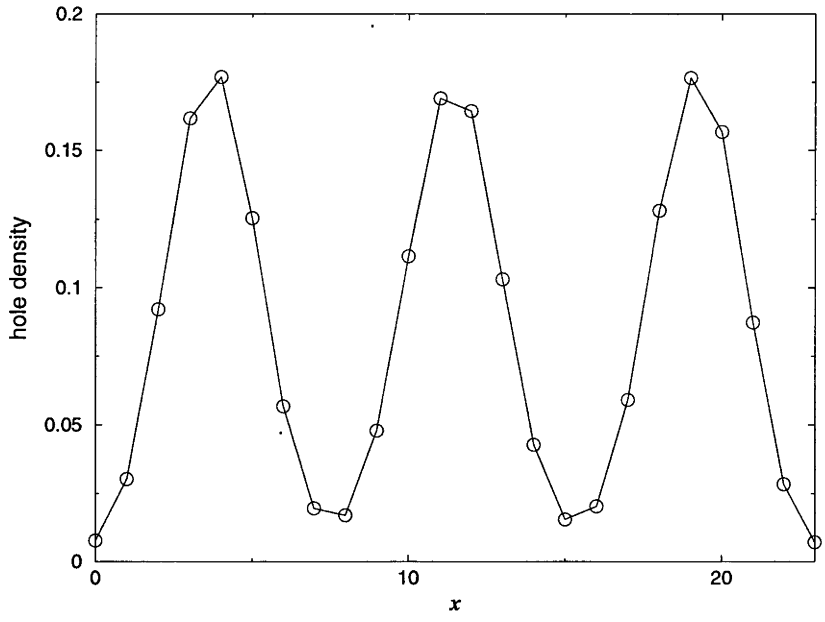

Figure 4.5: Hole density across the x direction of a 24×6 $t-J$ lattice, with 12 holes and $J/t = 0.35$.

phase separation.

An interesting explanation of the antiphase boundaries was suggested by Nagaev† [106]. This brings us back to the general theory of metal-insulator transition, as formulated by Mott [194], who pointed out that the number of free carriers should jump discontinuously at the transition. Hence, there has to be a region of phase separation near the metal insulator transition. The existence of phase separation associated with doping away from an antiferromagnetic phase was recognized prior to the discovery of high temperature superconductors [195, 196].

Nagaev refers to this phase as *nanoscale* phase separation [106, 193], where phase separation is accompanied by charge separation, which in a perfect isotropic crystal, form an almost periodic structure. Thus, a nanoscale phase separation is realized as a form of charge density wave. In this language the antiphase boundaries appear as the ferromagnetic droplets: a hole can delocalize over a finite domain by flipping the spins of the neighboring Cu ions, forming a small ferromagnetic islands known as ferrons [106]. It is interesting to note that if this is the origin of the antiphase boundaries then a second hole can lower its energy by localizing on the same ferron island, i.e., on the same antiphase boundary. This has the appearance of a real space pairing mechanism.

Hence, looking at the stripes as being a nanoscale phase separation, the an-

†For a review, see also reference [193] and references cited therein.

tiphase boundaries (periodic ferrons) will appear as a consequence of the periodic hole structure. At mean-field level this can be understood by recalling that the coexistence of a charge and spin density-wave will always gives rise to ferromagnetism [197, 198].

4.4.2 Geometrical ordering

From the conventional symmetry point of view, antiphase boundaries are an oddity. The spin and hole degrees of freedom are associated with continuous $SU(2)$ symmetries which simply do not allow for an Ising-like Z_2-symmetric domain wall. Strictly speaking, it is incorrect to talk about domain walls in the *spin* system. In chapter 2, it was shown that the construction of the spinon and holon basis for the Hubbard model is intimately connected with the lattice being bipartite, where hopping is allowed only between the two sublattices[†], say A and B. Hopping within a sublattice (A-A hopping or B-B hopping) does not preserve pseudospin. Clearly, there are two distinct ways that the bipartite lattice can be divided into sublattices, as one can start labeling with either an A site, or a B site. Thus there is a Z_2 degree of freedom associated with the construction, which is called 'sublattice parity' [199].

The bipartite property of the lattice is not apparent until the charge $SU(2)$ pseudospin symmetry is utilized, where it is necessary for the pseudospin operators (defined in Eq. (2.132)) to have a staggered phase. The spinons have zero pseudospin, so they do not see this staggered phase. It is coupled only to the holons, *i.e.* in the frame of reference of a holon, hopping flips the sublattice parity. This has the appearance of a Z_2 local gauge symmetry. This mechanism is essential for spin-charge separation in one-dimension, which leads to the question as to what is the effect of flipping the sublattice parity in higher dimensions. The wildly different properties of one-, two- and three-dimensional systems indicates that the available topological excitations of a bipartite lattice depend strongly on the dimensionality. Zaanen *et al.* [184] argue that the stripes just one such manifestation of topological excitations in two-dimensions.

The sublattice parity is also associated with spatial reflection (parity), because it is exactly the single-site spatial-reflection operator R that is responsible for flipping the sublattice parity (*cf.* section 2.5). The parity-symmetric two-dimensional doped Mott insulator (*i.e.* $t-J$ model) was studied at the mean-field level by Wen [200], where a topological excitation was found that corresponds to a Z_2 vortex. This applies a π phase-shift to holons as they move around the vortex. Although vortex

[†]Hopping within a sublattice is only allowed if the hopping integral is purely imaginary, or additional terms are present, such as a bond-charge interaction [96].

excitations are *prima facie* rather different to domain walls, the structure of the symmetries suggests that there may be a direct connection between the parity-symmetric Z_2 gauge symmetry and the Z_2 gauge symmetry arising from sublattice parity.

4.4.3 Lattice dynamics

The discovery of the isotope effect in conventional superconductors [201, 202] provided important clues as to the microscopic mechanism of superconductivity. The effect of changing isotope mass on the superconducting critical temperature T_c, implies that superconductivity is not a purely electronic interaction, but lattice vibrations (phonons) play an important role on the phenomena. Indeed, in conventional superconductors phonons play a pivotal role, mediating the effective attraction that enables the formation of the Cooper pairs [203,204]. Thus, the question of the magnitude of the phononic effects in the high T_c cuprate superconductors is of prime importance.

Studies of the isotope effect have been carried out in almost all known cuprates (for a review, see reference [205] and references therein). It is shown in Zhao *et al.* [206] that the oxygen-isotope effect in optimially doped cuprates is small and decreases with increasing T_c. On the other hand, studies again by Zhao *et al.* [207] show that the oxygen-isotope effect in $La_{2-x}Sr_xCuO_4$ increases with a decrease in doping, becoming very large in the deeply underdoped region. This suggests that the phonon modes related to oxygen vibrations are strongly coupled to the conduction electrons. In addition to the large oxygen-isotope effect, the copper-isotope effect in several cuprates is smaller than the oxygen-isotope effect in the deeply underdoped region, but stronger than the oxygen-isotope effect near optimal doping. This suggests that copper-dominated phonon modes are involved in the superconducting pairing.

Many models of electron-phonon coupling have been applied to the cuprates. From the point of view of numerical calculations using DMRG, a practical approach is to apply the adiabatic approximation method, as done by Kuwabara [208]. In this method the lattice bond variables are determined self-consistently, by applying the Hellmann-Feynman force equilibrium condition [209,210] at the end of each DMRG sweep, which determines the updated configuration of the lattice for the next sweep. With some effort, such an algorithm could be applied to a two-dimensional system, which would be useful for solving realistic models of phonon-mediated superconductivity [211,212].

A rather general problem with more realistic models of superconductivity, from

the viewpoint of obtaining numerical solutions, is that phenomonological interactions, spin-orbit couplings, phonons, additional bands *etc.* tend to break symmetries that exist in simpler models, or increase the computational effort required for an accurate solution beyond what is possible with the software and hardware technology available today[†]. With numerical methods that can take advantage of non-trivial symmetries of the model, it is advantageous to preserve as many symmetries as possible. Using the non-Abelian DMRG algorithm for example, it is quite likely that introducing a spin-orbit coupling via a phenomonological spin-$SU(2)$-breaking term would have a larger detrimental effect on the efficiency of the algorithm than introducing a true orbital degree of freedom that preserves total angular momentum $SU(2)$. Given the computationally-intensive nature of two-dimensional DMRG calculations, the large efficiency gain arising from utilizing additional symmetries is an important consideration affecting the feasibility of numerical calculations using DMRG.

[†]Indeed, this is arguably true even for the *simple* two-dimensional models of strongly-correlated electrons.

Conclusion

In this thesis the extension of the DMRG algorithm to explicitly preserve non-Abelian global symmetries was presented. This results in a substantial improvement to the accuracy and efficiency of the algorithm. The non-Abelian formulation of the DMRG algorithm hinges upon mostly well-established theory of group representations, most notably the Wigner-Eckart theorem, which enables the factoring-out of constraints imposed by the symmetry (which ordinarily appear as degenerate states), thereby reducing the overall dimension of the Hilbert space while also increasing the number of block-diagonal symmetry sectors of the Hamiltonian. This has the practical effect of reducing the number of basis states needed for a fixed accuracy, by a factor of five or more in some of the calculations presented in this thesis. The application of DMRG to the problems of greatest current interest (two-dimensional models, preferably with periodic boundary conditions) requires significantly more accuracy than what is typically needed for a one-dimensional model. Achieving this accuracy purely by increasing the number of states kept requires a very large amount of computation and is not yet practical except for very small systems. Thus a method of increasing the accuracy *without* increasing the number of basis states, such as the use of non-Abelian symmetries, is very important. Until recently there has been very little work done on the search for additional symmetries of non-integrable models. Even pseudospin symmetry of the Hubbard model was not discovered until as late as 1990 [94]. The potential for numerical algorithms that can make use of non-Abelian global symmetries provides additional impetus for the search for additional symmetries in physically-relevant models.

The non-Abelian formulation was not the only development pertaining to the DMRG algorithm itself that was presented in this thesis. Other results include;

- The wavefunction transformation required for fully utilizing reflection symmetry.

- Performance increases by diagonalizing the left and right block Hamiltonian

contributions to the superblock Hamiltonian.

- The use of the *truncated energy* as an alternative measure of the accuracy of the DMRG calculation.

The ground-state phase diagram of the Kondo lattice model was studied extensively, making explicit use of the $SO(4)$ pseudospin symmetry inherent in the model. The calculations presented here are significantly more accurate than previous numerical studies of the Kondo lattice model, which enabled us to obtain a variety of results for this model, such as;

- Calculations of the phase transition curve up to conduction-band filling $n = 0.95$ strongly suggest that the critical coupling J_c/t remains finite in the limit $n \to 1$, providing independent verification of the bosonization results of reference [137].

- Direct calculation of the magnetization indicates that the main phase transition is second order. The narrowness of the transition makes this difficult to observe by conventional techniques.

- A complex region of ferromagnetism, consisting of at least two distinct ferromagnetic phases, was found in the intermediate coupling regime for conduction-band filling $0.5 < n < 1$.

- The intermediate coupling ferromagnetic regime was shown to also exist in the periodic Anderson model.

The discovery of the intermediate coupling ferromagnetic region adds another dimension to the ongoing debate as to the size of the Fermi surface of the Kondo lattice model. It was not inevitable that the corresponding phase should appear in the periodic Anderson model. In the periodic Anderson model the f-band electrons are mobile, unlike the Kondo lattice case where $\langle c^{\dagger}_{i,\sigma} f_{i,\sigma} \rangle$ is strictly zero. Thus appearance of the same phase in the periodic Anderson model is also of great interest, in particular the appearance of spin correlations at wave number determined *only* by the conduction-band filling suggests that much of the physics of both models is still to be determined.

The use of $SU(2)$ symmetry of the $t - J$ model improves the accuracy of the DMRG calculations significantly. In this thesis, the numerical results were presented for the two-dimensional $t - J$ model, to demonstrate the potential for DMRG calculations on two-dimensional models and provide a verification of the results obtained

by Steven White [10], which, at the time of publication, generated much controversy. The main result of the numerical calculations is that, for the specific choice of half-open half-periodic boundary conditions, a striped phase does appear for physically-relevant coupling and most likely the hole-density per stripe is a constant as the system is doped and depends only on the coupling J/t. This is in agreement with the DMRG results obtained by Steven White [10]. However, it is difficult to extrapolate these results to the thermodynamic model and especially, the influence of the open boundary plays a large role in the transition from the striped phase to the phase-separated regime and a largely unknown role in the formation of the striped phase itself. Given the difficulty of applying the DMRG algorithm to two-dimensional models, the primary focus of future work in this area must surely be on the numerical algorithm itself. One line of inquiry that appears to be particularly promising is momentum space formulations making explicit use of non-Abelian lattice symmetries.

Appendix A

Symmetric Block Wavefunction Transform

In this Appendix, the basis transformation required to obtain an initial wavefunction at the mid-point of a reflection-symmetric DMRG calculation is derived. At the mid-point, the wavefunction can be written in matrix form as a tensor product of left and right basis states, firstly for the wavefunction at the previous sweep,

$$\Psi = (\psi_{a'a}) \, . \tag{A.1}$$

The wavefunction, at the end of the transformation process described in section 1.3.2 is given in a mixed basis,

$$\Phi = (\phi_{ba}) \, , \tag{A.2}$$

which is the tensor product of the left block basis of the current sweep with the right block basis of the previous sweep. The task is to find a transformation $T = (t_{ba})$ which gives the correspondence between the two basis sets, thereby allowing the wavefunction to be determined in the b basis only, as required for the DMRG algorithm when reflection symmetry is used.

The required transformation maximizes the overlap between the wavefunction at the current and the wavefunction at the previous sweep. The dimension of the $|a\rangle$ and $|b\rangle$ basis sets, N_a and N_b respectively, are not necessarily the same thus T is not in general a square matrix.

Consider first the case $N_b < N_a$. The rows of T can be constrained to be orthogonal and normalized via a set of Lagrange multipliers $\lambda_{a'a}/2$, represented as a matrix which can be taken to be symmetric. Thus the maximization problem is

$$F = \sum_{a,a',b} \phi_{ba} T_{ba'} \psi_{aa'} - \sum_{b'b} \frac{\lambda_{b'b}}{2} \sum_{a} \left(T_{b'a} T_{ba} - \delta_{b'b} \right) \, . \tag{A.3}$$

Taking the partial derivative with respect to $T_{\beta\alpha}$, one obtains

$$\frac{\partial F}{\partial T_{\beta\alpha}} = \sum_{\alpha} \phi_{\beta a}\psi_{\alpha a} - \sum_{b} \lambda_{\beta b} T_{b\alpha} \,. \tag{A.4}$$

The solution of $\frac{\partial F}{\partial T_{\beta\alpha}} = 0$ gives the desired transformation. Switching to matrix form,

$$\Phi\,\Psi^{\dagger} = \Lambda\, T \,, \tag{A.5}$$

where $\Lambda = (\lambda_{b'b})$ is an $N_b \times N_b$ symmetric matrix, Φ is an $N_b \times N_a$ matrix, Ψ is an $N_a \times N_a$ matrix and T is an $N_b \times B_a$ row-orthogonal matrix.

We now perform the singular value decomposition of the left-hand side of Eq. (A.5), giving,

$$\Phi\Psi^{\dagger} = U\, D\, V^{T} \,, \tag{A.6}$$

where U is an $N_b \times N_b$ orthogonal matrix, D is an $N_b \times N_b$ diagonal matrix containing the singular values and V^T is an $N_b \times N_a$ row-orthogonal matrix. The singular value decomposition of the right-hand side of Eq. (A.5) is performed for Λ and T separately, giving

$$\Lambda\, T = U\, D_{\Lambda}\, W^{T}\, X\, D_{T}\, V^{T} \,, \tag{A.7}$$

where D_Λ is an $N_b \times N_b$ diagonal matrix containing the singular values of Λ, W^T is a $N_b \times N_b$ orthogonal matrix, X is an $N_b \times N_b$ orthogonal matrix and D_T is an $N_b \times N_b$ diagonal matrix containing the singular values of T. Now Λ is symmetric, therefore the singular value decomposition reduces to a similarity transformation, giving $W = U$. But T is row-orthogonal therefore the singular values are identically equal to 1, giving $D_T = I$. Thus the singular values of Λ must coincide with the singular values of $\Phi\Psi^{\dagger}$, implying $D_\Lambda = D$. Thus,

$$\Phi\Psi^{\dagger} = U\, D\, V^{T} \;=\; U\, D\, U^{T}\, X\, V^{T} \,, \tag{A.8}$$

which implies that $X = U$. Thus, from the singular value decomposition of T,

$$T = X\, D_{T}\, V^{T} \;=\; U\, V^{T} \,, \tag{A.9}$$

where U and V^T are given by the decomposition of $\Phi\Psi^{\dagger}$ in Eq. (A.6). This completes the proof of the $N_b < N_a$ case. The proof for $N_b > N_a$ proceeds in exactly the same fashion, except that U becomes an $N_b \times N_a$ column-orthogonal matrix and V^T becomes an $N_a \times N_a$ orthogonal matrix.

Appendix B

Clebsch-Gordan, $6j$ and $9j$ Coefficients of $SU(2)$

This appendix lists explisit forms and symmetry relations of the $SU(2)$ Clebsch-Gordan, $6j$ and $9j$ Coefficients that are used in the non-Abelian DMRG, described in chapter 2.

Clebsch-Gordan Coefficients

An explicit form is:

$$\begin{aligned} C^{j_1\ j_2\ j}_{m_1 m_2 m} &= \delta_{m_1+m_2,m} \\ &\times \left[\frac{(2j+1)(j+j_1-j_2)!(j-j_1+j_2)!(j_1+j_2-j)!}{(j+j_1+j_2+1)!}\right]^{\frac{1}{2}} \\ &\times \left[\frac{(j+m)!(j-m!)}{(j_1+m_1)!(j_1-m_1)!(j_2+m_2)!(j_2-m_2)!}\right]^{\frac{1}{2}} \\ &\times \sum_s \frac{(-1)^{j_2+m_2+s}(j_2+j+m_1+s)!(j_1-m_1+s)!}{s!(j-j_1+j_2-s)!(j+m-s)!(j_1-j_2-m+s)!} \ . \end{aligned} \tag{B.1}$$

With arbitary precision integer arithmetic this can be evaluated as the square root of a rational number.

Orthogonality of rows:

$$\sum_{m_1 m_2} C^{j_1\ j_2\ j}_{m_1 m_2 m} C^{j_1\ j_2\ j'}_{m_1 m_2 m'} = \delta_{jj'}\delta_{mm'} \ . \tag{B.2}$$

Orthogonality of colums:

$$\sum_{jm} C^{j_1\ j_2\ j}_{m_1 m_2 m} C^{j_1\ j_2\ j}_{m_1' m_2' m} = \delta_{m_1 m_1'}\delta_{m_2 m_2'} \ . \tag{B.3}$$

The 'classical' symmetries form a group of order 12 and until the work of Regge [213] it was believed that these exhausted the symmetries. The true symmetry group is of order 72. The symmetry relations are (the group is generated by the first 4, the last two are for reference),

$$\begin{aligned}
C^{j_1\ j_2\ j}_{m_1 m_2 m} &= (-1)^{j_1+j_2-j} C^{j_1\ \ j_2\ \ j}_{-m_1,-m_2,-m}\,, \\
C^{j_1\ j_2\ j}_{m_1 m_2 m} &= (-1)^{j_1+j_2-j} C^{j_2\ j_1\ j}_{m_2 m_1 m}\,, \\
C^{j_1\ \ j_2\ \ j}_{m_1,m_2,m_1+m_2} &= C^{\frac{1}{2}(j_1+j_2+m_1+m_2)\ \frac{1}{2}(j_1+j_2-m_1-m_2)\ j}_{\frac{1}{2}(j_1-j_2+m_1-m_2),\frac{1}{2}(j_1-j_2-m_1+m_2),j_1-j_2}\,, \\
C^{j_1\ j_2\ j}_{m_1 m_2 m} &= (-1)^{j_2+m_2}\sqrt{\tfrac{2j+1}{2j_1+1}}\, C^{j\ \ j_2\ \ j_1}_{-m,m_2,-m_1}\,, \\
C^{j_1\ j_2\ j}_{m_1 m_2 m} &= (-1)^{j_1-m_1}\sqrt{\tfrac{2j+1}{2j_2+1}}\, C^{j_1\ \ j\ \ j_2}_{m_1,-m,-m_2}\,, \\
C^{j_1\ j_2\ j}_{m_1 m_2 m} &= (-1)^{j_2+m_2}\sqrt{\tfrac{2j+1}{2j_1+1}}\, C^{j_2\ \ j\ \ j_1}_{-m_2,m,m_1}\,,
\end{aligned} \tag{B.4}$$

$6j$ Coefficients

The simplest known explitit form is due to Racah [214, 215],

$$\begin{aligned}
\left\{ \begin{matrix} j_1 & j_2 & j \\ k_1 & k_2 & k \end{matrix} \right\} &= \Delta(j_1 j_2 j)\Delta(k_1 k_2 j)\Delta(j_1 k_2 k)\Delta(k_1 j_2 k) \\
&\times \sum_z \frac{(-1)^z (z+1)!}{(z-j_1-j_2-j)!(z-k_1-k_2-j)!(z-j_1-k_2-k)!(z-k_1-j_2-k)!} \\
&\times \frac{1}{(j_1+j_2+k_1+k_2-z)!(j_1+k_1+j+k-z)!(j_2+k_2+j+k-z)!}\,,
\end{aligned} \tag{B.5}$$

where $\Delta(abc)$ is the *triangle coefficient*,

$$\Delta(abc) = \epsilon_{abc}\left[\frac{(a+b-c)!(a-b+c)!(-a+b+c)!}{(a+b+c+1)!}\right]^{\frac{1}{2}}\,. \tag{B.6}$$

Here ϵ_{abc} enforces the *triangle condition*,

$$\epsilon_{abc} = \begin{cases} 1, & \text{if } c \in \{|a-b|, |a-b|+1, \ldots, a+b\}; \\ 0, & \text{otherwise.} \end{cases} \tag{B.7}$$

This is, despite the apparant asymmetry, in fact symmetric in all permutations of a, b, c.

Similarly to the case of the Clebsch-Gordan coefficients, the $6j$ coefficient can be evaluated reasonably efficiently as the square root of a rational number, using arbitary precision integer arithmetic. However this still requires a relatively large amount of CPU time per $6j$ coefficent. Thus the code used in this thesis stores

already-calculated coefficients in a hash table and uses the permutation symmetries of the $6j$ coefficients to avoid re-calculating coefficients that can be obtained by a permutation. The known symmetries of the $6j$ coefficients form a group of order 144, however the code in this thesis uses only the subset that are true permutations of the coefficients. These symmetries comprise all permutations of the columns and the exchange of any *pair* of elements in the top row with the corresponding elements in the bottom row. This forms a symmetry group of order 24.

$9j$ Coefficients

The DMRG code in this thesis uses the expansion of the $9j$ coefficients in terms of a summation over $6j$ coeffecients:

$$\begin{Bmatrix} j_{11} & j_{12} & j_{13} \\ j_{21} & j_{22} & j_{23} \\ j_{31} & j_{32} & j_{33} \end{Bmatrix} = \sum_k (-1)^{2k}(2k+1) \begin{Bmatrix} j_{11} & j_{21} & j_{31} \\ j_{32} & j_{33} & k \end{Bmatrix} \begin{Bmatrix} j_{12} & j_{22} & j_{32} \\ j_{21} & k & j_{23} \end{Bmatrix} \begin{Bmatrix} j_{13} & j_{23} & j_{33} \\ k & j_{11} & j_{12} \end{Bmatrix}. \tag{B.8}$$

From this, it can be shown that the $9j$ coefficient is zero unless the triangle conditions are fulfilled by the entries in each row and each column. There are 72 known symmetries of the $9j$ coefficent. The $9j$ coefficient is invarant under even permutations of its rows, even permutation of its columns and under interchange of rows and columns (transposition). It is multiplied by a factor $(-1)^{\sum_{ik} j_{ik}}$ under an odd permutation of its rows or columns.

In practice, for all two-site interactions of the form $[\boldsymbol{S}^{k_1} \otimes \boldsymbol{T}^{k_2}]^k$, at least one of the operators must transform as a rotational invariant which implies that one or more of the j_{ij} are zero. Thus the summation over k in Eq. (B.8) is over a single value and the calculation of the $9j$ coefficient is already rather fast. Indeed, it could be made faster since in this case the $9j$ coefficient can be expressed in terms of a *single* $6j$ coefficient, *e.g.* in the case of $j_{33} = 0$,

$$\begin{Bmatrix} j_{11} & j_{12} & j_{13} \\ j_{21} & j_{22} & j_{23} \\ j_{31} & j_{32} & 0 \end{Bmatrix} = \frac{(-1)^{j_{12}+j_{13}+j_{21}+j_{31}} \delta_{j_{13}j_{23}} \delta_{j_{31}j_{32}} \begin{Bmatrix} j_{12} & j_{22} & j_{32} \\ j_{21} & j_{11} & j_{23} \end{Bmatrix}}{[(2j_{31}+1)(2j_{13}+1)]^{\frac{1}{2}}}. \tag{B.9}$$

The location of the zero can be shifted to any position using the symmetry relations. However given the speed of the calculation of the $6j$ coefficients this would have negligable impact on the speed of the DMRG code.

References

[1] F. D. M. Haldane: Luttinger liquid theory of 1-D quantum fluids : I. Properties of the Luttinger model and their extension to general 1D interacting spinless Fermi gas, *J. Phys. C* **14** 2585, (1981).

[2] P. Bloom: Two-dimensional Fermi gas, *Phys. Rev. B* **12** 125, (1975).

[3] P. W. Anderson: "Luttinger-liquid" behavior of the normal metallic state of the 2D Hubbard model, *Phys. Rev. Lett.* **64** 1839, (1990).

[4] M. Gulácsi: Fermi-liquid versus non-Fermi-liquid behaviour, *Phil. Mag. B* **76** 731, (1997).

[5] D. P. Landau and K. Binder: *A Guide to Monte Carlo Simulations in Statistical Physics*, Cambridge University Press, Cambridge, 2000.

[6] S. R. White: Density Matrix Formulation for Quantum Renormalization Groups, *Phys. Rev. Lett.* **69** 2863, (1992).

[7] H. Sakamoto and K. Kubo: Metallic Ferromagnetism in a One-Dimensional Hubbard Model; Study Using the Density-Matrix Renormalization-Group Method, *J. Phys. Soc. Jpn* **65** 3732, (1996).

[8] M. Guerrero and R. M. Noack: Ferromagnetism and phase separation in one-dimensional $d-p$ and periodic Anderson models, *Phys. Rev. B* **63** 144423, (2001).

[9] Z. Weihong, J. Oitmaa, C.J. Hamer and R.J. Bursill: Numerical Studies of the two-leg Hubbard ladder, *J. Phys. C* **13** 433, (2001).

[10] S. R. White and D. J. Scalapino: Density Matrix Renormalization Group Study of the Striped Phase in the 2D t-J Model, *Phys. Rev. Lett.* **80** 1272, (1998).

[11] I. P. McCulloch, A. R. Bishop and M. Gulácsi: DMRG and the two dimensional $t - J$ Model, *Phil. Mag. B* **81** 1603, (2001).

[12] T. Xiang, J. Lou and Z. B. Su: Two-dimensional algorithm of the density matrix renormalization group, *Phys. Rev. B* **64** 104414, (2001).

[13] T. Xiang: Density-matrix renormalization-group method in momentum space, *Phys. Rev. B* **53** R10445, (1996).

[14] S. Nishimoto, E. Jeckelmann, F. Gebhard and R. M. Noack: Application of the Density-Matrix Renormalization-Group in momentum space, *cond-mat/*0110420.

[15] X. Wang and T. Xiang: Transfer-matrix density-matrix renormalization-group theory for thermodynamics of one-dimensional quantum systems, *Phys. Rev. B* **56** 5061, (1997).

[16] T. Nishino and K. Okunishi: Corner Transfer Matrix Renormalization Group Method, *J. Phys. Soc. Jpn.* **65** 891, (1996).

[17] C. Zhang, E. Jeckelmann and S. R. White: Density Matrix Approach to Local Hilbert Space Reduction, *Phys. Rev. Lett.* **80** 2661, (1998).

[18] T. Kühner and S. R. White: Dynamical correlation functions using the density matrix renormalization group, *Phys. Rev. B* **60** 335, (1999).

[19] J. Dukelsky and S. Pittel: A New Approach to Large-Scale Nuclear Structure Calculations, *Phys. Rev. C* **63** 061303, (2001).

[20] M. A. Martín-Delgado and G. Sierra: Density Matrix Renormalization Group Approach to an Asymptotically Free Model with Bound States, *Phys. Rev. Lett.* **83** 1514, (1999).

[21] S. Östlund and S. Rommer: Thermodynamic Limit of Density Matrix Renormalization, *Phys. Rev. Lett.* **75** 3537, (1995).

[22] S. Doniach: The Kondo lattice and weak antiferromagnetism, *Physica B* **91** 231, (1977).

[23] P. W. Anderson: The Resonating Valence Bond State in La_2CuO4 and Superconductivity, *Science* **235** 1196, (1987).

[24] F. C. Zhang and T. M. Rice: Effective Hamiltonian for the superconducting Cu oxides, *Phys. Rev. B* **37** 3759, (1987).

[25] T. Nishino and T. Hikihara: Density Matrix Renormalization Group — Introduction from a variational point of view, *Int. J. Mod. Phys.* **B13** 1, (1999).

[26] S. R. White: Strongly correlated electron systems and the density matrix renormalization group, *Phys. Rep.* **301** 187, (1998).

[27] S. K. Pati, S. Ramasesha and D. Sen: Exact and Approximate Theoretical Techniques for Quantum Magnetism in Low Dimensions, *cond–mat/*0106621.

[28] S. Caprara and A. Rosengren: Density-matrix renormalization group for fermions: Convergence to the infinite-size limit, *Nucl. Phys. B* **493** 640, (1997).

[29] P. Schmitteckert: PhD Thesis, *URL:* http://www/physik.Uni-Augsburg.de/~peters.

[30] K. G. Wilson: The renormalization group: Critial phenomena and the Kondo problem, *Rev. Mod. Phys.* **47** 773, (1975).

[31] P. A. Lee: Real-Space Scaling Studies of Localization, *Phys. Rev. Lett.* **42** 1492, (1979).

[32] P. A. Lee and D. S. Fischer: Anderson Localization in Two Dimensions, *Phys. Rev. Lett.* **47** 882, (1981).

[33] S. R. White and R. M. Noack: Real-Space Quantum Renormalization Groups, *Phys. Rev. Lett.* **68** 3487, (1992).

[34] C. Lanczos: An iteration method for the solution of the eigenvalue problem of linear differential and integral operators, *J. Res. Nat. Bur. Stand.* **45** 255, (1950).

[35] J. K. and Cullum R. A. Willoughby: *Lanczos algorithms for large symmetric eigenvalue computations*, Birkhauser, Boston, 1985.

[36] R. Lehoucq, K. Maschhof, D. Sorensen and C. Yang: ARPACK Users Guide, *URL:* http://www.caam.rice.edu/software/ARPACK/.

[37] F. D. M. Haldane: Nonlinear Field Theory of Large-Spin Heisenberg Antiferromagnets: Semiclassically Quantized Solitons of the One-Dimensional Easy-Axis Nel State, *Phys. Rev. Lett.* **50** 1153, (1983).

[38] X. Wang, S. Qin and L. Yu: Haldane gap for the $S = 2$ antiferromagnetic Heisenberg chain revisited, *Phys. Rev. B* **60** 14529, (1983).

[39] S. Moukouri and L. G. Caron: Ground-state properties of the one-dimensional Kondo lattice at partial band filling, *Phys. Rev. B* **52** R15723, (1995).

[40] U. Schollwöck: Marshall's sign rule and density-matrix renormalization-group acceleration, *Phys. Rev. B* **58** 8194, (1998).

[41] R. M. Noack, S. R. White and D. J. Scalapino: The Density Matrix Renormalization Group for Fermion Systems, in D. P. Landau, K. K. Mon and H. B. Schüttler (Eds.): *Computer Simulations in Condensed Matter Physics VII*, Spinger Verlag, Heidelberg, Berlin, 1994.

[42] E. S. Sørensen: Parity, precision and spin inversion within the density matrix renormalization group, *J. Phys. Cond. Mat* **10** 10655, (1998).

[43] S. R. White: Density-matrix algorithms for quantum renormalization groups, *Phys. Rev. B* **48** 10345, (1993).

[44] S. R. White: Spin Gaps in a Frustrated Heisenberg Model for CaV_4O_9, *Phys. Rev. Lett.* **77** 3633, (1996).

[45] S. Rommer and S. Östlund: Class of ansatz wave functions for the one-dimensional spin system and their relation to the density matrix renormalization group, *Phys. Rev. B* **55** 2164, (1997).

[46] I. Affleck, T. Kennedy, E. H. Leib and H. Tasaki: Rigorous results on valence-bond ground states in antiferromagnets, *Phys. Rev. Lett.* **59** 799, (1987).

[47] G. Bedürftig, B. Brendel, H. Frahm and R. M. Noack: Friedel oscillations in the open Hubbard chain, *Phys. Rev. B* **58** 10225, (1998).

[48] M. Andersson, M. Boman and S. Östlund: Density-matrix renormalization group for a gapless system of free fermions, *Phys. Rev. B* **59** 10493, (1999).

[49] T. J. Osborne and M. A. Neilsen: Entanglement, quantum phase transitions, and density matrix renormalization, *quant–ph/*0109024.

[50] J. Dukelsky, M. A. Martín-Delgado, T. Nishino and G. Sierra: Equivalence of Variational Matrix Product Method and the Density Matrix Renormalization Group, *Europhys. Lett.* **43** 457, (1998).

[51] H. Takasaki, T. Hikihara and T. Nishino: Fixed Point of the Finite-System DMRG, *J. Phys. Soc. Jpn.* **68** 1537, (1999).

[52] G. Sierra and T. Nishino: The Density Matrix Renormalization Group Method applied to Interaction Round a Face Hamiltonians, *Nucl. Phys. B* **495** 505, (1997).

[53] S. R. White and D. A. Huse: Numerical renormalization-group study of low-lying eigenstates of the antiferromagnetic $S = 1$ Heisenberg chain, *Phys. Rev. B* **48** 3844, (1993).

[54] M. S. L. du Croo de Jongh and J. M. J. van Leeuwen: Critical behaviour of the two-dimensional Ising model in a transverse field: A density-matrix renormalization calculation, *Phys. Rev. B* **57** 8494, (1998).

[55] R. J. Bursill: Density-matrix renormalization-group algorithm for quantum lattice systems with a large number of states per site, *Phys. Rev. B* **60** 1643, (1999).

[56] S. Laing and H. Pang: Approximate diagonalization using the density-matrix renormalization-group method: A two-dimensional-systems perspective, *Phys. Rev. B* **49** 9214, (1994).

[57] T. Nishino, Y. heida, K. Okunishi, N. Maeshima, Y. Akutsu and A. Gendiar: Two-Dimensional Tensor Product Variational Formulation, *cond–mat/*0011103.

[58] D. J. Scalapino and S. R. White: Numerical Results for the Hubbard Model: Implications for the High T_c Pairing Mechanism, *cond–mat/*0007515.

[59] Ö. Legeza and G. Fáth: Accuracy of the density-matrix renormalization-group method, *Phys. Rev. B* **53** 14349, (1996).

[60] D. L. Harrar II: On the Davidson and Jacobi-Davidson Methods for Large-Scale Eigenvalue Problems, *Preprint* Australian National University School of Mathematical Sciences, Research Report MRR99-047 (1999).

[61] A. Stathopoulos and Y. Saad: Restarting techniques for the (Jacobi-)Davidson Symmetric Eigenvalue Methods, *Elec. Trans. on Numer. Anal. (ETNA)* **7** 163, (1998).

[62] E. de Sturler: Improving the Convergence of the Jacobi-Davidson Algorithm, *Preprint* Technical Report UIUCDCS-R-2000-2173/UILU-ENG-2000-1730 (2000).

[63] K. A. Hallberg: Density-matrix algorithm for the calculation of dynamical properties of low-dimensional systems, *Phys. Rev. B* **52** R9827, (1995).

[64] T. D. Kühner and S. R. White: Dynamical correlation functions using the density matrix renormalization group, *Phys. Rev. B* **60** 335, (1999).

[65] I. Peschel, M. Kaulke and Ö. Legeza: Density-matrix spectra for integrable models, *Ann. Phys.* **8** 153, (1999).

[66] T. Nishino: Density Matrix Renormalization Group Method for 2D Classical Models, *J. Phys. Soc. Japan* **64** 3598, (1995).

[67] R. J. Baxter: *Exactly Solvable Models in Statistical Mechanics*, Academic Press, New York, 1982.

[68] M.-C. Chung and I. Peschel: Density-matrix spectra for two-dimensional quantum systems, *Phys. Rev. B* **62** 4191, (2000).

[69] I. Peschel and M.-C. Chung: Density Matrices for a Chain of Oscillators, *J. Phys. A* **32** 8419, (1999).

[70] S. R. White and D. A. Huse: Numerical renormalization-group study of low-lying eigenstates of the antiferromagnetic S=1 Heisenberg chain, *Phys. Rev. B* **48** 3844, (1993).

[71] M.-C. Chung and I. Peschel: Density-matrix spectra of solvable fermionic systems, *Phys. Rev. B* **64** 064412, (2001).

[72] I. Peschel and T. T. Truong: Corner Transfer Matrices and Conformal Invariance, *Z. Phys. B* **69** 385, (1987).

[73] T. T. Truong and I. Peschel: Diagonalization of finite-size corner transfer matrices and related spin chains, *Z. Phys. B* **75** 119, (1989).

[74] S. Daul: First and second order ferromagnetic transition at $T = 0$ in a 1D itinerant system, *Eur. Phys. J. B* **14** 649, (2000).

[75] I. P. McCulloch and M. Gulácsi: Density matrix renormalization group method and symmetries of the Hamiltonian, *Aust. J. Phys.* **53** 597, (2000).

[76] I. P. McCulloch and M. Gulácsi: Total Spin in DMRG, *Phil. Mag. Lett.* **81** 447, (2001).

[77] J.-P. Serre: *Linear Representations of Finite Groups*, Springer-Verlag, New York, 1977.

[78] W. Miller: *Symmetry groups and their applications*, Academic Press, New York, 1972.

[79] B. L. van der Waerden: *Group Theory and Quantum Mechanics*, Springer-Verlag, Berlin, 1974.

[80] J. F. Cornwell: *Group Theory in Physics, Volume I*, Academic Press, London, 1984.

[81] J. F. Cornwell: *Group Theory in Physics, Volume II*, Academic Press, London, 1984.

[82] M. Born, W. Heisenberg and P. Jordan: Zur Quantenmechanik II, *Z. Physik* **35** 557, (1926).

[83] E. P. Wigner: *Group Theory and Its Applications to the Quantum Mechanics of Atomic Spectra*, Academic Press, New York, 1959.

[84] L. C. Biedenharn and J. D. Louck: *Angular Momentum in Quantum Physics*, Addison-Wesley, Massachusetts, 1981.

[85] L. C. Biedenharn and J. D. Louck: *The Racah-Wigner Algebra in Quantum Theory*, Addison-Wesley, Massachusetts, 1981.

[86] V. Devanathan: *Angular Momentum Techniques on Quantum Mechanics*, Kluwer Academic Publishers, the Netherlands, 1999.

[87] C. N. Yang: η-pairing and Off-Diagonal Long-Range Order in a Hubbard Model, *Phys. Rev. Lett.* **63** 2144, (1989).

[88] J. J. Dongarra *et al.* : Basic Linear Algebra Subprograms, *URL:* http://www.netlib.org/blas/index.html.

[89] V. K. Agrawala: Wigner-Echart theorem for an arbitary group or Lie algebra, *J. Math. Phys.* **21** 1562, (1980).

[90] W. Tatsuaki: Interaction-round-a-face density-matrix renormalization-group method applied to rotational-invariant quantum spin chains, *Phys. Rev. E* **61** 3199, (2000).

[91] J. Hubbard: Electron Correlations in Narrow Energy Bands, *Proc. Roy. Soc. A* **276** 238, (1963).

[92] M. C. Gutzwiller: Effect of Correlation on the Ferromagnetism of Transition Metals, *Phys. Rev. Lett.* **10** 159, (1963).

[93] B. S. Shastry: Exact Integrability of the One-Dimensinoal Hubbard Model, *Phys. Rev. Lett.* **56** 2453, (1986).

[94] C. N. Yang and S. C. Zhang: SO_4 Symmetry in a Hubbard Model, *Mod. Phys. Lett. B* **4** 759, (1990).

[95] C. N. Yang: Concept of Off-Diagonal Long-Range Order and the Quantum Phases of Liquid He and of Superconductors, *Rev. Mod. Phys.* **32** 694, (1962).

[96] S. Q. Shen: Theorem on pesudospin and η-pairing superconductivity, *Phys. Rev. B* **54** 9039, (1996).

[97] V. E. Korepin and F. H. L. Essler, in The Hubbard Model, NATO ASI series, Series B, Vol. 343: *edited by D. Baeriswyl, D. K. Campbell, J. M. P. Carmelo, F. Guinea and E. Louis*, Plenum Press, New York, 1995.

[98] J. R. Schrieffer and P. A. Wolff: Relation between the Anderson and Kondo Hamiltonians, *Phys. Rev.* **149** 491, (1966).

[99] Y. Tokura, Y. Tomioka, H. Kuwahara, A. Asamitsu, Y. Moritomo and M. Kasai: Origins of colossal magnetoresistance in perovskite-type manganese oxides, *J. Appl. Phys.* **79** 5288, (1996).

[100] S. Jin, T. H. Tiefel, M. McCormack, R. A. Fasnacht, R. Ramesh and L. H. Chen: Thousandfold Change in Resistivity in Magnetorestitive La-Ca-Mn-O Films, *Science* **264** 413, (1994).

[101] Y. D. Chuan, A. D. Gromko, D. S. Dessau. T. Kimura, and Y. Tokura: Fermi surface nesting and nanoscale fluctuating charge/orbital ordering in colossal magnetoresistive oxides, *Science* **292** 1509, (2001).

[102] J. B. Goodenough: Theory of the Role of Covalence in the Perovskite-Type Manganites [La, M(II)]MnO_3, *Phys. Rev.* **100** 564, (1955).

[103] A. J. Millis, P. B. Littlewood and B. I. Shraiman: Double Exchange Alone Does Not Explain the Resistivity of $La_{1-x}Sr_xMnO_3$, *Phys. Rev. Lett.* **74** 5144, (1995).

[104] A. J. Millis, B. I. Shraiman and R. Mueller: Dynamic Jahn-Teller Effect and Colossal Magnetoresistance in $La_{1-x}Sr_xMnO_3$, *Phys. Rev. Lett.* **77** 175, (1996).

[105] A. J. Millis, R. Mueller and B. I. Shraiman: Fermi-liquid-to-polaron crossover. II. Double exchange and the physics of colossal magnetoresistance, *Phys. Rev. B* **54** 5405, (1996).

[106] E. L. Nagaev: Phase separation in high-temperature superonductors and related magnetic systems, *Physics - Uspekhi* **38** 497, (1995).

[107] G. Aeppli and Z. Fisk: Kondo Insulators, *Comments Cond. Mat. Phys.* **16** 155, (1992).

[108] Z. Fisk *et al.* : Kondo Insulators, *Physica B* **207** 798, (1995).

[109] H. Frölich and F. R. N. Nabarro: Orientation of nuclear spins in metals, *Proc. Roy. Soc. A* **175** 382, (1940).

[110] N. Andrei: Diagonalization of the Kondo Hamiltonian, *Phys. Rev. Lett.* **45** 379, (1980).

[111] P. B. Vigman: Exact solution of $s-d$ exchange model at $T=0$, *Sov. Phys. JETP Lett.* **31** 364, (1980).

[112] A. C. Hewson: *The Kondo Problem To Heavy Fermions*, Cambridge University Press, Cambridge, 1993.

[113] J. Kondo: Resistance Minimum in Dilute Magnetic Alloys, *Prog. Theor. Phys.* **32** 37, (1964).

[114] P. Nozières: Impuretés Magnétiques et Effet Kondo, *Ann. Phys. (France)* **10** 19, (1985).

[115] P. Nozières: Some comments on Kondo lattices and the Mott transition, *Eur. Phys. J. B* **6** 447, (1998).

[116] D. Meyer and W. Nolting: Kondo screening and exhaustion in the periodic Anderson model, *Phys. Rev. B* **61** 13456, (2000).

[117] S. Burdin, A. Georges and D. R. Grempel: Coherence Scale of the Kondo Lattice, *Phys. Rev. Lett.* **85** 1048, (2000).

[118] H. Tsunetsugu, M. Sigrist and K. Ueda: The ground-state phase diagram of the one-dimensional Kondo lattice model, *Rev. Mod. Phys.* **69** 809, (1997).

[119] B. Möller and P. Wölfe: Magnetic order in the periodic Anderson model, *Phys. Rev. B* **48** 10320, (1993).

[120] M. Troyer and D. Würtz: Ferromagnetism of the one-dimensional Kondo-lattice model: A quantum Monte Carlo study, *Phys. Rev. B* **47** 2886, (1993).

[121] C. C. Yu and S. R. White: Numerical renormalization group study of the one-dimensional Kondo insulator, *Phys. Rev. Lett.* **71** 3866, (1993).

[122] Z. Wang, X-P. Li and D-H Lee: Spin-triplet solitons in the one-dimensional symmetric Kondo lattice, *Phys. Rev. B* **47** 11935, (1993).

[123] S-Q. Shen: Total spin and antiferromagnetic correlation in the Kondo model, *Phys. Rev. B* **53** 14252, (1996).

[124] H. Tsunetsugu: Rigorous results for half-filled Kondo lattices, *Phys. Rev. B* **55** 3042, (1997).

[125] R. Jullien and P. Pfeuty: Analogy between the Kondo lattice and theHubbard model from renormalization-group calculations in one dimension, *J. Phys. F* **11** 353, (1981).

[126] H. Tsunetsugu, Y. Hatsugai, K. Ueda and M. Sigrist: Spin-liquid ground state of the half-filled Kondo lattice in one dimension, *Phys. Rev. B* **46** 3175, (1992).

[127] A. M. Tsvelik: Semiclassical solution of one dimensional model of Kondo insulator, *Phys. Rev. Lett.* **72** 1048, (1994).

[128] M. Sigrist, H. Tsunetsuga and K.o Ueda: Rigorous results for the one-electron Kondo-lattice model, *Phys. Rev. Lett.* **67** 2211, (1991).

[129] C. Lacroix: Some Exact Results for the Kondo Lattice With Infinite Exchange Interaction, *Solid State Commun.* **54** 991, (1985).

[130] M. Ogata and H. Shiba: Bethe-ansatz wave function, momentum distribution, and spin correlation in the one-dimensional strongly correlated Hubbard model, *Phys. Rev. B* **41** 2326, (1990).

[131] M. Sigrist, H. Tsunetsugu, K. Ueda and T. M. Rice: Ferromagnetism in the strong-coupling regime of the one-dimensional Kondo-lattice model, *Phys. Rev. B* **46** 13838, (1992).

[132] T. Yanagisawa and K. Harigaya: Ferromagnetic transition of the Kondo lattice with Coulomb repulsion: Exact results, *Phys. Rev. B* **50** 9577, (1994).

[133] M. A. Ruderman and C. Kittel: Indirect Exchange Coupling of Nuclear Magnetic Moments by Conduction Electrons, *Phys. Rev.* **96** 99, (1954).

[134] T. Kasuya: A theory of metallic ferro- and antiferromagnetism on Zener's model, *Prog. Theor. Phys. (Kyoto)* **16** 45, (1956).

[135] K. Yosida: Magnetic Properties of Cu – Mn Alloys, *Phys. Rev.* **106** 893, (1957).

[136] C. Zener: Interaction between the d-Shells in the Transition Metals. II. Ferromagnetic Compounds of Manganese with Perovskite Structure, *Phys. Rev.* **82** 403, (1951).

[137] G. Honner and M. Gulácsi: One-Dimensional Kondo Lattice at Partial Band Filling, *Phys. Rev. Lett.* **78** 2180, (1997).

[138] T. Yanagisawa and M. Shimoi: Exact Results in Strongly Correlated Electrons — Spin-Reflection Positivity and the Perron-Fronebius Theorem, *Int. J. Mod. Phys. B* **10** 3383, (1996).

[139] D. N. Aristov: Indirect RKKY interaction in any dimensionality, *Phys. Rev. B* **55** 8064, (1997).

[140] G. Honner: PhD Thesis: Interacting Electrons in Low-Dimensional Systems, Australian National University, 1998.

[141] P. W. Anderson and H. Hasegawa: Considerations on Double Exchange, *Phys. Rev.* **100** 675, (1955).

[142] F. Bloch: Inkohärente Röntenstreuung und Dichteschwankungen eines entarteten Fermigases, *Helv. Phys. Acta* **7** 385, (1934).

[143] S. Tomonaga: Remarks on Block's Method of Sound Waves Applied to Many-Fermion Problems, *Prog. Theor. Phys.* **5** 544, (1950).

[144] D. C. Mattis and E. H. Lieb: Exact Solution of a Many-Fermion System and its Associated Boson Field, *J. Math. Phys.* **6** 304, (1965).

[145] S. Coleman: Quantum sine-Gordon equation as the massive Thirring model, *Phys. Rev. D* **11** 2088, (1975).

[146] A. Luther and I. Peschel: Calculation of critical exponents in two dimensions from quantum field theory in one dimension, *Phys. Rev. B* **12** 3908, (1975).

[147] S. Mandelstam: Soliton operators for the quantized sine-Gordon equation, *Phys. Rev. D* **11** 3026, (1975).

[148] R. Heidenreich, B. Schroer, R. Seiler and D. Uhlenbrock: The Sine-Gordon equation and the one-dimensional electron gas, *Phys. Lett. A* **54** 119, (1975).

[149] G. Honner and M. Gulácsi: Ordering of localized moments in Kondo lattice models, *Phys. Rev. B* **58** 2662, (1998).

[150] J. Voit: One-dimensional Fermi liquids, *Rep. Prog. Phys.* **57** 977, (1994).

[151] M. Stone (Ed.): *Bosonization*, World Scientific, Singapore, 1994.

[152] R. Shankar: Bosonization: how to make it work for you in condensed matter, *Acta Phys. Pol.* **26** 1835, (1995).

[153] P. Pfeuty: An Exact Result for the 1D Random Ising Model in a Transverse Field, *Phys. Lett. A* **72** 245, (1979).

[154] D. S. Fisher: Random transverse field Ising spin chains, *Phys. Rev. Lett.* **69** 534, (1992).

[155] D. S. Fisher: Critical behavior of random transverse-field Ising spin chains, *Phys. Rev. B* **51** 6411, (1992).

[156] E. Dagotto, S. Yunoki, A. L. Malvezzi, A. Moreo and J. Hu: Ferromagnetic Kondo model for manganites: Phase diagram, charge segregation, and influence of quantum localized spins, *Phys. Rev. B* **58** 6414, (1998).

[157] H. Tsunetsugu, M. Sigrist and K. Ueda: Phase diagram of the one-dimensional Kondo-lattice model, *Phys. Rev. B* **47** 8345, (1993).

[158] N. Shibata, K. Ueda, T. Nishino and C. Ishii: Friedel oscillations in the one-dimensional Kondo lattice model, *Phys. Rev. B* **54** 13495, (1996).

[159] N. Shibata and K. Ueda: One Dimensional Kondo Lattice Model Studied by the Density Matrix Renormalization Group Method, *J. Phys. Cond. Mat.* **11** R1, (1999).

[160] O. Zachar, S. A. Kivelson and V. J. Emery: Exact Results for a 1D Kondo Lattice from Bosonization, *Phys. Rev. Lett.* **77** 1342, (1996).

[161] I. P. McCulloch, A. Juozapavičius, A. Rosengren and M. Gulácsi: Localized spin ordering in Kondo lattice models, *to be submitted.*

[162] K. Udea, T. Nishino and H. Tsunetsugu: Large Fermi surface of the one-dimensional Kondo lattice model, *Phys. Rev. B* **50** 612, (1994).

[163] S. Moukouri and L. G. Caron: Fermi surface of the one-dimensional Kondo lattice, *Phys. Rev. B* **54** 12212, (1996).

[164] J. M. Luttinger: Fermi Surface and Some Simple Equilibrium Properties of a System of Interacting Fermions, *Phys. Rev.* **119** 1153, (1960).

[165] M. Yamanaka, M. Oshikawa, and I. Affleck: Nonperturbative Approach to Luttinger's Theorem in One Dimension, *Phys. Rev. Lett.* **79** 1110, (1997).

[166] M. Guerrero and R. M. Noack: Phase diagram of the one-dimensional Anderson lattice, *Phys. Rev. B* **53** 3707, (1996).

[167] J. G. Bednorz and K. A. Müller: Possible High T_c Superconductivity in the Ba-La-Cu-O System, *Z. Phys. B* **64** 188, (1986).

[168] J. M. Tranquada, B. J. Sternlieb, J. D. Axe, Y. Nakamura and S. Uchida: Evidence for stripe correlations of spins and holes in copper oxide superconductors, *Nature* **375** 561, (1995).

[169] J. M. Tranquada, J. D. Axe, N. Ichikawa, Y. Nakamura, S. Uchida and B. Nachumi: Neutron-scattering study of stripe-phase order of holes and spins in $La_{1.48}Nd_{0.4}Sr_{0.12}CuO_4$, *Phys. Rev. B* **54** 7489, (1996).

[170] J. M. Tranquada, J. D. Axel, N. Ichikawa, A. R. Moodenbaugh, Y. Nakamura, and S. Uchida: Coexistence of, and Competition between, Superconductivity and Charge-Stripe Order in $La_{1.6-x}Nd_{0.4}Sr_xCuO_4$, *Phys. Rev. Lett.* **78** 338, (1997).

[171] K. Hermann: The program system BALSAC, *URL:* http://www.fhi-berlin.mpg.de/th/balsac/balm.0.html.

[172] V. J. Emery: Theory of the quasi-one-dimensional electron gas with strong "on-site" interactions, *Phys. Rev. B* **14** 2989, (1990).

[173] K. A. Chao, J. Spalek and A. M. Oleś: Kinetic exchange interaction in a narrow S-band, *J. Phys. C* **10** L271, (1977).

[174] E. Dagotto: Correlated electrons in high-temperature superconductors, *Rev. Mod. Phys.* **66** 763, (1994).

[175] V. J. Emery and G. Reiter: Quasiparticles in the copper-oxygen planes of high-Tc superconductors: An exact solution for a ferromagnetic background, *Phys. Rev. B* **38** 11938, (1988).

[176] J. Zaanen, A. M. Oleś and P. Horsch: Generalizing the t-J model: Triplet holes, *Phys. Rev. B* **46** 5798, (1992).

[177] K. Yosida: *Functional Analysis*, Springer-Verlag, Berlin, 1980.

[178] H. Itoyama, B. M. McCoy. and J. H. H. Perk: Level crossing, spontaneous parity violation, high T_c superconductivity mechanisms and the chiral Potts chain, *Int. J. Mod. Phys. B* **4** 995, (1990).

[179] V. J. Emery, S. A. Kivelson and H. Q. Lin: Phase separation in the $t - J$ model, *Phys. Rev. Lett.* **64** 475, (1990).

[180] Proceedings: Conference on Spectroscopies in Novel Superconductors, *J. Phys. Chem.* **59** No. 10 - 12 (1998).

[181] J. Zaanen and O. Gunnarsson: Charged magnetic domain lines and the magnetism of high-Tc oxides, *Phys. Rev. B* **40** 7391, (1989).

[182] S. A. Kivelson, V. J. Emery H. Q. Lin: Charge Ordering in High-Temperature Superconductors, *Physica C* **263** 44, (1996).

[183] J. Zaanen, M. L. Horbach and W. van Saarloos: Charged domain-wall dynamics in doped antiferromagnets and spin fluctuations in cuprate superconductors, *Phys. Rev. B* **53** 8671, (1996).

[184] J. Zaanen, O. Y. Osman, H. V. Kruis, Z. Nussinov and J. Tworzydlo: The geometric order of stripes and Luttinger liquids, *Phil. Mag. B* **81** 1485, (2001).

[185] S. R. White and D. J. Scalapino: Energetics of Domain Walls in the 2D t-J Model, *Phys. Rev. Lett.* **81** 3227, (1998).

[186] S. R. White and D. J. Scalapino: Phase separation and stripe formation in the two-dimensional $t - J$ model: A comparison of numerical results, *Phys. Rev. B* **61** 6320, (2000).

[187] C. S. Hellberg and E. Manousakis: Stripes and the t-J Model, *Phys. Rev. Lett.* **83** 132, (1999).

[188] J. Zaanen: Current Ideas on the Origin of Stripes, *J. Phys. Chem. Solids* **59** 1769, (1998).

[189] J. Zaanen: Why high-T_c is exciting, *cond–mat/*0103255.

[190] M. Morais-Smith, Y. M. Dimashko, N. Hasselmann and A. O. Caldeiro: Dynamics of stripes in doped antiferromagnets, *Phys. Rev. B* **58** 453, (1998).

[191] L. P. Pryadko, S. A. Kivelson, V. J. Emery, Y. B. Bazaliy and E. A. Demler: Topological doping and the stability of stripe phases, *Phys. Rev. B* **60** 7541, (1999).

[192] G. B. Martin, C. Gazza, J. C. Xavier, A. Feiguin, and E. Dagotto: Doped Stripes in Models for the Cuprates Emerging from the One-Hole Properties of the Insulator, *Phys. Rev. Lett.* **84** 5844, (2000).

[193] R. S. Markiewicz: A Survey of the Van Hove Scenario for High-T_c Superconductivity with Special Emphasis on Pseudogaps and Striped Phases, *J. Phys. Chem. Solids* **58** 1179, (1997).

[194] N. F. Mott: Metal-insulator transition, *Phil. Mag. B* **50** 161, (1984).

[195] P. B. Visscher: Phase separation instability in the Hubbard model, *Phys. Rev. B* **10** 943, (1974).

[196] E. L. Nagaev: *Physics of Magnetic Semiconductors*, Mir, Moscow, 1983.

[197] A. I. Rusinov, Do Chan Kat and Yu. V. Kopaev: Theory of superconductivity in the presence of electron-hole pairing in semimetals at $T = 0$, *Sov. Phys. JETP* **38** 991, (1974).

[198] M. Gulacsi and Zs. Gulacsi: Theory of coexistence between itinerant-electron antiferromagnetism and superconductivity, *Phys. Rev. B* **33** 6147, (1986).

[199] J. Zaanen and Z. Nussinov: Stripes and Nodal Fermions as Two Sides of the Same Coin, *cond–mat/*0006193.

[200] X. G. Wen: Mean-field theory of spin-liquid states with finite energy gap and topological orders, *Phys. Rev. B* **44** 2664, (1991).

[201] E. Maxwell: Isotope Effect in the Superconductivity of Mercury, *Phys. Rev.* **78** 477, (1950).

[202] C. A. Reynolds, B. Serin, W. H. Wright and L. Nesbitt: Superconductivity of Isotopes of Mercury, *Phys. Rev.* **78** 487, (1950).

[203] L. N. Cooper: Bound Electron Pairs in a Degenerate Fermi Gas, *Phys. Rev.* **104** 1189, (1956).

[204] J. Bardeen, L. N. Cooper and J. R. Schrieffer: Theory of Superconductivity, *Phys. Rev.* **108** 1175, (1957).

[205] G. M. Zhao: Experimental constraints on the physics of cuprates, *Phil. Mag. B* **81** 1335, (2001).

[206] G. M. Zhao, K. Conder, M. Angst, S. M. Kazakov, J. Karpinski, M. Maciejewski, C. Bougerol, J. S. Pshirkov and E. V. Antipov: Large oxygen-isotope effect in $Sr_{0.4}K_{0.6}BiO_3$: Evidence for phonon-mediated superconductivity, *Phys. Rev. B* **62** R11977, (2000).

[207] G. M. Zhao, K. Conder, H. Keller and K. A. Müller: Oxygen isotope effect in $La_{2-x}Sr_xCuO_4$: evidence for polaronic charge carriers and their condensation, *J. Phys. Cond. Mat.* **10** 9055, (1998).

[208] M. Kuwabara, Y. Shimoi and S. Abe: Polaron versus Bipolaron in Conducting Polymers: a Density Matrix Renormalization Group Study, *J. Phys. Soc. Jpn.* **67** 1521, (1998).

[209] Y. Shimoi and S. Abe: Competition between polarons and bipolarons in non-degenerate conjugated polymers, *Phys. Rev. B* **50** 14781, (1994).

[210] G. Z. Wen and W. P. Su: Effects of Electron Correlation on Doping in Conjugated Polymers- A Study of the SSHH and BKH Models Using the DMRG Method, *Synth. Met.* **78** 195, (1996).

[211] A. Bussmann-Holder, A. R. Bishop, H. Buettner, T.i Egami, R. Micnas and K. A. Müller: The Phase Diagram of High-T_c Superconductors in the Presence of Dynamic Stripes, *cond-mat/*0104089.

[212] A. Bussmann-Holder, K. A. Müller, R. Micnas, H. Buttner, A. Simon, A. R. Bishop and T. Egami: Theory of Dynamic Stripe Induced Superconductivity, *cond-mat/*0012448.

[213] T. Regge: Symmetry Properties of the Clebsch-Gordan coefficients, *Nuovo Cimento* **10** 544, (1958).

[214] G. Racah: theory of complex spectra II, *Phys. Rev.* **62** 438, (1942).

[215] G. Racah: theory of complex spectra III, *Phys. Rev.* **63** 367, (1943).